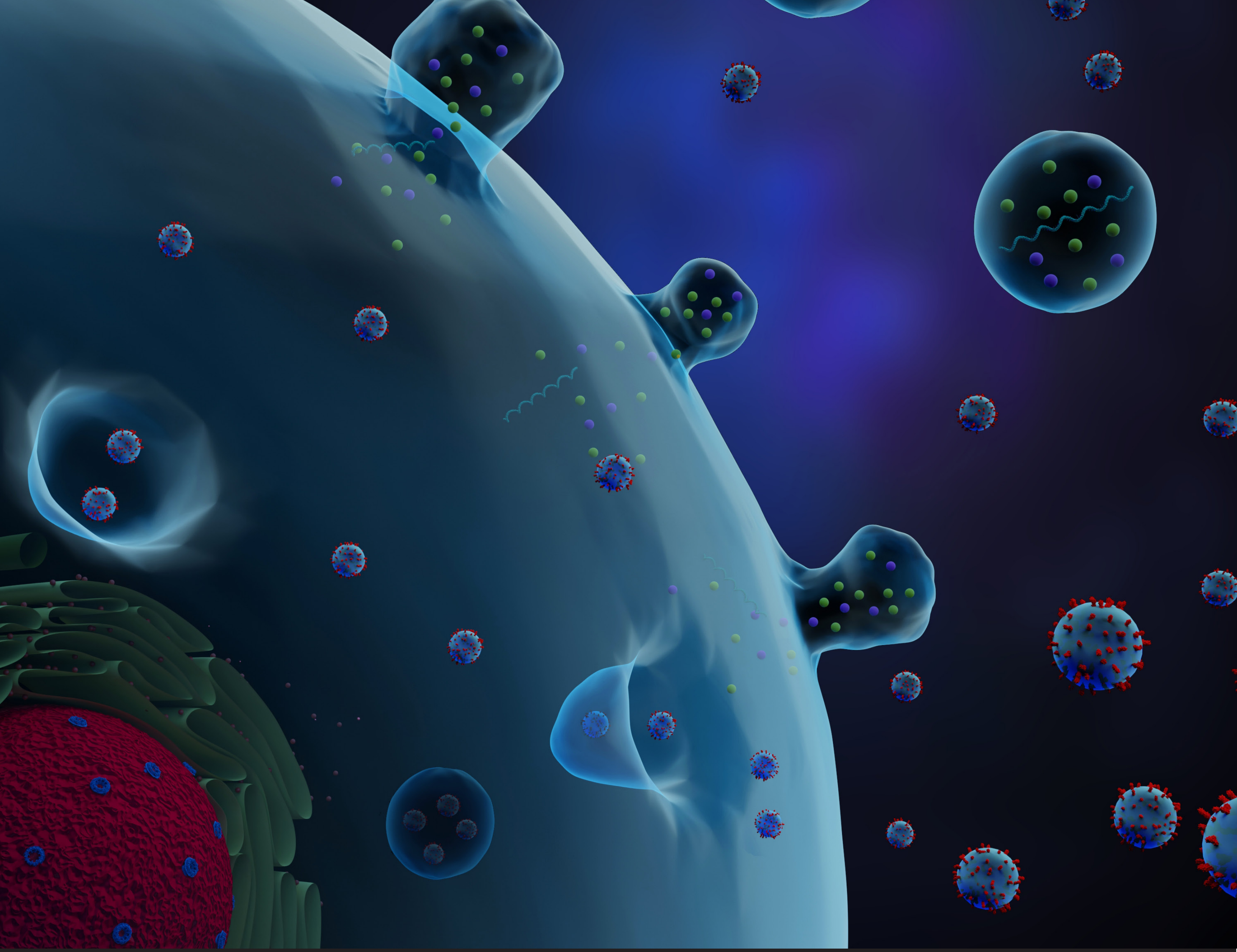

Exosome Production, Isolation and Applications: From Cancer Research to Therapeutic Targets

ARTICLE COLLECTION

WILEY

Sponsored by:

eppendorf


himac


himac

Contents

COVER IMAGE © SHUTTERSTOCK

Introduction

Extracellular vesicles (EVs), particularly exosomes, are small, membrane-bound particles that are released by cells and can be found in various biological fluids. They play a crucial role in intercellular communication and are involved in various physiological and pathological processes, including cancer. Tumor-derived exosomes promote cancer progression and metastasis, regulate drug resistance, and have been investigated clinically as diagnostic biomarkers, therapeutic targets, and drug-delivery vehicles. The bioprocess to isolate exosomes involves culturing cells, collecting their conditioned media, and using techniques like ultracentrifugation to separate and purify exosomes from other substances, enabling their characterization and use in various applications. This article collection focuses on the isolation of exosomes and their potential applications. The articles cover a range of topics, including the identification of novel small EV production modulators, effective methods for isolation and purification of EVs from plants, the use of engineered exosomes in tumor immunology, and the bioprocessing of mesenchymal stromal cell-derived EVs in stirred-tank bioreactors. Isolating exosomes is crucial for developing new diagnostic tools and cancer therapies due to their potential applications in cancer diagnosis and treatment.

First, Tang (2020) provides an overview of the current understanding of cancer exosomes and their clinical implications. The article discusses the potential use of exosomes as biomarkers for cancer diagnosis and prognosis and highlights the challenges associated with their isolation and characterization. Then, Alptekin (2022) discusses the potential use of engineered exosomes as immunotherapeutic agents in cancer. It highlights the ability of engineered exosomes to deliver therapeutic cargo, including proteins and nucleic acids, to specific cells in the tumor microenvironment. Yamamoto (2022) next describes a novel method for identifying small EV production modulators. They show the use of a luciferase-based quantification method to screen for small molecules that can modulate EV production. Following this, Wang (2021) describes the use of exosomal miRNA as a potential biomarker for breast cancer. The article describes the ability of circulating exosomal miR-363-5p to inhibit lymph node metastasis in breast cancer and its potential use as a noninvasive biomarker for the disease.

Next, Costa (2023) focuses on the bioprocessing of mesenchymal stromal cell-derived EVs in stirred-tank bioreactors. They demonstrate the importance of bioprocess control in the manufacture of EVs and describe the use of process analytical technology to optimize EV production. Huang (2021) then discusses the isolation and purification of EVs from plants. This article displays the potential applications of plant-derived EVs in agriculture and biotechnology and describes effective methods for their isolation and purification. Lastly, Ditte (2022) describes the role of EVs in the differentiation of neural stem cells. They exhibit the potential use of EVs as a therapeutic agent in neurodegenerative diseases.

This collection of articles showcases novel methods for the isolation, identification, and purification of EVs, which are crucial for the development of new diagnostic tools and therapies for various diseases. Additionally, despite the evolving landscape of EV research, ultracentrifuges remain the gold standard in their isolation. This emphasizes the significance of robust isolation techniques in advancing EV research. While challenges still exist, the potential applications of EVs in clinical practice make them an important area of research. Further exploration of EV biology and their clinical potential is necessary.

This article collection aims to inform researchers about new ultracentrifugation methods and applications for exosome isolation. For additional information, please visit Your Centrifuge Solutions - Eppendorf to learn more about enhancing your research options.

Christene A. Smith, PhD
Editor at Wiley

References

Tang, Z., Li, D., Hou, S., & Zhu, X. (2020). The cancer exosomes: Clinical implications, applications and challenges. Int J Cancer, 146(11), 2946-2959. https://doi.org/10.1002/ijc.32762

Alptekin, A., Parvin, M., Chowdhury, H. I., Rashid, M. H., & Arbab, A. S. (2022). Engineered exosomes for studies in tumor immunology. Immunol Rev, 312(1), 76-102. https://doi.org/10.1111/imr.13107

Yamamoto, A., Takahashi, Y., Inuki, S., Nakagawa, S., Nakao, K., Ohno, H., Doi, M., & Takakura, Y. (2022). The identification of novel small extracellular vesicle (sEV) production modulators using luciferase-based sEV quantification method. J Ex Bio, 1, e62. https://doi.org/10.1002/jex2.62

Wang, X., Qian, T., Bao, S., Zhao, H., Chen, H., Xing, Z., Li, Y., Zhang, M., Meng, X., Wang, C., Wang, J., Gao, H., Liu, J., Zhou, M., & Wang, X. (2021). Circulating exosomal miR-363-5p inhibits lymph node metastasis by downregulating PDGFB and serves as a potential noninvasive biomarker for breast cancer. Mol Oncol., 15(9), 2466-2479. https://doi.org/10.1002/1878-0261.13029

Costa, M. H. G., Costa, M. S., Painho, B., Sousa, C. D., Carrondo, I., Oltra, E., Pelacho, B., Prosper, F., Isidro, I., Alves, P., & Serra, M. (2023). Enhanced bioprocess control to advance the manufacture of mesenchymal stromal cell-derived extracellular vesicles in stirred-tank bioreactors. Biotechnol Bioeng.. Advance online publication. https://doi.org/10.1002/bit.28378

Huang, Y., Wang, S., Cai, Q., & Jin, H. (2021). Effective methods for isolation and purification of extracellular vesicles from plants. J. Integr. Plant Biol., 63(10), 2020-2030. https://doi.org/10.1111/jipb.13181

Ditte, Z., Silbern, I., Ditte, P., Urlaub, H., & Eichele, G. (2022). Extracellular vesicles derived from the choroid plexus trigger the differentiation of neural stem cells. J. Extracell. Vesicles., 11(1), e12276. https://doi.org/10.1002/jev2.12276

IJC
International Journal of Cancer

The cancer exosomes: Clinical implications, applications and challenges

Zhenye Tang[1,2], Dongpei Li[3], Shengping Hou[4] and Xiao Zhu[1,2]

[1]Guangdong Key Laboratory for Research and Development of Natural Drugs, Southern Marine Science and Engineering Guangdong Laboratory (Zhanjiang), The Marine Biomedical Research Institute, Guangdong Medical University, Zhanjiang, China
[2]Cancer Center, The Affiliated Hospital, Guangdong Medical University, Zhanjiang, China
[3]Medical College of Georgia, Augusta University, Augusta, GA
[4]The First Affiliated Hospital of Chongqing Medical University, Chongqing, China

The exosome is a small functional vesicle enriched in selected proteins, lipids and nucleic acids, displaying distinct molecular heterogeneity. Exosomes released can transform the extracellular matrix microenvironments, transmit signals and molecules to recipient cells and trigger changes in their pathophysiological functions. Tumor-derived exosomes mediate the interactions of tumor cells and microenvironment significantly, and they stimulate tumor growth and development through specific signaling pathways related to metastasis, therapeutic resistance and immunosuppression. Exosome biogenesis from tumors often represents abundant biological information, and novel and efficient isolation and detection methods of exosomes provide a promising approach for tumor diagnosis and prognosis estimation. Moreover, exosome can even be developed as therapeutic agents for multiple disease models based on effective material transport characteristics and biofilm specificity. This review reports the clinical implications and challenges of exosomes in cancer progression, therapy resistance, metastasis and immune escape, and underlying cancerogenic pathological phenotypes including fibrosis and viral infection.

Zhenye Tang and Dongpei Li contributed equally to this work.

Key words: cancer exosomes, biomarkers, cancer metastasis, challenges, isolation, drug carriers, therapeutic agents

Abbreviations: ACE: alternating current electrokinetic; AKI: acute kidney injury; ALK: anaplastic lymphoma kinase; AML: acute myeloid leukemia; ANXA6: annexin A6; BMSC: bone marrow-derived mesenchymal stem cell; CAF: cancer-associated fibroblast; CCA: cholangiocarcinoma; CCL2: C–C motif chemokine ligand 2; CCN2: connective tissue growth factor; CCRCC: clear cell renal cell carcinoma; circRNA: circular RNA; CLL: chronic lymphocytic leukemia; CP: chronic pancreatitis; CRC: colorectal cancer; CSCs: cancer stem cells; DC: dendritic cell; EGFR: epidermal growth factor receptor; EMT: epithelial–mesenchymal transition; EOC: epithelial ovarian cancer; ER: endoplasmic reticulum; ESCC: esophageal squamous cell carcinoma; EVs: extracellular vehicles; FGF2: fibroblast growth factor 2; GC: gastric cancer; GPI: glycosylphosphatidylinositol; GSC: glioma stem cell; HBMEC: human brain microvascular endothelial cell; Hbp1: high-mobility group box transcription factor 1; HCC: hepatocellular carcinoma; HGF: hepatocyte growth factor; HGSOC: high-grade serous ovarian cancer; HIF-1: alpha hypoxia-inducible factor-1 alpha; HNC: head and neck cancer; HSCs: hepatic stellate cells; HSP: heat shock protein; lncRNA: long-noncoding RNA; MDR: multi drug resistance; MDSC: myeloid-derived suppressor cell; MIF: migration inhibitory factor; miRNA: microRNA; MM: multiple myeloma; MSC: mesenchymal stem cell; MVB: multivesicular body; NAFLD: nonalcoholic fatty liver disease; nano-DLD: nanoscale deterministic lateral displacement; NK: Natural killer; NPC: nasopharyngeal carcinoma; NSCLC: nonsmall cell lung cancer; OSCC: oral squamous cell carcinoma; p120: p120-catenin; PDAC: pancreatic ductal adenocarcinoma; PD-L1: programmed death-ligand 1; PHD1 and 2: prolyl hydroxylase 1 and 2; PI: proteasome inhibitor; Prkar1a: protein kinase cAMP-dependent type I regulatory subunit alpha; PSCs: pancreatic stellate cells; PTC: papillary thyroid carcinoma; ROC: receiver operating characteristic; siRNA: small interfering RNA; TAM: tumor-associated macrophage; TLR2: Toll-like receptor 2; TLR3: Toll-like receptor 3; TLR7: Toll-like receptor 7; TNF: tumor necrosis factor; TSG101: tumor susceptibility 101 protein; TSP1: thrombospondin-1; VE-Cad: VE-cadherin; VEGF: vascular endothelial growth factor; VEGFa: vascular endothelial growth factor A

Conflict of interest: The authors declare that they have no competing interests.

Grant sponsor: Guangdong Science and Technology Department; **Grant numbers:** 2015A050502048, 2016A050503046; **Grant sponsor:** National Natural Science Foundation of China; **Grant numbers:** 81541153, 81873678; **Grant sponsor:** Southern Marine Science and Engineering Guangdong Laboratory Zhanjiang; **Grant number:** ZJW-2019-07; **Grant sponsor:** The Public Service Platform of South China Sea for R&D Biomedicine Resources; **Grant number:** GDMUK201808

DOI: 10.1002/ijc.32762

History: Received 6 Aug 2019; Accepted 25 Oct 2019; Online 5 Dec 2019

Correspondence to: Xiao Zhu, E-mail: xzhu@gdmu.edu.cn and xiao.zhu@uga.edu or Shengping Hou, E-mail: sphou828@cqmu.edu.cn

Introduction

Exosome is a member of extracellular vesicle and it is a recent popular research object in tumor biology study. Exosome derived from the multivesicular body (MVB) is a vesicle in diameter of 30–150 nm, which basically contains lipids, proteins and nucleic acids. Since exosome had been discovered for the first time in 1983 in serum medium,[1] it was seen as transportation for cellular waste, with little potential research values. Recently, this vesicle with lipid bilayer is found to be indicated to regulate tumor drug resistance, metastases and the suppressed immune response. Tumor-derived exosome can be captured efficiently with a wide variety of novel isolations, which reflects ample oncology information. Furthermore, exosome exists in serum, urine, saliva and any other body fluids universally, spreads *via* body fluids and releases and fuses with the cell membrane to exert physiological effects, these potential biocompatibilities help exosome lead to be transformed into tumor therapeutic agent carrier.

Exosome and Tumor Development

Therapy resistance

Tumor cells and exosomal RNAs. Tumor therapy resistance can be always seen clinically, frequently is associated with tumor-derived exosome that helps tumor cell be prone to regulate therapy resistance phenotype.[2] Wu *et al.*[3] revealed that nonsmall cell carcinoma cell-derived exosome contained anaplastic lymphoma kinase (ALK) carrier reduced the therapeutic effect of ALK inhibitors. Lobb *et al.*[4] demonstrated that mesenchymal nonsmall cell lung cancer (NSCLC) cells changed the chemotherapy tolerance of recipient cells with increased expressed exosomal ZEB1 mRNA (Table 1). Liu *et al.*[5] observed overexpressed exosomal miR-501 in doxorubicin-tolerant gastric cancer (GC) cell and proposed that miR-501 suppressed BLID and inhibited caspase-9/caspase-3 and phosphorylation of Akt (Table 1), offering an exploitable target miR-501 for drug-resistant GC availably. Tumor-related stroma cells can also release exosomes to activate antiviral/NOTCH3 pathways which contribute to breast cancer therapy resistance.[6] Higher levels of tumor-derived exosomes are prone to affect therapy resistance, and exosomal RNAs regulate major tumor therapy resistance, especially noncoding RNAs. Zeng *et al.*[7] tested and identified miR-151a loss pathway was key element of temozolomide-resistant glioblastoma multiforme, and miR-151a also provided a potential avenue for therapy-refractory GBMs (Table 1). Moreover, exosomal long-noncoding RNA (lncRNA) SBF2-AS1 (lncSBF2-AS1), could also increase temozolomide tolerance to glioblastoma mainly *via* exerting reconstructive action to tumor microenvironment (Table 1).[8] Qu *et al.*[9] reported an identified lncARSR which increased the expression of AXL and c-MET, was transmitted to renal epithelial cell carcinoma cells, increased sunitinib tolerance (Table 1). Exosomal RNA also represents a novel strategy in enhancing chemosensitivity in cancer, not only for increased therapy tolerance.[10] Liu *et al.*[11] reported colorectal cancer (CRC)-derived exosomal miR-128-3p, could be transmitted to resistant cells and upregulate the expression of E-calcium mucin to inhibit the oxaliplatin-mediated epithelial–mesenchymal transition (EMT), which was a crucial element contributing to resistance (Table 1).

CAF and exosomal RNAs. Exosome derived from cancer-associated fibroblast (CAF) is obviously associated with tumor tolerability, especially exosomal microRNAs (miRNAs), which is the dominating cause of drug and chemotherapy resistance. Richards *et al.*[12] demonstrated that CAFs treated by gemcitabine observably could release plentiful exosomes, which stimulated the expression of inductive factor Snail, further promoted tumor resistance and proliferation. Au *et al.*[13] utilized sequencing technology and further revealed exosomal miR-21 from CAFs was delivered to ovarian cancer cells, suppressed their apoptosis and promoted drug tolerance by binding the target APAF1 (Table 1). MiR-196a from CAF-derived exosome is also a crucial element which increased cisplatin resistance in head and neck cancer (HNC) *via* binding CDKN1B and ING5 (Table 1).[14] Hu *et al.* identified miRNAs accumulated in exosomes released by CAFs in CRC, further concluded that miR-92a-3p secreted from CAFs-derived exosomes could promote chemotherapy resistance *via* EMT (Fig. 1*a*) and decreased mitochondria apoptosis by inhibiting FBXW7 and MOAP1 through Wnt/beta-catenin pathway (Table 1 and Fig. 1*b*).[15] Inhibiting CAF-derived exosomal RNAs provides an alternative modality for the prediction and treatment of therapy resistance in cancer.

TAM and exosomal RNAs. Tumor-associated macrophage (TAM) is another crucial part contributing to poor tumor therapy efficacy and chemo-resistant phenotype. Mikamori *et al.*[16] analyzed and further assumed that it was miR-155 from TAM-derived exosomes that elevated the anti-apoptotic of gemcitabine-tolerant pancreatic ductal adenocarcinoma (PDAC), which provided a therapeutic miRNA target in promoting gemcitabine efficacy of PDAC (Table 1). Not only PDAC, Zhu *et al.*[17] found that exosomal miR-223 exerted a unique effect in the cross-talk between TAM and chemoresistant epithelial ovarian cancer (EOC) cell *via* miR-223/PTEN-PI3K/AKT signaling pathway (Table 1). It is well described that TAMs correlate with advanced GC with Cisplatin-dependent chemotherapy resistance as well. Zheng *et al.*[18] indicated that M2-type TAM transmitted secretive exosomes with miR-21 to GC tissue, consequently antagonized cell apoptosis and triggered PI3K/AKT axis *via* PTEN (Table 1).

MSC and exosomal RNAs. Mesenchymal stem cell (MSC) releases exosome to affect drug resistance of multiple myeloma (MM) within the bone marrow microenvironment. Qu *et al.*[19] evaluated PSMA3 sensitivity in proteasome inhibitors (PI) therapy and found that exosomes RNA PSMA3-AS1 and PSMA3 derived from MSCs could deliver PI resistance of multiple myeloma cells, made them be a promising therapeutic target for PI resistance and prognostic predictors for a clinical response (Table 1).

Table 1. The biomarkers of exosomes derived from various cells and clinical samples in tumors

Ingredients		Cancer types	Sources	Function	Mechanisms
microRNA	miR-9[51]	Glioma	Glioma cell	Metastasis	Angiogenesis
	miR-26a[52]		Glioma stem cell		
	miR-29a[56]		Glioma cell	Immunosuppression	Induce differentiation of myeloid-derived suppressor cells
	miR-92a[56]				
	miR-21[57]	Oral squamous cell carcinoma	Oral squamous cell carcinoma cell		Suppress T cells
	miR-128-3p[62]	Colorectal cancer	Colorectal cancer cell	Drug resistance	Inhibiting epithelial–mesenchymal transition
	miR-25-3p[48]			Metastasis	Angiogenesis
	miR-92a-3p[15]		Cancer-associated fibroblast	Chemotherapy resistance	Epithelial–mesenchymal transition and Wnt/beta-catenin pathway
	miR-151a[7]	Glioblastoma multiforme	Glioblastoma multiforme cell		MiR-151a loss-dependent pathway
	miR-223[17]	Epithelial ovarian cancer	Tumor-associated macrophage		MiR-223/PTEN-PI3K/AKT pathway
	miR-155[16]	Pancreatic ductal adenocarcinoma	Tumor-associated macrophage	Drug resistance	Anti-apoptotic
	miR-196a[14]	Head and neck cancer	Cancer-associated fibroblast		Binding CDKN1B and ING5
	miR-501[5]	Gastric cancer	Gastric cancer cell		Suppressing BLID and inhibited caspase-9/-3 and phosphorylation of Akt
	miR-221[107]		Bone marrow-derived mesenchymal stem cell		Promote adhesion to the matrix and metastatic proliferations
	miR-21[13]	Ovarian cancer	Cancer-associated fibroblast		Suppressing ovarian cancer apoptosis and promoting drug tolerance by binding the target APAF1
	miR-142-3p[38]	Colon cancer	Bone marrow-derived mesenchymal stem cell	Metastasis	Increasing the stemness of stromal cells
	miR-301a-3p[31]	Pancreatic tumor	Pancreatic tumor cell	Metastasis	Trigger the M2 polarization of macrophages and EMT.
	miR-193a-3p[29]	Lung cancer	Bone marrow-derived mesenchymal stem cell	Metastasis	STAT3 signaling and epithelial–mesenchymal transition
	miR-210-3p[29]				
	miR-5100[29]				
	miR-23a[50]		Lung cancer cell		Angiogenesis
	miR-27b-3p[36]	Multiple myeloma	Cancer-associated fibroblast		Reprogramming bone marrow microenvironment
	miR-214-3p28[36]				

(Continues)

Table 1. The biomarkers of exosomes derived from various cells and clinical samples in tumors (Continued)

Ingredients		**Cancer types**	**Sources**	**Function**	**Mechanisms**
	miR-105[28]	Breast cancer	Breast cancer cell		Metabolic reprogramming and alteration of molecular characteristics
	miR-126[78]				
	miR-122[27]	Gastric cancer	Gastric cancer cell		Attenuating glucose uptake by niche cells
	miR-130a[47]				Angiogenesis
	miR-103[53]	Hepatocellular carcinoma	Hepatocellular carcinoma cell		Attenuate the endothelial junction integrity
	miR-21[54]				Induce cancer-associated fibroblasts to release angiogenic cytokines
	miR-23a[62]			Immunosuppression	Suppress T function
	miR-21[43]	Colorectal cancer	Colorectal cancer cell	(Liver) metastasis	Block Toll-like receptor 7 in liver macrophage and elicit secretive interleukin-6 (IL-6) to involve in inflammatory premetastatic niche
	miR-23a[49]	Nasopharyngeal carcinoma	Nasopharyngeal carcinoma cell	Metastasis	Angiogenesis
	miR-19b-3p[46]	Colorectal cancer	–		Epithelial–mesenchymal transition
	miR-1290[71]	Pancreatic cancer	Pancreatic cancer cell	Fibrosis	Trigger α-smooth muscle Actin (ACTA2) and induced genes as well as ERK/Akt signaling and type I C-peptide biosynthesis
Long noncoding RNA	SBF2 AS1[8]	Glioblastoma	Glioblastoma cell	Drug resistance	Exerting reconstructive action to tumor microenvironment
	lncARSR[9]	Renal cell carcinoma	Renal cell carcinoma cell		Increasing expression of AXL and c-MET
	lncRNA-UCA1[32]	Bladder cancer	Bladder cancer cell	Metastasis	Remodeling tumor microenvironment
	lncRNA-APC1[55]	Colorectal cancer	Colorectal cancer cell	Antitumor	Inhibit angiogenesis
	lncRNA H19[10]		Cancer-associated fibroblast	Chemoresistance	–
Circular RNA	circPTGR1[22]	Hepatocellular carcinoma	Hepatocellular carcinoma cell	Metastasis	–
	circNRIP1[29]	Gastric cancer	Gastric cancer cell		Block the expression of miR-149-5p and trigger energy metabolism-related AKT/mTOR axis
Other noncoding RNA	Y RNA hY4[64]	Chronic lymphocytic leukemia	Chronic lymphocytic leukemia cell	Immunosuppression	Release cytokines and activate programmed death ligand-1
	PSMA3[19]	Mesenchymal stem cell	Multiple myeloma	Drug resistance	Deliver proteasome inhibitors resistance of multiple myeloma cell
	PSMA3-AS1[19]				
Protein	ANXA6[44]	Breast cancer	Breast cancer cell	(lung) Metastasis	

(Continues)

Table 1. The biomarkers of exosomes derived from various cells and clinical samples in tumors (Continued)

Ingredients	Cancer types	Sources	Function	Mechanisms
				Induce Ccl2 and broaden Ly6C(+)CCR2 (+) monocyte in the pulmonary premetastatic niche
Programmed death ligand-1[63]	Glioblastoma	Glioblastoma cell	Immunosuppression	Block T cell activation
Heat shock protein 70[58]	Breast cancer	Cancer cell		Activate myeloid-derived suppressor cell
	Lung cancer			
	Ovarian cancer			Activate Stat3 in myeloid-derived suppressor cell
Heat shock protein 72[59]	–	–		
Epidermal growth factor receptor[42]	Gastric cancer	Gastric cancer cell	(liver) Metastasis	Inducing hepatocyte growth factor and targeting c-MET
Ubiquitin protein ligase E3 component n-recognin 2[37]	Gastric cancer	Mesenchymal stem cell	Metastasis	WNT/beta-serial protein pathway
Wnt4[34]	Colorectal cancer	Colorectal cancer cell		Achieve β-catenin translocation into the nucleus in adjacent normal tissue

Cancer metastasis

To some extent, noncoding RNA in exosomes can reflect the tumor-related biological information.[20] Tumor-related exosome regulates the tumor metastasis, and this function mainly depends on exosomal RNA. Fish *et al.*[21] performed a systematic search to identify breast cancer-specific small noncoding RNAs, which drove the metastasis of cancer cells existed in extracellular vehicles mightily. Wang *et al.*[22] sequenced exosomal circular RNA (circRNA) and assumed that circPTGR1 in exosomes regulated higher metastatic hepatocellular carcinoma (HCC) cells to confer metastasis potential on lower or no metastatic potential, resulting in increasing their migratory and invasive abilities (Table 1). Besides, novel function exosomal protein Myoferlin was also validated to facilitate tumor metastasis.[23] Exosomal new functional ingredients call for novel strategies to further reveal this emerging metastatic correlation in human cancer.

Premetastasis microenvironment. Conventionally, primary tumor cells are viewed to spread into distant organs, which contribute to new tumors regeneration, such as brain metastasis.[24] Nonetheless, another dominant view is that the primary tumor such as ovarian cancer releases extracellular vehicles (EVs) that induce premetastatic niche formation to assist tumor cells root in the metastases and grow further.[25] There are shreds of evidence unveiling that targeting premetastatic niche cancer therapy is considered as a promising strategy to intervene in cancer metastasis.

Metabolic microenvironment. Alterations in tumor metabolism are evident hallmarks of metastatic living tumors. Tumor cell can educate fibroblast to be translated into CAF, which is a major cellular component of tumor microenvironment in most solid cancers. Zhao *et al.*[26] utilized intra-exosomal metabolomics and identified that exosomes derived from CAFs provided tumor cells major carbon metabolomics and better contributed to adaptions of the invasive tumor under nutrient deficiency. Cancer reprograms metabolic mechanism mainly *via* exosomes, especially exosomal miRNA which concomitantly facilitates tumor progression. Fong *et al.*[27] found that GC-derived exosomal miR-122 attenuated glucose uptake by niche cells *via* the downregulated glycolytic enzyme pyruvate kinase, showing how cancer cells confined glucose uptake by normal cells in the premetastatic niche (Table 1). Significantly, the underlying interrelation between cancer-derived exosomal miRNAs and stromal cells modulates metabolic state of living tumors. Yan *et al.*[28] observed that breast cancer-derived exosomal miR-105 stimulated metabolic reprogramming of stromal cells and altered the molecular characteristics which helped tumor cell accommodate metabolic microenvironment. Remarkably, Zhang *et al.*[29] discovered that circNRIP1 blocked the expression of miR-149-5p and triggered AKT/mTOR axis which enabled energy metabolism, induced GC metabolic alterations and bolstered

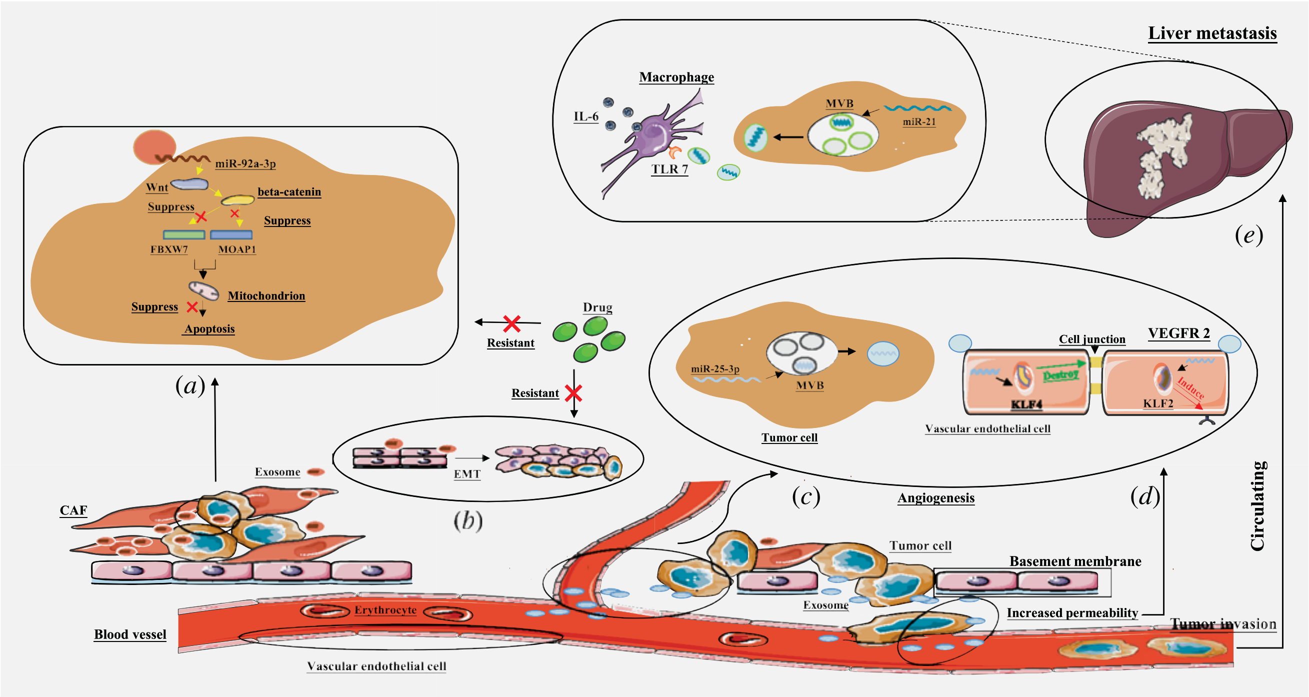

Figure 1. The exosomes in cancer drug resistance and metastasis. (*a*) The cancer-associated fibroblasts secret exosomes with miR-92a-3p induce epithelial–mesenchymal transition (EMT); (*b*) The cancer-associated fibroblasts secret exosomes with miR-92a-3p inhibit mitochondria apoptosis; (*c*) Tumor cells release exosomes with miR-25-3p to induce angiogenesis; (*d*) Tumor cell release exosomes with miR-25-3p to increased permeability. (*e*) Tumor cell releases exosomes with miR-21 to trigger inflammatory premetastatic niche formation. [Color figure can be viewed at wileyonlinelibrary.com]

invasive spread (Table 1). Maybe circRNA acts as a tumor promotor as well as a miRNA sponge in tumor metabolic system.[30] Anyway, emerging evidences reveal the pivotal role of exosomes in tumor initiation and aggressiveness, through reprogramming systemic metabolism noticeably.

Hypoxic microenvironment. Exosome and its components coactivate intercellular cross-talk between metastatic malignancy and normal tissue under environmental low oxygen tension. Wang *et al.*[31] purposed that anoxic pancreatic tumor cells recruited exosomal miR-301a-3p to trigger the M2 polarization of macrophages through the PTEN/PI3Kγ axis, led to a greater invasive depth of cancer cells as well as EMT (Table 1). And Xue *et al.*[32] isolated and identified hypoxic bladder cancer cell-derived exosomes, and their result showed that oncogenic lncRNA-UCA1-enriched exosomes remodeled tumor microenvironment to facilitate tumor growth (Table 1). Perhaps exosomal RNAs are critical for microenvironmental cross-talk and modulate malignant behaviors of solid tumors. Also, exosomes transfer specific signaling proteins to coordinate regional or distant spread in hypoxic surroundings. Chen *et al.*[33] performed omics profiling and reported that transcriptional and translational downregulations of human colon cancer-associated genes activated exosomes as well as proteinic factors modifications in endoplasmic reticulum (ER), which was relevant to a higher risk of malignant metastatic behaviors. And Huang *et al.*[34] proposed that hypoxic CRC cells promoted Wnt4-carried exosomes to achieve β-catenin translocation into the nucleus in adjacent normal tissue, which further drove CRC metastasis (Table 1). Thus, hypoxic microenvironment is a potent factor in augmenting metastasis and it remains a major therapeutic challenge in clinic, however.

Bone marrow microenvironment. Tumor-derived exosome is recognized to involve in the formation of bone marrow microenvironment. Yan *et al.*[35] provided evidence that acute myeloid leukemia (AML) cells secreted exosomes to express DKK1 and upregulated normal hematopoiesis and osteogenesis, resulting in osteoblast loss bone marrow microenvironment. It indicates that leukemia-derived exosomes support the bone marrow niche which facilitates invasion. Meanwhile, exosomes derived from multiple myeloma could educate the marrow CAFs to modify the bone marrow microenvironment *via* overexpressed miR-27b-3p and miR-214-3p[36] showed that tumor-derived exosomes also confer the microenvironment-reprogrammed capability to other cells.

As another significant ingredient in the tumorous bone marrow microenvironment, MSC transfers bioactive vehicles to affect the tumor-related premetastasis. In GC microenvironment, Mao *et al.*[37] provided evidence to show that exosome derived from p53 deficient bone marrow-derived MSC (BMSC) loaded ubiquitin protein ligase E3 component n-recognin 2 (UBR2) and facilitated GC metastasis *via* the

Wnt/beta-catenin pathway (Table 1). Exosomes released from BMSCs also transmitted miR-142-3p to increase the stemness of stromal cells, which contributed to higher metastatic colon cancer cells.[38] Unlike normal MSCs, tumor-related MSCs not only possess a strong ability to promote tumor progression and but also confers this ability on normal MSCs. Tumor-related MSC secreted CCR2 ligands, CCL2 and CCL7 abundantly, which recruited macrophage and drove MSC to induce macrophage infiltration into melanoma or lymphoma, explained how normal MSC be converted to tumor-related MSC.[39]

Organ-specific metastasis. Integrin can accelerate lung epithelial cells and liver Kupffer cells to absorbed exosomes to establish a premetastasis niche.[40] That indicated that exosomes are key to the formation of a suitable premetastatic microenvironment between primary tumors and distal organs, which most commonly involved organs are the liver and lung and bone.

Liver metastasis. Tumor-derived exosomes intake by liver-specific cells prepare the premetastatic niche. Costa-Silva *et al.*[41] demonstrated that migration inhibitory factor (MIF) in exosomes secreted from PDAC stimulated Kupffer cells to structure liver fibrosis premetastatic niche and primed liver metastatic. And Zhang *et al.*[42] showed that GC-secreted exosomes allowed epidermal growth factor receptor (EGFR) to be transmitted to liver, subsequently activated hepatocyte growth factor (HGF) and targeted c-MET (Table 1). Another suspicious clinical predictor, such as miRNA, also leads to liver metastasis. Shao *et al.*[43] identified that CRC-derived exosomes enriched in miR-21 blocked Toll-like receptor 7 (TLR7) in liver macrophage, as well as eliciting former to release secretive interleukin-6 (IL-6), resulting in inflammatory premetastatic niche formation *via* miR-21-TLR7-IL-6 signaling pathway (Table 1, Fig. 1*e*). Emerging evidence reveals that exosome represents a vital mediator of the liver-metastatic cascade in malignancy.

Lung metastasis. Lung premetastatic niche constructed by primary tumor-derived exosomes benefits cancer metastasis. Keklikoglou *et al.*[44] also showed that breast cancer-derived annexin A6 (ANXA6) in chemotherapy-treated exosomes stimulated NF-kappaB-dependent endothelial cell, induced Ccl2 and broaden Ly6C(+)CCR2(+) monocyte in the pulmonary premetastatic niche to facilitate lung metastasis stimulates endothelial cells (Table 1). Lobb *et al.*[45] detected tumor exosomal RNAs through and showed that exosomes enriched in RNAs could stimulate Toll-like receptor 3 (TLR3) in lung epithelial cells, which was conducive to release chemokine in the lung and recruited neutrophil. This study further indicated that the role of lung epithelial cells in the lung metastatic niche formation. Moreover, EMT is characterized by conferring tumor cell a high lung metastatic potential. Wang *et al.*[46] found that exosomal miR-19b-3p delivered to clear cell renal cell carcinoma (CCRCC) cells were capable to activate EMT by upregulating the expression of PTEN, which made CCRCC possess lung metastasis capability (Table 1).

Angiogenesis. Angiogenesis involves new blood vessels growing from the existing blood vessels and complex endothelial cell activities, always with increased vascular permeability, which is conducive to tumor proliferation and migration. Emerging evidence indicates exosomal miRNAs mediate tumor-associated angiogenesis. Yang *et al.*[47] performed sequential differential centrifugation and identified that exosomal miR-130a derived from GC cells could activate vascular cells *via* binding c-MYB, indicated that miR-130a drove angiogenesis (Table 1). Zeng *et al.*[48] validated that miR-25-3p, a metastasis-promoting miRNA existing in CRC cells, could be transferred to endothelial cells *via* exosomes, regulated the expression of VEGFR2 by targeting KLF2 and KLF4, further contributed to increased vascular permeability and angiogenesis (Table 1 and Figs. 1*c* and 1*d*). Also, melanoma-derived exosomal miR-155-5p could induce fibroblasts to express of proangiogenic factors, including vascular endothelial growth factor A (VEGFa), fibroblast growth factor 2 (FGF2) and etc. *via* upregulated cytokine signaling 1 (Table 1), which provided novel strategies to suppress melanoma proliferation. Angiogenesis is not a simple one-to-one correspondence regulated by exosomal miRNAs. Bao *et al.*[49] detected and identified that highly enriched miR-23a regulated angiogenesis by targeting gene TSGA10 in nasopharyngeal carcinoma (NPC; Table 1). Under the hypoxic circumstance, Hsu *et al.*[50] found that lung cancer-derived suppressing miR-23a in exosomes could upregulate prolyl hydroxylase 1 and 2 (PHD1 and 2), accumulated hypoxia-inducible factor-1 alpha (HIF-1 alpha) in endothelial cells so as to induce angiogenesis and promote vascular permeability (Table 1). In human glioma, Chen *et al.*[51] measured the expression of miR-9 and elucidated that upregulated exosomal miR-9 released from glioma cells was absorbed by vascular endothelial cells and targeted COL18A1, THBS2, PTCH1 and PHD3, contributing to promoted angiogenesis (Table 1). Similarly, glioma stem cells (GSC)-derived activated exosomal miR-26a downregulated PTEN and promoted angiogenesis of human brain microvascular endothelial cell (HBMEC) *via* PI3K/Akt signaling pathway[52] (Table 1). Angiogenesis is also valuable in accelerating HCC proliferation. Fang *et al.*[53] sequenced and quantitated PCR and found that HCC cell-derived exosomes transmitted miR-103 into endothelial cells attenuated the endothelial junction integrity by downregulating VE-Cadherin (VE-Cad), p120-catenin (p120) and zonula occludens 1 (Table 1). Also, there is emerging evidence indicating that HCC-derived exosomal miR-21 targeting PTEN led to the activation of PDK1/AKT signaling in HSCs, which educated CAFs released angiogenic cytokines, including VEGF, MMP2, MMP9, bFGF and TGF-beta (Table 1).[54] To abate angiogenesis remains a severe challenge for tumor treatment. Wang *et al.*[55] examined the expression of lncRNA-APC1 and unveiled that lncRNA-APC1 activated by APC suppressed CRC angiogenesis *via* targeting Rab5b mRNA, which could inhibit tumor angiogenesis in CRC (Table 1). This finding advances our understanding of APC-regulated lncRNA-APC1 procedure which downregulates angiogenesis provides an exploitable therapeutic approach for CRC.

Immunosuppression

Exosomes and MDSC. Myeloid-derived suppressor cell (MDSC) plays a crucial part in regulating the immunosuppressive microenvironment and assisting tumor to escape the immune response. Guo *et al.*[56] elucidated that glioma exosomal miR-29a and miR-92a induced differentiation of functional MDSCs by binding high-mobility group box transcription factor 1 (Hbp1) and cAMP-reliant type I regulatory subunit alpha (Prkar1a) respectively to mediate the formation of immunosuppressive microenvironments in tumors (Table 1). Compared to a normoxic condition, hypoxic evolution mediated by exosomes is also of great significance to the tumor immunosuppressive microenvironment which involves MDSC. Li *et al.*[57] reported that hypoxic oral squamous cell carcinoma (OSCC)-derived exosomes activated T-cell inadequately and improved the suppressive effect of MDSCs on gamma delta T cells through a miR-21/PTEN/PD-L1 signaling pathway (Table 1). Exosomes with overexpressed membranous heat-shock protein (HSP) are capable to communicate with MDSCs *via* the toll-like receptor 2 (TLR2). Gobbo *et al.*[58] compared cancer-derived exosomes various samples with different approaches and demonstrated that cancer cells were observed to secrete plentiful exosomes with HSP70 to activate MDSCs *via* HSP70/TLR2 in breast cancer, lung cancer and ovarian cancer (Table 1). This result also reveals that cisplatin or 5FU combined with A8 was a promising approach to suppress MDSCs. Similarly, Chalmin *et al.*[59] also found that Hsp72 also released IL-6 to activate Stat3 in MDSCs *via* TLR2/MyD88-dependent signaling pathway, which was conducive to suppress tumor immune surveillance as well (Table 1).

Exosomes and PD-L1. Circulating cancer cells frequently escape immunological surveillance *via* exosomes-displaying programmed death-ligand 1 (PD-L1).[60] Poggio *et al.*[61] demonstrated that exosomal PD-L1 triggered the silent expression of T cell, while blocked PD-L1 can induce antitumor immune response and provide efficient remissions for tumor patients. The result unveils that PD-L1 remains an unexplored target. Liu *et al.*[62] provided a new perspective that ER stress urged HCC cells to secrete exosomes to stimulate PD-L1 activation in macrophages, consequently suppressed T-cell function *via* miR-23a-PTEN-AKT regulated axis in HCC (Table 1). Ricklefs *et al.*[63] hypothesized and further identified that glioblastoma exosomal PD-L1 mediated by IFN-gamma induced PD-L1-dependent inhibition of T cell function. Also, in chronic lymphocytic leukemia (CLL), exosomal noncoding Y RNA hY4 stimulated monocytes to change phenotypes, which results in secreting cytokines including C–C motif chemokine ligand 2 (CCL2), CCL4 and interleukin-6 and activated PD-L1 to induce monocytes and macrophages skewed toward pro-tumorigenic phenotypes, this further suggests that stimulated PD-L1 mediated immune escape from another perspective.[64]

Pathological phenotypes

Fibrosis. Drug therapy potently alleviates the migration of highly metastatic CRC *via* ameliorating the fibrotic decompensation of the metastatic organ. Perhaps there is an underlying link between fibrosis status and tumor invasion,[65,66] but this potential pathological phenotype still requires more clear elucidations. Cai *et al.*[67] suggested that exosomes cause major alterations in liver fibrosis, HCC and other liver diseases. And Chen *et al.*[68] reported that connective tissue growth factor (CCN2) involved live fibrosis, and hepatic stellate cells (HSCs) displayed CCN2, α-smooth muscle actin or collagen 1 (α1) while concomitant expression of exosomal miR-199a-5p was blocked, resulted in fibrogenic gene transcriptional and translational upregulations. Also, lncRNAs involve in inducing HSCs and subsequent liver fibrosis, which mechanically help exosomal MALAT1 trigger HSCs *via* miR-26b expression.[69] Strikingly, fibrosis also participates in other human organs' injury developments, and this represents a terrible risk factor of tumor initiation. Xu *et al.*[70] proposed that PM elicited pulmonary epithelium-secreted exosomes which contained ample miRNAs, gradually led to pulmonary diseases such as fibrosis and concomitant carcinogenesis. Masamune *et al.*[71] found that pancreatic cancer cells transmitted exosomes with miR-1290 to pancreatic stellate cells (PSCs), whose α-smooth muscle actin (ACTA2) and fibrosis-induced genes was highly stimulated, as well as the inductions of ERK/Akt signaling and type I C-peptide biosynthesis (Table 1). Together, cancer-containing exosomes involve in cell–cell communication and dynamically modulate gene expressions, and this is conducive to make fibrosis optimize tumor microenvironment, targeting this interaction may provide strategic approaches for vanishing fibroproliferative cancer.

Viral infection. Exosomes carry bioactive substances including nucleic acid and protein, which are converted into tools to modulate virus propagation and infection. Mata-Rocha *et al.*[72] discovered that cervical cancer samples derived abundant exosomal HPV DNA such as oncogenes E6/E7. Zhou *et al.*[73] identified that newcastle disease virus (NDV)-infected cervical cancer cells also released exosomes loading several specific miRNAs to suppress IFN signaling and enhance NDV replication. And Ikoma *et al.*[74] confirmed that exosomal miRNAs which were linked to virus and living tumor allowed precise detections from patient populations with KSHV-related Kaposi's sarcoma. A viral protein, EBV-encoded latent membrane protein 1 (LMP1), derives from infected tumor cells and manipulates the host exosomes channel. Meckes *et al.*[75]

identified that exosomes derived from EBV-infected NPC cells used ample viral oncogenes, LMP1 and viral miRNAs to trigger significant signatures in recipient cells and tuned the cancer-linked microenvironment. Strikingly, Santangelo *et al.*[76] reported that exosomes mediated the correlation among hepatocyte and immune microenvironment, mainly patients with HCV infection displayed degranulation downregulation natural killer (NK) cells which was linked to miR-122-5p or miR-222-3p. Exosomes and their cargo correlate with not only tumorigenesis potential under virus-infected status but also virus-associated immunopathogenesis, perhaps also involve in pathophysiological states in living tumors, even assist cancer cells to block innate immune cells.

Exosomes and antitumor immune response

Natural killer cell-mediated immune response. NK cells exert rapid immune effect to metastatic or hematological malignancies, which have been confirmed and clinically exploited the antitumor characteristics. Zhu *et al.*[77] explored that NK-92MI cells produce exosomes with two functional NK proteins, perforin, FasL and secreted tumor necrosis factor (TNF)-alpha, which affected the cell proliferation, to exert cytotoxic effects on melanoma cells without side effects. Furthermore, Wu *et al.*[78] studied NK cell-derived exosomes and their result revealed that at NK-derived exosome presented perforin, granzyme A, granzyme B, granulysin and FasL could mediate cytotoxicity against cancer cells *via* caspase-independent and caspase-dependent cell death signaling pathways. Not only proteins presented on NK cells, exosomal tumor suppressor miR-186 also showed cytotoxicity to the amplified neuroblastoma. Neviani *et al.*[79] demonstrated that miR-186 transmitted to NK cells resulted in prevention of neuroblastoma tumorigenic potential and suppressed the silent NK cells regulated TGFbeta1-dependent signaling pathway. NK cells activate multiple killing pathways *via* exosomes, and this trait makes them a promising perspective on clinical immunotherapy.

Dendritic cell-mediated immune response. Exosomes constitute a stable correlation between antigens and immune cells by binding dendritic cell (DCs) and facilitating immune surveillance of activated T cell.[80] That is to say, unlike NK cells, DCs could regulate tumor immune *via* exosomes with various approaches. Rao *et al.*[81] found that exosomes derived from HCC presented carcinogenic antigens induced DCs to exert a strong immune response that increased T cells and improved the HCC immune microenvironment.

The Innovative Approaches to Detect Tumor-Derived Exosomes from Clinical Samples

Microfluidic techniques

Microfluidic chip represents a comprehensive and noninvasive diagnostic tool for exosome-reliant separation and analysis. Wunsch *et al.*[82] developed nanoscale deterministic lateral displacement (nano-DLD) arrays which could isolate exosomes as low as 20 nm, with a high percentage of purified exosomes <150 nm. This technique constructs a platform to classify tumor-associated molecular EVs. Fang *et al.*[83] proposed a microfluidic chip based on immune capture, which could extract exosomes with immune capture function from small quantified breast cancer samples and help clinical diagnosis of breast cancer patients. Ibsen *et al.*[84] designed an alternating current electrokinetic (ACE) microarray device, which allowed the isolation of glioblastoma-derived exosomes from a plasma sample (30–50 µl), as well as apparently simplifying processing steps and enabling less time required. Another comprehensive exosome analysis tool and potential noninvasive diagnostic platform, ExoPCD-chip, is a two-stage microfluidic platform whose isolation and analysis applied for liver cancer-derived exosomes as low as 4.39×10^3 particles/ml from a serum sample (30 µl) within 3.5 hr.[85] Microfluidic chip is capable to effectively isolate exosomal ingredients as well. Reategui *et al.*[86] established a microfluidic platform named (EV)HB-Chip which captured glioblastoma multiforme-derived characteristic exosomal RNA within 3 hr, contributing to identifying specific genes and subtypes of this disease. Dorayappan *et al.*[87] demonstrated a specific microfluidic-based internal separation device for the establishment of exosomal protein profiles of high-grade serous ovarian cancer (HGSOC) within 20 min, overcoming contamination problems and making new findings for early exosome-based detection. Consequently, the microfluidic chip undoubtedly lays a solid foundation for early diagnosis and prognosis of cancer and it is substantially better than many other existing methods.

Aptasensor techniques

The characteristic small size of the exosome makes its quantitative detection more complicated, and it remains a major problem to detect cancer-specific exosomes due to technical restrictions and biological challenges. Nonetheless, the aptasensor technique with the advantages of low cost, simple operation and small sample volume has a broad prospect. Xia *et al.*[88] invented a colorimetric aptasensor that mechanically relied on the conjunct administration of carbon nanotubes and aptamer, which enabled the detection of the limit of 5.2×10^5 particles/µl (Table 2). The result proves that a visible approach to capture exosomes is perfectly constructed. Also, the aptasensor technique can apply for the isolation of tumor-derived exosomes. Huang *et al.*[89] provided sufficient evidences that an electrochemical aptasensor based on Hemin/G-Quadruplex-Assisted Signal Amplification could detect exosomes derived from GC limit of 9.54×10^2 particles/µl (Table 2), which was a visible and sensitive platform for the early diagnosis of GC. Wang *et al.*[90] demonstrated another efficient surface plasmon resonance (SPR)-reliant aptasensor for breast cancer, which allowed the detection of the limit of 5×10^3 particles/ml (Table 2), as well as offering an avenue to capture breast cancer-derived exosomes consequently. Liu

Table 2. The innovative approaches to detect exosomes from clinical samples

Methods	Cancer types	Mechanisms	Traits	
Aptasensor technology	Colorimetric aptasensor[88]	–	The integration of carbon nanotubes and aptamer	Enable the detection of limit of 5.2×10^5 particles/µl
	Electrochemical aptasensor[89]	Gastric cancer	Hemin/G-Quadruplex-Assisted Signal Amplification	Permit the detection of limit of 9.54×10^2/µl
	Surface plasmon resonance aptasensor[90]	Breast cancer	Surface plasmon resonance	Allow the detection of limit of 5×10^3 exosomes/µl
	Thermophoretic aptasensor[91]	Gastric cancer	Thermophoretic enrichment of exosomes conjugated with aptamers	Capture 7 kinds of EVs protein biomarkers with the limit of a serum sample (<1 microl), as well as costing only 1 dollar within 3 hr
		Lung cancer		
		Ovarian cancer		
		Prostatic cancer		
		Hepatocellular carcinoma		
		Lymphomas		
Microfluidic technology	Nanoscale deterministic lateral displacement arrays[82]	–	Nanoscale deterministic lateral displacement	Isolate exosomes as low as 20 nm with a high percentage of purified exosomes <150 nm
	Microfluidic chip[83]	Breast cancer	Immunocapture	With small samples quantized
	Alternating current electrokinetic microarray microarray chip device[84]	Glioblastoma	Alternating current electrokinetic microarray	With a plasma sample (30–50 µl), as well as simplifying processing steps and decreasing required time
	ExoPCD-chip[85]	Liver cancer	Two-stage microfluidic platform	With the limit of exosomes as low as 4.39×10^3 particles/ml from a serum sample (30 µl) within 3.5 hr
	(EV)HB-Chip[86]	Glioblastoma multiforme	Microfluidic platform	Capture exosomal RNA within 3 hr
	In-house microfluidic-based device[87]	High-grade serous ovarian cancer	Based on in-house microfluidic isolation and protein profiling	Profile protein within 20 min and overcome contamination issues

et al.[91] reported that a thermophoretic aptasensor based on enrichment of exosomes conjugated with aptamers could detect the tumor-derived EVs and seven kinds of EVs protein biomarkers from a serum sample (<1 µl), including breast cancer, lung cancer, ovarian cancer, prostatic cancer, HCC and lymphomas, which only cost one dollar within 3 hr (Table 2). This vital finding provides an unprecedented quantification method to detect ample purer cancer-derived exosomes efficiently in multiple cancer samples.

The Clinical Applications of Tumor Exosomes

Diagnosis biomarkers

Exosomal ingredients are always highly expressed in cancer progression, which can be detected in the early stage of cancer. Li *et al.*[92] described the potential diagnosis value of ample exosomal RNAs, such as miRNAs, circRNAs and lncRNAs in plasma *via* long RNA sequencing. Fan *et al.*[93] validated almost 2,000 upregulated and downregulated circRNAs in esophageal squamous cell carcinoma (ESCC) tissue, filling the diagnostic circRNAs gap in ESCC. Jin *et al.*[94] observed and identified ample special miRNAs which could differentiate adenocarcinoma and squamous cell carcinoma in NSCLC. These highly sensitive miRNAs biomarkers are conducive to diagnose early NSCLC. Liu *et al.*[95] utilized receiver operating characteristic (ROC) curve analysis and identified distinct diagnostic plasma miR-486-5p of CRC. Taylor *et al.*[96] utilized miRNA profiling to further assessed the prospects exosomal miRNAs as promising diagnostic markers of ovarian cancer. Lai *et al.*[97] analyzed the level of miRNAs and glypican-1 in PDAC and chronic pancreatitis (CP), concluded that miRNA is more advantageous in diagnosing PDAC. However, available RNA biomarkers for cholangiocarcinoma (CCA) and HCC has not been discovered. Arbelaiz *et al.*[98] discovered abundant oncogenic proteins from human saliva and serum. And in GC microenvironment, Fu *et al.*[99] proposed that TRIM3 protein upregulated stem cell factor and EMT regulatory factor inhibited metastatic proliferation, suggesting another strategic approach to optimize diagnosis of patients with GC. Common tumor-related exosome ingredients including RNA and protein are not availably detected in prostate cancer, other exosomal ingredients, like small metabolites, are significantly lower in urine from prostate cancer patients.[100] Similarly, the high-level of exosome lipids in urine is also remarkably different, which has the value of diagnosing prostate cancer.[101] Further researches focusing on intrinsically bioactive ingredients loaded by exosomes might offer a unique avenue on tumor aggressiveness and concomitantly enhance our understanding of potentially harmful factors in cancer patients.

Therapeutic applications

RNA therapeutic agents. Exosome-dependent RNA therapy such as small interfering RNA (siRNA) loading significantly impairs malignancies. For instance, Kamerkar *et al.*[102] proposed a CD47-reliant engineered exosome that specially deliver siRNA to target oncogenic KRAS mutation, which drove pancreatic cancer. To make exosomes be envisioned as a generic siRNA delivery system raises great interests in gene therapy. To exploit the reproducible siRNA loading method, Stremersch *et al.*[103] reported a novel nanoplatform that realized exosome-like microvesicles surface-binding cholesterol-attached siRNA. Pi *et al.*[104] presented another modified exosome that relied on RNA nanotechnology, which allowed cholesterol to anchor RNA and resulted in RNA ligand-displaying on membranal exosomes, when these exosomes integrated with prostate-specific membrane antigen aptamer or breast-specific EGFR aptamer, subsequently suppressed prostate and breast cancer xenograft. In order to better encapsulate miRNA in plasma-derived exosomes and preserves their target specificity, Li *et al.*[105] designed an exosomes fused with CD9 and HuR that triggered the enrichment of miR-155 in EVs, subsequently was delivered to recipient cells and achieved the endogenous target specificity. Hobor *et al.*[106] demonstrated an RNA-binding Syncrip's amino-terminal domain selectively targeted miRNA in exosome-like vesicles through the recognition between the N-terminal unit for RNA (NURR) and Syncrip's RRM 5′ as well as hEXO sequence. Thus, to engineer exosomes for RNA loading by binding a functionalized fusion protein is flexible and feasible. In sum, these results define the underlying value of versatile exosomal RNA-dependent cancer therapeutics, and provide several optimization schemes for optimizing exosome-mediated delivery as well.

Drug carriers. To reverse the drug resistant-cancer cell subpopulations is a crying need to prompt outcomes of patients with malignancies in clinic. Drug-modified exosomes can solve this problem, which has made rapid progress. Ma *et al.*[107] found that tumor regenerated cells can absorb exosomes packaged with antitumor drugs, including efflux of interventional drugs and acceleration of drug entry into the nucleus, which raised interests in reversing drug resistance. And Kim *et al.*[108] demonstrated a novel exosome-based system named paclitaxel-loading exosomes, further improved efficacy in the treatment of multidrug resistant cancer cells, through sonication-modified membranal reformation of exosome-like vesicles. Importantly, loading of conventional methods is too low for proteinic drug loading and exists obvious lack of target cell specificity, leads exosome-like vesicles to be restricted by intracellular transmission of drug-based therapeutics. Yim *et al.*[109] proposed a systematic nanoplatform, protein loading *via* optically reversible protein–protein interaction (EXPLORs), which utilized blue light to achieve carry of diverse functional proteins including Cre recombinase into exosome-like microvesicles. Lin *et al.*[110] revealed a novel exosome-reliant delivery nanoplatform modified by the micelle-aided manner, which installed an integrin α3β1-binding octapeptide cNGQGEQc for NSCLC targeting, for integrin α3β1 specifically displayed on NSCLC cells. Kooijmans *et al.*[111] designed a nanoparticle that displayed on exosome surface *via* glycolipatidylinositol (GPI) to enhance target cell specificity and enable exosomes to achieve therapeutic applicability. And Qi *et al.*[112] developed an exogenous exosomes-dependent cluster of dual-functional superparamagnetic nanoparticles, which contributed to higher cancer targeting specificity in the magnetic field. Above all, the design of exosomal drug carriers with efficient delivery ability represents an important step in the development of tumor therapeutic agents.

Challenges and Future Outlook

Although we have achieved good results in targeted cancer therapies and immunotherapies, malignant tumors are still difficult to cure and more specific mechanisms of tumor metastasis, drug resistance and immunosuppression are still at an early stage and remain elusive. What's more, potential cancer-related pathological phenotypes like fibrosis and viral infection provide a specific perspective for revealing the rationale of cancer-derived exosomes in physiopathologic lesions, which may contribute to the progress of personalized cancer therapy 1 day. Tumor cells and related significant changes, release multifunctional tumor-derived exosomes, reshape the surrounding microenvironment and resist antitumor therapy in the process of tumorigenesis. In addition, tumor cells secrete exosomes, which change the microenvironment of distal organs through the composition of various body fluids such as lungs and liver, contributing to better tumor growth. Immune release and immunosuppression occur before cancer invades, and also due to exosome-mediated changes in the density of various immune cells, targeting tumor-related exosome therapy. More and more evidences show that exosomes are involved in tumor invasion, which may be an exploitable target. Furthermore, compared to the existing biology-based drug delivery system, the application of stem cell exosomes has several merits. These cell-derived and nanoscale vesicles are abundant in body fluids, including peripheral blood, urine, cerebrospinal fluid and supernatant of cultured cells *in vitro*, which have significantly superior biocompatibility to deliver their contents, such as genetic information and proteins, through the fusion of cell membranes. These superiorities have led to new therapeutic applications, especially contribute to potent detection of bioactive markers, drug delivery cargo and therapeutics of patients with cancer. The current development of exosomal drug delivery technology has markedly changed the current status of cancer patients. The delivery of chemical drugs such as RNA therapeutic exosomes has gradually turned to the clinical application of tumors. In particular, nanotechnology-modified exosomes possess superior biocompatibility which are prone to become a “future star” of antitumor vaccines. Also, exosomes have broad prospects in pharmaceutical and health care. In brief, although the further study of exosomes as an agent or a drug carrier remains basically stuck in the early theoretical stage, these must be transformed into practical applications for the benefit of patients in clinic.

Acknowledgements

This work was supported partly by Southern Marine Science and Engineering Guangdong Laboratory Zhanjiang (ZJW-2019-07); National Natural Science Foundation of China (81541153 and 81873678); Guangdong Provincial Science and Technology Department (2016A050503046, 2015A050502048 and 2016B030309002); and The Public Service Platform of South China Sea for R&D Marine Biomedicine Resources (GDMUK201808). The funders had no role in study design, data collection and analysis, decision to publish or preparation of the manuscript.

References

1. Johnstone RM, Adam M, Hammond JR, et al. Vesicle formation during reticulocyte maturation. Association of plasma membrane activities with released vesicles (exosomes). *J Biol Chem* 1987;262:9412–20.
2. Li I, Nabet BY. Exosomes in the tumor microenvironment as mediators of cancer therapy resistance. *Mol Cancer* 2019;18:32.
3. Wu H, Zeng C, Ye Y, et al. Exosomes from irradiated nonsmall cell lung cancer cells reduced sensitivity of recipient cells to anaplastic lymphoma kinase inhibitors. *Mol Pharm* 2018;15: 1892–900.
4. Lobb RJ, van Amerongen R, Wiegmans A, et al. Exosomes derived from mesenchymal non-small cell lung cancer cells promote chemoresistance. *Int J Cancer* 2017;141:614–20.
5. Liu X, Lu Y, Xu Y, et al. Exosomal transfer of miR-501 confers doxorubicin resistance and tumorigenesis via targeting of BLID in gastric cancer. *Cancer Lett* 2019;459:122–34.
6. Boelens MC, Wu TJ, Nabet BY, et al. Exosome transfer from stromal to breast cancer cells regulates therapy resistance pathways. *Cell* 2014;159: 499–513.
7. Zeng A, Wei Z, Yan W, et al. Exosomal transfer of miR-151a enhances chemosensitivity to temozolomide in drug-resistant glioblastoma. *Cancer Lett* 2018;436:10–21.
8. Zhang Z, Yin J, Lu C, et al. Exosomal transfer of long non-coding RNA SBF2-AS1 enhances chemoresistance to temozolomide in glioblastoma. *J Exp Clin Cancer Res* 2019;38:166.
9. Qu L, Ding J, Chen C, et al. Exosome-transmitted lncARSR promotes Sunitinib resistance in renal cancer by acting as a competing endogenous RNA. *Cancer Cell* 2016;29:653–68.
10. Ren J, Ding L, Zhang D, et al. Carcinoma-associated fibroblasts promote the stemness and chemoresistance of colorectal cancer by transferring exosomal lncRNA H19. *Theranostics* 2018;8 (14):3932–48.
11. Liu T, Zhang X, Du L, et al. Exosome-transmitted miR-128-3p increase chemosensitivity of oxaliplatin-resistant colorectal cancer. *Mol Cancer* 2019;18:43.
12. Richards KE, Zeleniak AE, Fishel ML, et al. Cancer-associated fibroblast exosomes regulate survival and proliferation of pancreatic cancer cells. *Oncogene* 2017;36:1770–8.
13. Au Yeung CL, Co NN, Tsuruga T, et al. Exosomal transfer of stroma-derived miR21 confers paclitaxel resistance in ovarian cancer cells through targeting APAF1. *Nat Commun* 2016;7: 11150.
14. Qin X, Guo H, Wang X, et al. Exosomal miR-196a derived from cancer-associated fibroblasts confers cisplatin resistance in head and neck cancer through targeting CDKN1B and ING5. *Genome Biol* 2019;20:12.
15. Hu JL, Wang W, Lan XL, et al. CAFs secreted exosomes promote metastasis and chemotherapy resistance by enhancing cell stemness and epithelial-mesenchymal transition in colorectal cancer. *Mol Cancer* 2019;18:91.
16. Mikamori M, Yamada D, Eguchi H, et al. MicroRNA-155 controls exosome synthesis and promotes gemcitabine resistance in pancreatic ductal adenocarcinoma. *Sci Rep* 2017;7:42339.
17. Zhu X, Shen H, Yin X, et al. Macrophages derived exosomes deliver miR-223 to epithelial ovarian cancer cells to elicit a chemoresistant phenotype. *J Exp Clin Cancer Res* 2019;38:81.
18. Zheng P, Chen L, Yuan X, et al. Exosomal transfer of tumor-associated macrophage-derived miR-21 confers cisplatin resistance in gastric cancer cells. *J Exp Clin Cancer Res* 2017; 36:53.
19. Xu H, Han H, Song S, et al. Exosome-transmitted PSMA3 and PSMA3-AS1 promote proteasome inhibitor resistance in multiple myeloma. *Clin Cancer Res* 2019;25:1923–35.
20. Silva M, Melo SA. Non-coding RNAs in exosomes: new players in cancer biology. *Curr Genomics* 2015;16:295–303.
21. Fish L, Zhang S, Yu JX, et al. Cancer cells exploit an orphan RNA to drive metastatic progression. *Nat Med* 2018;24:1743–51.
22. Wang G, Liu W, Zou Y, et al. Three isoforms of exosomal circPTGR1 promote hepatocellular carcinoma metastasis via the miR449a-MET pathway. *EBioMedicine* 2019;40:432–45.
23. Blomme A, Fahmy K, Peulen O, et al. Myoferlin is a novel exosomal protein and functional regulator of cancer-derived exosomes. *Oncotarget* 2016;7:83669–83.
24. Zhang L, Zhang S, Yao J, et al. Microenvironment-induced PTEN loss by exosomal microRNA primes brain metastasis outgrowth. *Nature* 2015;527:100–4.
25. Feng W, Dean DC, Hornicek FJ, et al. Exosomes promote pre-metastatic niche formation in ovarian cancer. *Mol Cancer* 2019;18:124.
26. Zhao H, Yang L, Baddour J, et al. Tumor microenvironment derived exosomes pleiotropically modulate cancer cell metabolism. *Elife* 2016;5: e10250.
27. Fong MY, Zhou W, Liu L, et al. Breast-cancer-secreted miR-122 reprograms glucose metabolism in premetastatic niche to promote metastasis. *Nat Cell Biol* 2015;17:183–94.
28. Yan W, Wu X, Zhou W, et al. Cancer-cell-secreted exosomal miR-105 promotes tumour growth through the MYC-dependent metabolic reprogramming of stromal cells. *Nat Cell Biol* 2018;20:597–609.
29. Zhang X, Wang S, Wang H, et al. Circular RNA circNRIP1 acts as a microRNA-149-5p sponge to promote gastric cancer progression via the AKT1/mTOR pathway. *Mol Cancer* 2019;18:20.
30. Liu J, Li D, Luo H, et al. Circular RNAs: the star molecules in cancer. *Mol Aspects Med* 2019;70: 50–67.
31. Wang X, Luo G, Zhang K, et al. Hypoxic tumor-derived Exosomal miR-301a mediates M2 macrophage polarization via PTEN/PI3Kgamma to promote pancreatic cancer metastasis. *Cancer Res* 2018;78:4586–98.
32. Xue M, Chen W, Xiang A, et al. Hypoxic exosomes facilitate bladder tumor growth and development through transferring long non-coding RNA-UCA1. *Mol Cancer* 2017;16:143.
33. Chen JT, Liu CC, Yu JS, et al. Integrated omics profiling identifies hypoxia-regulated genes in HCT116 colon cancer cells. *J Proteomics* 2018; 188:139–51.
34. Huang Z, Yang M, Li Y, et al. Exosomes derived from hypoxic colorectal cancer cells transfer Wnt4 to normoxic cells to elicit a prometastatic phenotype. *Int J Biol Sci* 2018;14:2094–102.
35. Kumar B, Garcia M, Weng L, et al. Acute myeloid leukemia transforms the bone marrow niche into a leukemia-permissive microenvironment through exosome secretion. *Leukemia* 2018;32: 575–87.
36. Frassanito MA, Desantis V, Di Marzo L, et al. Bone marrow fibroblasts overexpress miR-27b and miR-214 in step with multiple myeloma progression, dependent on tumour cell-derived exosomes. *J Pathol* 2019;247:241–53.

37. Mao J, Liang Z, Zhang B, et al. UBR2 enriched in p53 deficient mouse bone marrow mesenchymal stem cell-exosome promoted gastric cancer progression via Wnt/beta-catenin pathway. *Stem Cells* 2017;35:2267–79.
38. Li H, Li F. Exosomes from BM-MSCs increase the population of CSCs via transfer of miR-142-3p. *Br J Cancer* 2018;119:744–55.
39. Lin LY, Du LM, Cao K, et al. Tumour cell-derived exosomes endow mesenchymal stromal cells with tumour-promotion capabilities. *Oncogene* 2016;35:6038–42.
40. Hoshino A, Costa-Silva B, Shen TL, et al. Tumour exosome integrins determine organotropic metastasis. *Nature* 2015;527: 329–35.
41. Costa-Silva B, Aiello NM, Ocean AJ, et al. Pancreatic cancer exosomes initiate pre-metastatic niche formation in the liver. *Nat Cell Biol* 2015; 17:816–26.
42. Zhang H, Deng T, Liu R, et al. Exosome-delivered EGFR regulates liver microenvironment to promote gastric cancer liver metastasis. *Nat Commun* 2017;8:15016.
43. Shao Y, Chen T, Zheng X, et al. Colorectal cancer-derived small extracellular vesicles establish an inflammatory premetastatic niche in liver metastasis. *Carcinogenesis* 2018;39:1368–79.
44. Keklikoglou I, Cianciaruso C, Guc E, et al. Chemotherapy elicits pro-metastatic extracellular vesicles in breast cancer models. *Nat Cell Biol* 2019;21:190–202.
45. Liu Y, Gu Y, Han Y, et al. Tumor Exosomal RNAs promote lung pre-metastatic niche formation by activating alveolar epithelial TLR3 to recruit neutrophils. *Cancer Cell* 2016;30:243–56.
46. Wang L, Yang G, Zhao D, et al. CD103-positive CSC exosome promotes EMT of clear cell renal cell carcinoma: role of remote MiR-19b-3p. *Mol Cancer* 2019;18:86.
47. Yang H, Zhang H, Ge S, et al. Exosome-derived miR-130a activates angiogenesis in gastric cancer by targeting C-MYB in vascular endothelial cells. *Mol Ther* 2018;26:2466–75.
48. Zeng Z, Li Y, Pan Y, et al. Cancer-derived exosomal miR-25-3p promotes pre-metastatic niche formation by inducing vascular permeability and angiogenesis. *Nat Commun* 2018;9:5395.
49. Bao L, You B, Shi S, et al. Metastasis-associated miR-23a from nasopharyngeal carcinoma-derived exosomes mediates angiogenesis by repressing a novel target gene TSGA10. *Oncogene* 2018;37:2873–89.
50. Hsu YL, Hung JY, Chang WA, et al. Hypoxic lung cancer-secreted exosomal miR-23a increased angiogenesis and vascular permeability by targeting prolyl hydroxylase and tight junction protein ZO-1. *Oncogene* 2017;36: 4929–42.
51. Chen X, Yang F, Zhang T, et al. MiR-9 promotes tumorigenesis and angiogenesis and is activated by MYC and OCT4 in human glioma. *J Exp Clin Cancer Res* 2019;38:99.
52. Wang ZF, Liao F, Wu H, et al. Glioma stem cells-derived exosomal miR-26a promotes angiogenesis of microvessel endothelial cells in glioma. *J Exp Clin Cancer Res* 2019;38:201.
53. Fang JH, Zhang ZJ, Shang LR, et al. Hepatoma cell-secreted exosomal microRNA-103 increases vascular permeability and promotes metastasis by targeting junction proteins. *Hepatology* 2018; 68:1459–75.
54. Zhou Y, Ren H, Dai B, et al. Hepatocellular carcinoma-derived exosomal miRNA-21 contributes to tumor progression by converting hepatocyte stellate cells to cancer-associated fibroblasts. *J Exp Clin Cancer Res* 2018;37:324.
55. Wang FW, Cao CH, Han K, et al. APC-activated long noncoding RNA inhibits colorectal carcinoma pathogenesis through reduction of exosome production. *J Clin Invest* 2019;129: 727–43.
56. Guo X, Qiu W, Wang J, et al. Glioma exosomes mediate the expansion and function of myeloid-derived suppressor cells through microRNA-29a/Hbp1 and microRNA-92a/Prkar1a pathways. *Int J Cancer* 2019;144:3111–26.
57. Li L, Cao B, Liang X, et al. Microenvironmental oxygen pressure orchestrates an anti- and protumoral gammadelta T cell equilibrium via tumor-derived exosomes. *Oncogene* 2019;38: 2830–43.
58. Gobbo J, Marcion G, Cordonnier M, et al. Restoring anticancer immune response by targeting tumor-derived exosomes with a HSP70 peptide aptamer. *J Natl Cancer Inst* 2016;108: djv330.
59. Chalmin F, Ladoire S, Mignot G, et al. Membrane-associated Hsp72 from tumor-derived exosomes mediates STAT3-dependent immunosuppressive function of mouse and human myeloid-derived suppressor cells. *J Clin Invest* 2010;120:457–71.
60. Guo Y, Ji X, Liu J, et al. Effects of exosomes on pre-metastatic niche formation in tumors. *Mol Cancer* 2019;18:39.
61. Poggio M, Hu T, Pai CC, et al. Suppression of Exosomal PD-L1 induces systemic anti-tumor immunity and memory. *Cell* 2019;177: 414–27.e13.
62. Liu J, Fan L, Yu H, et al. Endoplasmic reticulum stress promotes liver cancer cells to release Exosomal miR-23a-3p and up-regulate PD-L1 expression in macrophages. *Hepatology* 2019;70: 241–58.
63. Ricklefs FL, Alayo Q, Krenzlin H, et al. Immune evasion mediated by PD-L1 on glioblastoma-derived extracellular vesicles. *Sci Adv* 2018;4: eaar2766.
64. Haderk F, Schulz R, Iskar M, et al. Tumor-derived exosomes modulate PD-L1 expression in monocytes. *Sci Immunol* 2017;2:eaah5509.
65. Zhu X, Zhang J, Fan W, et al. The rs391957 variant cis-regulating oncogene GRP78 expression contributes to the risk of hepatocellular carcinoma. *Carcinogenesis* 2013;34:1273–80.
66. Zhu X, Chen L, Fan W, et al. An intronic variant in the GRP78, a stress-associated gene, improves prediction for liver cirrhosis in persistent HBV carriers. *PLoS One* 2011;6: e21997.
67. Cai S, Cheng X, Pan X, et al. Emerging role of exosomes in liver physiology and pathology. *Hepatol Res* 2017;47:194–203.
68. Chen L, Chen R, Velazquez VM, et al. Fibrogenic signaling is suppressed in hepatic stellate cells through targeting of connective tissue growth factor (CCN2) by cellular or Exosomal MicroRNA-199a-5p. *Am J Pathol* 2016; 186:2921–33.
69. Dai X, Chen C, Xue J, et al. Exosomal MALAT1 derived from hepatic cells is involved in the activation of hepatic stellate cells via miRNA-26b in fibrosis induced by arsenite. *Toxicol Lett* 2019; 316:73–84.
70. Xu Z, Wang N, Xu Y, et al. Effects of chronic PM2.5 exposure on pulmonary epithelia: transcriptome analysis of mRNA-exosomal miRNA interactions. *Toxicol Lett* 2019;316:49–59.
71. Masamune A, Yoshida N, Hamada S, et al. Exosomes derived from pancreatic cancer cells induce activation and profibrogenic activities in pancreatic stellate cells. *Biochem Biophys Res Commun* 2018;495:71–7.
72. Mata-Rocha M, Rodriguez-Hernandez RM, Chavez-Olmos P, et al. Presence of HPV DNA in extracellular vesicles from HeLa cells and cervical samples. *Enferm Infecc Microbiol Clin* 2019. https://doi.org/10.1016/j.eimc.2019.06.011. [Epub ahead of print].
73. Zhou C, Tan L, Sun Y, et al. Exosomes carry microRNAs into neighboring cells to promote diffusive infection of Newcastle disease virus. *Viruses* 2019;11:E527.
74. Ikoma M, Gantt S, Casper C, et al. KSHV oral shedding and plasma viremia result in significant changes in the extracellular tumorigenic miRNA expression profile in individuals infected with the malaria parasite. *PLoS One* 2018;13: e0192659.
75. Meckes DG Jr, Gunawardena HP, Dekroon RM, et al. Modulation of B-cell exosome proteins by gamma herpesvirus infection. *Proc Natl Acad Sci USA* 2013;110:E2925–33.
76. Santangelo L, Bordoni V, Montaldo C, et al. Hepatitis C virus direct-acting antivirals therapy impacts on extracellular vesicles microRNAs content and on their immunomodulating properties. *Liver Int* 2018;38:1741–50.
77. Zhu L, Kalimuthu S, Gangadaran P, et al. Exosomes derived from natural killer cells exert therapeutic effect in melanoma. *Theranostics* 2017;7:2732–45.
78. Wu CH, Li J, Li L, et al. Extracellular vesicles derived from natural killer cells use multiple cytotoxic proteins and killing mechanisms to target cancer cells. *J Extracell Vesicles* 2019;8: 1588538.
79. Neviani P, Wise PM, Murtadha M, et al. Natural killer-derived Exosomal miR-186 inhibits neuroblastoma growth and immune escape mechanisms. *Cancer Res* 2019;79:1151–64.
80. Mallegol J, Van Niel G, Lebreton C, et al. T84-intestinal epithelial exosomes bear MHC class II/peptide complexes potentiating antigen presentation by dendritic cells. *Gastroenterology* 2007;132:1866–76.
81. Rao Q, Zuo B, Lu Z, et al. Tumor-derived exosomes elicit tumor suppression in murine hepatocellular carcinoma models and humans in vitro. *Hepatology* 2016;64:456–72.
82. Wang J, Li W, Zhang L, et al. Chemically edited exosomes with dual ligand purified by microfluidic device for active targeted drug delivery to tumor cells. *ACS Appl Mater Interfaces* 2017;9:27441–52.
83. Fang S, Tian H, Li X, et al. Clinical application of a microfluidic chip for immunocapture and quantification of circulating exosomes to assist breast cancer diagnosis and molecular classification. *PLoS One* 2017;12:e0175050.

84. Ibsen SD, Wright J, Lewis JM, et al. Rapid isolation and detection of exosomes and associated biomarkers from plasma. *ACS Nano* 2017;11: 6641–51.
85. Xu H, Liao C, Zuo P, et al. Magnetic-based microfluidic device for on-Chip isolation and detection of tumor-derived exosomes. *Anal Chem* 2018;90:13451–8.
86. Reategui E, van der Vos KE, Lai CP, et al. Engineered nanointerfaces for microfluidic isolation and molecular profiling of tumor-specific extracellular vesicles. *Nat Commun* 2018;9:175.
87. Dorayappan KDP, Gardner ML, Hisey CL, et al. A microfluidic chip enables isolation of exosomes and establishment of their protein profiles and associated signaling pathways in ovarian cancer. *Cancer Res* 2019;79:3503–13.
88. Xia Y, Liu M, Wang L, et al. A visible and colorimetric aptasensor based on DNA-capped single-walled carbon nanotubes for detection of exosomes. *Biosens Bioelectron* 2017; 92:8–15.
89. Huang R, He L, Xia Y, et al. A sensitive Aptasensor based on a hemin/G-Quadruplex-assisted signal amplification strategy for electrochemical detection of gastric cancer exosomes. *Small* 2019;15:e1900735.
90. Wang Q, Zou L, Yang X, et al. Direct quantification of cancerous exosomes via surface plasmon resonance with dual gold nanoparticle-assisted signal amplification. *Biosens Bioelectron* 2019; 135:129–36.
91. Liu C, Zhao J, Tian F, et al. Low-cost thermophoretic profiling of extracellular-vesicle surface proteins for the early detection and classification of cancers. *Nat Biomed Eng* 2019;3: 183–93.
92. Li Y, Zhao J, Yu S, et al. Extracellular vesicles Long RNA sequencing reveals abundant mRNA, circRNA, and lncRNA in human blood as potential biomarkers for cancer diagnosis. *Clin Chem* 2019;65:798–808.
93. Fan L, Cao Q, Liu J, et al. Circular RNA profiling and its potential for esophageal squamous cell cancer diagnosis and prognosis. *Mol Cancer* 2019;18:16.
94. Jin X, Chen Y, Chen H, et al. Evaluation of tumor-derived exosomal miRNA as potential diagnostic biomarkers for early-stage non-small cell lung cancer using next-generation sequencing. *Clin Cancer Res* 2017;23:5311–9.
95. Liu X, Chen X, Zeng K, et al. DNA-methylation-mediated silencing of miR-486-5p promotes colorectal cancer proliferation and migration through activation of PLAGL2/IGF2/beta-catenin signal pathways. *Cell Death Dis* 2018;9:1037.
96. Taylor DD, Gercel-Taylor C. MicroRNA signatures of tumor-derived exosomes as diagnostic biomarkers of ovarian cancer. *Gynecol Oncol* 2008;110:13–21.
97. Lai X, Wang M, McElyea SD, et al. microRNA signature in circulating exosomes is superior to exosomal glypican-1 levels for diagnosing pancreatic cancer. *Cancer Lett* 2017;393:86–93.
98. Arbelaiz A, Azkargorta M, Krawczyk M, et al. Serum extracellular vesicles contain protein biomarkers for primary sclerosing cholangitis and cholangiocarcinoma. *Hepatology* 2017;66:1125–43.
99. Fu H, Yang H, Zhang X, et al. TRIM3 is a novel marker and therapy target for gastric cancer. *J Exp Clin Cancer Res* 2018;37:162.
100. Puhka M, Takatalo M, Nordberg ME, et al. Metabolomic profiling of extracellular vesicles and alternative normalization methods reveal enriched metabolites and strategies to study prostate cancer-related changes. *Theranostics* 2017;7:3824–41.
101. Skotland T, Ekroos K, Kauhanen D, et al. Molecular lipid species in urinary exosomes as potential prostate cancer biomarkers. *Eur J Cancer* 2017;70:122–32.
102. Kamerkar S, LeBleu VS, Sugimoto H, et al. Exosomes facilitate therapeutic targeting of oncogenic KRAS in pancreatic cancer. *Nature* 2017;546:498–503.
103. Stremersch S, Vandenbroucke RE, Van Wonterghem E, et al. Comparing exosome-like vesicles with liposomes for the functional cellular delivery of small RNAs. *J Control Release* 2016; 232:51–61.
104. Pi F, Binzel DW, Lee TJ, et al. Nanoparticle orientation to control RNA loading and ligand display on extracellular vesicles for cancer regression. *Nat Nanotechnol* 2018;13:82–9.
105. Li Z, Zhou X, Wei M, et al. In vitro and in vivo RNA inhibition by CD9-HuR functionalized exosomes encapsulated with miRNA or CRISPR/dCas9. *Nano Lett* 2019;19:19–28.
106. Hobor F, Dallmann A, Ball NJ, et al. A cryptic RNA-binding domain mediates Syncrip recognition and exosomal partitioning of miRNA targets. *Nat Commun* 2018;9:831.
107. Ma J, Zhang Y, Tang K, et al. Reversing drug resistance of soft tumor-repopulating cells by tumor cell-derived chemotherapeutic microparticles. *Cell Res* 2016;26:713–27.
108. Kim MS, Haney MJ, Zhao Y, et al. Development of exosome-encapsulated paclitaxel to overcome MDR in cancer cells. *Nanomedicine* 2016;12: 655–64.
109. Yim N, Choi C. Extracellular vesicles as novel carriers for therapeutic molecules. *BMB Rep* 2016;49:585–6.
110. Lin Q, Qu M, Zhou B, et al. Exosome-like nanoplatform modified with targeting ligand improves anti-cancer and anti-inflammation effects of imperialine. *J Control Release* 2019; 311-312:104–16.
111. Kooijmans SA, Aleza CG, Roffler SR, et al. Display of GPI-anchored anti-EGFR nanobodies on extracellular vesicles promotes tumour cell targeting. *J Extracell Vesicles* 2016;5:31053.
112. Qi H, Liu C, Long L, et al. Blood exosomes endowed with magnetic and targeting properties for cancer therapy. *ACS Nano* 2016;10: 3323–33.

Received: 27 April 2022 | Accepted: 27 May 2022
DOI: 10.1111/imr.13107

INVITED REVIEW

Immunological Reviews WILEY

Engineered exosomes for studies in tumor immunology

Ahmet Alptekin[1] | **Mahrima Parvin**[1] | **Hasanul I. Chowdhury**[1] |
Mohammad H. Rashid[2] | **Ali S. Arbab**[1]

[1]Georgia Cancer Center, Augusta University, Augusta, Georgia, USA
[2]Cedars-Sinai Medical Center, Los Angeles, California, USA

Correspondence
Ali S. Arbab, Georgia Cancer Center, 1410 Laney Walker Blvd., Room # 3315, Augusta, GA 30912, USA.
Email: aarbab@augusta.edu

Funding information
American Heart Association, Grant/Award Number: 19TPA34850076; National Institute of Neurological Disorders and Stroke, Grant/Award Number: R01NS110378

Summary

Exosomes are a type of extracellular vesicle (EV) with diameters of 30–150 nm secreted by most of the cells into the extracellular spaces and can alter the microenvironment through cell-to-cell interactions by fusion with the plasma membrane and subsequent endocytosis and release of the cargo. Because of their biocompatibility, low toxicity and immunogenicity, permeability (even through the blood–brain barrier (BBB)), stability in biological fluids, and ability to accumulate in the lesions with higher specificity, investigators have started making designer's exosomes or engineered exosomes to carry biologically active protein on the surface or inside the exosomes as well as using exosomes to carry drugs, micro RNA, and other products to the site of interest. In this review, we have discussed biogenesis, markers, and contents of various exosomes including exosomes of immune cells. We have also discussed the current methods of making engineered and designer's exosomes as well as the use of engineered exosomes targeting different immune cells in the tumors, stroke, as well as at peripheral blood. Genetic engineering and customizing exosomes create an unlimited opportunity to use in diagnosis and treatment. Very little use has been discovered, and we are far away to reach its limits.

KEYWORDS
engineered exosomes, designer's exosomes, manipulation of biogenesis, exosomes, and immune cells, separation of exosomes, therapeutic exosomes

1 | INTRODUCTION

Exosomes are a type of extracellular vesicle (EV) with diameters of 30–150 nm secreted by most of the cells into the extracellular spaces and can alter the microenvironment through cell-to-cell interactions by fusion with the plasma membrane and subsequent endocytosis and release of their cargo.[1–6] Irrespective of the origin of parent cells, exosomes share common features such as certain tetraspanins (CD9, CD63, and CD81), heat shock proteins (HSP 60, Hsp 70, and Hsp 90), biogenesis-related proteins (Alix and TSG 101), membrane transport and fusion proteins (GTPases, annexins, and Rab proteins), nucleic acids (mRNA, miRNA, and long noncoding RNAs and DNAs), and lipids (cholesterol and ceramide).[2,7,8] Because of their biocompatibility, low toxicity and immunogenicity, permeability (even through the blood–brain barrier (BBB)), stability in biological fluids, and ability to accumulate in the lesions with higher specificity,[9–15] investigators have started making designer's exosomes or engineered exosomes to carry biologically active protein on the surface or inside the exosomes as well as using exosomes to carry drugs, micro RNA, and other products to the site of interest.[11,16–19]

This article is part of a series of reviews covering Extracellular vesicles appearing in Volume 312 of *Immunological Reviews*.

When searched in PubMed using the term exosomes, there were only 84 publications between 1950 and 2000. However, using the same search word there were 5001 publications in 2021, and 1402 are published as review articles. When the search term is used as “exosomes in immunology” PubMed produce 581 publications in 2021 including 215 review articles. A total of 123 publications since 2010 mentioned the term “engineered exosomes” in the title or the abstract and only 21 publications dealt with engineered exosomes in immunology since 2010. Among them, only 6 review articles discuss the application of engineered exosomes in immunotherapy.[16,20–24] It is obvious that engineered exosomes in the field of immunotherapy are still in infancy and untapped.

Recently our laboratory has achieved a few milestones in exosome technology: (1) we developed a platform to make engineered exosomes using nontumorous HEK293 cells that carry and express specific cell-targeting peptides to detect specific cells in vivo when administered intravenously; (2) we used these engineered exosomes as a therapeutic probe to deplete specific cells in the body; (3) we optimized the methods to collect a uniform-sized large amount of exosomes from different cells using a combination of size exclusion and centrifugal filters in shortest possible time; (4) we showed differential biodistribution of exosomes collected from different cells in tumor-bearing animals using clinically relevant single-photon emission computed tomography (SPECT).[25,26] In this review article, we will revisit the current version of the biogenesis of exosomes using tumorous and nontumorous cells, how to manipulate the biogenesis mechanism to make engineered exosomes to express protein or RNA of interest in the exosomes and how to make designer's exosomes to carry nanoparticles, micro RNA, chemotherapeutics, and others. All possible biogenesis of engineered exosomes and their applications will be around the subject matters of immunotherapy, especially targeting tumor microenvironment (TME).

2 | CURRENT VIEW OF BIOGENESIS OF EXOSOMES

The biogenesis of exosomes starts from the process of plasma membrane invagination, the formation of early and late endosomes, the formation of the multivesicular body (MVB), the generation of exosomes as intraluminal vesicles (ILVs), and the secretion of the ILVs as exosomes extracellularly.[27] MVB is composed of ILV particles of different sizes, which range from a few nanometers (nm) to micrometers (μm). The common consensus is that size of the exosomes ranges from 30 to 150 nm.[28] The biogenesis of exosomes is a highly regulated process and involves many steps and proteins.[29] First ubiquitin-binding protein Golgi-Localized γ-Ear-Containing ARF-Binding (GGA), Vps27/Hse1, and clathrin form an endosomal clathrin coat, which acts as a cargo loading site for ESCRT machinery. The ESCRTs ESCRT-0, -I, -II, -III, and Vps4 then form the multivesicular body. Interestingly, the ESCRTs are also involved in the invagination of multivesicular body and formation of ILVs[7] where ESCRT III takes part in scission[1] of ILVs in the lumen. Along with ESCRTs syndecan, ceramide and tetraspanins are involved in ILVs biogenesis.[30] Several ESCRT and related proteins including HRS, STAM1, TSG101, ALIX, and VPS4 are involved in MVB docking[31] with membrane and SNAREs are responsible for fusion of MVB with membrane and release of ILVs.[32] In contrast to exosomes, microvesicles, another type of EV sizing 100–1000 nm are generated by direct outward budding of the plasma membrane with the help of several GTPases. Figure 1 shows the current view of exosome biogenesis.

2.1 | Importance of tetraspanins and their manipulation for biogenesis

EVs are secreted by all types of cells. Among the EVs, exosomes contain a specific amount and types of components based on the cell of origin. Alongside genetic materials and lipids, proteins are one of the major components in the exosomes. Exosomes show protein heterogeneity because the parent cells are secreted from having different types of protein contents. One of the large protein families present on the surface of exosomes is tetraspanins. Exosomes have their tetraspanin-enriched microdomains (TEMs) and form a cluster on the surface. By their cluster, they can interact with numerous signaling molecules.[33,34] Almost all exosomes have three major types of tetraspanins CD63, CD9, and CD81, which are also being used as exosome markers. Tetraspanins are involved in exosome biogenesis processes and sorting cargo of the exosomes. Tetraspanins are also involved in the attachment with the target cell as well as in antigen presentation.[35] They also regulate cellular motility and migration and have shown their role in the metastasis of tumors.[36] CD63 interacts by its C terminal with protein complex and attaches the exosomes with membrane to clathrin-dependent pathways.[37] CD9 marker is not specific for endosomes small vesicles (like exosomes) because the presence of this marker in large vesicles was also noted.[38] CD9 transfer from the endoplasmic reticulum to Golgi in B cell has the involvement of CD81.[39] CD9 and CD81 have been shown to interact with G proteins.[40] Additional to these, tetraspanins have different other functions.

2.2 | Manipulation biogenesis to control the contents of the exosomes in the lumen and on its surface

To meet up the protein deficiency and dysfunction, overexpression of the target protein is a way to increase the protein content of exosomes.[41] In this process, certain proteins in the donor cells are overexpressed and that overexpressed protein goes to exosomes by their normal sorting. Excessive protein-containing exosomes are released from cells and can be collected for using further studies or therapies. The downside of this process is possible cytotoxicity and the proliferation inhibition of donor cells. An alternative approach to this process is using ubiquitin. Ubiquitin is one of the most abundant proteins.[42] By using Ubiquitin, a target

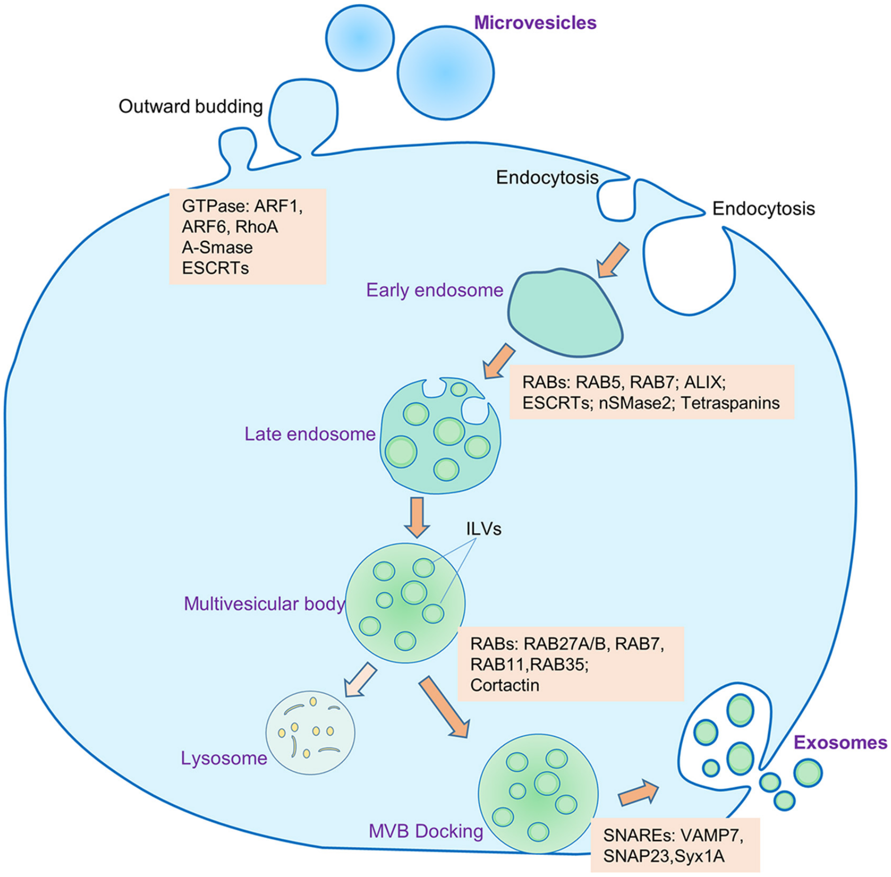

FIGURE 1 Biogenesis and secretion of exosomes and microvesicles. Microvesicles are generated by outward budding of the plasma membrane with the help of several GTPases. The process of biogenesis and release of exosomes into the extracellular space encompasses several distinct steps: (1) invagination of plasma membrane and formation of early endosomes, (2) inward protrusion of early endosomal membrane to generate late endosomes, (3) formation of multivesicular bodies (MVBs) that contain intraluminal vesicles (ILVs), (4) docking of the MVBs to the cellular plasma membrane, (5) exocytosis of the exosomes into the extracellular milieu. Some of the MVBs may go into lysosomal degradation. Several molecules are involved in the biogenesis and release of microvesicles and exosomes. ESCRT, endosome sorting complex required for transport; RAB, RAS-related protein; ALIX, ALG-2 interacting protein X; nSMase2, neutral sphingomyelinase 2; SNARE, soluble NSF attachment protein receptor; VAMP7, vesicle-associated membrane protein 7; SNAP23, synaptosomal-associated protein 23; Syx1A, syntaxin 1A; ARF, ADP, ribosylation factor; RohA, Ras homolog family member A; A-SMase, acid sphingomyelinase

protein can be expressed 10-fold higher than normal by conjugating the target protein in the C terminal of ubiquitin, which has been shown in HEK 293 cell.[43] In exosomes, MHC-II β-chain cytoplasmic tail ubiquitination turns them to be sorted, therefore this ubiquitination platform could be used to package cargo protein in exosomes.[44]

2.3 | Biogenesis of exosomes in immune cells

Similar to other cells, immune cells also release exosomes abundantly that carry membranous, cytosolic, and even nuclear molecules (DNA, RNA) characteristic of the cells of origin. Given the numerous types of immune cells, exosomes derived from immune cells play crucial and complex physiological and pathological roles within the already complex immune system. Functional molecules of exosomes, derived from various immune cells and their effects are summarized in Figure 2.

2.3.1 | Macrophages

Macrophages are innate immune cells, which exert diverse functions through their secreted exosomes and are shown to be involved in the progression of the disease by their bioactive molecules.[45,46] The biogenesis of exosomes in macrophages is the same as in other cell types. Different studies have confirmed that the exosome contents of macrophages and the surface proteins are secretory cell-specific.[47] As macrophages are of three types, M0 (nonpolarized), M1, and M2 (polarized), there are three types of macrophage-derived exosomes, and different studies investigated the role of M0, M1, and M2 macrophage-derived exosomes.[48–50] Macrophage-derived exosomes are shown to exert their effects in different pathological conditions by activating different gene signaling pathways; mostly for progression and metastasis.[51]

The main content of macrophage exosomes are miRNAs, long noncoding RNAs (lncRNAs), and proteins.[52] Some miRNAs are found in higher levels in M2 macrophage-derived exosomes than in

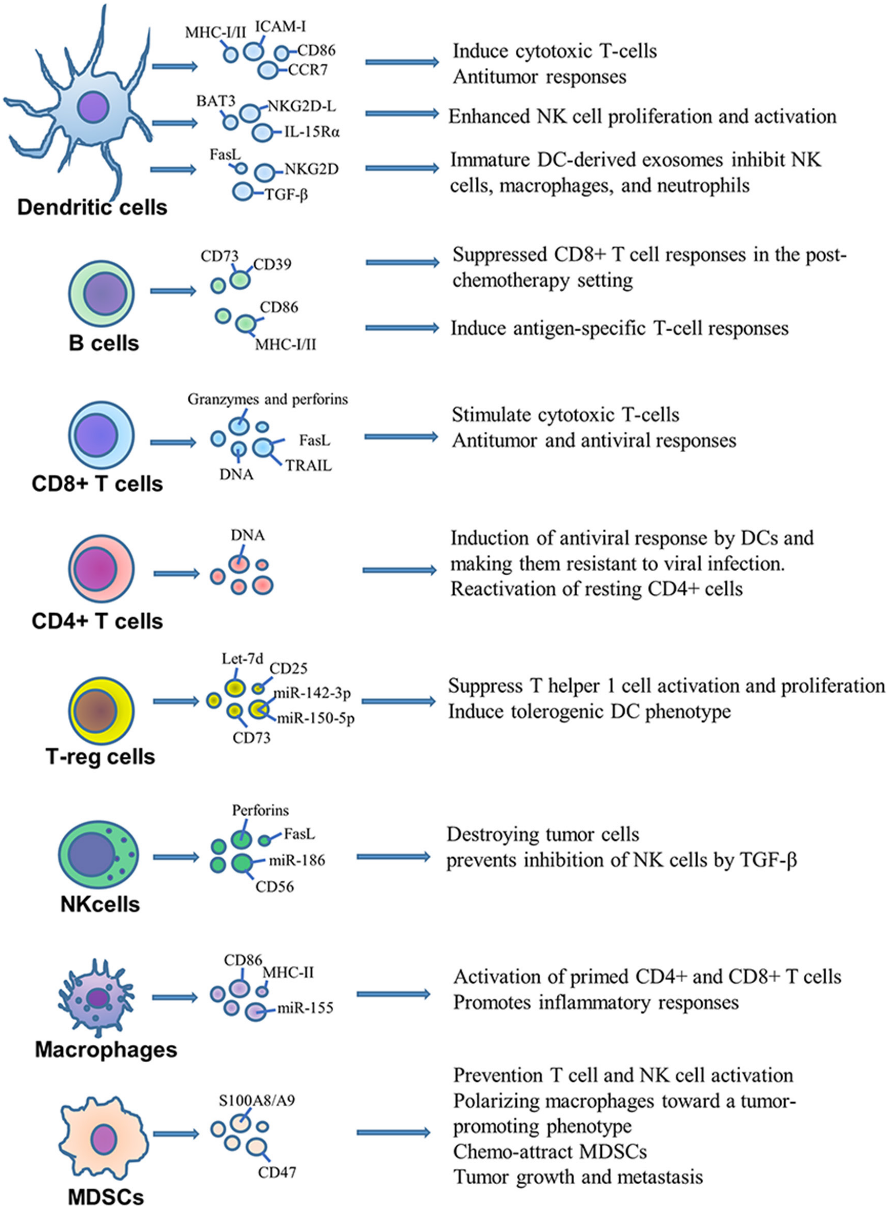

FIGURE 2 Functional molecules in the exosomes released from different immune cells

M1 macrophage-derived exosomes.[53] Among the major miRNA in macrophage-derived exosomes for cancer progression, drug resistance and cancer inhibitions are miR-29a, miR-92a-2, miR-95, miR-125a/b, miR-142, miR-21, miR-155, miR-7, and miR-146a. The major proteins present in the macrophage-derived exosome are ApoE, IL-6, and AMAD15.[53] Other components in macrophage exosomes are mRNA, tRNA, and ribosome but there is no evidence of active DNA.[54,55]

2.3.2 | Myeloid-derived suppressor cells

MDSCs are myeloid heterogeneous cells grouped in an immature state. The major two subgroups of MDSC are monocytic MDSC (M-MDSC) and granulocytic MDSC (G-MDSC), which are differentiated based on Ly6C high (M-MDSC) or Ly6G high (G-MDSC). Annexins, tetraspanins, cytoskeletal proteins, and heat shock proteins (HSPs) are common in exosomes released by MDSC, which are similar to other cell-derived exosomes. Tetraspanins (including CD9, CD177), Hsp70, Hsp90α, Hsp90β, Alix, and the ESCRT complex are characteristic proteins of exosome biogenesis and cargo sorting are also present in MDSC exosomes.[56] Some pro-inflammatory proteins S100A8/9, CD47, and thrombospondin-1 as well as platelet factor-4 are also enriched in exosomes are also enriched in MDSC-derived exosomes. MDSC-derived exosomes contain abundant ubiquitinated proteins such as the ubiquitinated histones, and the nonhistone nuclear protein high mobility group box (HMBG).[57] Transforming growth factor-β1(TGF-β1) is 4.3 times higher in MDSC-derived exosomes than in the MDSC cell.[58] Cancer progression miRNAs are abundant in exosomes derived from MDSC, which are mainly miR-146a, miR-146b, miR-155, miR-125b, miR-100, let-7e, miR-125a, and miR-99b.[59]

2.3.3 | T cells

Like many other cells, T cells also release exosomes but very few studies have been conducted about the T cell exosome biogenesis. T cell released exosomes mostly showed the immune modulation function.[60–62] Cytotoxic T cells release the lethal protein perforin as well as granzymes to the target cell through exosomes.[63] Even apoptosis changes the protein content of T cell released exosomes when compared between an activated T cell released exosome and apoptotic T cell released exosome.[64,65] One of the components of T cell exosomes is FasL, secreted as "lethal exosomes" following activation-induced fusion of the MVB with the plasma membrane.[65] Along with FasL, APO2 ligand (APO2L)/TNF-related apoptosis-inducing ligand (TRAIL) has also been found in T cell exosomes.[66] A study demonstrated that T cell exosomes express thrombospondin-1 receptor CD47 and it regulates endothelial cell responses to vascular endothelial growth factor (VEGF).[67]

2.3.4 | Dendritic cells

Dendritic cells (DCs) are regarded as specialized and most potent antigen-presenting cells (APC) mediating crucial functions in innate and adaptive immune responses. They can efficiently process and present antigens followed by triggering the proliferation, activation, and differentiation of naive T cells.[68] Research has shown that like DCs, exosomes released from activated DC also express MHCII complex and T cell co-stimulatory molecules and are involved in antigen presentation.[69,70] It has been found that exosomes derived from mature DCs contain CCR7, a chemokine receptor that directs mature DCs to peripheral lymphoid tissues which also analogously regulates the increased accumulation of these exosomes in the spleen and inflammatory responses upon injection in mice.[71] Although DC-derived exosomes can activate T cells through stable interactions with TCR complexes, the extent of the activation depends on DC developmental stage. Generally, T cells are more efficiently activated by mature DCs than immature DCs, and mature DCs release exosomes to facilitate immune-stimulatory responses, whereas immature DC exosomes exhibit a potent immune-suppressive response.[72,73] Immunosuppressive molecules, such as TGF-β, NKG2D, and death ligand FasL expressed by immature DCs following response to tumors, can inhibit natural killer (NK) cells, macrophages, and neutrophils.[74,75] Furthermore, DC-derived exosomes expressing HLA-B associated transcript-3 (BAT3) bound to NKp30 receptor in NK cells and stimulate the secretion of TNF-α and IFN-γ.[76] Through IL-15Rα and NKG2D, DC-derived exosomes also enhanced NK cell proliferation and activation.[20]

3 | CURRENT METHODS TO DIFFERENTIATE EXOSOMES VS EV PARTICLES

EVs are divided into three main classes[77]: Exosomes, Microvesicles (also known as microparticles or ectosomes), and apoptotic bodies. Exosomes are produced within the endosomal network as MVB, which are released upon fusion with the plasma membrane. Exosomes are identified by specific markers, for example, Alix, tetraspanin. These markers denote their specific endocytic origins and a combination of the markers is preferred. Microvesicles are formed by outward budding and fission of the plasma membrane. Apoptotic bodies are released as blebs of cells undergoing apoptosis. Characteristics and main differences between different EVs are shown in Table 1.

3.1 | Specific markers of exosomes

Several exosomal proteins have been identified and are generally been used as exosome markers. A summary of common exosomal protein markers, their location in the exosomes, and collection and detection methods of these proteins is shown in Table 2 and Figure 3.

Alix (or PDCD6IP, also known as Programmed cell death 6-interacting protein) regulates the endolysosomal system and regulates neuronal death as demonstrated by the upregulation of Alix in degenerating hippocampal neurons after epileptic seizures.[103]

EDIL 3 (or EGF Like Repeats and Discoidin I-Like Domains Protein 3, also known as Developmental Endothelial Locus 1) is a pro-angiogenic factor and a regulator of endothelial cell adhesion and migration.[104] It is an extracellular matrix protein that contains 3 EGF-like domains. One of the domains contains an RGD (Arg–Gly–Asp) motif, which facilitates its interaction with integrins.[105]

HSP70 (heat shock proteins) are membrane-bound and extracellularly located proteins that maintain protein homeostasis as a chaperone in the cytosol. It also has cytoprotective effects. Since the synthesis of HSPs is induced by stress, heat, and other chemical and mechanical stimuli, a variety of HSPs (namely HSP70 and HSP90) have been frequently found in the plasma membrane of the tumor cells. HSPs are isolated by ultracentrifugation.[97]

Several isolation methods have been developed to detect exosomes but the combination of methods yields the best results. Exosome markers like PDCD6IP (Programmed cell death 6-interacting protein, also known as Alix), CD24, CPNE3, EDIL3, Fibronectin, FLOT1, HSP70, TEX, TfR, and TSG101 can be detected by ultracentrifugation.[82,83] Immunohistochemistry detects exosomes like CD9, CD24, CD63, CPNE3, Exo-PD-L1, and CD81.[86]

TEX (or tumor-derived exosomes) are ubiquitously present in the plasma and TME in all body fluids of cancer patients.[106] These exosomes facilitate immune-regulatory activities.[98]

Pineles et al. (2022) conducted an observational cohort study on term/near-term neonates undergoing therapeutic hypothermia (TH) for hypoxic-ischemic encephalopathy (HIE), where they purified CNS exosomes from serum using several established methods. In this study, the researchers concluded that CNS exosome cargo acts as biomarkers that correspond with the severity of brain injury, response to TH, and quantify pharmacological response to neuroactive therapeutic/adjuvant agents. Synaptopodin (SYNPO) is a protein contained within the neonatal CNS exosomes and is specific to HIE.[107]

TABLE 1 Characteristics and main differences between extracellular vesicles subtype[78–81]

Traits	Exosomes	Microvesicles	Apoptotic bodies
Biogenesis	Endosomal origin and exocytosis	Outward budding of the plasma membrane	Outward blebbing and fragmentation of the plasma membrane
Release time	Ten minutes or more	Few seconds	–
Pathways	ESCRT-dependent Tetraspanin-dependent Ceramide-dependent Stimuli-dependent	Ca2+-dependent Stimuli- and cell-dependent	Apoptosis-related
Size	30–150 nm	100–1000 nm	1000-5000 nm
Appearance-electron microscopy	Spheroid/cup shape	Irregular and electron-dense	Heterogeneous
Density	1.13–1.19 g/ml	1.04–1.07 g/ml	1.16–1.28 g/ml
Isolation method	ultracentrifugation, ultrafiltration, precipitation, size exclusion chromatography, immunoaffinity capture-based, microfluidics-based, polymer-based, etc.	Ultracentrifugation	No standardized protocol
Content	Proteins, nucleic acids, lipids, and metabolites	Proteins, nucleic acids, lipids, and metabolites	DNA fragments and histone, chromatin remnants, cell organelles, cytosol portions, degraded proteins
Typical constituent proteins	Tetraspanins (CD9, CD63, CD81), ESCRT proteins (Alix, TSG101), Integrins (-α, -β), heat shock proteins (HSP90, HSP70)	Anexin V, Flotillin-2, Selectins, Integrins, CD40 ligand, metalloproteinase	Anexin V, DNA, histones
Function	Cell-cell communication	Cell-cell communication	Product of programmed cell death. Removal of unwanted cells

3.2 | Specific markers for immune cell-derived exosomes

Various cellular components take part in the formation of both the innate and adaptive components of the immune system. Among the several biological functions of exosomes on immune systems, the most significant ones are immunomodulation including immune suppression and various anti-inflammatory processes; cell-to-cell communication including antigen presentation, NK cell, and T cell activation.[108]

Among all the immune-cell-derived exosomes, DC-derived exosomes are the most vital as they exist in multiple populations, and effectively initiate the antigen-specific immune response by efficient activation and proliferation of T cells, thus promoting immunity. A combination of various cell markers is used to identify the DCs. Exosomes derived from DCs have an essential role in several diseases, including autoimmune diseases, cardiovascular diseases for example, acute MI, or transplant medicine.[109] Leone et al. demonstrated that DCs are identified by CD107a/LAMP-1 (lysosome-associated membrane protein-1) and CD107b/LAMP-2 (lysosome-associated membrane protein-2) that are present on the surface of DCs.[110] APC-derived exosomes originate from inward invagination of the internal vesicles of the MHC class II compartment (MIIC). Immunoelectron microscopy of B cells and DCs demonstrates that MVE (multivesicular endosomes) limiting membranes fuse with the plasma membranes and the internal vesicles within the MVE express MIIC-specific markers LAMP-1, MHC-II, CD63 and CD82.[111] DC-derived exosomes stimulate the proliferation of allogeneic lymphocytes. On the other hand, APC-derived exosomes express MHC-II and stimulate T cells.[112] DC-derived exosomes that express MHC-I and CD86 can effectively generate CD8+ T cell response against tumors.[69] The long-term culture method which supports the production of myeloid-like and immature myeloid DC,[113] both lack expression of MHC-II or CD40 but myeloid-like DC expresses CD11c, CD11b, CD80, CD86, and immature DC expresses FcγII/IIIR.[114]

Macrophage-derived exosomes are of monocytic lineage. These exosomes participate in immune response after cardiac injury following MI or other cardiac injuries through the recruitment of other macrophage components. Following MI (or cardiac injury), for the first few days, the M1 macrophage peaks, then macrophages shift from M1 to M2. This shift signifies the pro-inflammatory and pro-phagocytic response of M1 macrophage and the anti-inflammatory response of M2.[115] Notable microRNA contained within the exosomes taking part in this process are miR-155, miR-19, miR-21, miR-146, and miR-223. Of note, these miRNAs inhibit fibroblast proliferation and stimulate inflammation, which in turn creates a pro-inflammatory environment in cardiac muscles. Detecting these miRNAs in macrophage-derived exosomes can provide a significant clinical understanding of myocardial diseases.[116]

TABLE 2 Exosome protein markers

Exosome markers	Location	Collection and detection methods	References
Alix (PDCD6IP)	Cytoplasm	Ultracentrifugation	82,83
CD9	Plasma membrane	Immunohistochemistry	84–86
CD24	Plasma	Ultracentrifugation; Immunohistochemistry	87,88
CD63	Plasma membrane and cytosol	Immunohistochemistry	86,89,90
CD81	Plasma membrane	Immunohistochemistry	84
CPNE3	Plasma	Ultracentrifugation; Immunohistochemistry	91
EDIL3	Plasma	Ultracentrifugation	87,92
Exo-PD-L1	Serum	Immunohistochemistry	93
Fibronectin	Plasma	Ultracentrifugation	87,94
FLOT1	Plasma membrane	Ultracentrifugation, immunoblotting	95,96
HSP70	Serum, plasma membrane	Ultracentrifugation	97
TEX	Plasma	Density gradient ultracentrifugation; size exclusion chromatography (SEC); Differential centrifugation; Ultrafiltration	98
TfR	Perinuclear or plasma membrane	Ultracentrifugation; Size-exclusion chromatography (SEC)	99,100
TSG101	Cytoplasm	Ultracentrifugation, immunoblotting	101,102

Abbreviations: CPNE3, Copine III; EDIL3, EGF-Like Repeats and Discoidin I-Like Domains Protein 3; Exo-PD-L1, Exosomal programmed cell-death ligand 1; FLOT1, flotillin 1; PDCD6IP, Programmed cell death 6-interacting protein; TEX, Tumor-Derived Exosomes; TfR, Transferrin receptor; TSG101, Tumor susceptibility gene 101.

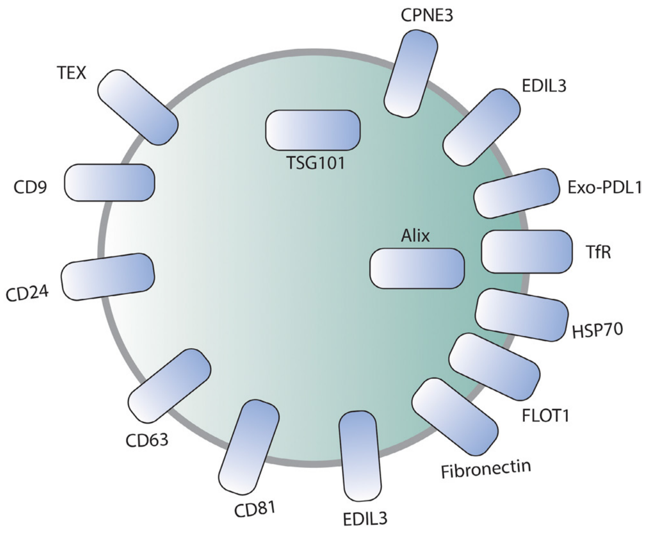

FIGURE 3 Schematic diagram showing common exosomal markers

B-cell-derived exosomes contain MHC-II complexes. Schroeder et al demonstrated that in HNSCC (head neck squamous cell carcinoma) involving B cells PD-1, CTLA, LAG3, and CD137 are increased in some patients.[117] PD-1 expression decreases BCR signaling, and subsets of PD-1 may also be found to be elevated in hepatocellular cancer and thyroid cancer.[91] CTLA4 expression, which is associated with inhibitory effects on immunoglobulin production, is reported to be elevated in B cell malignancies and malignant melanoma,[118] LAG3 (CD223) is a "checkpoint receptor" that regulates TCR signaling and function.[119] CD137, expressed on activated B cells in peripheral blood and on tonsillar B cells, in turn, enhances B cell proliferation, improves survival, and induces secretion of TNF-α & -β.[120] Mature B cells express CD39 ("B cell activation marker") and CD73 on their surface. CD39 and CD73 are considered "immunological switches," that shift from pro- to anti-inflammatory activity in the cells, create an immunocompromised environment, and contribute to the progression of cancer.[121]

T cell-derived exosomes are determined by their surface markers, CD3, CD4, CD8, CD27, and CD28. Loss of CD27/CD28 has been associated with suppressive function and cancer cells maintain their proliferative capacity.[61] Wahlgren et al.[122] showed that exosomes from IL-2, anti-CD3, and anti-CD28 stimulated T cells to express CD9, CD63, and CD81 markers on their surface. These exosomes carry RANTES (CCL5) which promotes cytotoxic response.

4 | CURRENT METHODS OF SEPARATION/COLLECTION OF EXOSOMES

The most commonly used methods of exosome isolation are ultracentrifugation and precipitation. The gold standard for exosome isolation is ultracentrifugation. Precipitation is another most common method for exosome isolation from plasma. Coughlan et al. (2020) used ExoQuick® ULTRA EV Isolation Kit for Serum and Plasma (Systems Biosciences) for precipitation of exosomes due to the ease of extracellular vesicle preparation, significantly depleted number of both IgGs or albumin, and relative enrichment of exosomes based on Nanoparticle Tracking Analysis (NTA) assessment of size and concentration.[123] Ultracentrifugation method produces highly enriched EVs but it is low-throughput and specific infrastructure (i.e., ultracentrifuge) and expertise is required to be performed correctly.[123] Precipitation methods are significantly faster than ultracentrifugation methods and they prepare higher concentrations of exosomes. It also produces extracellular vesicles that have a significantly low number of both IgGs and albumin. A schematic summary of the processes involved in different exosome isolation techniques is shown in Figure 4.

For isolating exosomes, several techniques have been developed by exploiting a particular trait, such as the size, density, and surface markers of exosomes. However, each of these techniques comes with its own limitations which must be addressed for downstream applications. The advantages and disadvantages of commonly applied methods are shown in Table 3.

While the precipitation method provides the most effective exosome isolation (~90%), it takes a long time to achieve exosomes via this method. On the other hand, differential centrifugation takes less time (~9 hours) but the EV yield is variable, sometimes as low as 2%. AF4 (Asymmetric flow field-flow fractionation) process takes only 1 hour but its sample preparation may take up to 3 days. Newer, methods are quick, easier to detect, and can be commercially used.

Helwa et al.[143] compared different exosome extraction methods. They used 6 different volumes of human serum samples versus commercial serum samples from human donors and concluded that even with limited amounts of biological samples, commercial kits miRCURY, ExoQuick, and TEIR are suitable alternatives to ultracentrifugation. Also, exosomes isolated by these techniques and serum volumes had similar zeta potentials to previous studies. In this study, the NTA results showed that all isolation techniques produced exosomes within the expected size range (30–150 nm).

Additionally, exosome isolation methods can be categorized based on their recovery time and assay time (Tables 4 and 5).

Newer methods have been developed that aim for better recovery and specificity. These include:

- Acoustics (or acoustic-based separation methods)[144]: This exosome separation method uses acoustic frequency (as high as ~40 MHz) through a series of cell-removal and exosome-isolation modules and can separate particles based on their physical properties such as size difference, and acoustic contrast factors.[145] Current methods are only based on biological fluids (e.g., undiluted blood samples). This method requires specialized equipment and significant time owing to its preprocessing of liquid samples.[146]
- Alternating current electrophoretic[147]: Another rapid exosome isolation technique is alternating current electrokinetic (ACE) microarray that has been shown to rapidly isolate and recover glioblastoma exosomes from undiluted human plasma samples.[147] This method requires a small plasma sample and can take up to 15 minutes to isolate exosomes. This method is used to isolate various sample types including undiluted blood, plasma, serum, high-molecular-weight DNA, viruses from high conductance buffers, and drug delivery nanoparticles. The principle of this method is based on creating an alternating current (AC) electric field by generating a dielectrophoretic (DEP) separation force generated by the ACE microarray.[148]
- Field-flow fractionation (FFF): Field-flow fractionation is a chromatography-like separation technique that is based on the principle of fractionation of macromolecules, colloids, and particles. A laminar flow of liquid between two walls is pushed by an external field force.[149] It is a rarely used method of exosome separation.[150]
- Asymmetric flow field-flow fractionation (AFFF, A4F, or AF4): The principles of AF4 isolation methods are based on the techniques of "field-flow fraction (FFF)" which was developed in 1966 by Giddings.[151] The AF4 instruments are commercially available and require minimal expertise (requires only basic knowledge of software) and can separate exomeres from other exosome subpopulations. Although the AF4 fractionation step takes only one hour, the total steps from cell culture to exosome/exomere isolation from the conditioned media by ultracentrifugation can take approximately three days. Although this method certainly has some major advantages, the significant drawbacks this method possesses are its inability to handle large samples and its inadequate separation of exosomes based on their sizes.[29]
- Deterministic lateral displacement (DLD) arrays: DLD is a passive microfluidic technique that separates particles based on their size, shape, deformability, and charge. A flat microfluidic channel is filled with a regular array of micropillar obstacles, which creates a periodic flow pattern in a "zigzag" manner, creating the potential for the separation of both cellular and nanoparticles. It is a low-cost separation method.[152]
- (Moved up) Field-free viscoelastic flow: This method is based on the principle that particle migration is caused by size-dependent elastic forces in a viscoelastic medium. This method is more precise than other microfluidics techniques because it is possible to separate particles of submicrometer diameter from a very small volume of samples.[153]
- Fluorescence-activated sorting (especially for larger EVs including large apoptotic bodies and large oncosomes): This sorting method separates specific cell populations by phenotypes that can be detected by flow cytometry. This method is best for characterizing a single cell population without being contaminated by other cell populations.[154]
- High-throughput/high-pressure methods such as fast protein/high-performance liquid chromatography (FPLC/ HPLC) that involve some form of chromatography
- Hydrostatic filtration dialysis: Musante et al.[155] demonstrated that urine exosomal vesicles can be effectively isolated by hydration pressure pushed through a dialysis membrane and samples passing through a dialysis membrane of 1000 kDa molecular weight cut-off are separated based on their sizes.
- Ion exchange chromatography (IEX): It is a chromatographic separation method that separates molecules based on the net

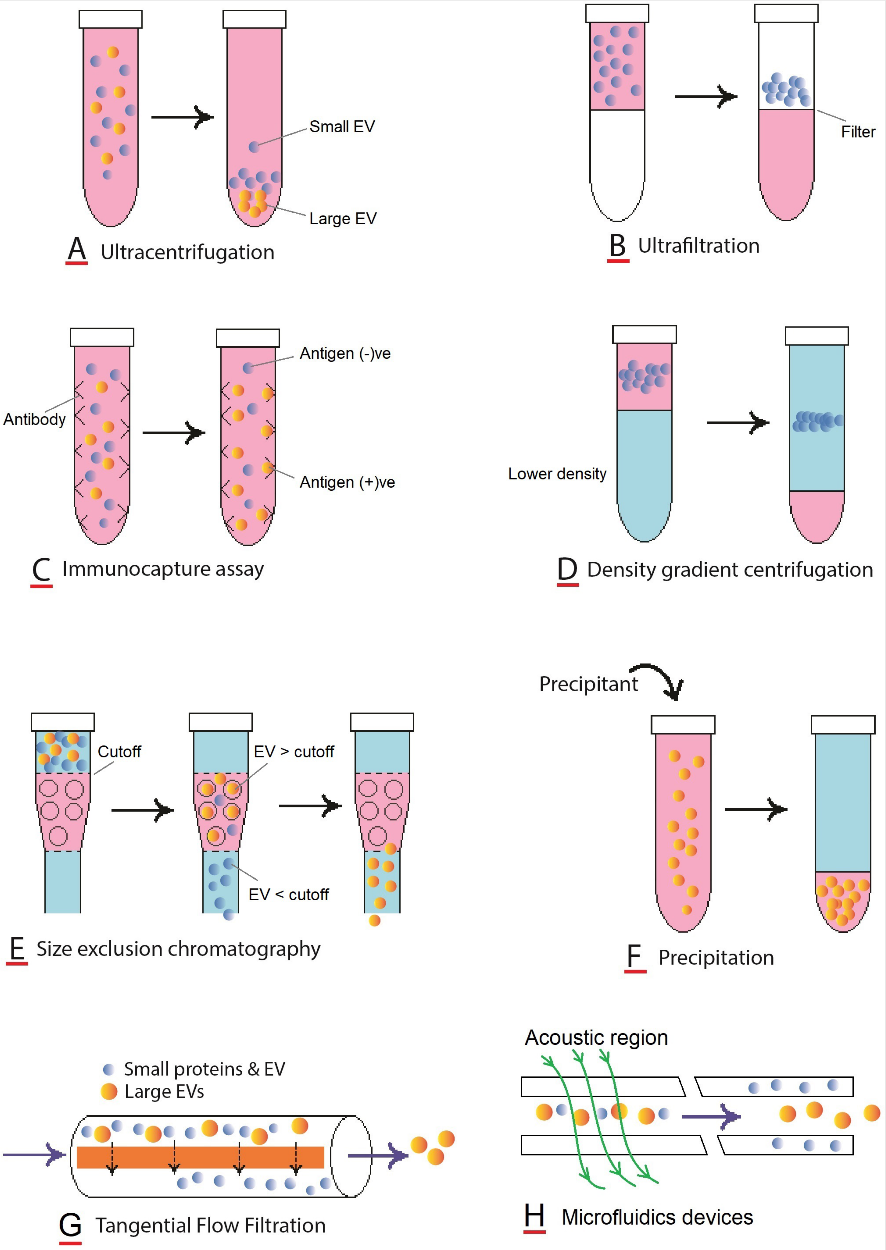

FIGURE 4 Schematic presentation of processes involved in different techniques of exosome isolation

charge on the surface of the proteins. Depending on the ion, IEX is divided into 2 types, cation IEX and anion IEX. Since different proteins have different charges on their surface, this method of separation can easily isolate based on even the tiniest ion change on the surface of the proteins.[156]

- Microfiltration: In order to isolate urinary exosomes, microfiltration methods are developed that uses a hydrophilized, commercially available membrane. This method can isolate LMW proteins from HMW proteins irrespective of the abundance of proteins in the cell sample population.[157]
- Column-based separation protocols yield exosomes with high purity but they produce diluted exosomes and this process is time-consuming. This method of separation involves size exclusion chromatography.[158,159]

4.1 | Importance of heterogeneity of exosomes

Exosomes are a heterogeneous group of EVs and their heterogeneity is due to their varied size, constituents, function, and cellular origin, which adds complexity to their characterization. Such diversity is likely because of the limiting membrane of MVBs during ILV formation or differences in molecular routes partaken during exosome biogenesis.[160] This heterogeneity leads to differential exosome qualitative and quantitative content which in turn produces miscellaneous exosome subpopulations that are distinct in both their biophysical properties and composition. Generally, we can separate exosomes based on their sizes. Large exosomes (Exo-L) are 90–150 nm; small exosomes (Exo-S) are 60–80 nm in size, and the smallest exosomes are exomeres that are 30–35 nm in size. The exomeres

TABLE 3 Exosome isolation methods

	Advantages	Disadvantages	References
Ultracentrifugation (Most commonly used method) [Differential centrifugation (DC)]	• Highly enriched EVs are produced. • Easiest and most widely used method. • Can analyze large volumes of samples. • Can analyze multiple samples at the same time.	• Not clinically applicable as it is laborious, time-consuming, and low throughput. • Specific equipment and expertise are required. • The absolute separation of EVs is not possible. • EVs can be damaged due to exosome clumping. • EV Recovery is only 2% to 80%. • Cannot isolate pure EV.	87,111,123–127
Precipitation	• Six times faster than ultracentrifugation. • 2.5-fold higher concentration of exosomes per ml. • Highly reproducible. • Produces extracellular vesicles that have a significantly low number of both IgGs and albumin. • Clinically applicable. • EV recovery is 90% • Fast, inexpensive, • Requires no special equipment • Can be used for both low- and high-sample volumes.	• Unable to isolate pure EVs. • Aggregation of exosomes. • Not suitable for identification of EV-associated biomarkers	123–125,128
Size exclusion chromatography (SEC)	• Clinically applicable. • Allows for size-based separation on a single column. • Can be used to obtain smaller size EVs. • EV recovery is 40%-90%. • Removes soluble components.	• Processing time is higher. • Exosomes can be degraded due to buffer selection.	124,125
Ultrafiltration (UF)	• Faster method. • Superior to other methods for using large volumes of EV-containing fluids. • Remove soluble components & separate exosomes from big particles. • Inexpensive because of cheaper equipment.	• Not clinically applicable. • Exosomes get attached to the filter pores and result in exosome loss. • Large vesicles can be damaged or deformed while passing through the membrane. • Cannot isolate pure EV.	87,124,125,129–131
Immuno-capture assays (ICA)	• Clinically applicable. • Simultaneously parallel ICA can be performed. • Isolate subpopulations of EVs. • Can efficiently detect members of the tetraspanin family, (e.g., CD81, CD9, and CD63). • Direct separation of exosomes from cell culture supernatant or bodily fluids is possible. • Highly specific. • High purity	• Time-consuming (can take up to hours). • Cannot isolate large-volume samples. • Expensive equipment. • Low exosome yield.	87,124,125,132,133
Density gradient centrifugation (DGC)	• Can separate low-density exosomes from other EVs. • Separate EVs devoid of protein contaminants. • highly purified EVs.	• Not clinically applicable as it is laborious, time-consuming, and low throughput. • Low exosome recovery rate.	87,111,134,135

(Continues)

TABLE 3 (Continued)

		Advantages	Disadvantages	References
Polymer-based precipitation		• Easy to use. • No need for specialized equipment. • Can be used for large samples.	• Nonexosomal contaminants may be present. • Cannot isolate pure EV.	136
Microfluidics		• Rapid analysis is possible due to the short time. • Micro devices are used.	• Low exosome yield. • Low reproducibility.	124,137,138
Tangential flow filtration		• Concentrate from large amounts of cell culture media. • Higher yield of EVs. • High reproducibility. • Produces exosome with fewer albumin contaminants. • Time-efficient.	• Costly method due to expensive equipment and the use of disposable filters.	139–142
Commercial kits	miRCURY ExoQuick TEIR	• Suitable alternatives to UC. • Similar zeta potentials to UC.		143

Abbreviations: UC, Ultracentrifugation; TEIR, Total Exosome Isolation Reagent.

are only recently discovered using asymmetric flow field-flow fractionation. Their study showed that exomeres can transfer functional cargo. In this study, AREG-containing exomeres and exosomes elicited prolonged EGFR effect to modulate EGFR trafficking in intestines, and significantly enhanced the growth of colonic tumor organoids. The increased activity of nanoparticle AREG elicited effects at 1:1,000th of the concentration of rAREG.[29,161] Furthermore, separation with density centrifugation exosomes can be classified as high and low-density exosomes.[78]

Lee, Sang-Soo, et al. identified a new group of EV in the P200 vesicles that were smaller than exosomes in size. Exosomes and the P200 vesicles are found in CM (conditioned medium) of human cell lines. These involve a different biogenesis pathway that is independent of the endocytic pathway. While exosome markers (e.g., Hsp70, TSG101, and CD63) are present in both P100 and P200 vesicle types, the CD81 exosome marker is not detected in the smaller EVs. The addition of the P200 vesicles to human cell cultures enhanced exosome production and cell proliferation.[162]

5 | METHODS OF ENGINEERING EXOSOMES USING DNA TECHNOLOGY

As the research enlightened exosomes' stability, low immunogenicity, and permeability in the body, the idea of using exosomes as a diagnostic and therapeutic tool has emerged. Genetic engineering became a major tool for generating modified exosomes. These engineering processes served to display a peptide/protein on the surface as a cargo or targeting sequence, load cargo into exosomes, and escape micropinocytosis in the circulation.

5.1 | Methods of designing exosomes to carry payload outside the exosomes

In one of the earliest studies of exosome engineering, Delcayre et al. reported that the lactadherin protein binds to exosome lipids with its C1C2 domain and presents on the exosome surface. They showed that engineered fusion proteins with C1C2 domains were presented in the exosomes and called this Exosome Display Technology.[163] Another group used a similar strategy, engineered lactadherin with Gaussia luciferase, and overexpressed this construct in B16-BL6 cells. Following the exosome isolation and intravenous injection into mice, they could track exosomes in mice with bioluminescence imaging.[164] Gassart et al. utilized the cytosolic domain of TM Env protein from the bovine leukemia virus and fused it with the CD8 ectodomain. Expression of this construct resulted in a CD8 enrichment in exosomes.[165]

LAMP2b is another useful exosome membrane protein expressed in murine exosomes[76] and widely engineered to present polypeptides in exosome surfaces. Inserting a polypeptide following its N terminal signal peptide results in the expression of the polypeptide fused with Lamp2b protein and presentation on the surface

TABLE 4 Categorizing isolation methods based on EV recovery

Isolation method	% yield
Precipitation	90 [111,125–127,129–133]
Size exclusion chromatography (SEC)	40-90
Ultrafiltration (UF)	10-80
Differential centrifugation (DC)	2-80
Density gradient centrifugation (DGC)	10
Immunocapture assays (ICA)	

TABLE 5 Categorizing isolation methods based on assay time

Isolation method	Hours
Precipitation	0.3-12 [111,125–127,129–133]
Size exclusion chromatography (SEC)	0.3
Ultrafiltration (UF)	0.5
Differential centrifugation (DC)	3-9
Immunocapture assays (ICA)	4-20
Density gradient centrifugation (DGC)	16-90

of exosomes. Alverez-Erviti et al.[12] fused the neuron-specific peptide RVG to the LAMP2b DNA sequence and generated engineered exosomes with RVG peptides to target neurons. After loading exosomes with siRNA by electroporation, they observed a significant uptake of exosomes to the brain of wild-type mice, which resulted in specific knockdown of BACE1, a target in Alzheimer's disease, in mRNA and protein level. Bellavia et al.[166] utilized the Interleukin-3 fragment fused LAMP2b to target chronic myelogenous leukemia cells. By loading engineered exosomes with Imatinib or siRNA against BCR-ABL, they could inhibit the growth of CML cells in vitro and in vivo.

Stickney et al.[167] investigated the use of exosomal surface proteins as an anchor for fluorescent proteins and demonstrated the feasibility of CD63, CD9, and CD81 fusions with RFP. They also showed the possibility of presenting fluorescent protein either in the lumen or at the surface, depending on the location of the inserted fluorescent protein in the CD63 sequence. Besides well-known exosomal surface proteins, Ohno et al. presented GE11 peptide on exosome surface by genetic engineering of platelet-derived growth factor receptor in HEK293 cells. By inserting Let-7a miRNA into modified exosomes with liposomes, they successfully targeted EGFR-expressing cancer cells in $RAG2^{-/-}$ mice and inhibited tumor growth.[168] Curley et al.[169] also investigated the topology of CD63, exosomal membrane protein, to optimize engineering exosomes to use delivering proteins and peptides.

Dooley et al.[170] conducted a comprehensive study to identify exosomal proteins to carry proteins/peptides on the surface and inside the exosomes. Apart from previous studies, they conjugated GFP to candidate proteins to make this study a functional assay with ELISA and flow cytometry. After optimizing exosomes to work, followed by proteomics, they identified Prostaglandin F2 receptor negative regulator protein, PTGFRN, a previously unreported scaffold protein, to efficiently present GFP on the exosome's surface. Finally, they completed the study with optimization of truncated PTGFRN, which has the potential to become a standard of exosome modification. The same group used PTGFRN as a scaffold to carry IL12 on the surface of the exosome, generating engineered exosome exoIL12. Intra-tumoral injections of exoIL12 showed greater antitumor activity than recombinant IL12 in the MC38 tumor model in mice. exoIL12 also demonstrated one typical advantage that is expected from engineered exosome treatment, compared to recombinant protein counterparts, prolonged half-life/retention. The complete response to exoIL12 at a rate of 63% compared to 0% at recombinant IL12 shows exosomes have the potential to bring many protein-based therapies into the clinic.[171]

Gao et al.[172] developed a novel method to use exosomes for targeting and therapeutic purposes. They identified the CP05 peptide as a CD63 ligand using the phage display technology. By conjugating CP05 with different targeting peptides (M12 for muscle, RVG for neuron, SP94 for hepatocellular carcinoma), they achieved specific targeting of exosomes to target tissue. Furthermore, they showed dual-labeling with neuron-specific NP41 peptide and fluorescein isothiocyanate fluorescent marker, allowing feasible tracking and detecting of specific cells. Also using the amide linker, they conjugated antisense oligonucleotides for exon skipping therapy in Duchene muscular dystrophy in the mouse model and demonstrated an enhanced dystrophin expression. This approach could have great translational potential since it allows for modification of native exosomes of the organism and involves minimum disturbance. For example, it would be possible to collect exosomes from patients, label them with CP05-conjugated proteins or peptides, and give them back for diagnostic, and therapeutic purposes.

Other than genetic engineering of membrane proteins to load cargo on the surface, another method to conjugate peptides into the exosome membrane is click chemistry. Jia et al.[173] modified the exosome membrane by inserting (1-Ethyl-3-[3-dimethylaminoprop yl]-carbodiimide hydrochloride-N-Hydroxysuccinimide (EDC-NHS) and attaching a neuropilin-targeting RGE peptide to target glioma. With the addition of curcumin and super paramagnetic iron oxide nanoparticle (SPION) into the exosome by electroporation, they showed SPION-labeled exosomes enriched in glioma on magnetic resonance imaging (MRI). The tumor volume is decreased and survival increased in the mouse glioma model. Kim et al.[174] also used 1,2-Distearoyl-sn-glycero-3-phosphorylethanolamine (DSPE) and polyethylene glycol to incorporate AA ligand (which has a high affinity for sigma receptors in nonsmall cell lung carcinoma) into macrophage-derived exosomes. After loading paclitaxel into exosomes by sonication, they demonstrate that modified exosomes specifically target the pulmonary metastasis of the Lewis lung carcinoma mouse model and improve survival. Choi et al.[175] modified exosomes by mannose-conjugated polyethylene glycol modification of exosomal membrane to target DCs. To increase immune response, monophosphoryl lipid A (adjuvant) loaded into exosomes in the presence of DMSO, and they managed to target DCs specifically and increased inflammatory cytokines TNF-α and IL-6. Figure 5 shows currently available methods to display protein on exosome surface.

5.2 | Methods to load cargo into exosomes

Exosome lumen can be used to carry protein and nucleic acid cargoes, as the content can travel without risk of degradation or unintended interaction. In one approach, Lai et al.[176] genetically engineered cells to express nuclear localization signal (NLS) fused carrier protein (GFP) with MS2 coat protein (MS2CP) that would work as a dock inside the exosome. They also expressed a reporter mRNA with MS2 binding site (MBS), which will bind to MS2CP of docking protein. As a result, exosomes collected from these cells contained carrier protein with attached mRNA, fused with their MS2CP and MBS domains, respectively. Another docking approach utilized by Yim et al.[177] who used the interaction between photoreceptor cryptochrome 2 (CRY2) and CIBN, truncated version of CRY-interaction basic-loop-helix 1 protein in a technique they called "EXPLOR." by genetically integrating CIBN into the luminal side of CD9 and CRY2 into cargo protein, they were able photo-activate docking of cargo protein to CD9 through CRY2 and CIBN interaction and generated exosomes filled with cargo protein in the presence of blue light. They successfully delivered Cre-carrying exosomes into the brain of lox EYFP transgenic mice and demonstrated the expression of EYFP proteins in vivo. Further, this group used the same experimental design to introduce super-repressor IκB (srIκB), an engineered protein without phosphorylation sites, which inhibits translocation of nuclear factor κB into the nucleus to prevent sepsis. After generating engineered exosomes in HEK293T cells, they have shown that local injection of engineered exosomes significantly reduced inflammatory response and mortality in the septic mouse model.[178]

Dooley et al.,[170] who identified PTGFRN protein to carry cargoes on exosome surfaces, also studied proteins to carry cargo inside the exosomes. They identified BASP1 as associated with the inner leaflet of membranes. Further optimization with truncation of BASP1 identified eight amino acid peptides efficiently load GFP into exosomes, comparable to full-length BASP2 protein. Furthermore, an ovalbumin-loaded exosome, exoOVA, successfully induced IFNγ and OVA-reactive CD8 T cells much more efficiently than Ovalbumin alone. This also indicates the advantage of using engineered exosomes over recombinant protein counterparts.

Sterzenbach et al.[17] reported that the late-domain pathway could be used to load molecules into exosomes. They fused the WW tag into Cre recombinase, which is recognized by late-domain containing protein Ndfip1, ubiquitylated, and subsequently loaded into exosomes. Upon nasal administration of these engineered exosomes, exosomes were taken up by floxed reporter cells, resulting in tdTomato expression, indicating functional delivery of proteins. They also found that proteinase K treatment did not diminish WW-Cre protein in the absence of Triton X-100, showing the cargo protein is located inside the exosome. We also employed this approach in our lab and found that WW tagged Neuroglobins enriched in exosomes (unpublished).

It might be argued that protein loading techniques into exosomes with physical force and disruption may damage the exosome membrane and cause content loss. Busatto et al.[179] have used cationic amphiphilic molecules, which can penetrate membranes, to load proteins inside exosome.

There are several methods developed to load nucleic acid into the exosomes. Li et al.[180] employed Human Antigen R (HuR), an

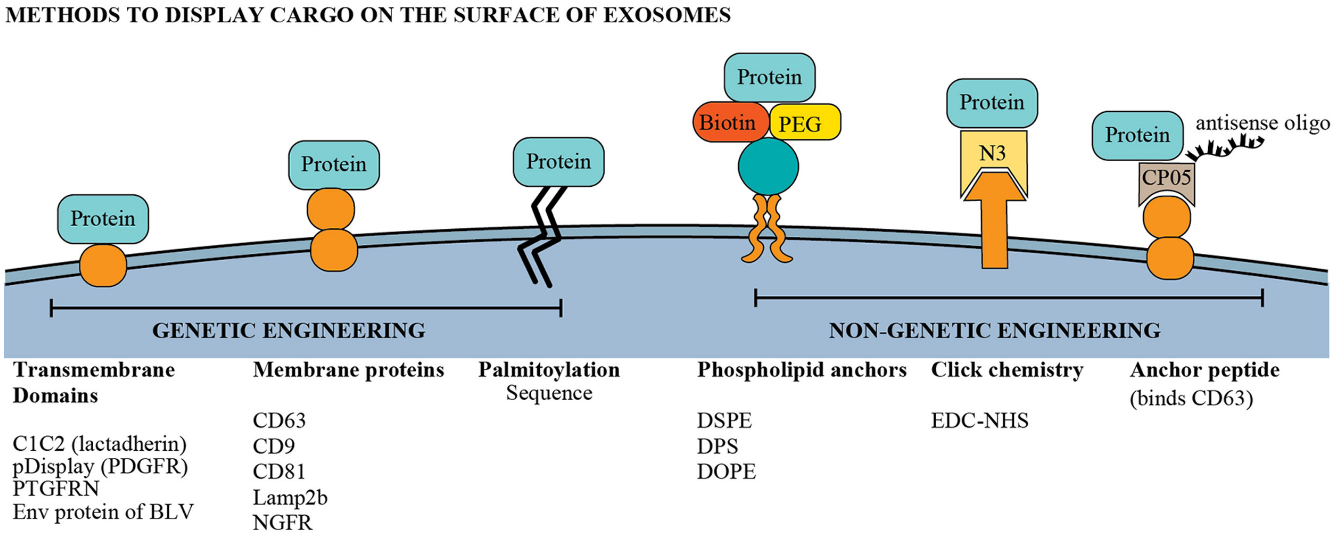

FIGURE 5 Current methods to display a cargo on the surface of exosomes. PDGFR, Platelet-derived growth factor receptor; PTGFRN, Prostaglandin F2 Receptor Inhibitor; BLV, Bovine Leukemia Virus; LAMP2b, Lysosome-associated membrane protein 2; NGFR, Nerve Growth Factor Receptor; DSPE, 1,2-Distearoyl-snglycero-3-phosphorylethanolamine; DMPE, 1,2-Dimyristoyl-sn-glycero-3-phosphoethanolamine; DOPE, 1,2-dioleoyl-sn-glycero-3-phosphoethanolamine; PEG, Polyethylene glycol; EDC-NHS, (1-Ethyl-3-[3-dimethylami- nopropyl]-carbodiimide hydrochloride – N-Hydroxysuccinimide; N3, azide radical

RNA binding protein, into the luminal surface of exosomal membrane protein CD9 and loaded exosomes with specific miRNA, which bound to HuR through Adenylate-uridylate-rich elements (AU-rich elements). As a result, after successfully delivering engineered exosomes to target cells, they reduced the target protein expression in vivo and in vitro. They also delivered CRISPR/dCas9 system in vivo by adding AU-rich elements to dCas9 mRNA and repressed C/ebpα expression. Kojima et al.[181] developed an RNA packaging device using archaeal ribosomal protein L7Ae that binds to the C/D_{box} RNA structure. They conjugated L7Ae into the C terminus of CD63 to place inside exosomes and inserted the C/D_{box} region in the 3′-untranslated region of reporter gene coding nanoluc bioluminescence reporter protein. Along with RVG targeting peptide attached to exosome in LAMP2b exosomal membrane protein, they demonstrated that exosomes targeted the brain and delivered their mRNA, and detected luminescence in target cells. Figure 6 shows genetic engineering and physical methods to load cargo into exosomes.

5.3 | Immunological use of engineered exosomes

Huang et al. modified HELA cells by overexpression α-Lactalbumin (α-LA), a breast-specific protein expressed in human breast cancers, and collected α-LA-enriched exosomes. After loading TLR3 agonist Hiltonol and immunogenic cell death inducer human neutrophil elastase, they treated mouse breast tumor models with this exosome. They found an increased accumulation of DCs and CD8 T cells in the tumor and reduced tumor size in MDA-MB-231 tumor-bearing mice.[182]

Antigen-presenting features of DCs are key in inducing the immune response. Dendritic cell exosomes have the potential to induce the immune system. Hong et al.[183] modified dendritic cell-derived exosome to utilize MHC-I molecule on the surface of exosome by integrating respiratory syncytial virus antigen. Despite the failure to activate CD8 T cells in vivo, it is in vitro success proves that it works but needs further optimization. In another effort, Kim et al.[184] genetically engineered K562 cells by overexpressing human leukocyte antigen-A2 and costimulatory molecules CD80, CD83, and 41BBL to use exosomes to stimulate antigen-specific CD8 T cells. This effort to overcome the inherent difficulty of exosome generation in DCs for the same purpose proved successful in cell culture by having a comparable CD8 stimulation. This approach could be used for adoptive cell therapies. In another attempt to employ exosomes in immune system activation, Morishita et al.[185] developed a lactadherin with streptavidin fusion protein and genetically engineered murine B16-BL6 melanoma cells. After collecting modified exosomes, they incubated exosomes with biotinylated CpG DNA (innate immune response activators) and labeled these exosomes using streptavidin on the exosome surface. They reported these engineered exosomes activated DC2.4 cells and enhanced their tumor antigen presentation.

Exosomes, through engineering surface proteins, can turn into immunological reagents. Hartman et al.[186] used the C1C2 domain of lactadherin to present carcinoembryonic antigen (CEA) and human epidermal growth factor receptor 2 (HER2) tumor-associated antigens on exosome surface to antigen-presenting cells to enhance the anti-tumor immune response. By fusing CEA and HER2 to the C1C2 domain, they expressed these antigens on the exosome surface and enhanced T and B cell responses. Shi et al.[187] turned exosomes into immunological mediators by anchoring anti-CD3 and anti-HER2 into the exosomal membrane by PDGFR. By dual targeting T cells and HER2-expressing cancer cells, the directed T cell demonstrated anti-tumor activity in the mouse breast cancer model. We used LAMP2b protein to display CD206-targeting peptide to target M2 type of macrophages and Fc fragment of mouse IgG2b to bind natural killer cells, aiming antibody-dependent cellular cytotoxicity (ADCC) to eliminate M2 type macrophages. Our engineered exosomes specifically targeted M2 macrophages and significantly reduced CD206+ cells in vivo. Further treatment with engineered exosomes reduced tumor growth and prevented early metastasis in 4T1 tumors in mice.[26] Figure 7 shows the immunological use of engineered exosomes.

Fan et al. followed a hybrid approach in engineering exosomes for immunotherapy. First, they collected ovalbumin-induced dendritic cell exosomes, which already express MHC and CD86, needed for T cell activation. Then, they enriched the exosome membrane with anti-CD3 and anti-EGFR receptors to bind T cells and B16-OVA tumor cells, respectively, and induce cytotoxicity by bringing them into the vicinity. Engineered exosome treatment resulted in an immune response augmented with a PD-L1 inhibitor, decreased tumor size, and increased survival in the B-16 OVA tumor model in mice.[188]

In the TME, one commonly studied phenomenon is the M1 and M2 macrophages and their pro-inflammatory and immunosuppressive roles, respectively. Gunassekaran et al.[189] engineered M1-derived exosomes to deliver siRNA and miRNA to M2 type of macrophages to induce M2 to M1 polarization. To achieve this, M1 exosomes were transfected with miR-5aa-3p and NK-κB siRNA. To target M2 macrophages, IL4R-binding peptide attached to exosome membrane using DOPE-PEG amine. The engineered exosomes achieved M2 to M1 polarization and reduced the tumor volume in the 4T1 mouse breast tumor model. Engineered exosomes could also modify the immune system through their displayed proteins. Conceição et al.[190] engineered exosomes as a decoy for interleukin 6 (IL-6), a key mediator of inflammation in skeletal muscle, to inhibit the IL-6 trans-signaling pathway and inflammation. They found engineered exosomes reduced STAT3 signaling, which indicates the inhibition of the inflammation and shows it can be used in Duchenne treatment to reduce muscle wasting as an alternative to anti-inflammatories. Duong et al.[191] have engineered exosomes by presenting the TNFα receptor on their surface to antagonize TNFα and prevent inflammation in vitro model.

FIGURE 6 Methods to load cargo inside exosomes. (A) Genetic engineering methods to load exosomes with protein and nucleic acid. MS2CP, MS2 coat protein; MBS, MS2 binding site; CRY2, cryptochrome 2; CIBN, truncated version of CRY-interaction basicloop- helix 1 protein; NLS, nuclear localization signal; BASP1, Brain Abundant Membrane Attached Signal Protein 1; HuR, Human Antigen R. (B) Physical methods to load proteins and nucleic acids into exosomes

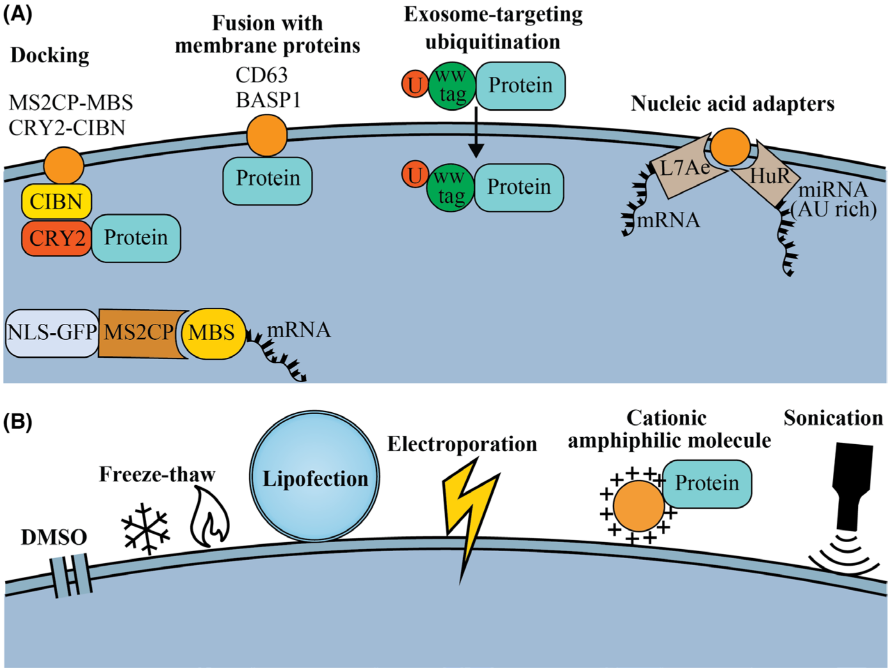

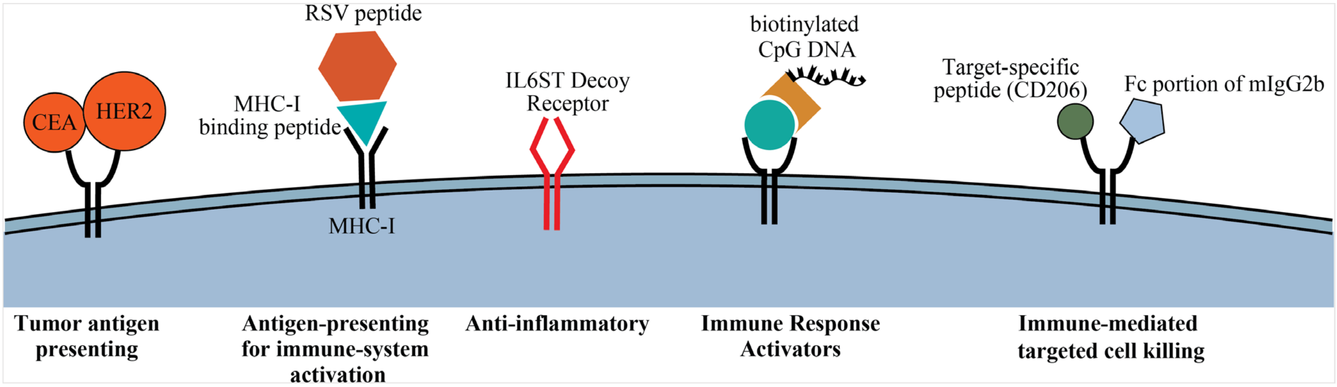

FIGURE 7 Immunological use of engineered exosomes. CEA, carcinoembryonic antigen; HER2, human epidermal growth factor receptor 2; RSV, respiratory syncytial virus; IL6ST, Interleukin 6 Cytokine Family Signal Transducer, mIgG2b, mouse immunoglobulin G 2b

5.4 | Engineered exosomes in metastasis

Tumor exosomes indicate the immune status and play a significant role in metastasis. In an in-depth study, Chen et al.[192] found that PD-L1, which suppresses immune response against the tumor, on exosomes was abundant in metastatic melanoma compared to healthy donors. Exosomal PD-L1 was found to inhibit CD8 T cells and correlated with poor Pembrolizumab (antibody against PD-L1 receptor, PD-1) response. This indicates that tumors use exosomes as "decoy" to overcome immune responses.

One of the central concepts in cancer metastasis research is the "seed and soil" hypothesis. Suetsugu et al.[193] tagged CD63 exosome membrane protein with GFP in tumor cells and tracked the exosome traffic in mouse breast cancer models. They were able to track tumor-derived exosomes in organs and tumor-associated cells in the circulation and demonstrated the use of exosome tracking in investigating cancer metastasis. This approach would be particularly useful in metastasis research by tracking exosome traffic from cancer cells. Pucci et al.[194] adopted a methodical approach to investigating tumor cell communications by modifying melanoma to express luciferase. They found luciferase activity in tumor-draining lymph nodes and identified $CD169^+$ macrophages as a tumor suppressor that prevents tumor exosome spread. This study proves that the exosome study holds a great potential to understand metastasis. Pucci's group further engineered exosomes to express bacterial Sortase A on PDGFR or dNGFR membrane proteins, which transfers substrate peptides (e.g., biotin-containing peptides) to N terminal glycine of surface proteins. Compared to employing GFP-labeled exosome, this method showed 10–100 fold increased sensitivity in detecting exosome-target cell interaction and a promising strategy to study specific exosome-cell interactions.[195]

FIGURE 8 Engineering methods to extend half-life of exosomes in circulation. SIRPα, signal regulatory protein; GNSTM, glycosylation motif

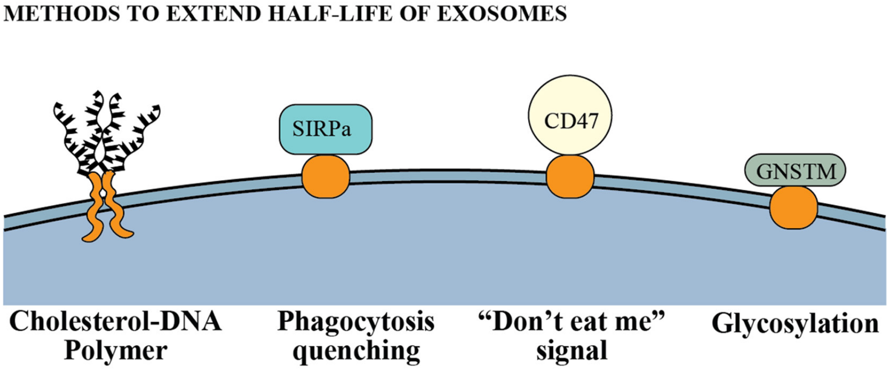

5.5 | Engineered exosomes in various diseases

Organ and tissue-specific exosome delivery are achieved by also physical forces. Lee et al. loaded mesenchymal stem cell-derived exosomes with iron oxide nanoparticles by supplying them in cell culture to increase the delivery to target organs. By implanting a magnet next to the heart, they achieved an increased delivery into the infarcted myocardium.[196] In another concept study, researchers labeled exosomes through their transferrin receptor using superparamagnetic iron oxide nanoparticles conjugated to transferrin with the help of carboxylated chitosan. Exosomes are loaded with BAY55-9837 peptide for type 2 diabetes mellitus treatment and targeted to pancreatic islet cells using magnets to attract SPION labeled exosomes. They observed a significant increase in delivery of exosomes and alleviation of hyperglycemia in db/db diabetic mice.[197] Mizuta et al.[198] also used magnetic nanogels to increase the delivery of exosomes. After hybridizing exosomes with magnetic nanogels, magnetic force significantly improved the delivery of exosomes to cells in culture.

Liu et al. utilized the intrinsic feature of ferritin use as an MRI contrast reagent and engineered exosomes to carry ferritin in modified lactadherin transmembrane protein on the exosome surface. With this, they were able to use exosomes as MRI contrast reagents without the need for further labeling.[199] Furthermore, with further modification to target specific cells, engineered exosomes could be used to image cells or tissue in the body.

Maguire et al. found that Adeno-associated virus (AAV) generating cells also release the virus in exosomes, and called these "vexosomes." They found vexosomes have outperformed AAV alone in transfecting the cells. Further modification of the exosome membrane with biotin attachment and magnetic bead labeling, followed by attraction with magnets in cell culture further improved the transfection efficiency.[200] Maguire's group further explored the exosome-associated AAV gene delivery/therapy in the mouse. They found the same level of exosome-associated AAV delivery in blood, but lesser performance, still comparable in the spleen, lymph node, and liver compared to conventional AAV.[201] With the use of engineered exosome-associated AAV to target specific cells, exosomes would be a new and more effective method to be used in gene delivery and therapy.

Jhan et al.[202] fused exosomes with synthetic lipids to increase the number of vesicles and increased the vesicle amount 6–43 fold. Their siRNA cargo loading and delivery were successful. Sato et al.[203] used freeze-thaw cycles to fuse functional lipids with exosome membrane. Although these processes have the advantage of increasing quantity and modifying membranes, many cargo proteins might be lost, and surface proteins lessened through the process.

Membrane receptors are major drug targets, and molecular assays in protein's native conformation are crucial in biotechnology and clinical research. Desplantes et al.[204] engineered exosomes to study multiple membrane proteins by directing membrane proteins to exosome membranes by conjugating patented "DCTM" peptides.

Exosomes are subject to elimination via multiple mechanisms in circulation, and there are various studies to prolong exosome half-life in the organism (Figure 8). Hung et al.[205] observed an insufficient peptide presentation in engineered LAMP2b of exosomes. They hypothesized that glycosylation would protect these peptides and demonstrated that glycosylation protects peptides in LAMP2b and enhances the delivery of exosomes to recipient cells. Kamerkar et al.[206] found that CD47, a ligand for signal regulatory protein (SIRPα), is crucial in protecting exosomes from micropinocytosis, the presence of CD47 on the surface protects exosomes from phagocytosis. They also showed loading exosomes with KrasG12D shRNA, which targets a common mutation in pancreatic cancer, proved to suppress pancreatic tumor growth and metastasis in mice in the presence of CD47. Another group investigated different aspect and use of CD47 interaction. Koh et al.[207] stated that CD47 is present in most tumors, making the tumors immune to phagocytosis. They overexpressed SIRPα in HEK293 cells and generated SIRPα-enriched exosomes using pDisplay. By saturating all CD47 (don't eat me) receptors of tumors with these engineered exosomes, they showed a significant decrease in tumor volume of CT26.CL25 in immunocompetent BALB/c mice, but not in HT29 in BALB/c nude mice, indicates T cell immunity may be required for effective treatment in CD47 blockade. In another attempt to prevent the elimination of exosomes, Lathwal et al.[208] used cholesterol-modified DNA tethers and complementary DNA block copolymers to enhance the stability of exosomes. They found modified exosomes have fourfold higher blood circulation time. The methods to extend exosome half-life in the organism are described in Figure 8.

6 | USE OF ENGINEERED EXOSOMES FOR TARGETING SPECIFIC CELLS IN VIVO

Based on the above description and details of the engineering method of exosomes using DNA technology, it should be obvious to the readers that engineered exosomes could be the next nanotechnology that would be widely used to target specific cells in vivo not only to determine the distribution of specific cells and enhance the functional status of specific cells but also to target and deplete the specific cells. Irrespective of the origin or parent cells, exosomes share common features such as certain tetraspanins (CD9, CD63, and CD81), heat shock proteins (HSP 60, Hsp 70, and Hsp 90), biogenesis-related proteins (Alix and TSG 101), membrane transport and fusion proteins (GTPases, annexins, and Rab proteins), nucleic acids (mRNA, miRNA, and long noncoding RNAs and DNAs), and lipids (cholesterol and ceramide).[2,7,8] Investigators have started making engineered exosomes to carry biologically active protein on the surface or inside the exosomes and using exosomes to carry drugs to the site of interest.[11,16–19] Recently, our laboratory has achieved a few milestones in exosome technology.[25,26] Our laboratory is heavily engaged in the investigations of the TME and microenvironment of cerebrovascular diseases (CVD). We are working on determining the roles of myeloid cells, especially MDSC and immune suppressive M2 macrophages in the TME, and the roles of neutrophils on the exacerbation of edema in stroke or their roles in tumors following therapies. The following paragraphs will detail the methods and possible utility of immune cell-specific engineered exosomes that can be used to target and deplete cells in the TME or CVD.

6.1 | Engineered exosomes to target M2-macrophages

Depending on the stimuli, macrophages undergo a series of functional reprogramming as described by two different polarization states, known as M1 (classically activated) and M2 (alternatively activated).[209,210] Phenotypically, M1 macrophages express high levels of major histocompatibility complex class II (MHC II), the CD68 marker, and co-stimulatory molecules CD80 and CD86. On the other hand, M2 macrophages express high levels of MHC II, CD163, CD206/MRC1, Arg-1 (mouse only), and others. M2-polarized macrophages are induced by IL-4, IL-13, IL-21, and IL-33 cytokines.[211,212] M2 macrophages release high levels of IL-10, transforming growth factor-beta (TGF-β), and low levels of IL-12 and IL-23 (type 2 cytokines). M2 macrophages also produce CCL-17, CCL-22, and CCL-24 chemokines that regulate the recruitment of Tregs, Th2, eosinophils, and basophils (type-2 pathway) in tumors.[213,214] The Th2 response is associated with the anti-inflammatory and immunosuppressive microenvironment. CD206, also known as mannose receptor (MR), is a 175 kD type-I membrane protein and is expressed predominantly by alternatively activated M2 macrophages and resident tissue macrophages mostly in the lungs, spleen, and liver.[215] It functions in endocytosis and phagocytosis and plays an important role in immune homeostasis by scavenging unwanted mannoglycoproteins.[216] Alternately activated M2 macrophages are known to be associated with therapy-resistant, metastasis, and poor survival in different malignant tumors.[217–219] Figure 9 shows an increased number of M2 macrophages in metastatic breast cancer and there is poor overall survival and disease-free survival in tumors showing a higher number of MRC1.

In recent years, investigators have identified a peptide sequence CSPGAKVRC or its linear form CSPGAK that binds specifically to CD206+ M2 macrophages in the tumors and sentinel lymph nodes in different tumor models.[220,221] It is to note that the linear form of this peptide CSPGAK also binds to human M2 macrophages.[221] We have developed engineered exosomes that carry these peptides and precisely detected M2 macrophages both in vitro and in vivo and showed our results in recent publications.[26,222] We have used nontumorous cells (HEK-293 cells) to develop the engineered endosome carrying M2-macrophages targeting peptides as well as the Fc-portion of mouse IgG2b (Fc-mIgG2b) on the surface to target and deplete alternatively activated immunosuppressive CD206+ M2 macrophages in vivo through ADCC and apply these engineered exosomes to alter immunosuppressive TME to enhance the effect of different therapies (including immunotherapy) to decrease tumor burden and improve survival. Figure 10 shows the vector design and mechanisms of action of the engineered exosomes to initiate ADCC to kill targeted cells.

6.2 | The exosome is a better vehicle to enhance antibody-dependent cellular cytotoxicity

ADCC is a nonphagocytic mechanism by which most NK cells (effector cells) can kill antibody-coated target cells in the absence of complement and without major histocompatibility complex (MHC).[223] Targeted therapy utilizing monoclonal antibodies (mAbs) has instituted immunotherapy as a robust new tool to fight against cancer and other noncancerous disorders, such as cryoglobulinemia, Wegener's granulomatosis, and bullous pemphigoid.[224,225] As mAb therapy has revolutionized immunotherapies, ADCC has become more applicable in a clinical context. Clinical trials have demonstrated that many mAbs perform somewhat by eliciting ADCC.[226] Antibodies serve as a bridge between Fc-receptors on the effector cell and the target antigen on the cell that is to be killed. Crosslinking of receptors in both effector cells and target cells is required for triggering the cytotoxic event. ADCC occurs through various pathways, including (a) release of cytotoxic granules; (b) TNF family death receptors signaling; (c) release of pro-inflammatory cytokines, such as IFN-γ.[227] Both the uptake of perforin and granzymes by target cells and TNF family death receptor signaling induce target cell apoptosis,[228] while effector cell-released IFN-γ actuates nearby immune cells to stimulate antigen presentation and adaptive immune responses.[229] Our goal is to target the Fc gamma-receptor (FcγR)-based platform to deplete M2 macrophages (Figure 10). We have identified the sequence of

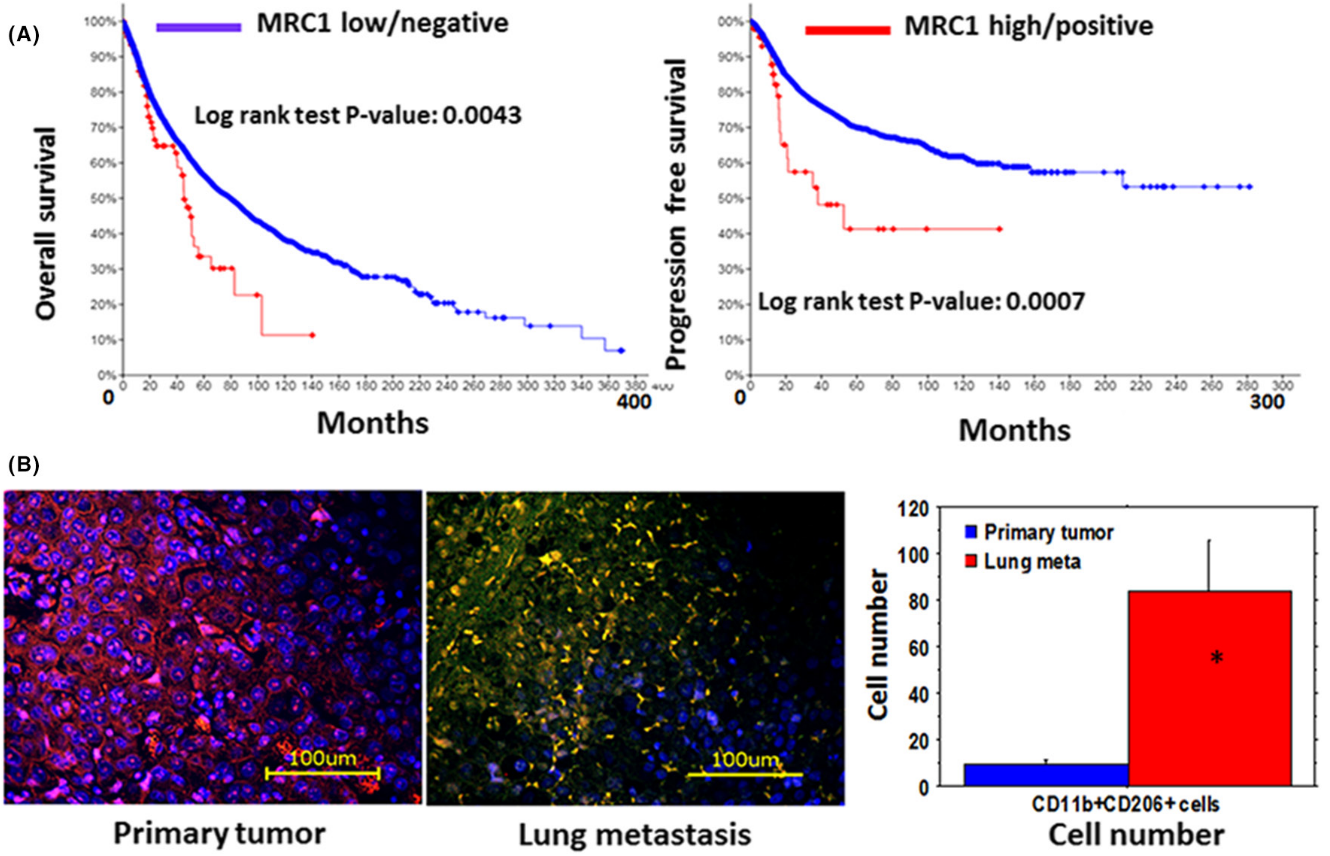

FIGURE 9 (A) Disease-free and overall survival of patients with different cancers expressing mannose receptor (MRC1) in the tumor tissues (TCGA data). (B) Increased number of CD206+/CD11b+ cells in lung metastasis (middle panel, yellow cells) from breast cancer compared to that in the primary tumor (left panel). Quantitative analysis showed a significantly increased number of CD11b+CD206+ cells. The samples are from multiple patients and randomly selected histochemical sections ($n = 6$). * = $P < 0.01$

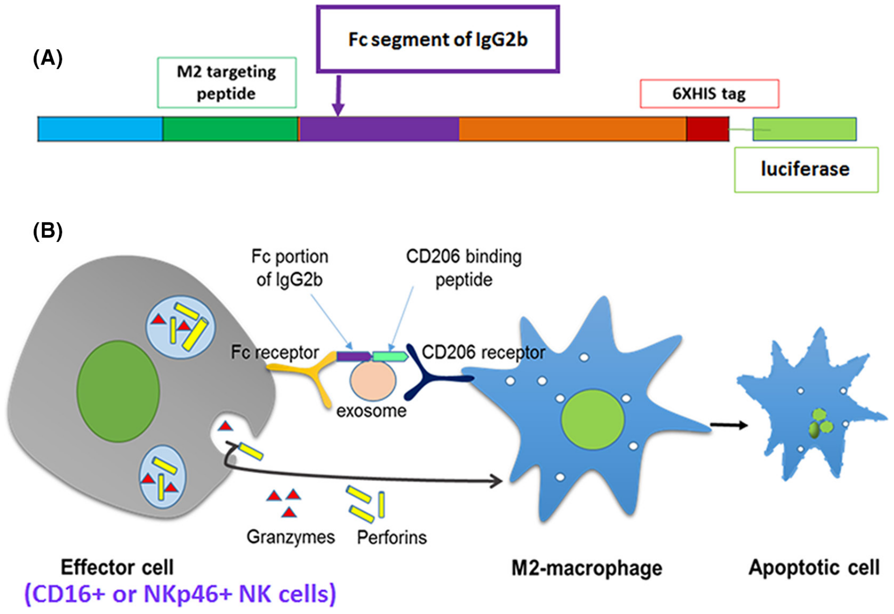

FIGURE 10 (A) Vector design to express M2 targeting peptide and Fc-mIgG2b on exosomes. (B) Cartoon to show the mechanisms of ADCC through engineered exosomes

the Fc-mIgG2b that triggers FcγR-mediated phagocytosis and cytotoxicity[230] and recently we have reported the utility of engineered exosomes as imaging and therapeutic probes.[26] It is to note that we have also identified the sequence Fc portion of human IgG that triggers FcγR-mediated phagocytosis and cytotoxicity for designing human M2 macrophages targeting engineered exosomes.

Because of the cellular origin, exosomes show enhanced permeability even through the intact BBB, which is an advantage

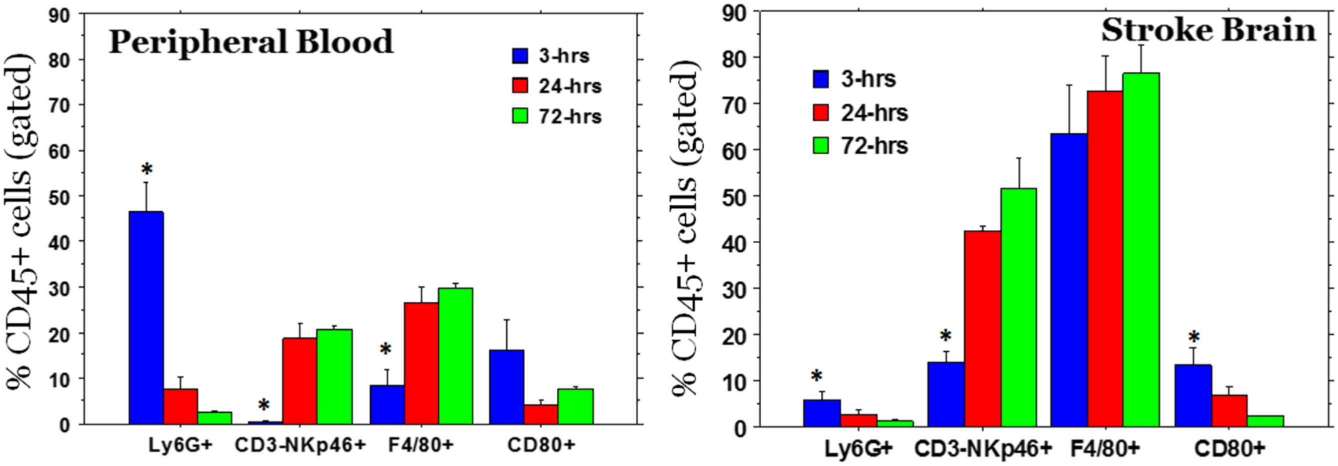

FIGURE 11 Mobilization of neutrophils and M1 macrophages in the peripheral blood and in the stroke area was observed as early as 3 hrs. Whereas other cell types such as NK cells and macrophages (F4/80+, which also contain M2 type macrophages) gradually increased in the stroke areas. Following collection of peripheral blood from each stroke animal, animals were euthanized and perfused with ice cold PBS and the brain tissues from stroke area were collected and single cell suspensions were made for flow cytometry. * = significant differences

over synthetic nanoparticles.[231–234] Exosomes are also shown to utilize enhanced permeability and retention (EPR) effects.[234,235] Due to higher stability in biological fluids and enhanced permeability, exosomes are better for targeted delivery of therapeutic payloads.[231–234,236] Investigators have used either synthetic nanoparticles or fusion protein to deliver Fc-IgG2b to initiate ADCC but because of the rigid body, synthetic nanoparticles rely most on the ERP effect and reports are showing a lack of ADCC following tagging with gold nanoparticles.[237–241] Moreover, due to a size-dependent manner, synthetic nanoparticles can be cleared by the kidneys or reticuloendothelial system, even with targeting moieties.[242–244] On the other hand, fusion protein-based ADCC did not show promise due to rapid clearance and nonspecific bindings.[245–248] Antibody-mediated ADCC also depends on the antibody design with intact Fc-portion and specific attachment to the target cells.[249] Most of the antibodies that are used to initiate ADCC are monoclonal.[250] We postulate that engineered exosomes developed in nontumorous cells, HEK293, will be a better choice to carry therapeutic payloads to enhance ADCC.

6.3 | Engineered exosomes to target Myeloid-derived suppressor cells or CSF1R+ myeloid cells

Our decade-long investigations and investigations by others proved that bone marrow-derived progenitor cells (BMDPC) influence the TME tremendously causing dynamic changes from inflammatory to the immunosuppressive milieu, neovascularization, recurrence, local invasion, and distal metastasis.[251–258] These dynamic changes are pronounced due to mobilization and accumulation of BMDPC following different therapies including radiation, chemo, and antiangiogenic causing therapy resistance.[253,254,256,259–261] Based on the status of the microenvironment such as inflammatory vs immunosuppressive, the treatment effects differ significantly and the recent addition of immunotherapy also becomes noneffective in the solid tumors.[255,256,262,263] Recently, we have pointed out the involvement of myeloid cells in the development of therapy resistance and recurrence of different tumors.[255,256,264,265] In our recent publications, we have used small molecular agents that inhibit CSF1R tyrosine kinase and showed the retardation of growth of GBM and breast cancers, which was corroborated with animal models where all CSF1R+ cells were conditionally depleted.[253,256,266,267] Therefore, using DNA engineering technology we can make exosomes to carry CSF1R targeting peptides and use payloads for depleting the myeloid cells at different stages of TME status. We have already identified a truncated version (peptide sequences from 36 aa to 147 aa) of CSF1 protein, which showed 100% sensitivity to react with CSF1R and made vectors for making engineered exosomes. We used a similar platform as shown in Figure 10 to make the vector and engineered exosomes. We are also in preparation to make targeting exosomes without inserting Fc-mIgG2b to see the distribution of CSF1R+ cells in the TME at different stages of TME following therapy. We stipulate that our engineered exosomes to target and deplete CSF1R+ cells along with established immunotherapy (anti-PD1) will show synergistic effects.

6.4 | Engineered exosomes to target neutrophils

Each year more than 795 000 people in the United States have a stroke and it kills about 140 000 people, placing a $34 billion annual economic burden on society.[268] Though major advances in our understanding of cerebral ischemia have been made, the need for novel effective therapies remains imperative. Unfortunately, the success of different therapies is highly variable, and none can be employed early before significant vascular pathology and damage to the brain have occurred. Activated neutrophils have pivotal roles in acute ischemic brain injury, atherosclerosis, and thrombus formation.[269] Neutrophils are the most abundant polymorph

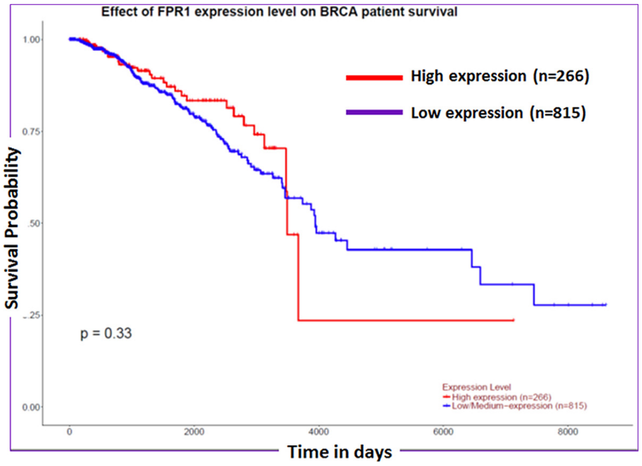

FIGURE 12 Survival probability in BRCA+ breast cancer patients expressing FPR1. (TCGA data from UACLAN)

nuclear (PMN) white blood cells (WBCs) in the blood and make up part of the innate immune system. Neutrophils are an essential part of the inflammatory cascade, being the first cell type to migrate from the bloodstream to the site of inflammation.[270,271] Following recruitment, neutrophils get activated and subsequently express adhesion molecules and release reactive oxygen species, cytokines/chemokines, and proteolytic enzymes causing damage to the tissues.[272,273] Infiltration of neutrophils in the ischemia-reperfusion stroke area occurs early, at the same time as brain injury. This increased accumulation of neutrophils is associated with stroke severity,[274] infarct volume,[275] and worse functional outcomes.[276] Several studies have started to evaluate broadly targeting anti-neutrophil treatments to minimize stroke injury and to improve stroke outcomes.[269,277,278]

Our laboratory studies in male B6 mice (10-12 months old) (Figure 11) show the mobilization of neutrophils (Ly6G+), natural killer (NK) cells (NKp46+CD3-), macrophages (F4/80), and M1 macrophages (CD80) in the peripheral blood and at the sites of a stroke at 3, 24, and 72 hours after stroke.

Recent studies also pointed out the involvement of tumor-associated neutrophils (TAN) and tumor-associated macrophages (TAM) in maintaining the inflammatory or immunosuppressive TME that dictates the effect of therapies.[217–219,279–286] Neutrophils are the most abundant polymorph nuclear (PMN) cells available in the peripheral blood and early accumulated tumor-associated cells following therapies that make the inflammatory milieu.[280,286–290] However, based on the tumor cell-secreted cytokines and chemokines due to therapy insults, tumor-associated TAN polarized into N1 (CD11b+Ly6G+CD206-TNF-α+) and N2 (CD11b+Ly6G+CD206+IL10+) phenotypes.

Neutrophil migration to sites of inflammation and subsequent activation and multiple functions are highly regulated and orchestrated processes that are controlled by interactions between numerous receptors and their cognate ligands. FPRs are G protein-coupled receptors that transduce chemotactic signals in phagocytes and mediate host-defense as well as inflammatory responses including cell adhesion, directed migration, granule release, and superoxide production.[291] Although there are a few ligands that are an agonist for FPRs, we cannot utilize those for targeting neutrophils because they may stimulate the neutrophils for hyperfunctioning. Chemotaxis inhibitory protein of S. aureus is a native protein and part of it is FTFEPF, which shows FPR (specially FPR1) antagonistic activity.[292] A coronavirus 229E-derived 12-mer peptide (ETYIKPWWVWL) was identified as a potent antagonist of FPR1 with a Ki of 230 nM.[293] Investigators have pointed out a lower survival probability if FPR1 is highly expressed in breast cancer patients (Figure 12). We have used our platform (vector design, Figure 10) to make engineered exosomes to target and deplete activated neutrophils at the lesions (stroke or tumors) and in the peripheral blood. Our initial studies showed decreased number of neutrophils in the stroke areas following IV administration of the engineered exosomes.

7 | KEY TAKEAWAYS

Genetic engineering and customizing exosomes create an unlimited opportunity to use in diagnosis and treatment. Very little use has been discovered, and we are far away to reach its limits.

Exosomes, in a sense, work like hormones and transfer messages between cells. They have, along with potentially bigger extracellular vesicles, the potential to revolutionize cancer metastasis research and expand our understanding of it.

Because the human body already has exosomes, making use of their own exosomes after isolation and extracorporal modifications with treatment/diagnosis approaches that are already in use could fasten the entering of exosomes into the clinic. For example, after collecting patients' exosomes, they could be loaded with an Alzheimer's drug that has poor blood–brain barrier permeability. And at the same time, exosomes could be tagged with neuron-specific peptides to increase the permeability and targeting capabilities.

Because exosomes carry proteins, lipids, nucleic acid, and metabolites from their parental cells, it should be considered a transfusion/transplant. Until the safety of extra-corporal sourced exosomes, its clinical use will not be possible. Once the safety of these extra-corporal exosomes is proven, we could see many different uses of it in near future. Another way to overcome this safety concern is to collect and modify exosomes with already approved treatment modalities, which could be more safe and potential translate into the clinic in a short time.

ACKNOWLEDGEMENTS

The study was funded by American Heart Associate (AHA) grant 19TPA34850076 and part of the Georgia Cancer Center start-up fund and NIH grant R01NS110378 to ASA.

CONFLICT OF INTEREST

None declared.

DATA AVAILABILITY STATEMENT

Data derived from public domain resources. Data available on request from the authors.

ORCID

Ahmet Alptekin https://orcid.org/0000-0002-7039-1911
Ali S. Arbab https://orcid.org/0000-0003-2902-3671

REFERENCES

1. van Niel G, D'Angelo G, Raposo G. Shedding light on the cell biology of extracellular vesicles. *Nat Rev Mol Cell Biol*. 2018;19:213.
2. Li X, Corbett AL, Taatizadeh E, et al. Challenges and opportunities in exosome research—Perspectives from biology, engineering, and cancer therapy. *APL Bioeng*. 2019;3(1):011503.
3. Valadi H, Ekstrom K, Bossios A, Sjostrand M, Lee JJ, Lotvall JO. Exosome-mediated transfer of mRNAs and microRNAs is a novel mechanism of genetic exchange between cells. *Nat Cell Biol*. 2007;9(6):654-659.
4. Lorentzen E, Dziembowski A, Lindner D, Seraphin B, Conti E. RNA channelling by the archaeal exosome. *EMBO Rep*. 2007;8(5):470-476.
5. Denzer K, Kleijmeer MJ, Heijnen HF, Stoorvogel W, Geuze HJ. Exosome: from internal vesicle of the multivesicular body to intercellular signaling device. *J Cell Sci*. 2000;113(Pt 19):3365-3374.
6. Zhang W, Peng P, Shen K. Role of exosome shuttle RNA in cell-to-cell communication. *Acta Acad Med Sinicae*. 2016;38(4):480-483.
7. Colombo M, Raposo G, Théry C. Biogenesis, secretion, and intercellular interactions of exosomes and other extracellular vesicles. *Annu Rev Cell Dev Biol*. 2014;30(1):255-289.
8. Kalluri R. The biology and function of exosomes in cancer. *J Clin Invest*. 2016;126(4):1208-1215.
9. ELA S, Mager I, Breakefield XO, Wood MJ. Extracellular vesicles: biology and emerging therapeutic opportunities. *Nat Rev Drug Discov*. 2013;12(5):347-357.
10. Lener T, Gimona M, Aigner L, et al. Applying extracellular vesicles based therapeutics in clinical trials – an ISEV position paper. *J Extracell Vesicles*. 2015;4:30087.
11. Jiang XC, Gao JQ. Exosomes as novel bio-carriers for gene and drug delivery. *Int J Pharm*. 2017;521(1-2):167-175.
12. Alvarez-Erviti L, Seow Y, Yin H, Betts C, Lakhal S, Wood MJ. Delivery of siRNA to the mouse brain by systemic injection of targeted exosomes. *Nat Biotechnol*. 2011;29(4):341-345.
13. El Andaloussi S, Lakhal S, Mager I, Wood MJ. Exosomes for targeted siRNA delivery across biological barriers. *Adv Drug Deliv Rev*. 2013;65(3):391-397.
14. El-Andaloussi S, Lee Y, Lakhal-Littleton S, et al. Exosome-mediated delivery of siRNA in vitro and in vivo. *Nat Protoc*. 2012;7(12):2112-2126.
15. Mashouri L, Yousefi H, Aref AR, Ahadi Am, Molaei F, Alahari SK. Exosomes: composition, biogenesis, and mechanisms in cancer metastasis and drug resistance. *Mol Cancer* 2019;18(1):75.
16. Bellavia D, Raimondi L, Costa V, et al. Engineered exosomes: a new promise for the management of musculoskeletal diseases. *Biochim Biophys Acta Gen Subj*. 2018;1862(9):1893-1901.
17. Sterzenbach U, Putz U, Low L-H, Silke J, Tan S-S, Howitt J. Engineered exosomes as vehicles for biologically active proteins. *Mol Ther*. 2017;25(6):1269-1278.
18. Luan X, Sansanaphongpricha K, Myers I, Chen H, Yuan H, Sun D. Engineering exosomes as refined biological nanoplatforms for drug delivery. *Acta Pharmacol Sin*. 2017;38:754.
19. Tian T, Zhang H-X, He C-P, et al. Surface functionalized exosomes as targeted drug delivery vehicles for cerebral ischemia therapy. *Biomaterials*. 2018;150:137-149.
20. Kugeratski FG, Kalluri R. Exosomes as mediators of immune regulation and immunotherapy in cancer. *FEBS J*. 2021;288(1):10-35.
21. Taghikhani A, Farzaneh F, Sharifzad F, Mardpour S, Ebrahimi M, Hassan ZM. Engineered tumor-derived extracellular vesicles: potentials in cancer immunotherapy. *Front Immunol*. 2020;11:221.
22. Kawikova I, Askenase PW. Diagnostic and therapeutic potentials of exosomes in CNS diseases. *Brain Res*. 2015;1617:63-71.
23. Pi YN, Xia BR, Jin MZ, Jin WL, Lou G. Exosomes: powerful weapon for cancer nano-immunoengineering. *Biochem Pharmacol*. 2021;186:114487.
24. Tan A, De La Peña H, Seifalian AM. The application of exosomes as a nanoscale cancer vaccine. *Int J Nanomed*. 2010;5:889-900.
25. Rashid MH, Borin TF, Ara R, et al. Differential in vivo biodistribution of 131I-labeled exosomes from diverse cellular origins and its implication for theranostic application. *Nanomedicine*. 2019;21:102072.
26. Rashid MH, Borin TF, Ara R, Alptekin A, Liu YT, Arbab AS. Generation of novel diagnostic and therapeutic exosomes to detect and deplete protumorigenic M2 macrophages. *Adv Ther-Germany*. 2020;3(7):1900209.
27. Abels ER, Breakefield XO. Introduction to extracellular vesicles: biogenesis, RNA cargo selection, content, release, and uptake. *Cell Mol Neurobiol*. 2016;36(3):301-312.
28. Doyle LM, Wang MZ. Overview of extracellular vesicles, their origin, composition, purpose, and methods for exosome isolation and analysis. *Cell*. 2019;8(7):727.
29. Zhang Q, Higginbotham JN, Jeppesen DK, et al. Transfer of functional cargo in exomeres. *Cell Rep*. 2019;27(3):940-954.e946.
30. Teng F, Fussenegger M. Shedding light on extracellular vesicle biogenesis and bioengineering. *Adv Sci*. 2020;8(1):2003505.
31. Colombo M, Moita C, van Niel G, et al. Analysis of ESCRT functions in exosome biogenesis, composition and secretion highlights the heterogeneity of extracellular vesicles. *J Cell Sci*. 2013;126(Pt 24):5553-5565.
32. Han J, Pluhackova K, Bockmann RA. The multifaceted role of SNARE proteins in membrane fusion. *Front Physiol*. 2017;8:5.
33. Charrin S, le Naour F, Silvie O, Milhiet PE, Boucheix C, Rubinstein E. Lateral organization of membrane proteins: tetraspanins spin their web. *Biochem J*. 2009;420(2):133-154.
34. Hemler ME. Tetraspanin functions and associated microdomains. *Nat Rev Mol Cell Biol*. 2005;6(10):801-811.
35. Andreu Z, Yáñez-Mó M. Tetraspanins in extracellular vesicle formation and function. *Front Immunol*. 2014;5:442.
36. Wang JC, Bégin LR, Bérubé NG, et al. Down-regulation of CD9 expression during prostate carcinoma progression is associated with CD9 mRNA modifications. *Clin Cancer Res*. 2007;13(8):2354-2361.
37. Rous BA, Reaves BJ, Ihrke G, et al. Role of adaptor complex AP-3 in targeting wild-type and mutated CD63 to lysosomes. *Mol Biol Cell*. 2002;13(3):1071-1082.
38. Bobrie A, Colombo M, Krumeich S, Raposo G, Thery C. Diverse subpopulations of vesicles secreted by different intracellular mechanisms are present in exosome preparations obtained by differential ultracentrifugation. *J Extracell Vesicles*. 2012;1.
39. Susa KJ, Seegar TC, Blacklow SC, Kruse AC. A dynamic interaction between CD19 and the tetraspanin CD81 controls B cell co-receptor trafficking. *eLife*. 2020;9:e52337.
40. Little KD, Hemler ME, Stipp CS. Dynamic regulation of a GPCR-tetraspanin-G protein complex on intact cells: central role of CD81 in facilitating GPR56-Galpha q/11 association. *Mol Biol Cell*. 2004;15(5):2375-2387.
41. Liu C, Su C. Design strategies and application progress of therapeutic exosomes. *Theranostics*. 2019;9(4):1015-1028.
42. Swatek KN, Komander D. Ubiquitin modifications. *Cell Res*. 2016;26(4):399-422.

43. Chen W, Huang Y, Han J, et al. Immunomodulatory effects of mesenchymal stromal cells-derived exosome. *Immunol Res*. 2016;64(4):831-840.
44. Gauvreau ME, Côté MH, Bourgeois-Daigneault MC, et al. Sorting of MHC class II molecules into exosomes through a ubiquitin-independent pathway. *Traffic*. 2009;10(10):1518-1527.
45. Wang M, Su Z, Amoah BP. Crosstalk among colon cancer-derived exosomes, fibroblast-derived exosomes, and macrophage phenotypes in colon cancer metastasis. *Int Immunopharmacol*. 2020;81:106298.
46. Wang R, Ji Q, Meng C, et al. Role of gingival mesenchymal stem cell exosomes in macrophage polarization under inflammatory conditions. *Int Immunopharmacol*. 2020;81:106030.
47. Rana S, Yue S, Stadel D, Zöller M. Toward tailored exosomes: the exosomal tetraspanin web contributes to target cell selection. *Int J Biochem Cell Biol*. 2012;44(9):1574-1584.
48. Xia Y, He XT, Xu XY, Tian BM, An Y, Chen FM. Exosomes derived from M0, M1 and M2 macrophages exert distinct influences on the proliferation and differentiation of mesenchymal stem cells. *PeerJ*. 2020;8:e8970.
49. Kim H, Wang SY, Kwak G, Yang Y, Kwon IC, Kim SH. Exosome-guided phenotypic switch of M1 to M2 macrophages for cutaneous wound healing. *Adv Sci*. 2019;6(20):1900513.
50. Bardi GT, Smith MA, Hood JL. Melanoma exosomes promote mixed M1 and M2 macrophage polarization. *Cytokine*. 2018;105:63-72.
51. Walker ND, Elias M, Guiro K, et al. Exosomes from differentially activated macrophages influence dormancy or resurgence of breast cancer cells within bone marrow stroma. *Cell Death Dis*. 2019;10(2):59.
52. Si L, Bai J, Fu H, Qiu H, Guo R. The functions and potential roles of extracellular vesicle noncoding RNAs in gynecological malignancies. *Cell Death Dis*. 2021;7(1):258.
53. Binenbaum Y, Fridman E, Yaari Z, et al. Transfer of miRNA in macrophage-derived exosomes induces drug resistance in pancreatic adenocarcinoma. *Cancer Res*. 2018;78(18):5287-5299.
54. Zhang L, Xu X, Su X. Noncoding RNAs in cancer immunity: functions, regulatory mechanisms, and clinical application. *Mol Cancer*. 2020;19(1):48.
55. Wang M, Zhou L, Yu F, Zhang Y, Li P, Wang K. The functional roles of exosomal long non-coding RNAs in cancer. *Cell Mol Life Sci*. 2019;76(11):2059-2076.
56. Chen M, Chen J, Huang W, et al. Exosomes from human induced pluripotent stem cells derived mesenchymal stem cells improved myocardial injury caused by severe acute pancreatitis through activating Akt/Nrf2/HO-1 axis. *Cell Cycle*. 2022;1-12.
57. Adams KR, Chauhan S, Patel DB, et al. Ubiquitin conjugation probed by inflammation in myeloid-derived suppressor cell extracellular vesicles. *J Proteome Res*. 2018;17(1):315-324.
58. Geis-Asteggiante L, Belew AT, Clements VK, et al. Differential content of proteins, mRNAs, and miRNAs suggests that MDSC and their exosomes may mediate distinct immune suppressive functions. *J Proteome Res*. 2018;17(1):486-498.
59. Daveri E, Vergani E, Shahaj E, et al. microRNAs shape myeloid cell-mediated resistance to cancer immunotherapy. *Front Immunol*. 2020;11:1214.
60. Segura E, Amigorena S, Théry C. Mature dendritic cells secrete exosomes with strong ability to induce antigen-specific effector immune responses. *Blood Cells Mol Dis*. 2005;35(2):89-93.
61. Zhang H, Xie Y, Li W, Chibbar R, Xiong S, Xiang J. CD4(+) T cell-released exosomes inhibit CD8(+) cytotoxic T-lymphocyte responses and antitumor immunity. *Cell Mol Immunol*. 2011;8(1):23-30.
62. Mittelbrunn M, Gutiérrez-Vázquez C, Villarroya-Beltri C, et al. Unidirectional transfer of microRNA-loaded exosomes from T cells to antigen-presenting cells. *Nat Commun*. 2011;2:282.
63. Peters PJ, Borst J, Oorschot V, et al. Cytotoxic T lymphocyte granules are secretory lysosomes, containing both perforin and granzymes. *J Exp Med*. 1991;173(5):1099-1109.
64. Tucher C, Bode K, Schiller P, et al. Extracellular vesicle subtypes released from activated or apoptotic T-lymphocytes carry a specific and stimulus-dependent protein cargo. *Front Immunol*. 2018;9:534.
65. Mazzeo C, Calvo V, Alonso R, Mérida I, Izquierdo M. Protein kinase D1/2 is involved in the maturation of multivesicular bodies and secretion of exosomes in T and B lymphocytes. *Cell Death Differ*. 2016;23(1):99-109.
66. Martínez-Lorenzo MJ, Anel A, Gamen S, et al. Activated human T cells release bioactive Fas ligand and APO2 ligand in microvesicles. *J Immunol*. 1999;163(3):1274-1281.
67. Kaur S, Singh SP, Elkahloun AG, Wu W, Abu-Asab MS, Roberts DD. CD47-dependent immunomodulatory and angiogenic activities of extracellular vesicles produced by T cells. *Matrix Biol*. 2014;37:49-59.
68. Mellman I. Dendritic cells: master regulators of the immune response. *Cancer Immunol Res*. 2013;1(3):145-149.
69. Zitvogel L, Regnault A, Lozier A, et al. Eradication of established murine tumors using a novel cell-free vaccine: dendritic cell-derived exosomes. *Nat Med*. 1998;4(5):594-600.
70. Lindenbergh MFS, Stoorvogel W. Antigen presentation by extracellular vesicles from professional antigen-presenting cells. *Annu Rev Immunol*. 2018;36:435-459.
71. Wei G, Jie Y, Haibo L, et al. Dendritic cells derived exosomes migration to spleen and induction of inflammation are regulated by CCR7. *Sci Rep*. 2017;7:42996.
72. Pelissier Vatter FA, Cioffi M, Hanna SJ, et al. Extracellular vesicle- and particle-mediated communication shapes innate and adaptive immune responses. *J Exp Med*. 2021;218(8):e20202579.
73. Seo N. Exosome-mediated immune regulation and its clinical application. *Trends Immunotherapy*. 2020;4(1):36-41.
74. Batlle E, Massagué J. Transforming growth factor-β signaling in immunity and cancer. *Immunity*. 2019;50(4):924-940.
75. Kim SH, Bianco N, Menon R, et al. Exosomes derived from genetically modified DC expressing FasL are anti-inflammatory and immunosuppressive. *Mol Ther*. 2006;13(2):289-300.
76. Simhadri VR, Reiners KS, Hansen HP, et al. Dendritic cells release HLA-B-associated transcript-3 positive exosomes to regulate natural killer function. *PLoS One*. 2008;3(10):e3377.
77. Yáñez-Mó M, Siljander PR, Andreu Z, et al. Biological properties of extracellular vesicles and their physiological functions. *J Extracell Vesicles*. 2015;4:27066.
78. Willms E, Johansson HJ, Mäger I, et al. Cells release subpopulations of exosomes with distinct molecular and biological properties. *Sci Rep*. 2016;6:22519.
79. Borges FT, Reis LA, Schor N. Extracellular vesicles: structure, function, and potential clinical uses in renal diseases. *Braz J Med Biol Res*. 2013;46(10):824-830.
80. Ståhl A-L, Johansson K, Mossberg M, Kahn R, Karpman D. Exosomes and microvesicles in normal physiology, pathophysiology, and renal diseases. *Pediatr Nephrol*. 2019;34(1):11-30.
81. Théry C, Ostrowski M, Segura E. Membrane vesicles as conveyors of immune responses. *Nat Rev Immunol*. 2009;9(8):581-593.
82. Cabezas A, Bache KG, Brech A, Stenmark H. Alix regulates cortical actin and the spatial distribution of endosomes. *J Cell Sci*. 2005;118(Pt 12):2625-2635.
83. Nakamichi E, Sakakura H, Mii S, et al. Detection of serum/salivary exosomal Alix in patients with oral squamous cell carcinoma. *Oral Dis*. 2021;27(3):439-447.
84. Deneka M, Pelchen-Matthews A, Byland R, Ruiz-Mateos E, Marsh M. In macrophages, HIV-1 assembles into an intracellular plasma membrane domain containing the tetraspanins CD81, CD9, and CD53. *J Cell Biol*. 2007;177(2):329-341.
85. Miyado K, Yamada G, Yamada S, et al. Requirement of CD9 on the egg plasma membrane for fertilization. *Science*. 2000;287(5451):321–324.
86. Khushman M, Bhardwaj A, Patel GK, Laurini JA, et al. Exosomal markers (CD63 and CD9) expression pattern using

immunohistochemistry in resected malignant and nonmalignant pancreatic specimens. *Pancreas* 2017, 46, 782–788.
87. Boriachek K, Islam MN, Möller A, et al. Biological functions and current advances in isolation and detection strategies for exosome nanovesicles. *Small*. 2018;14(6):1702153.
88. Keller S, Rupp C, Stoeck A, et al. CD24 is a marker of exosomes secreted into urine and amniotic fluid. *Kidney Int*. 2007;72(9):1095-1102.
89. Nieuwenhuis HK, van Oosterhout JJ, Rozemuller E, et al. Studies with a monoclonal antibody against activated platelets: Evidence that a secreted 53,000-molecular weight lysosome-like granule protein is exposed on the surface of activated platelets in the circulation. *Blood*. 1987;70(3):838-845.
90. Toothill VJ, Van Mourik JA, Niewenhuis HK, et al. Characterization of the enhanced adhesion of neutrophil leukocytes to thrombin-stimulated endothelial cells. *J Immunol*. 1990;145(1):283-291.
91. Sun B, Li Y, Zhou Y, et al. Circulating exosomal CPNE3 as a diagnostic and prognostic biomarker for colorectal cancer. *J Cell Physiol*. 2019;234(2):1416-1425.
92. Beckham Carla J, Olsen J, Yin P-N, et al. Bladder cancer exosomes contain EDIL-3/Del1 and facilitate cancer progression. *J Urol*. 2014;192(2):583-592.
93. Li C, Li C, Zhi C, et al. Clinical significance of PD-L1 expression in serum-derived exosomes in NSCLC patients. *J Transl Med*. 2019;17(1):355.
94. Purushothaman A, Bandari SK, Liu J, Mobley JA, Brown EE, Sanderson RD. Fibronectin on the surface of myeloma cell-derived exosomes mediates exosome-cell interactions. *J Biol Chem*. 2016;291(4):1652-1663.
95. Skottvoll FS, Berg HE, Bjørseth K, et al. Ultracentrifugation versus kit exosome isolation: nanoLC–MS and other tools reveal similar performance biomarkers, but also contaminations. *Fut Sci*. 2019;5(4):FSO359.
96. Vaswani K, Mitchell MD, Holland OJ, et al. A method for the isolation of exosomes from human and bovine milk. *J Nutr Metabol*. 2019;2019:5764740.
97. Multhoff G. Heat shock protein 70 (Hsp70): membrane location, export and immunological relevance. *Methods*. 2007;43(3):229-237.
98. Whiteside TL, Diergaarde B, Hong C-S. Tumor-derived exosomes (TEX) and their role in immuno-oncology. *Int J Mol Sci*. 2021;22(12):6234.
99. Gross CN, Irrinki A, Feder JN, Enns CA. Co-trafficking of HFE, a nonclassical major histocompatibility complex class I protein, with the transferrin receptor implies a role in intracellular iron regulation. *J Biol Chem*. 1998;273(34):22068-22074.
100. Díaz-Varela M, de Menezes-Neto A, Perez-Zsolt D, et al. Proteomics study of human cord blood reticulocyte-derived exosomes. *Sci Rep*. 2018;8(1):14046.
101. Welsch S, Habermann A, Jäger S, et al. Ultrastructural analysis of ESCRT proteins suggests a role for endosome-associated tubular-vesicular membranes in ESCRT function. *Traffic*. 2006;7(11):1551-1566.
102. Fernandez-Llama P, Khositseth S, Gonzales PA, Star RA, Pisitkun T, Knepper MA. Tamm-Horsfall protein and urinary exosome isolation. *Kidney Int*. 2010;77(8):736-742.
103. Trioulier Y, Torch S, Blot B, et al. Alix, a protein regulating endosomal trafficking, is involved in neuronal death*. *J Biol Chem*. 2004;279(3):2046-2052.
104. Aoki M, Kanamori M, Ohmori K, et al. Expression of developmentally regulated endothelial cell locus 1 was induced by tumor-derived factors including VEGF. *Biochem Biophys Res Commun* 2005;333(3):990-995.
105. Hidai C, Kawana M, Kitano H, Kokubun S. Discoidin domain of Del1 protein contributes to its deposition in the extracellular matrix. *Cell Tissue Res*. 2007;330(1):83-95.
106. Muller L, Simms P, Hong C-S, et al. Human tumor-derived exosomes (TEX) regulate Treg functions via cell surface signaling rather than uptake mechanisms. *OncoImmunology*. 2017;6(8):e1261243.
107. Pineles B, Mani A, Sura L, et al. Neuronal exosome proteins: novel biomarkers for predicting neonatal response to therapeutic hypothermia. *Arch Dis Child Fetal Neonatal Ed*. 2022;107(1):60.
108. Tavasolian F, Hosseini AZ, Rashidi M, et al. The impact of immune cell-derived exosomes on immune response initiation and immune system function. *Curr Pharm Des*. 2021;27(2):197-205.
109. Yin W, Ouyang S, Luo Z, et al. Immature exosomes derived from microRNA-146a overexpressing dendritic cells act as antigen-specific therapy for myasthenia gravis. *Inflammation*. 2017;40(4):1460-1473.
110. Leone DA, Peschel A, Brown M, et al. Surface LAMP-2 is an endocytic receptor that diverts antigen internalized by human dendritic cells into highly immunogenic exosomes. *J Immunol*. 2017;199(2):531.
111. Raposo G, Nijman HW, Stoorvogel W, et al. B lymphocytes secrete antigen-presenting vesicles. *J Exp Med*. 1996;183(3):1161-1172.
112. Zitvogel L, Fernandez N, Lozier A, et al. Dendritic cells or their exosomes are effective biotherapies of cancer. *Eur J Cancer*. 1999;35(Suppl 3):S36-S38.
113. Ni K, O'Neill HC. Long-term stromal cultures produce dendritic-like cells. *Br J Haematol*. 1997;97(4):710-725.
114. Quah B, Ni K, O'Neill HC. In vitro hematopoiesis produces a distinct class of immature dendritic cells from spleen progenitors with limited T cell stimulation capacity. *Int Immunol*. 2004;16(4):567-577.
115. Mongue-Din H, Patel AS, Looi YH, et al. NADPH oxidase-4 driven cardiac macrophage polarization protects against myocardial infarction-induced remodeling. *JACC Basic Transl Sci*. 2017;2(6):688-698.
116. Diehl P, Fricke A, Sander L, et al. Microparticles: major transport vehicles for distinct microRNAs in circulation. *Cardiovasc Res*. 2012;93(4):633-644.
117. Schroeder JC, Puntigam L, Hofmann L, et al. Circulating exosomes inhibit B cell proliferation and activity. *Cancer*. 2020;12(8):2110.
118. Do P, Beckwith KA, Cheney C, et al. Leukemic B cell CTLA-4 suppresses costimulation of T cells. *J Immunol*. 2019;202(9):2806-2816.
119. Andrews LP, Marciscano AE, Drake CG, Vignali DAA. LAG3 (CD223) as a cancer immunotherapy target. *Immunol Rev*. 2017;276(1):80-96.
120. Zhang X, Voskens CJ, Sallin M, et al. CD137 promotes proliferation and survival of human B cells. *J Immunol*. 2010;184(2):787-795.
121. Antonioli L, Pacher P, Vizi ES, Haskó G. CD39 and CD73 in immunity and inflammation. *Trends Mol Med*. 2013;19(6):355-367.
122. Wahlgren J, Karlson TDL, Glader P, Telemo E, Valadi H. Activated human T cells secrete exosomes that participate in IL-2 mediated immune response signaling. *PLoS One*. 2012;7(11):e49723.
123. Coughlan C, Bruce KD, Burgy O, et al. Exosome isolation by ultracentrifugation and precipitation and techniques for downstream analyses. *Curr Protoc Cell Biol*. 2020;88(1):e110.
124. Ayala-Mar S, Donoso-Quezada J, Gallo-Villanueva RC, Perez-Gonzalez VH, González-Valdez J. Recent advances and challenges in the recovery and purification of cellular exosomes. *Electrophoresis*. 2019;40(23-24):3036-3049.
125. Coumans FAW, Brisson AR, Buzas EI, et al. Methodological guidelines to study extracellular vesicles. *Circ Res*. 2017;120(10):1632-1648.
126. Taylor DD, Zacharias W, Gercel-Taylor C. Exosome isolation for proteomic analyses and RNA profiling. *Methods Mol Biol*. 2011;728:235-246.
127. Witwer KW, Buzás EI, Bemis LT, et al. Standardization of sample collection, isolation and analysis methods in extracellular vesicle research. *J Extracellular Vesicles*. 2013;2(1):20360.

128. Kim J, Shin H, Kim J, Kim J, Park J. Isolation of high-purity extracellular vesicles by extracting proteins using aqueous two-phase system. *PLoS One*. 2015;10(6):e0129760.
129. Alvarez ML, Khosroheidari M, Kanchi Ravi R, DiStefano JK. Comparison of protein, microRNA, and mRNA yields using different methods of urinary exosome isolation for the discovery of kidney disease biomarkers. *Kidney Int*. 2012;82(9):1024-1032.
130. Quintana JF, Makepeace BL, Babayan SA, et al. Extracellular Onchocerca-derived small RNAs in host nodules and blood. *Parasit Vectors*. 2015;8:58.
131. Cheruvanky A, Zhou H, Pisitkun T, et al. Rapid isolation of urinary exosomal biomarkers using a nanomembrane ultrafiltration concentrator. *Am J Physiol Renal Physiol*. 2007;292(5):F1657-F1661.
132. Jakobsen KR, Paulsen BS, Bæk R, Varming K, Sorensen BS, Jørgensen MM. Exosomal proteins as potential diagnostic markers in advanced non-small cell lung carcinoma. *J Extracell Vesicles*. 2015;4:26659.
133. Oksvold MP, Neurauter A, Pedersen KW. Magnetic bead-based isolation of exosomes. *Meth Molec Biol*. 2015;1218:465-481.
134. Gonzales PA, Zhou H, Pisitkun T, et al. Isolation and purification of exosomes in urine. *Meth Molec Biol*. 2010;641:89-99.
135. Poliakov A, Spilman M, Dokland T, Amling CL, Mobley JA. Structural heterogeneity and protein composition of exosome-like vesicles (prostasomes) in human semen. *Prostate*. 2009;69(2):159-167.
136. Lane RE, Korbie D, Anderson W, Vaidyanathan R, Trau M. Analysis of exosome purification methods using a model liposome system and tunable-resistive pulse sensing. *Sci Rep*. 2015;5:7639.
137. Bhagat AAS, Kuntaegowdanahalli SS, Papautsky I. Continuous particle separation in spiral microchannels using dean flows and differential migration. *Lab Chip*. 2008;8(11):1906-1914.
138. Winkleman A, Perez-Castillejos R, Gudiksen KL, Phillips ST, Prentiss M, Whitesides GM. Density-based diamagnetic separation: devices for detecting binding events and for collecting unlabeled diamagnetic particles in paramagnetic solutions. *Anal Chem*. 2007;79(17):6542-6550.
139. Watson DC, Yung BC, Bergamaschi C, et al. Scalable, cGMP-compatible purification of extracellular vesicles carrying bioactive human heterodimeric IL-15/lactadherin complexes. *J Extracell Vesicles*. 2018;7(1):1442088.
140. Grimm KM, Trigona WL, Heidecker GJ, et al. An enhanced and scalable process for the purification of SIV gag-specific MHC tetramer. *Protein Expr Purif*. 2001;23(2):270-281.
141. Dizon-Maspat J, Bourret J, D'Agostini A, Li F. Single pass tangential flow filtration to debottleneck downstream processing for therapeutic antibody production. *Biotechnol Bioeng*. 2012;109(4):962-970.
142. Busatto S, Vilanilam G, Ticer T, et al. Tangential flow filtration for highly efficient concentration of extracellular vesicles from large volumes of fluid. *Cell*. 2018;7(12):273.
143. Helwa I, Cai J, Drewry MD, et al. A comparative study of serum exosome isolation using differential ultracentrifugation and three commercial reagents. *PLoS One*. 2017;12(1):e0170628.
144. Lee K, Shao H, Weissleder R, Lee H. Acoustic purification of extracellular microvesicles. *ACS Nano*. 2015;9(3):2321-2327.
145. Li M, Rai AJ, DeCastro GJ, et al. An optimized procedure for exosome isolation and analysis using serum samples: Application to cancer biomarker discovery. *Methods*. 2015;87:26-30.
146. Wu M, Ouyang Y, Wang Z, et al. Isolation of exosomes from whole blood by integrating acoustics and microfluidics. *Proc Natl Acad Sci USA*. 2017;114(40):10584-10589.
147. Ibsen SD, Wright J, Lewis JM, et al. Rapid isolation and detection of exosomes and associated biomarkers from plasma. *ACS Nano*. 2017;11(7):6641-6651.
148. Ramos A, Morgan H, Green NG, Castellanos A. Ac electrokinetics: a review of forces in microelectrode structures. *J Phys D Appl Phys*. 1998;31(18):2338-2353.
149. Schimpf ME. POLYMERS | field flow fractionation. In: Wilson ID, ed. *Encyclopedia of Separation Science*. Academic Press; 2000:3906-3915.
150. Petersen KE, Shiri F, White T, et al. Exosome isolation: cyclical electrical field flow fractionation in low-ionic-strength fluids. *Anal Chem*. 2018;90(21):12783-12790.
151. Giddings JC. A new separation concept based on a coupling of concentration and flow nonuniformities. *Sep Sci*. 1966;1(1):123-125.
152. Hochstetter A, Vernekar R, Austin RH, et al. Deterministic lateral displacement: challenges and perspectives. *ACS Nano*. 2020;14(9):10784-10795.
153. Liu C, Ding B, Xue C, Tian Y, Hu G, Sun J. Sheathless focusing and separation of diverse nanoparticles in viscoelastic solutions with minimized shear thinning. *Anal Chem*. 2016;88(24):12547-12553.
154. Liao J, Liu R, Shi YJ, Yin LH, Pu YP. Exosome-shuttling microRNA-21 promotes cell migration and invasion-targeting PDCD4 in esophageal cancer. *Int J Oncol*. 2016;48(6):2567-2579.
155. Musante L, Tataruch D, Gu D, et al. A simplified method to recover urinary vesicles for clinical applications and sample banking. *Sci Rep*. 2014;4(1):7532.
156. Kadakeri S, Arul MR, Bordett R, Duraisamy N, Naik H, Rudraiah S. 6 – Protein synthesis and characterization. In: Wei G, Kumbar SG, eds. *Artificial Protein and Peptide Nanofibers*. Woodhead Publishing; 2020:121-161.
157. Merchant ML, Powell DW, Wilkey DW, et al. Microfiltration isolation of human urinary exosomes for characterization by MS. *PROTEOMICS – Clin Appl*. 2010;4(1):84-96.
158. Li P, Kaslan M, Lee SH, Yao J, Gao Z. Progress in exosome isolation techniques. *Theranostics*. 2017;7(3):789-804.
159. Welton JL, Webber JP, Botos LA, Jones M, Clayton A. Ready-made chromatography columns for extracellular vesicle isolation from plasma. *J Extracell Vesicles*. 2015;4:27269.
160. Kalluri R, LeBleu VS. The biology, function, and biomedical applications of exosomes. *Science*. 2020;367(6478):eaau6977.
161. Zhang H, Freitas D, Kim HS, et al. Identification of distinct nanoparticles and subsets of extracellular vesicles by asymmetric flow field-flow fractionation. *Nat Cell Biol*. 2018;20(3):332-343.
162. Lee S-S, Won J-H, Lim GJ, et al. A novel population of extracellular vesicles smaller than exosomes promotes cell proliferation. *Cell Commun Signal*. 2019;17(1):95.
163. Delcayre A, Estelles A, Sperinde J, et al. Exosome Display technology: applications to the development of new diagnostics and therapeutics. *Blood Cells Mol Dis*. 2005;35(2):158-168.
164. Takahashi Y, Nishikawa M, Shinotsuka H, et al. Visualization and in vivo tracking of the exosomes of murine melanoma B16-BL6 cells in mice after intravenous injection. *J Biotechnol*. 2013;165(2):77-84.
165. De Gassart A, Trentin B, Martin M, et al. Exosomal sorting of the cytoplasmic domain of bovine leukemia virus TM Env protein. *Cell Biol Int*. 2009;33(1):36-48.
166. Bellavia D, Raimondo S, Calabrese G, et al. Interleukin 3- receptor targeted exosomes inhibit in vitro and in vivo Chronic Myelogenous Leukemia cell growth. *Theranostics*. 2017;7(5):1333-1345.
167. Stickney Z, Losacco J, McDevitt S, Zhang Z, Lu B. Development of exosome surface display technology in living human cells. *Biochem Biophys Res Commun*. 2016;472(1):53-59.
168. Ohno S, Takanashi M, Sudo K, et al. Systemically injected exosomes targeted to EGFR deliver antitumor microRNA to breast cancer cells. *Mol Ther*. 2013;21(1):185-191.
169. Curley N, Levy D, Do MA, et al. Sequential deletion of CD63 identifies topologically distinct scaffolds for surface engineering of exosomes in living human cells. *Nanoscale*. 2020;12(22):12014-12026.
170. Dooley K, McConnell RE, Xu K, et al. A versatile platform for generating engineered extracellular vesicles with defined therapeutic properties. *Mol Ther*. 2021;29(5):1729-1743.
171. Lewis ND, Sia CL, Kirwin K, et al. Exosome surface display of IL12 results in tumor-retained pharmacology with superior potency and

limited systemic exposure compared with recombinant IL12. *Mol Cancer Ther*. 2021;20(3):523-534.
172. Gao X, Ran N, Dong X, et al. Anchor peptide captures, targets, and loads exosomes of diverse origins for diagnostics and therapy. *Sci Transl Med*. 2018;10(444):eaat0195.
173. Jia G, Han Y, An Y, et al. NRP-1 targeted and cargo-loaded exosomes facilitate simultaneous imaging and therapy of glioma in vitro and in vivo. *Biomaterials*. 2018;178:302-316.
174. Kim MS, Haney MJ, Zhao Y, et al. Engineering macrophage-derived exosomes for targeted paclitaxel delivery to pulmonary metastases: in vitro and in vivo evaluations. *Nanomedicine*. 2018;14(1):195-204.
175. Choi ES, Song J, Kang YY, Mok H. Mannose-modified serum exosomes for the elevated uptake to murine dendritic cells and lymphatic accumulation. *Macromol Biosci*. 2019;19(7):1900042.
176. Lai CP, Kim EY, Badr CE, et al. Visualization and tracking of tumour extracellular vesicle delivery and RNA translation using multiplexed reporters. *Nat Commun*. 2015;6(1):7029.
177. Yim N, Ryu SW, Choi K, et al. Exosome engineering for efficient intracellular delivery of soluble proteins using optically reversible protein-protein interaction module. *Nat Commun*. 2016;7:12277.
178. Choi H, Kim Y, Mirzaaghasi A, et al. Exosome-based delivery of super-repressor IκBα relieves sepsis-associated organ damage and mortality. Science *Advances* 2020;6(15):eaaz6980.
179. Busatto S, Iannotta D, Walker SA, Di Marzio L, Wolfram J. A simple and quick method for loading proteins in extracellular vesicles. *Pharmaceuticals*. 2021;14(4):356.
180. Li Z, Zhou X, Wei M, et al. In vitro and in vivo RNA inhibition by CD9-HuR functionalized exosomes encapsulated with miRNA or CRISPR/dCas9. *Nano Lett*. 2019;19(1):19-28.
181. Kojima R, Bojar D, Rizzi G, et al. Designer exosomes produced by implanted cells intracerebrally deliver therapeutic cargo for Parkinson's disease treatment. *Nat Commun*. 2018;9(1):1305.
182. Huang L, Rong Y, Tang X, et al. Engineered exosomes as an in situ DC-primed vaccine to boost antitumor immunity in breast cancer. *Mol Cancer*. 2022;21(1):45.
183. Hong S, Ruan S, Greenberg Z, He M, McGill JL. Development of surface engineered antigenic exosomes as vaccines for respiratory syncytial virus. *Sci Rep*. 2021;11(1):21358.
184. Kim S, Sohn HJ, Lee HJ, et al. Use of engineered exosomes expressing HLA and costimulatory molecules to generate antigen-specific CD8+ T cells for adoptive cell therapy. *J Immunotherapy*. 2017;40(3):83-93.
185. Morishita M, Takahashi Y, Matsumoto A, Nishikawa M, Takakura Y. Exosome-based tumor antigens-adjuvant co-delivery utilizing genetically engineered tumor cell-derived exosomes with immunostimulatory CpG DNA. *Biomaterials*. 2016;111:55-65.
186. Hartman ZC, Wei J, Glass OK, et al. Increasing vaccine potency through exosome antigen targeting. *Vaccine*. 2011;29(50):9361-9367.
187. Shi X, Cheng Q, Hou T, et al. Genetically engineered cell-derived nanoparticles for targeted breast cancer immunotherapy. *Mol Ther*. 2020;28(2):536-547.
188. Fan M, Liu H, Yan H, et al. A CAR T-inspiring platform based on antibody-engineered exosomes from antigen-feeding dendritic cells for precise solid tumor therapy. *Biomaterials*. 2022;282:121424.
189. Gunassekaran GR, Poongkavithai Vadevoo SM, Baek MC, Lee B. M1 macrophage exosomes engineered to foster M1 polarization and target the IL-4 receptor inhibit tumor growth by reprogramming tumor-associated macrophages into M1-like macrophages. *Biomaterials*. 2021;278:121137.
190. Conceição M, Forcina L, Wiklander OPB, et al. Engineered extracellular vesicle decoy receptor-mediated modulation of the IL6 trans-signalling pathway in muscle. *Biomaterials*. 2021;266:120435.
191. Duong N, Curley K, Brown A, et al. Decoy exosomes as a novel biologic reagent to antagonize inflammation. *Int J Nanomedicine*. 2019;14:3413-3425.
192. Chen G, Huang AC, Zhang W, et al. Exosomal PD-L1 contributes to immunosuppression and is associated with anti-PD-1 response. *Nature*. 2018;560(7718):382-386.
193. Suetsugu A, Honma K, Saji S, Moriwaki H, Ochiya T, Hoffman RM. Imaging exosome transfer from breast cancer cells to stroma at metastatic sites in orthotopic nude-mouse models. *Adv Drug Deliv Rev*. 2013;65(3):383-390.
194. Pucci F, Garris C, Lai CP, et al. SCS macrophages suppress melanoma by restricting tumor-derived vesicle-B cell interactions. *Science*. 2016;352(6282):242-246.
195. Hamilton N, Claudio NM, Armstrong RJ, Pucci F. Cell Surface Labeling by Engineered Extracellular Vesicles. *Advanced biosystems*. 2020;4(12):e2000007.
196. Lee JR, Park BW, Kim J, et al. Nanovesicles derived from iron oxide nanoparticles-incorporated mesenchymal stem cells for cardiac repair. *Sci Adv*. 2020;6(18):eaaz0952.
197. Zhuang M, Du D, Pu L, et al. SPION-decorated exosome delivered BAY55-9837 targeting the pancreas through magnetism to improve the blood GLC response. *Small*. 2019;15(52):e1903135.
198. Mizuta R, Sasaki Y, Kawasaki R, et al. Magnetically navigated intracellular delivery of extracellular vesicles using amphiphilic nanogels. *Bioconjug Chem*. 2019;30(8):2150-2155.
199. Liu T, Zhu Y, Zhao R, Wei X, Xin X. Visualization of exosomes from mesenchymal stem cells in vivo by magnetic resonance imaging. *Magn Reson Imaging*. 2020;68:75-82.
200. Maguire CA, Balaj L, Sivaraman S, et al. Microvesicle-associated AAV vector as a novel gene delivery system. *Mol Ther*. 2012;20(5):960-971.
201. Breuer CB, Hanlon KS, Natasan JS, et al. In vivo engineering of lymphocytes after systemic exosome-associated AAV delivery. *Sci Rep*. 2020;10(1):4544.
202. Jhan YY, Prasca-Chamorro D, Palou Zuniga G, et al. Engineered extracellular vesicles with synthetic lipids via membrane fusion to establish efficient gene delivery. *Int J Pharm*. 2020;573:118802.
203. Sato YT, Umezaki K, Sawada S, et al. Engineering hybrid exosomes by membrane fusion with liposomes. *Sci Rep*. 2016;6(1):21933.
204. Desplantes R, Lévêque C, Muller B, et al. Affinity biosensors using recombinant native membrane proteins displayed on exosomes: application to botulinum neurotoxin B receptor. *Sci Rep*. 2017;7(1):1032.
205. Hung ME, Leonard JN. Stabilization of exosome-targeting peptides via engineered glycosylation. *J Biol Chem*. 2015;290(13):8166-8172.
206. Kamerkar S, LeBleu VS, Sugimoto H, et al. Exosomes facilitate therapeutic targeting of oncogenic KRAS in pancreatic cancer. *Nature*. 2017;546(7659):498-503.
207. Koh E, Lee EJ, Nam G-H, et al. Exosome-SIRPα, a CD47 blockade increases cancer cell phagocytosis. *Biomaterials*. 2017;121:121-129.
208. Lathwal S, Yerneni SS, Boye S, et al. Engineering exosome polymer hybrids by atom transfer radical polymerization. *Proc Natl Acad Sci USA*. 2021;118(2):e2020241118.
209. Sica A, Mantovani A. Macrophage plasticity and polarization: in vivo veritas. *J Clin Invest*. 2012;122(3):787-795.
210. Mantovani A, Sozzani S, Locati M, et al. Infiltration of tumours by macrophages and dendritic cells: tumour-associated macrophages as a paradigm for polarized M2 mononuclear phagocytes. *Novartis Found Symp*. 2004;256:137-145. discussion 146-138, 259-169.
211. Pesce J, Kaviratne M, Ramalingam TR, et al. The IL-21 receptor augments Th2 effector function and alternative macrophage activation. *J Clin Invest*. 2006;116(7):2044-2055.
212. Kurowska-Stolarska M, Stolarski B, Kewin P, et al. IL-33 amplifies the polarization of alternatively activated macrophages that contribute to airway inflammation. *J Immunol*. 2009;183(10):6469-6477.

213. Germano G, Allavena P, Mantovani A. Cytokines as a key component of cancer-related inflammation. *Cytokine*. 2008;43(3):374-379.
214. Sica A, Allavena P, Mantovani A. Cancer related inflammation: the macrophage connection. *Cancer Lett*. 2008;267(2):204-215.
215. Gordon S, Plüddemann A. Tissue macrophages: heterogeneity and functions. *BMC Biol*. 2017;15(1):53.
216. Azad AK, Rajaram MVS, Schlesinger LS. Exploitation of the macrophage mannose receptor (CD206) in infectious disease diagnostics and therapeutics. *J Cytol Mol Biol*. 2014;1(1):1000003.
217. Qiu S-Q, Waaijer SJH, Zwager MC, de Vries EGE, van der Vegt B, Schröder CP. Tumor-associated macrophages in breast cancer: Innocent bystander or important player? *Cancer Treat Rev*. 2018;70:178-189.
218. DeNardo DG, Brennan DJ, Rexhepaj E, et al. Leukocyte complexity predicts breast cancer survival and functionally regulates response to chemotherapy. *Cancer Discov*. 2011;1(1):54-67.
219. Shree T, Olson OC, Elie BT, et al. Macrophages and cathepsin proteases blunt chemotherapeutic response in breast cancer. *Genes Dev*. 2011;25(23):2465-2479.
220. Scodeller P, Simón-Gracia L, Kopanchuk S, et al. Precision targeting of tumor macrophages with a CD206 binding peptide. *Sci Rep*. 2017;7(1):14655.
221. Asciutto EK, Kopanchuk S, Lepland A, et al. Phage-display-derived peptide binds to human CD206 and modeling reveals a new binding site on the receptor. *J Phys Chem B*. 2019;123(9):1973-1982.
222. Rashid MH, Borin TF, Ara R, et al. CD206 positive M2-macrophage targeting engineered exosomes as a potential diagnostic and therapeutic tool. *Cancer Res*. 2019;79(13_Supplement):1139.
223. Teillaud JL. Antibody-dependent Cellular Cytotoxicity (ADCC). In: *eLS*. Chichester: John Wiley & Sons, Ltd; 2006:1-8.
224. Polansky M, Eisenstadt R, DeGrazia T, Zhao X, Liu Y, Feldman R. Rituximab therapy in patients with bullous pemphigoid: a retrospective study of 20 patients. *J Am Acad Dermatol*. 2019;81(1):179-186.
225. Sneller MC. Rituximab and Wegener's granulomatosis: Are B cells a target in vasculitis treatment? *Arthritis Rheum*. 2005;52(1):1-5.
226. Aldeghaither DS, Zahavi DJ, Murray JC, et al. A mechanism of resistance to antibody-targeted immune attack. *Cancer Immunol Res*. 2019;7(2):230-243.
227. Wang W, Erbe AK, Hank JA, Morris ZS, Sondel PM. NK cell-mediated antibody-dependent cellular cytotoxicity in cancer immunotherapy. *Front Immunol*. 2015;6:368.
228. Smyth MJ, Cretney E, Kelly JM, et al. Activation of NK cell cytotoxicity. *Mol Immunol*. 2005;42(4):501-510.
229. Srivastava RM, Lee SC, Andrade Filho PA, et al. Cetuximab-activated natural killer and dendritic cells collaborate to trigger tumor antigen-specific T-cell immunity in head and neck cancer patients. *Clin Cancer Res*. 2013;19(7):1858-1872.
230. Qin H, Lerman B, Sakamaki I, et al. Generation of a new therapeutic peptide that depletes myeloid-derived suppressor cells in tumor-bearing mice. *Nat Med*. 2014;20(6):676-681.
231. Srivastava A, Filant J, Moxley KM, Sood A, McMeekin S, Ramesh R. Exosomes: a role for naturally occurring nanovesicles in cancer growth, diagnosis and treatment. *Curr Gene Ther*. 2015;15(2):182-192.
232. Haqqani AS, Delaney CE, Tremblay TL, Sodja C, Sandhu JK, Stanimirovic DB. Method for isolation and molecular characterization of extracellular microvesicles released from brain endothelial cells. *Fluids Barriers CNS*. 2013;10(1):4.
233. Lakhal S, Wood MJ. Exosome nanotechnology: an emerging paradigm shift in drug delivery: exploitation of exosome nanovesicles for systemic in vivo delivery of RNAi heralds new horizons for drug delivery across biological barriers. *BioEssays*. 2011;33(10):737-741.
234. Sun D, Zhuang X, Zhang S, et al. Exosomes are endogenous nanoparticles that can deliver biological information between cells. *Adv Drug Deliv Rev*. 2013;65(3):342-347.
235. Kibria G, Ramos EK, Wan Y, Gius DR, Liu H. Exosomes as a drug delivery system in cancer therapy: potential and challenges. *Mol Pharm*. 2018;15(9):3625-3633.
236. Boukouris S, Mathivanan S. Exosomes in bodily fluids are a highly stable resource of disease biomarkers. *Proteomics Clin Appl*. 2015;9(3-4):358-367.
237. Rückert R, Herz U, Paus R, et al. IL-15-IgG2b fusion protein accelerates and enhances a Th2 but not a Th1 immune response in vivo, while IL-2-IgG2b fusion protein inhibits both. *Eur J Immunol*. 1998;28(10):3312-3320.
238. Czajkowsky DM, Hu J, Shao Z, Pleass RJ. Fc-fusion proteins: new developments and future perspectives. *EMBO Mol Med*. 2012;4(10):1015-1028.
239. Ahmed M, Pan DW, Davis ME. Lack of in vivo antibody dependent cellular cytotoxicity with antibody containing gold nanoparticles. *Bioconjug Chem*. 2015;26(5):812-816.
240. Leon PE, He W, Mullarkey CE, et al. Optimal activation of Fc-mediated effector functions by influenza virus hemagglutinin antibodies requires two points of contact. *Proc Natl Acad Sci*. 2016;113(40):E5944-E5951.
241. Sioud M, Westby P, Olsen JKE, Mobergslien A. Generation of new peptide-Fc fusion proteins that mediate antibody-dependent cellular cytotoxicity against different types of cancer cells. *Mol Ther Methods Clin Dev*. 2015;2:15043.
242. Han SG, Lee JS, Ahn K, et al. Size-dependent clearance of gold nanoparticles from lungs of Sprague–Dawley rats after short-term inhalation exposure. *Arch Toxicol*. 2015;89(7):1083-1094.
243. Hoshyar N, Gray S, Han H, Bao G. The effect of nanoparticle size on in vivo pharmacokinetics and cellular interaction. *Nanomedicine*. 2016;11(6):673-692.
244. Alexis F, Pridgen E, Molnar LK, Farokhzad OC. Factors affecting the clearance and biodistribution of polymeric nanoparticles. *Mol Pharm*. 2008;5(4):505-515.
245. Arora T, Padaki R, Liu L, et al. Differences in binding and effector functions between classes of TNF antagonists. *Cytokine*. 2009;45(2):124-131.
246. Gillies SD, Young D, Lo KM, Roberts S. Biological activity and in vivo clearance of antitumor antibody/cytokine fusion proteins. *Bioconjug Chem*. 1993;4(3):230-235.
247. Wu B, Sun Y-N. Pharmacokinetics of peptide–Fc fusion proteins. *J Pharm Sci*. 2014;103(1):53-64.
248. Datta-Mannan A, Lu J, Witcher DR, Leung D, Tang Y, Wroblewski VJ. The interplay of non-specific binding, target-mediated clearance and FcRn interactions on the pharmacokinetics of humanized antibodies. *MAbs*. 2015;7(6):1084-1093.
249. Zahavi D, AlDeghaither D, O'Connell A, Weiner LM. Enhancing antibody-dependent cell-mediated cytotoxicity: a strategy for improving antibody-based immunotherapy. *Antibody Therapeutics*. 2018;1(1):7-12.
250. Gül N, van Egmond M. Antibody-dependent phagocytosis of tumor cells by macrophages: a potent effector mechanism of monoclonal antibody therapy of cancer. *Cancer Res*. 2015;75(23):5008-5013.
251. Rashid MH, Borin TF, Ara R, et al. Critical immunosuppressive effect of MDSCderived exosomes in the tumor microenvironment. *Oncol Rep*. 2021;45(3):1171-1181.
252. Angara K, Arbab AS. Chapter 16 – Mechanisms of glioblastoma resistance to antiangiogenic agents and reversal approaches. In: Paulmurugan R, Massoud TF, eds. *Glioblastoma Resistance to Chemotherapy: Molecular Mechanisms and Innovative Reversal Strategies*. Vol 15. Academic Press; 2021:429-452.
253. Ali S, Borin TF, Piranlioglu R, et al. Changes in the tumor microenvironment and outcome for TME-targeting therapy in glioblastoma: a pilot study. *PLoS One*. 2021;16(2):e0246646.
254. Achyut BR, Shankar A, Iskander ASM, et al. Chimeric Mouse model to track the migration of bone marrow derived cells in

glioblastoma following anti-angiogenic treatments. *Cancer Biol Ther*. 2016;17(3):280-290.
255. Achyut BR, Arbab AS. Myeloid cell signatures in tumor microenvironment predicts therapeutic response in cancer. *Onco Targets Ther*. 2016;9:1047-1055.
256. Achyut BR, Shankar A, Iskander AS, et al. Bone marrow derived myeloid cells orchestrate antiangiogenic resistance in glioblastoma through coordinated molecular networks. *Cancer Lett*. 2015;369(2):416-426.
257. Arbab AS. Activation of alternative pathways of angiogenesis and involvement of stem cells following anti-angiogenesis treatment in glioma. *Histol Histopathol*. 2012;27(5):549-557.
258. Ali MM, Janic B, Babajani-Feremi A, et al. Changes in vascular permeability and expression of different angiogenic factors following anti-angiogenic treatment in rat glioma. *PLoS One*. 2010;5(1):e8727.
259. Scarlett CJ. Contribution of bone marrow derived cells to the pancreatic tumor microenvironment. *Front Physiol*. 2013;4:56.
260. Vorontsova A, Kan T, Raviv Z, Shaked Y. The dichotomous role of bone marrow derived cells in the chemotherapy-treated tumor microenvironment. *J Clin Med*. 2020;9(12):3912.
261. Hirata E, Sahai E. Tumor microenvironment and differential responses to therapy. *Cold Spring Harb Perspect Med*. 2017;7(7):a026781.
262. Denis M, Duruisseaux M, Brevet M, Dumontet C. How can immune checkpoint inhibitors cause hyperprogression in solid tumors? *Front Immunol*. 2020;11:492.
263. Liu J, Chen Z, Li Y, Zhao W, Wu J, Zhang Z. PD-1/PD-L1 checkpoint inhibitors in tumor immunotherapy. *Front Pharmacol*. 2021;12(2339):731798.
264. Achyut BR, Arbab AS. Myeloid derived suppressor cells: fuel the fire. *Biochem Physiol*. 2014;3(3):e123.
265. Achyut BR, Arbab AS. Taming immune suppressor: application of myeloid-derived suppressor cells in anti-cancer gene therapy. *Transl Cancer Res*. 2017;6:S160-S162.
266. Borin TF, Angara K, Rashid M, et al. CSF-1R inhibitor prevented pre-metastatic lung niches in metastatic mammary tumor. *Cancer Res*. 2017;77(13_Supplement):1043.
267. Khan M, Hasan MM, Barnett A, et al. Co-axial electrospraying of injectable multi-cancer drugs nanocapsules with polymer shells for targeting aggressive breast cancers. *Cancer Nanotechnol*. 2022;13(1):6.
268. Yang Q, Tong X, Schieb L, et al. Vital signs: recent trends in stroke death rates – United States, 2000-2015. *MMWR Morb Mortal Wkly Rep*. 2017;66(35):933-939.
269. Jickling GC, Liu D, Ander BP, Stamova B, Zhan X, Sharp FR. Targeting neutrophils in ischemic stroke: translational insights from experimental studies. *J Cereb Blood Flow Metab*. 2015;35(6):888-901.
270. Downing LJ, Strieter RM, Kadell AM, et al. Neutrophils are the initial cell type identified in deep venous thrombosis induced vein wall inflammation. *ASAIO J*. 1996;42(5):M677-M682.
271. Schabitz WR, Minnerup J. Neutrophils in acute stroke pathophysiology. *Stroke*. 2019;50(3):e44-e45.
272. Jasper AE, McIver WJ, Sapey E, Walton GM. Understanding the role of neutrophils in chronic inflammatory airway disease. *F1000Res*. 2019;8:1-17. F1000 Faculty Rev-1557.
273. Aronowski J, Roy-O'Reilly MA. Neutrophils, the felons of the brain. *Stroke*. 2019;50(3):e42-e43.
274. Kim J, Song TJ, Park JH, et al. Different prognostic value of white blood cell subtypes in patients with acute cerebral infarction. *Atherosclerosis*. 2012;222(2):464-467.
275. Buck BH, Liebeskind DS, Saver JL, et al. Early neutrophilia is associated with volume of ischemic tissue in acute stroke. *Stroke*. 2008;39(2):355-360.
276. Kumar AD, Boehme AK, Siegler JE, Gillette M, Albright KC, Martin-Schild S. Leukocytosis in patients with neurologic deterioration after acute ischemic stroke is associated with poor outcomes. *J Stroke Cerebrovasc Dis*. 2013;22(7):e111-e117.
277. Hayakawa K, Mishima K, Irie K, et al. Cannabidiol prevents a post-ischemic injury progressively induced by cerebral ischemia via a high-mobility group box1-inhibiting mechanism. *Neuropharmacology*. 2008;55(8):1280-1286.
278. Chou WH, Choi DS, Zhang H, et al. Neutrophil protein kinase Cdelta as a mediator of stroke-reperfusion injury. *J Clin Invest*. 2004;114(1):49-56.
279. Lecot P, Sarabi M, Pereira Abrantes M, et al. Neutrophil heterogeneity in cancer: from biology to therapies. *Front Immunol*. 2019;10:2155.
280. Long W, Chen J, Gao C, Lin Z, Xie X, Dai H. Brief review on the roles of neutrophils in cancer development. *J Leukoc Biol*. 2021;109(2):407-413.
281. Wu L, Saxena S, Awaji M, Singh RK. Tumor-associated neutrophils in cancer: going pro. *Cancer*. 2019;11(4):564.
282. Keibel A, Singh V, Sharma MC. Inflammation, microenvironment, and the immune system in cancer progression. *Curr Pharm Des*. 2009;15(17):1949-1955.
283. Santana Carrero RM, Beceren-Braun F, Rivas SC, et al. IL-15 is a component of the inflammatory milieu in the tumor microenvironment promoting antitumor responses. *Proc Natl Acad Sci*. 2019;116(2):599.
284. Chen X, Gao A, Zhang F, et al. ILT4 inhibition prevents TAM- and dysfunctional T cell-mediated immunosuppression and enhances the efficacy of anti-PD-L1 therapy in NSCLC with EGFR activation. *Theranostics*. 2021;11(7):3392-3416.
285. Eisinger S, Sarhan D, Boura VF, et al. Targeting a scavenger receptor on tumor-associated macrophages activates tumor cell killing by natural killer cells. *Proc Natl Acad Sci U S A*. 2020;117(50):32005-32016.
286. Rosales C. Neutrophil: a cell with many roles in inflammation or several cell types? *Front Physiol*. 2018;9:113.
287. Shinde-Jadhav S, Mansure JJ, Rayes RF, et al. Role of neutrophil extracellular traps in radiation resistance of invasive bladder cancer. *Nat Commun*. 2021;12(1):2776.
288. Hedrick CC, Malanchi I. Neutrophils in cancer: heterogeneous and multifaceted. *Nat Rev Immunol*. 2021;22(3):173-187.
289. Wisdom AJ, Hong CS, Lin AJ, et al. Neutrophils promote tumor resistance to radiation therapy. *Proc Natl Acad Sci*. 2019;116(37):18584.
290. Masucci MT, Minopoli M, Carriero MV. Tumor associated neutrophils. their role in tumorigenesis, metastasis, prognosis and therapy. *Front Oncol*. 2019;9:1146.
291. He H-Q, Ye RD. The formyl peptide receptors: diversity of ligands and mechanism for recognition. *Molecules*. 2017;22(3):455.
292. Haas PJ, de Haas CJ, Kleibeuker W, et al. N-terminal residues of the chemotaxis inhibitory protein of Staphylococcus aureus are essential for blocking formylated peptide receptor but not C5a receptor. *J Immunol*. 2004;173(9):5704-5711.
293. Mills JS. Peptides derived from HIV-1, HIV-2, Ebola virus, SARS coronavirus and coronavirus 229E exhibit high affinity binding to the formyl peptide receptor. *Biochim Biophys Acta*. 2006;1762(7):693-703.

Received: 29 April 2022 | Revised: 12 September 2022 | Accepted: 14 September 2022

DOI: 10.1002/jex2.62

RESEARCH ARTICLE

The identification of novel small extracellular vesicle (sEV) production modulators using luciferase-based sEV quantification method

Aki Yamamoto[1] | **Yuki Takahashi**[1] | **Shinsuke Inuki**[2] | **Shumpei Nakagawa**[3] | **Kodai Nakao**[1] | **Hiroaki Ohno**[2] | **Masao Doi**[3] | **Yoshinobu Takakura**[1]

[1] Department of Biopharmaceutics and Drug Metabolism, Graduate School of Pharmaceutical Sciences, Kyoto University, Sakyo-ku, Kyoto, Japan

[2] Department of Bioorganic Medicinal Chemistry and Chemogenomics, Graduate School of Pharmaceutical Sciences, Kyoto University, Sakyo-ku, Kyoto, Japan

[3] Department of Systems Biology, Graduate School of Pharmaceutical Sciences, Kyoto University, Sakyo-ku, Kyoto, Japan

Correspondence
Yuki Takahashi, Department of Biopharmaceutics and Drug Metabolism, Graduate School of Pharmaceutical Sciences, Kyoto University, Sakyo-ku, Kyoto 606–8501, Japan.
Email: ytakahashi@pharm.kyoto-u.ac.jp

Funding information
Japan Society for the Promotion of Science, Grant/Award Number: 21K19908

Abstract

Small extracellular vesicles (sEVs) are nano-sized vesicles secreted from various cells that contain bioactive metabolites and function as key regulators for intercellular communication. sEVs modulate diverse biological and pathological processes in the body, and the amount of circulating sEVs has been reported to correlate with certain disease progression. Therefore, the identification of small molecular compounds that can control sEV production may become a novel therapeutic strategy. In this study, a rapid, highly sensitive sEV quantification method utilizing fusion proteins consisting of Gaussia luciferase (gLuc) reporter protein and sEV markers (CD63 and CD82) was developed. A total of 480 compounds were screened to identify potent inducers and inhibitors of gLuc activity. Two novel compounds, KPYC08425 and KPYC12163, showed significant and dose-dependent changes in gLuc activity with minimal cytotoxicity based on the LDH assay. The efficacy of these two compounds was further evaluated by protein quantification of the isolated sEVs. Further evaluation of KPYC12163 suggested that the autolysosomal pathway may be involved in its inhibitory effect on sEV production.

KEYWORDS
autophagy, extracellular vesicles, luminescence, modulators, nanovesicles, quantification, screening

1 | INTRODUCTION

Small extracellular vesicles (sEVs) are a heterogeneous group of lipid-bilayered nanovesicles secreted by nearly all cell types that play a key role in intercellular communication (el Andaloussi et al., 2013; Lässer et al., 2011; Théry et al., 2018). They contain nucleic acids, proteins, lipids and other biologically active metabolites derived from the producing cells, which are delivered to neighbouring and distant cells to modulate diverse biological and pathological processes in the body (van Niel et al., 2018; Zaborowski et al., 2015). The nature and abundance of sEVs are dependent on the type of sEV-producing cells, as well as its physiological or pathological state and ultimately influence its function in the body. Normally, sEVs function to maintain homeostasis and regulate immune responses (Tkach & Théry, 2016; Yáñez-Mó et al., 2015); however, sEVs can also play a role in disease onset and progression. For example, in the case of cancer, tumour cell-derived sEVs are known to facilitate disease progression by promoting tumorigenesis, immune escape and metastasis (Becker et al., 2016).

Owing to its role in disease progression, the identification of small molecular compounds that can regulate sEV production is becoming increasingly popular as a novel therapeutic strategy (Catalano & O'Driscoll, 2020; Datta et al., 2018; Kulshreshtha

---

s://doi.org/10.1002/jex2.62

et al., 2019). Investigation of sEV biogenesis pathways has led to reports of various agents that modulate sEV biogenesis/release in recent years (Catalano & O'Driscoll, 2020; Emam et al., 2018; García-Seisdedos et al., 2020; Khan et al., 2018; Kulshreshtha et al., 2019; Ludwig et al., 2020; Zhang et al., 2020). Previously, one of the main setbacks in identifying potent sEV production modulators was the lack of a sensitive, high throughput system for quantifying sEV production. Generally, sEV quantification requires time-consuming purification steps involving ultracentrifugation or size exclusion chromatography. These steps eliminate protein contamination that could potentially influence the quantification assay, however, significantly decreases the throughput. The development of a cell-based assay system utilizing CD63-GFP allowed for quantitative high-throughput screening (HTS) of existing drug libraries to identify potent modulators of sEV production (Datta et al., 2018; Im et al., 2019; Zhang et al., 2020). Nonetheless, these assay systems relied on the changes in intracellular CD63-GFP signals to identify potent activators and inhibitors of sEV production, thus, not directly measuring sEV production.

Therefore, in this study, a rapid, highly sensitive sEV quantification method utilizing Gaussia luciferase (gLuc) reporter protein was developed and used to screen for potential sEV production modulators. gLuc protein fused to sEV marker proteins, CD63 and CD82, were utilised to label the inner spaces of the sEV membrane to quantify sEV production based on the chemiluminescence of the cell supernatant. Because the gLuc fusion proteins could also be present as soluble proteins or as parts of cell debris in the supernatant, pre-treatment conditions, including centrifugation (to eliminate cells/cell debris) and proteinase K treatment (to eliminate soluble proteins), were evaluated. After confirming the validity of the developed assay, 480 compounds from our in-house chemical libraries were screened to identify potent regulators of sEV production. The selected hit compounds from the screen were then further validated for their ability to modulate sEV production.

2 | MATERIALS AND METHODS

2.1 | Cell culture

Murine melanoma cell line B16BL6 was obtained from RIKEN BioResource Center (Tsukuba, Japan) and was cultured in Dulbecco's modified Eagle's medium (DMEM; Nissui Co., Ltd., Tokyo, Japan) supplemented with 10% heat-inactivated foetal bovine serum (FBS), 2 g/L D-glucose and 100 IU/ml penicillin/100 μg/ml streptomycin/2 mM L-glutamine (PSG; Nacalai Tesque Inc., Kyoto, Japan). Human lung carcinoma cell line A549, human embryonic kidney cell line HEK293 and murine fibroblast cell line NIH3T3 were purchased from the American Type Culture Collection (ATCC; Rockville, MD, USA) and were cultured in DMEM supplemented with 10% FBS and PSG. Murine colorectal cancer cell line Colon26, obtained from the Cancer Chemotherapy Center of the Japanese Foundation for Cancer Research (Tokyo, Japan) and murine macrophage cell line RAW264.7, purchased from ATCC, were cultured in Roswell Park Memorial Institute (RPMI) 1640 medium (Nissui Co., Ltd.) supplemented with 10% FBS and PSG. All cell lines were cultured in 37°C incubator with 5% CO_2.

2.2 | Plasmid DNA (pDNA)

Coding sequence of CD63-gLuc was obtained as previously described (Charoenviriyakul et al., 2018). CD82 mRNA was extracted from RAW264.7 cells and subjected to RT-PCR to obtain the cDNA sequence. The chimeric sequence of CD82-gLuc was prepared by using a 2-step PCR method with the following primers: CD82 Fw: 5′-ATGCAGATCTTGCAGAATGGGGGCAGGCTGTGTCAAAGTCACCAA-3′; CD82 Rv: 5′-GTACTTGGGGACCTTGCTGTAGTCTTCAGAATG-3′; gLuc Fw: 5′-AGACTACAGCAAGGTCCCCAAGTACGGTAAGCCCACCGAGAACAACGAAGAC-3′; and gLuc Rv: 5′-CTACGCTAGCTTAGTCACCACCGGCCCCCTTGA-3′. The constructed chimeric sequence was initially subcloned into the BglII/NheI site of the pcDNA3.1 vector (Invitrogen, Carlsbad, CA, USA) and subsequently subcloned into the pROSA-mcs vector. The promoter and enhancer coding sequences of pBROAD2-mcs (InvivoGen, San Diego, CA, USA) were amplified by PCR and subcloned into the SdaI/HindIII site of the pCpGfree-mcs vector (Thermo Fisher Scientific, Waltham, MA, USA) to form the pROSA-mcs vector. To construct the pROSA constructs encoding the corresponding fusion proteins, the chimeric sequences of CD63-gLuc and CD82-gLuc were subcloned into the KpnI/PmeI site of the pROSA-mcs vector.

Coding sequence of CD63 was subcloned into the pEGFP-N1 vector (BD Biosciences Clontech, Palo Alto, CA, USA), and the constructed chimeric sequence of CD63-EGFP was then subcloned into the BamHI/XbaI site of the pcDNA3.1 vector (Invitrogen). The coding sequence of mCherry was prepared from the pPK2-BAR-mCherry vector (Takara Bio Inc., Shiga, Japan), and the coding sequence for Lamp2c was obtained as previously described (Matsumoto et al., 2021). The chimeric sequence of mCherry-Lamp2c was prepared by using a 2-step PCR method with the following primers: mCherry Fw: 5′-CTTTCTGTTCCTAGGAGCCGTTCAGTCCAATGCAGGTGTGAGCAAGGGCGAGGAGGA-3′; mCherry Rv: 5′-TCTGTCAAATTAACTATCAAACCCTTGTACAGCTCGTCCATGCC-3′; Lamp2c Fw: 5′-TTGATAGTTAATTTGACAGA-3′; and Lamp2c Rv: 5′-GGGGGGCTTAAGTTACAGAGTCTGATATCCAGCATAGGTC-3′. To construct the pROSA construct encoding mCherry-Lamp2c, the chimeric sequence was subcloned into the KpnI/AflII site of the pROSA-mcs vector.

pDNAs encoding CD63-gLuc or CD82-gLuc were individually transfected into B16BL6 cells with polyethyleneimine (PEI) "max" (Polysciences, Warrington, PA, USA). Briefly, 80 μl PEI "max" solution (0.323 mg/ml, pH 8.0) and 10 μg pDNA were individually diluted to 500 μl with 150 mM NaCl, mixed, and incubated at room temperature for 15 min to form the PEI-DNA complex. This solution was then added to the cells and incubated for 24 h. The medium was changed to Opti-MEM (Thermo Fisher Scientific) and incubated for an additional 24 h.

2.3 | Chemistry

KPYC08425 was purchased from ChemDiv (CAS Registry Number: 300402-36-2).

KPYC12163 was synthesised in one step from flazin, which was prepared according to literature procedures (Tang et al., 2008) (Figure S1A). The reaction was performed using syringe-septum cap techniques under argon atmosphere. Wakosil C-300 was used for flash chromatography. ^{1}H NMR spectrum was recorded using a JEOL ECA-500 spectrometer (JEOL Ltd., Tokyo, Japan) at 500 MHz frequency (Figure S1B). Chemical shifts are reported in δ (ppm) relative to Me_4Si (in DMSO-d_6) as an internal standard. ^{13}C NMR spectrum was recorded using a JEOL ECA-500 spectrometer (JEOL Ltd.) (Figure S1C) and referenced to the residual DMSO signal (in DMSO-d_6). Exact mass (HRMS) spectrum was recorded on a JMS-HX/HX110A mass spectrometer.

Tryptamine (128 mg, 0.799 mmol), EDC·HCl (230 mg, 1.20 mmol), HOBt·H_2O (184 mg, 1.20 mmol) and triethylamine (0.17 ml, 1.2 mmol) were added to a stirred solution of flazin (123 mg, 0.399 mmol) in DMF (8.0 ml) at 0°C. After stirring for 10 h at room temperature, the mixture was diluted with $CHCl_3$. The organic layer was washed with saturated $NaHCO_3$ aq. and brine and dried over Na_2SO_4. The filtrate was concentrated under reduced pressure to give a residue, which was purified by flash chromatography over silica gel with EtOAc:$CHCl_3$:AcOH (80:19:1) to give KPYC12163 as a pale yellow solid (55 mg, 31% yield): mp 252–254°C; ^{1}H NMR (500 MHz, DMSO-d_6) δ 3.07(t, $J = 7.4$ Hz, 2H), 3.72(td, $J = 7.4$, 5.4 Hz, 2H), 4.72(d, $J = 6.1$ Hz, 2H), 5.49(t, $J = 6.1$ Hz, 1H), 6.64(d, $J = 2.6$ Hz, 1H), 7.00(t, $J = 7.4$ Hz, 1H), 7.09(t, $J = 7.4$ Hz, 1H), 7.29(s, 1H), 7.34(t, $J = 7.4$ Hz, 1H), 7.37(d, $J = 7.4$ Hz, 1H), 7.46(d, $J = 2.6$ Hz, 1H), 7.64(t, $J = 7.4$ Hz, 1H), 7.69(d, $J = 7.4$ Hz, 1H), 7.82(d, $J = 7.4$ Hz, 1H), 8.41(d, $J = 7.4$ Hz, 1H), 8.78(s, 1H), 8.83(t, $J = 5.4$ Hz, 1H), 10.88(s, 1H), 11.47(s, 1H); ^{13}C NMR (125 MHz, DMSO-d_6) δ 25.3, 55.9, 109.0, 110.9, 111.3, 111.7, 112.2, 112.6, 118.2, 118.4, 120.2, 120.9, 121.0, 121.9, 122.6, 127.2, 128.7, 130.2, 131.31, 131.32, 136.2, 139.5, 141.3, 151.5, 157.2, 164.2, one CH_2 peak was buried in the solvent signals; HRMS (FAB) m/z: $[M + H]^+$ calculated for $C_{27}H_{23}N_4O_3$, 451.1765; found, 451.1777.

2.4 | sEV isolation

Conditioned medium of CD63-gLuc or CD82-gLuc-transfected B16BL6 cells were collected and subjected to sequential centrifugation at 300 × *g* for 10 min, 2000 × *g* for 20 min and 10,000 × *g* for 30 min to remove cell debris and large vesicles. Subsequently, the supernatant was passed through 0.2 μm syringe filters and spun at 100,000 × *g* for 1–2 h (Himac CP80WX ultracentrifuge; Hitachi Koki, Tokyo, Japan). The resulting sEV pellets were washed three times with filtered phosphate-buffered saline (PBS), and the final sEV pellets were resuspended in small volumes of PBS (50–100 μl).

For proteinase K treatment, Proteinase K (ProK; Nacalai Tesque Inc.) was added to the sEV samples to a final concentration of 1 mg/ml and incubated at 37°C for 10 min to digest the surface proteins. Phenylmethylsulfonyl fluoride (PMSF) was then added to a final concentration of 5 mM and incubated at 25°C for 10 min to inhibit ProK activity. The gLuc activity of the sEV samples was measured as described below. The gLuc activity of the ProK-digested sEV samples was calculated as the percentage of gLuc activity of the untreated sEV samples.

2.5 | Single-tube luciferase assay

Untreated and ProK-treated CD63-gLuc and CD82-gLuc labelled sEV samples were lysed with lysis buffer and mixed with sea pansy luciferase assay reagent (PicaGene Dual; Toyo Ink Co., Tokyo, Japan) to measure the chemiluminescence using a luminometer (Lumat LB 9507; EG&G Berthold, Bad Wildbad, Germany).

2.6 | Chemiluminescence-based sEV quantification assay

pDNAs were individually transfected into B16BL6 cells with PEI max, as described above, and seeded in a 96-well plate (2×10^4 cells/well). After 24 h of incubation, the cells were treated with or without 5 mg/ml GW4869 (item no. 13127; Cayman Chemical, Ann Arbor, MI, USA) suspended in Opti-MEM (Thermo Fisher Scientific) and incubated for an additional 24 h. The conditioned medium of each sample was subjected to sequential centrifugation at 300 × *g* for 10 min, 2000 × *g* for 20 min and 10,000 × *g* for 30 min. At each centrifugation step, ProK-treated and untreated samples were prepared. Additionally, cell lysates for each sample were prepared by washing the cells once with PBS and subsequently lysing with lysis buffer. The chemiluminescence of all samples was measured via a single-tube luciferase assay. The gLuc activity of the supernatant was divided by the gLuc activity of the lysate to calculate the lysate-corrected RLU for each sample. Subsequently, the effect of GW4869 on sEV production was determined by calculating the ratio of the lysate-corrected gLuc activity of GW4869-treated samples to the control (DMSO). Additionally, the gLuc activity of the ProK-digested samples was calculated as the ratio of gLuc activity of the untreated samples.

2.7 | Construction of CD63-gLuc stably expressing B16BL6 cell line

pDNA encoding CD63-gLuc was transfected into B16BL16 cells using Lipofectamine 2000 (Invitrogen). Briefly, 0.5 μg pDNA and 1.5 μl Lipofectamine 2000 were individually diluted in 25 μl Opti-MEM, mixed, and incubated at room temperature for 20 min to form the Lipofectamine-DNA complex. This solution was then added to the cells and incubated for 24 h. Cell cloning was initiated by limiting dilution, and the clone with the highest expression of CD63-gLuc activity was selected. CD63-gLuc protein expression was confirmed by zymography, as described below, and the validity of the sEV quantification assay was confirmed using GW4869 in the established cell line.

For gLuc zymography, B16BL6 cells stably expressing CD63-gLuc (B16BL6-CD63-gLuc) were lysed using the lysis buffer supplied by the PicaGene Dual Sea Pansy Luminescence Kit (Toyo Ink Co.). Zymography of CD63-gLuc was performed as previously described (Takahashi et al., 2013). Briefly, cell lysate samples were subjected to 10% sodium dodecyl sulphate-polyacrylamide gel electrophoresis (SDS-PAGE) under non-reducing conditions. The gel was washed twice with 2.5% Triton X-100 for 30 min, once with PBS for 30 min, and then reacted with the sea pansy luciferase assay reagent (Toyo Ink Co.). Chemiluminescence was detected using the LAS-3000 imaging system (Fujifilm, Tokyo, Japan).

2.8 | nanoparticle tracking analysis (NTA)

Culture media of B16BL6 and B16BL6-CD63-gLuc subjected to sequential centrifugation at 300 × *g* for 10 min, 2000 × *g* for 20 min, or sEVs isolated from B16BL6-CD63-gLuc were used as samples. sEV samples were isolated as described in the previous section, and diluted at 1/20, 1/40, 1/80, 1/160, 1/320, 1/640, 1/1280 ratio using lysis buffer. For each sample, the gLuc activity and the particle numbers were measured via single-tube luciferase assay and NTA. NTA was performed using ViewSizer 3000 (Horiba Scientific, Kyoto, Japan) with 450 nm 250 mW, 520 nm 12 mW and 635 nm 8 mW lasers; data were analysed using the software provided by the instrument.

2.9 | WST-8 cell viability assay

The viability of B16BL6 and B16BL6-CD63-gLuc cells were measured using the WST-8 colorimetric assay (Cell Counting Reagent SF; Nacalai Tesque Inc.) according to the manufacturer's instructions. Briefly, 1×10^3 or 1×10^4 cells of both cell lines were seeded into a 96-well plate and incubated for 24 h. Necessary reagents were added to the cells and incubated for an additional 2 h to allow for the formation of formazan dye. Absorbance of the samples were read at 450 nm (reference at 620 nm) using the Multiskan FC microplate reader (Thermo Fisher Scientific).

2.10 | Screening of sEV modulators

Total of 480 compounds selected from our in-house chemical libraries were used for screening. For each screening, 240 compounds were assayed, and the selected compounds were assayed again to ensure reproducibility of data. B16BL6-CD63-gLuc cells were seeded into three 96-well plate (1×10^4 cells/well) and incubated for 24 h. At the either ends of the 96-well plates (columns 1 and 12), wells for DMSO and GW4869-treated cells were prepared to account for variabilities that may arise within or between the 96-well plates. The cells were treated with 10 μM compound (final DMSO concentration 0.5%) and incubated for an additional 24 h. Conditioned media were collected and centrifuged at 700 × *g* for 1 h at 25°C (Plate Spin; Kubota, Tokyo, Japan), which is equivalent to 2000 × *g* for 20 min, to remove cell debris. Cell lysates were prepared by washing the cells once with PBS and subsequently lysing with lysis buffer. After centrifugation, the supernatants were collected, diluted with lysis buffer and transferred into a 384-well plate to allow for the simultaneous measurement of the samples. Chemiluminescence was recorded using FDSS/μCELL plate reader (Hamamatsu Photonics K.K., Shizuoka, Japan). Baseline chemiluminescence was recorded initially at 27°C every 5 s; sea pansy luciferase assay reagent (Toyo Ink Co.) was added to the supernatant 2 min after the start of the measurement, and the chemiluminescence was recorded every 5 s for the next 10 min. Recorded gLuc activity data were integrated over the 10 min intervals to determine the integrated RLU of each sample. This integrated RLU of the compound-treated samples were normalised to the integrated chemiluminescence of the control to determine the $\text{RLU}_{\text{Compound}}/\text{RLU}_{\text{DMSO}}$ (Figure S2). Compounds with ≥ 2.6-fold increase or ≤ 0.6-fold decrease in gLuc activity compared to control were considered to show notable changes in gLuc activity. Twenty-one compounds in total were selected based on the above criteria; however, one of the compounds was not tested further due to structural similarities with another one of the selected compounds.

Subsequently, supernatant and cell lysate samples of the selected 20 compounds were remeasured via single-tube luciferase assay using Lumat LB 9507 (EG&G Berthold). Compounds that showed robust and reproducible changes in CD63-gLuc activity were identified as potential modulators of sEV production.

2.11 | Evaluation of the effect of the identified compounds on gLuc enzyme reaction

To determine the effect of the candidate compounds on the luciferase enzyme activity, conditioned media of B16BL6 cells treated with 5 or 10 μM of KPYC08425 or KPYC12163, respectively, were collected and mixed with gLuc-LA labelled sEVs. The gLuc activity of each sample was subsequently measured via single-tube luciferase assay.

2.12 | Dose-response and cytotoxicity assay

For the dose-response assay, B16BL6-CD63-gLuc cells were seeded in a 96-well plate (5×10^4 cells/ml/well) and incubated for 24 h. The cells were then treated with varying doses (0.3–3 μM) of the candidate compounds and incubated for an additional 24 h. One hundred microlitres of the conditioned media and cell lysate samples were collected as described above for single-tube luciferase assay.

For the cytotoxicity assay, the remaining conditioned medium was used to measure the release of lactate dehydrogenase (LDH) using the Cytotoxicity LDH Assay Kit-WST (Dojindo Laboratories, Kumamoto, Japan), according to the manufacturer's instructions. Briefly, the remaining culture medium from each condition was transferred to a 96-well plate and mixed with the assay buffer to quantify LDH release. The absorbance of the samples was read at 490 nm using a microplate reader (Varioskan Lux; Thermo Fisher Scientific).

2.13 | sEV protein quantification

B16BL6-CD63-gLuc cells were seeded in a 150-mm dish (4×10^6 cells/dish) and incubated for 24 h. The cells were then treated with 1 or 3 μM KPYC08425 or KPYC12163, respectively. After 24 h incubation, the conditioned medium was subjected to sequential centrifugation, filtration and ultracentrifugation, as described above. Protein concentrations were determined using the Quick Start Bradford protein assay (Bio-Rad, Hercules, CA, USA).

2.14 | Transmission electron microscopy (TEM) observations

For observation of sEVs isolated from compound-treated cells, sEV samples were prepared as described in the previous section. The isolated sEVs were fixed with 4% paraformaldehyde and layered on a carbon/Formvar film-coated TEM grid (Okenshoji Co., Ltd., Tokyo, Japan) for 20 min at room temperature. After washing with PBS, the samples were treated with 1% glutaraldehyde for 5 min and washed four times with distilled water. Finally, the samples were stained with 1% uranyl acetate for 2 min. Observations were performed using a transmission electron microscope (Hitachi, H-7650; Tokyo, Japan).

For the observation of ultrathin sections of compound-treated cells, B16BL6 cells (8.4×10^3 cells/well) were seeded into a Nunc Lab-Tek Chamber Slide system (Thermo Fisher Scientific) and incubated for 24 h. The cells were treated with 1 μM KPYC12163 or GW4869 and incubated for additional 24 h. The cells were then washed twice with PBS, fixed with a solution containing 4% paraformaldehyde and 2% glutaraldehyde solution overnight at 4°C, and subsequently post-fixed with 1% osmium tetroxide for 90 min. The cells were then dehydrated with a graded series (50%–100%) of ethanol baths and embedded in epoxy resin. Ultrathin sections were cut with an ultramicrotome and stained with uranyl acetate and lead citrate. Observations were performed using a transmission electron microscope (JEOL, JEM-1400 Flash; Tokyo, Japan).

2.15 | Western blotting

Cell lysates were prepared as described above. For western blotting of sEV markers (Alix, Hsp70, CD63 and Calnexin), sEVs and lysate samples (0.5 μg protein/sample) were reduced with 100 mM dithiothreitol (DTT) at 95°C for 3 min and subjected to

10% SDS-PAGE. The separated proteins were transferred to a polyvinylidene fluoride membrane (PVDF; Merck Millipore, Ltd., Billerica, MA, USA) and blocked with Blocking One reagent (Nacalai Tesque Inc.) for 30 min. The membranes were then incubated for 1 h at 25°C or overnight at 4°C with the following primary antibodies: mouse anti-AIP1(49/AIP1) antibody (catalogue no. 611620; 1:1000; BD Biosciences, San Jose, CA, USA), rabbit anti-Hsp70 antibody (catalogue no. 4872s; 1:1000; Cell Signaling Technology, Danvers, MA, USA), anti-CD63(H-193) antibody (catalogue no. sc-15363; 1:200; Santa Cruz Biotechnology, Dallas, TX, USA), and rabbit anti-Calnexin (H-70) antibody (catalogue no. sc-11397; 1:1000; Santa Cruz Biotechnology). The membranes were subsequently incubated for 1 h at 25°C with the following horseradish peroxidase (HRP)-conjugated secondary antibodies: rabbit anti-mouse IgG antibody (catalogue no. 61–6520; 1:1000; Thermo Fisher Scientific) and goat anti-rabbit IgG-HRP (catalogue no. 7074P2; 1:2000; Cell Signaling Technology). Following incubation, the membranes were washed twice with 0.1% Tween 20 Tris-buffered saline (TBS-T), once with TBS, and then reacted with Immobilon Western Chemiluminescent HRP substrate (Merck Millipore Ltd.). Chemiluminescence was detected using the LAS-3000 imaging system (Fujifilm).

Western blotting of lysosome and autophagosome markers (Lamp2(alias CD107b) and LC3BII, respectively) was performed as described above using the following primary antibodies: mouse anti-CD107b (Mac-3, M3/84) antibody (catalogue no. 108501; 1:200; BioLegend, San Diego, CA, USA), rabbit anti-LC3BII (EPR18709) antibody (catalogue no. ab192890; 1:2000; Abcam, Cambridge, United Kingdom), and rabbit anti-GAPDH (EPR16891) antibody (catalogue no. ab181602; 1:10,000; Abcam). The following HRP-conjugated secondary antibodies were utilised for detection: rabbit anti-mouse IgG antibody (1:1000, Thermo Fisher Scientific) and goat anti-rabbit IgG HRP (1:2000; Cell Signaling Technology).

2.16 | Fluorescence microscopy observations

pDNAs encoding CD63-EGFP and mCherry-Lamp2c were transfected into B16BL6 cells in a 10:1 ratio with PEI max as described above and seeded in a 6-well plate (2×10^5 cells/ml/well). After 24 h, the cells were treated with 1 μM KPYC12163 or GW4869 and incubated for additional 24 h. The cells were then washed twice with PBS and fixed with 4% paraformaldehyde solution. The fluorescence signals of CD63-EGFP and mCherry-Lamp2c were observed using fluorescence microscopy (Biozero BZ-X710; Keyence Ltd., Osaka, Japan).

2.17 | Statistical analysis

Differences among data sets were statistically analysed by Student's *t*-test for paired comparisons and by Tukey-Kramer test for multiple comparisons. Values were considered statistically significant at $p < 0.05$.

3 | RESULTS

3.1 | Development and optimisation of a sensitive sEV quantification method using gLuc fusion proteins

To determine whether the changes in sEV production could be detected by the changes in the supernatant gLuc activity, B16BL6 cells transiently transfected with CD63-gLuc or CD82-gLuc constructs were treated with or without GW4869. GW4869 is a neutral sphingomyelinase inhibitor that is known to interfere with sEV secretion and vesicle trafficking (Trajkovic et al., 2008); hence, was utilised as a positive control in the assay. The inhibitory effect of GW4869 on sEV production was confirmed in Figure S3A. The conditioned media were subjected to sequential centrifugation, and the supernatant samples at each centrifugation step were treated with or without ProK to determine the optimal pre-treatment conditions. Remnants of gLuc fusion proteins maybe present in the supernatant as larger vesicles/cell debris or as a soluble gLuc fusion protein and could potentially impact the estimation of sEV production. Therefore, the gLuc activity of samples after each centrifugation step, and in the presence or absence of ProK was measured to determine the most optimal pre-treatment condition to accurately estimate the sEV production. The results showed that regardless of the ProK treatment, a reduction in supernatant gLuc activity was observed for all GW4869-treated groups (Figure 1a). Although both fusion proteins showed a reduction in gLuc activity in the presence of GW4869, comparison of the gLuc activity in samples treated with or without ProK showed a significant reduction in CD82-gLuc samples treated with ProK (Figure 1b), suggesting a greater presence of soluble proteins in the CD82-gLuc samples. In contrast, minimal differences in gLuc activity were observed for CD63-gLuc samples treated with or without ProK when treated with centrifugation >2000 × *g* for 20 min, suggesting minimal presence of soluble proteins after sufficient centrifugation. Based on these findings, CD63-gLuc was determined to accurately reflect the amount of sEVs in the supernatant samples, even without the additional step of ProK treatment. Further, the gLuc activity of the cell lysate samples was measured to determine whether any changes observed in the supernatant gLuc activity were primarily due to differences in protein expression within the cell

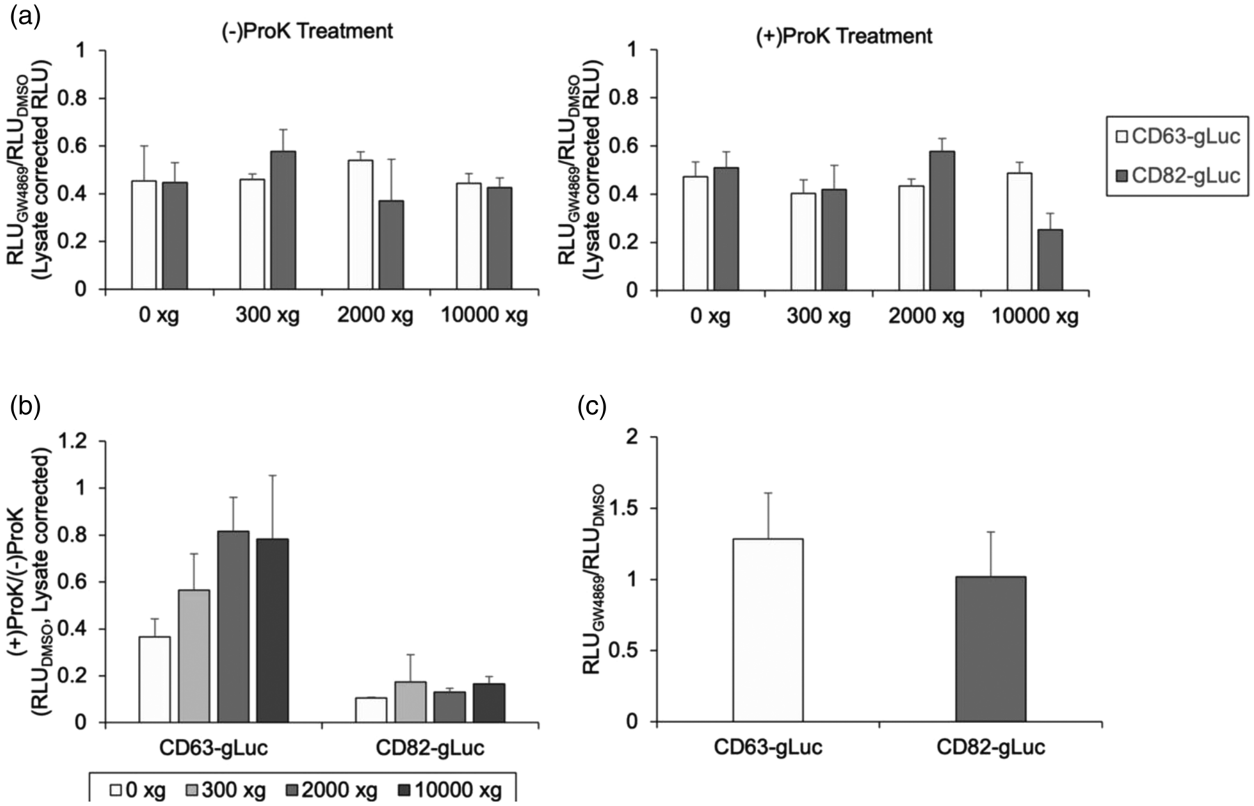

FIGURE 1 Quantification of sEV production utilizing gLuc fusion proteins. CD63-gLuc and CD82-gLuc transfected B16BL6 cells were treated with or without 5 μg/ml GW4869 and the conditioned media were subjected to sequential centrifugation. (a) gLuc activity at each centrifugation step was measured and expressed as the ratio to DMSO (control), left graph represents the gLuc activity of ProK (+) samples, right graph represents the gLuc activity of ProK (−) samples. (b) Ratio of gLuc activities between ProK-treated and untreated samples when subjected to centrifugation at 2000 × *g* for 20 min. (c) gLuc activity of the cell lysates was measured and expressed as the percentage of control. All data are expressed as the mean ± standard deviation ($n = 3$).

(Figure 1c). Cell lysate samples prepared from GW4869-treated cells had comparable gLuc activity to that of control, suggesting that the reduction in the supernatant gLuc activity resulted from a decrease in sEV production rather than a decrease in the expression of the gLuc fusion proteins.

Because transient transfection may result in variability in the level of fusion protein expression per sample, B16BL6-CD63-gLuc cell line was generated for subsequent screening. CD63-gLuc was selected since it (1) required less pre-treatment, as indicated by the comparable gLuc activity between untreated and ProK-treated samples, and (2) exemplified high sensitivities to changes in sEV production caused by the presence or absence of GW4869. Expression of CD63-gLuc in the stable cell line was confirmed by gLuc zymography, which showed a band near the expected molecular weight of 44 kDa (Figure S4A); the band observed above the 63 kDa mark likely represented the fusion protein between the glycosylated CD63 and gLuc protein. The correlation between the gLuc activity and the particle numbers of the B16BL6-CD63-gLuc cell-derived sEVs was confirmed by luciferase assay and NTA, respectively. Results showed a direct correlation between the gLuc activity and the particle numbers (Figure S4B), which further substantiated the use of gLuc activity data as a convenient estimation for sEV quantification in the gLuc reporter cell line. Stable expression of CD63-gLuc in B16BL6 cell lines showed no influence on cell viability compared to non-transfected B16BL6 cells; moreover, no significant differences in the number of particles secreted into the supernatant were observed between B16BL6 and B16BL6-CD63-gLuc cell lines (Figure S4C-D). This suggests that the genetic modification used to establish the stable cell line has minimal impact on the cell and its ability to produce sEVs. Finally, the validity of the assay was confirmed using GW4869 (Figure S4E). A significant reduction in gLuc activity was detected in samples subjected to centrifugation >2000 × *g* for 20 min., which supported the successful development of a sensitive sEV quantification method utilizing CD63-gLuc fusion protein.

3.2 | KPYC08425 and KPYC12163 were identified as potential sEV production modulators via screening

Two-hundred forty compounds selected from our in-house chemical libraries were initially screened with CD63-gLuc activity as the readout. This led to identification of four compounds that showed mild effects on sEV production; these four compounds

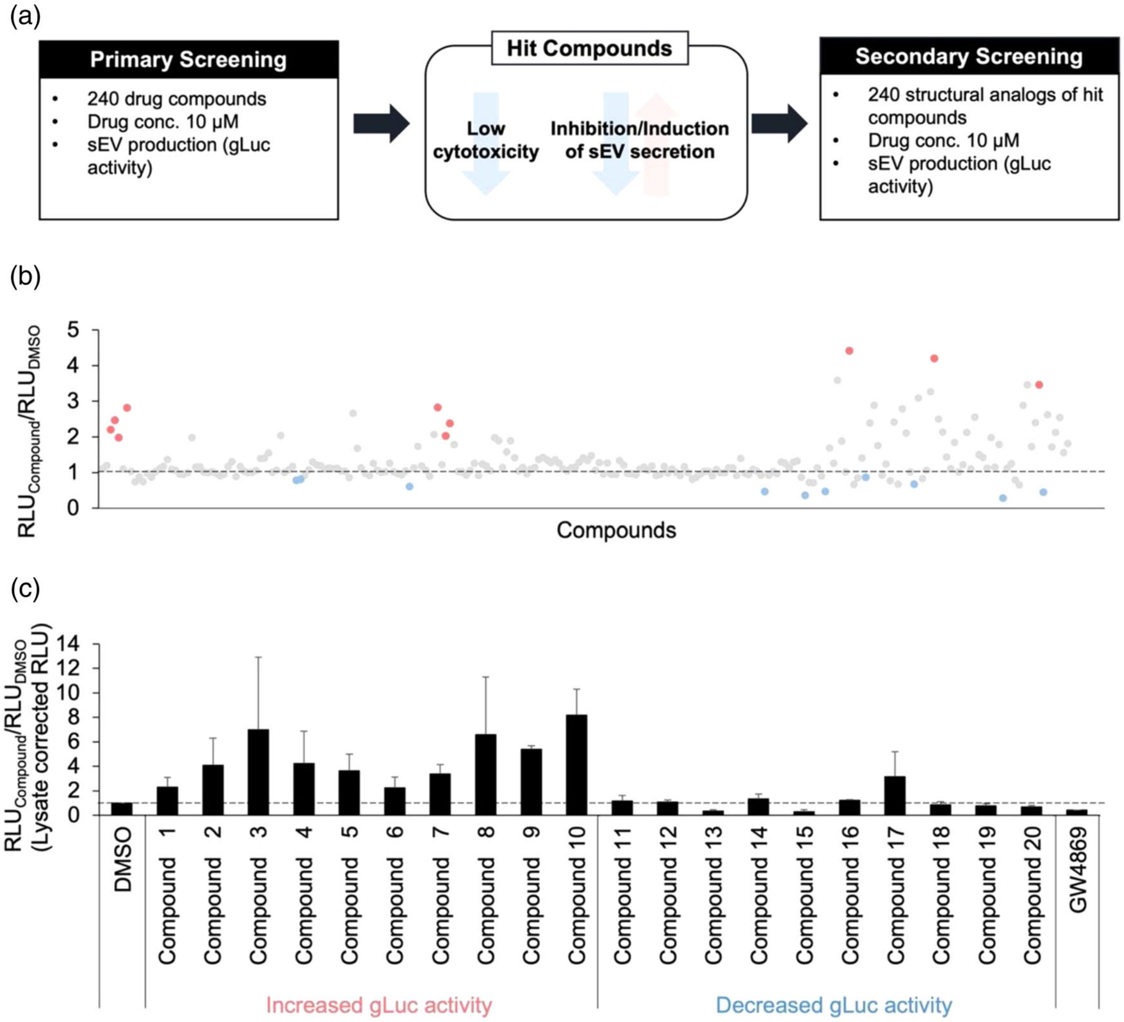

FIGURE 2 KPYC08425 and KPYC12163 were identified as potential sEV production modulators after two rounds of screening. (a) Schematic flow chart of the screening process. Two-hundred forty structural analogues of the hit compounds identified from the primary screening were subsequently screened using the developed sEV quantification assay. (b) gLuc activity was measured using FDSS/μCELL. (c) gLuc activity of the selected 20 compounds was remeasured using a luminometer. Results are expressed as the ratio of gLuc activity of the compounds to control, and all data are expressed as the mean ± standard deviation ($n = 3$).

contained either a carbazole, imidazopyridine, thiophen, or phenol scaffolds (Figure S5). To identify more potent sEV modulators, additional 240 structural analogues containing one of the four scaffolds identified were selected from our in-house chemical libraries and screened (Figure 2a); highlighted in red are compounds that showed increased CD63-gLuc activity and highlighted in blue are compounds that showed decreased CD63-gLuc activity (Figure 2b). The gLuc activity of the highlighted compounds was remeasured using single-tube luciferase assay (Figure 2c) to confirm their stimulatory or inhibitory effect. Based on these assays, cells treated with compounds 3, 8 and 10 showed a notable increase in gLuc activity, while those treated with compounds 13 and 15 showed a substantial decrease in gLuc activity. However, significant reduction in the lysate gLuc activity was observed for compounds 3, 10 and 15, suggesting changes in CD63-gLuc expression in these compound-treated cells, rather than a change in sEV production. Thus, compound 8(KPYC08425) and compound 13(KPYC12163) were identified as compounds that can produce potent and reproducible effects on CD63-gLuc activity (Figure 3a).

To validate the effects of the identified compounds, its effect on the gLuc enzyme reaction, dose-response and cytotoxicity was assessed subsequently. The addition of the compounds into the reaction mixture hardly changed the chemiluminescence emitted by the gLuc enzyme when reacted with its substrate, coelenterazine (Figure 3b), suggesting that the changes observed in the gLuc activity were not a result of altered enzyme-substrate interaction. Significant changes in gLuc activity of B16BL6-CD63-gLuc cells treated with these two compounds were observed in a dose-dependent manner, with relatively low cellular toxicity at the investigated doses (Figure 3c and d), supporting its effect on modulating the amount of CD63-gLuc secreted into the supernatant. Although greater effects were observed at higher doses, increased cellular toxicities became more prominent at doses >5 μM (data not shown); therefore, subsequent experiments were conducted utilizing <3 μM as the dose.

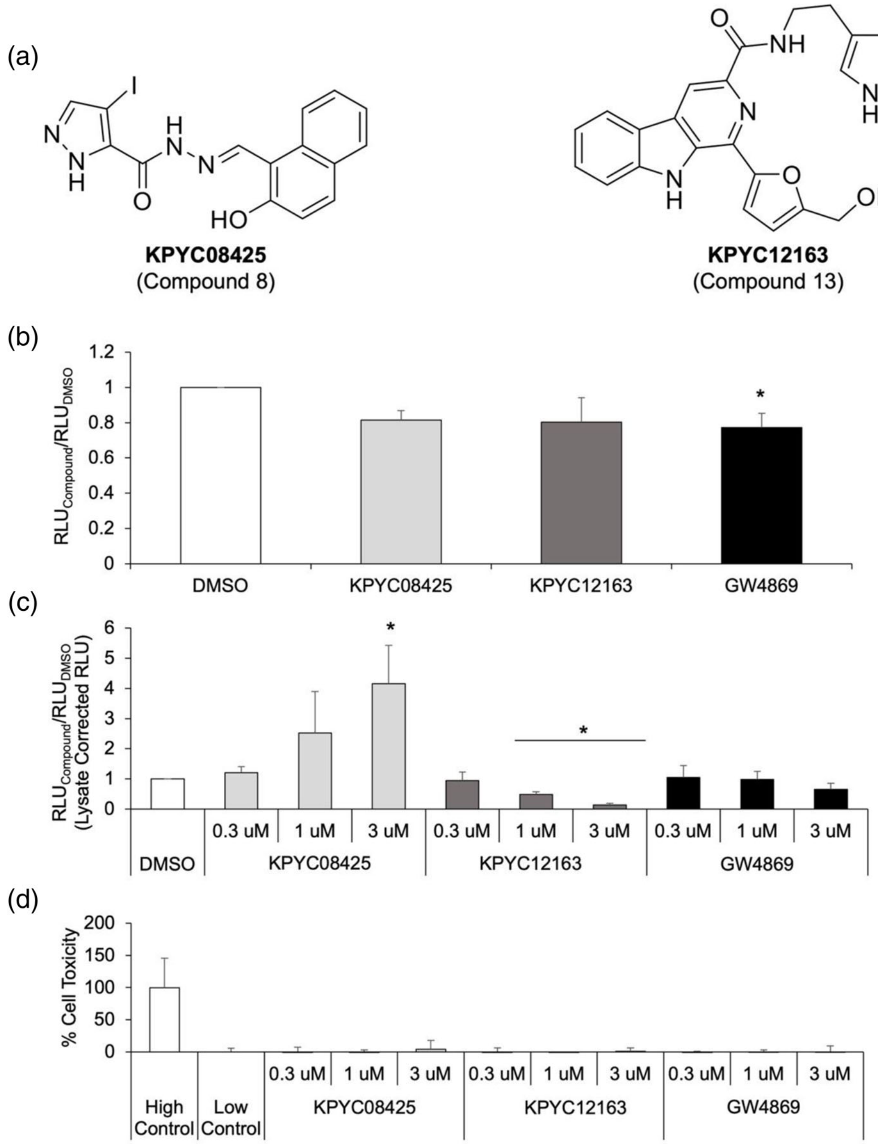

FIGURE 3 KPYC08425 and KPYC12163 induces dose-dependent effects on gLuc activity with minor effects on enzyme activity and cytotoxicity. (a) Structural formulae of the identified hit compounds. (b) The effect of compounds on gLuc enzyme activity was determined by mixing the compound-treated conditioned medium with gLuc-LA sEVs and measuring the gLuc activity. (c) Dose-response of the compounds was evaluated by treating the cells with the indicated doses of the compounds and measuring the gLuc activity. The results are expressed as the ratio of the gLuc activity of the compounds to control activity. (d) Cytotoxicity of the compounds at the indicated doses were evaluated by LDH assay. All data are expressed as the mean ± standard deviation ($n = 3$). *$p < 0.05$ compared to DMSO using Tukey-Kramer test for (b and c).

3.3 | KPYC08425 and KPYC12163 were validated as effective sEV production modulators

To confirm the effects of the candidate compounds on sEV production, sEVs were isolated from the conditioned medium of the compound-treated cells by ultracentrifugation, and the sEV protein yields were assessed. Addition of 1 μM KPYC08425 showed a 1.5-fold increase in sEV protein yield compared to control (Figure 4a). Addition of 3 μM KPYC12163 resulted in approximately 70% reduction in sEV protein yield compared to control (Figure 4b). Additionally, TEM observation of these isolated sEVs revealed a round-shaped, bi-layered vesicle that were approximately 100 nm in size, which are consistent with classic sEV morphology and size (Figure 4c). These findings validated the identified compounds as potent modulator of sEV production. Since KPYC12163 showed a robust inhibitory effect on sEV production, subsequent studies were conducted to investigate its role in sEV production.

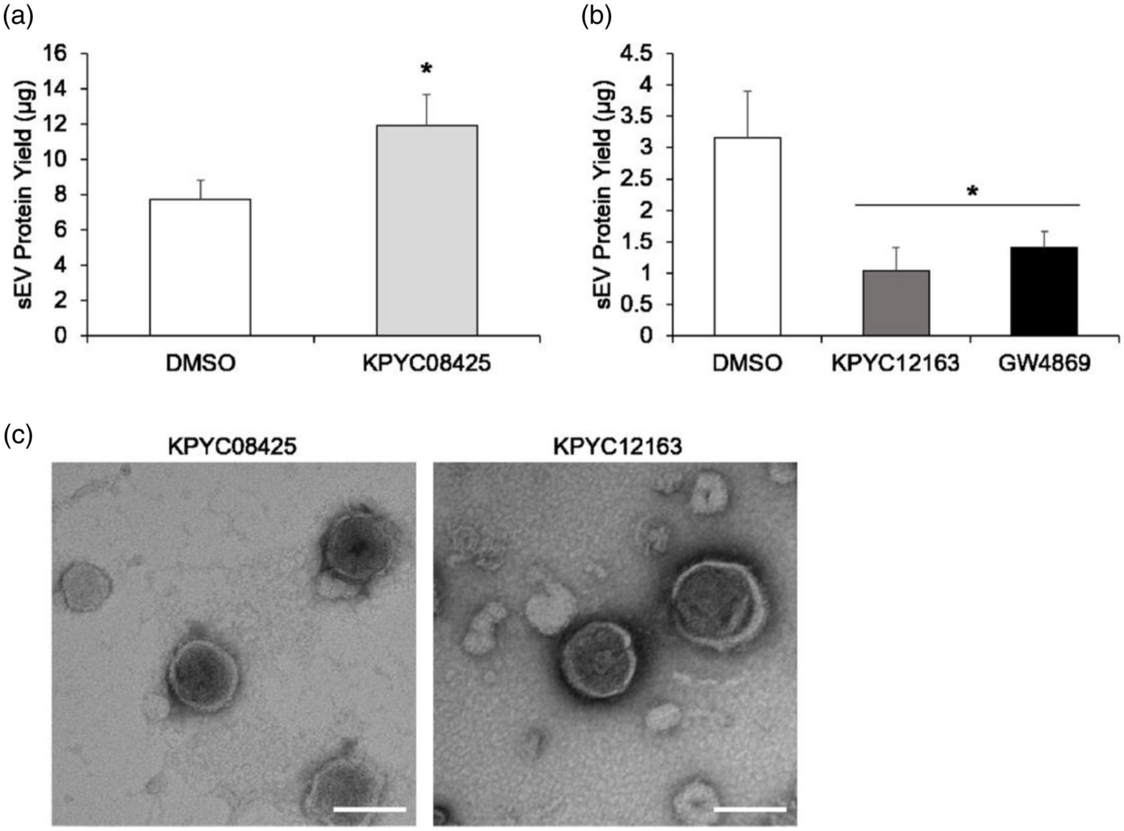

FIGURE 4 KPYC08425 and KPYC12163 modulated sEV production. sEVs were isolated from KPYC08425 (a) or KPYC12163-treated cells (b) by ultracentrifugation and quantified by Bradford protein assay. All data are expressed as the mean ± standard deviation ($n = 3$). $^*p < 0.05$ compared to DMSO using Student's t-test for (a) and Tukey-Kramer test for (b). (c) Isolated sEVs were observed under a transmission electron microscope (TEM) (scale bar = 100 nm).

3.4 | KPYC12163 may be inhibiting sEV release thereby stimulating the autolysosomal pathway

First, to determine whether the inhibitory effect of KPYC12163 was cell-type specific, CD63-gLuc was transiently transfected into various cell lines, and the changes in gLuc activity upon the addition of the compounds were evaluated. Results showed a decreasing trend in gLuc activity in all cell lines treated with KPYC12163 compared to control (Figure 5a), which suggested that the inhibitory effect of KPYC12163 may occur in multiple different cell lines.

Next, the cargo contents of the isolated sEVs were determined by western blotting. The presence of sEV markers, including Alix, Hsp70, and CD63, and the absence of endoplasmic reticulum marker, Calnexin, was confirmed in the compound-treated B16BL6-CD63-gLuc-derived sEVs (Figure 5b). sEVs isolated from KPYC12163-treated cells showed decreased band intensity for all sEV markers compared to control; however, the lysate samples of KPYC12163- and GW4869-treated cells showed increased band intensity for Hsp70. This led to an interesting hypothesis that the compounds were involved in the accumulation of sEVs within the cell, thereby resulting in decreased sEV release.

Generally, sEVs are harboured in multivesicular bodies (MVBs) in the form of intraluminal vesicles (ILVs) within the cell prior to its release. TEM observation of KPYC12163-treated B16BL6 cells showed increased accumulation of vacuoles within the cell compared to control; accumulation was also observed in GW4869-treated cells, but to a lesser extent as compared to KPYC12163-treated cells (Figure 5c). However, due to the similarities in size and morphology, the observed vacuoles could not be distinguished from MVBs by TEM observations. Thus, to evaluate the accumulation of MVBs, CD63-EGFP and mCherry-Lamp2c were utilised to label the sEVs, and the changes in fluorescent signals upon the addition of compounds were assessed. Results showed a notable increase in CD63-EGFP signals, and surprisingly, a decrease in mCherry-Lamp2c signal upon KPYC12163-treatment compared to control (Figure 5d). GW4869 showed a comparable signal for CD63-EGFP and a slight reduction in mCherry-Lamp2c signal.

Since Lamp2c proteins also localise in the lysosomal membrane, it was hypothesised that the reduction in mCherry-Lamp2c signal may be reflective of induced autophagy. Western blot analysis of Lamp2c (lysosome marker) and LC3BII (autophagosome marker) showed decreased band intensity for Lamp2c and increased band intensity for LC3BII in KPYC12163-treated cell lysates

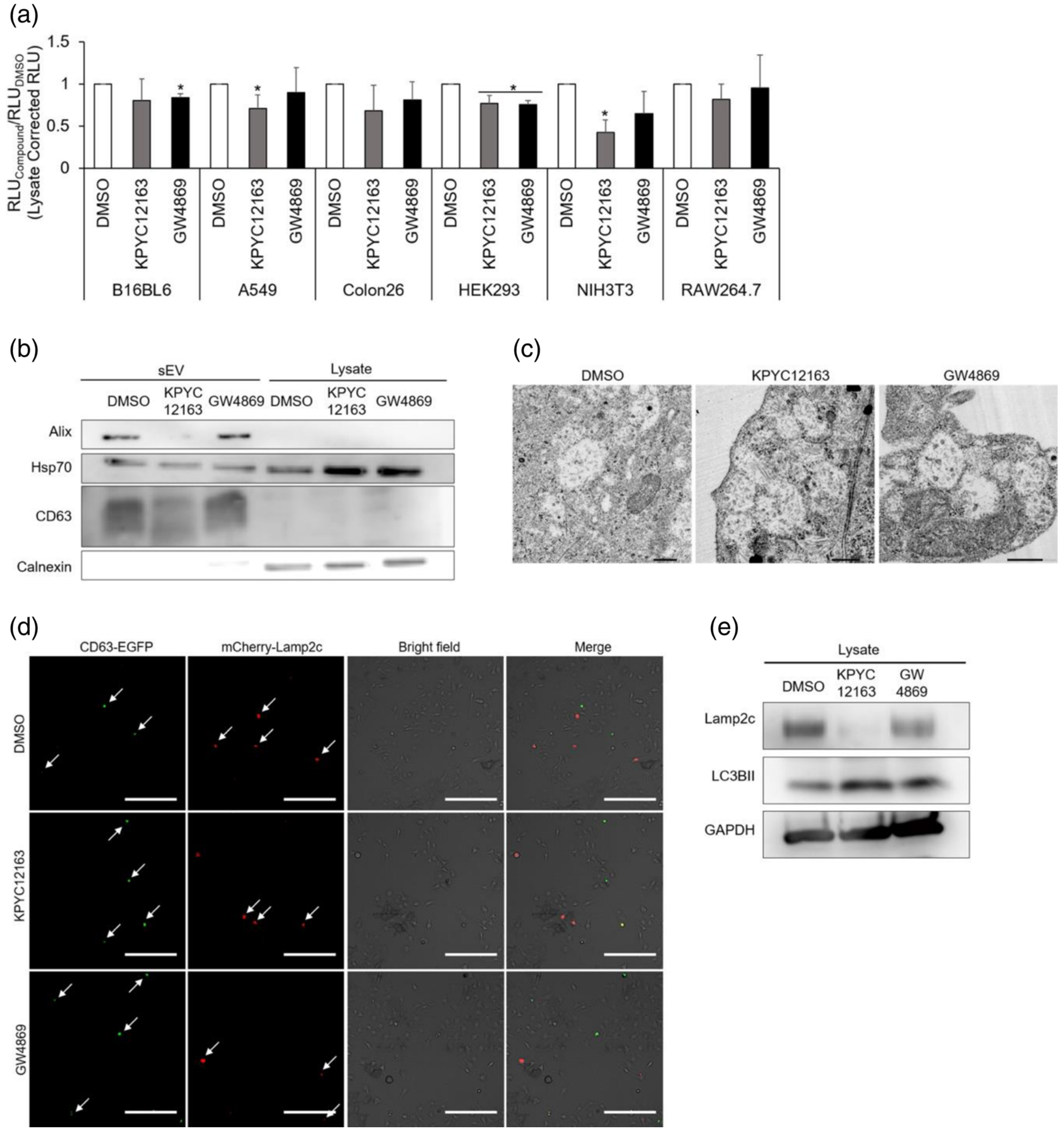

FIGURE 5 Autolysosomal pathway may be involved in the inhibitory effect of KPYC12163. (a) B16BL6, A549, Colon26, HEK293, NIH3T3 and RAW264.7 cells were treated with 1 μM of KPYC12163 or GW4869 and the gLuc activities of the supernatant and cell lysates were measured. Results are expressed as the ratio of gLuc activity of the compounds to that of the control. All data are expressed as the mean ± standard deviation ($n = 3$). $^*p < 0.05$ compared to DMSO using Tukey-Kramer test. (b) Western blotting for Alix, Hsp70, CD63 and calnexin in sEVs and cell lysates prepared from control or compound-treated B16BL6-CD63-gLuc cells (0.5 μg protein/lane). (c) Ultrathin sections of B16BL6 cells treated with 1 μM of KPYC12163 or GW4869 as observed by TEM (scale bar = 1 μm). (d) B16BL6 cells transfected with CD63-EGFP and mCherry-Lamp2c were treated with 1 μM of KPYC12163 or GW4869 and fixed with 4% paraformaldehyde. The fluorescence signals of CD63-EGFP and mCherry-Lamp2c were observed under a fluorescent microscopy (original magnification x200, scale bar = 100 μm). (e) Western blotting for Lamp2c (lysosome marker), LC3BII (autophagosome marker) and GAPDH in control or compound-treated B16BL6 cell lysates.

(Figure 5e). Taken together, these results suggested that KPYC12163 inhibited sEV release, thereby causing an accumulation of sEVs within the cell, which then stimulated the induction of autophagy to breakdown the excess sEVs within the cell (Figure 6).

4 | DISCUSSION

In the current study, a convenient and highly sensitive sEV quantification method was developed by genetically labelling sEVs with gLuc reporter proteins. The use of luciferase fused to sEV marker proteins for sEV quantification has been previously reported (Hikita et al., 2018), and the luminescence intensity was shown to have a strong positive correlation with the number of

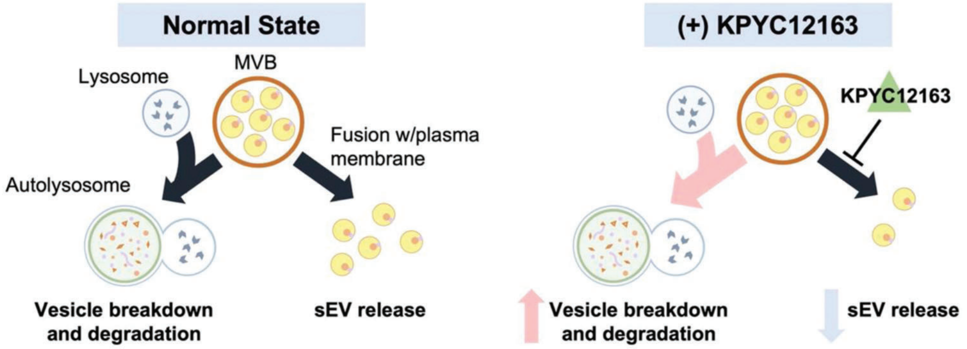

FIGURE 6 Proposed mechanism of KPYC12163. Under normal state, MVBs either fuse with the plasma membrane to release the sEVs or fuse with the lysosome to form autolysosome for degradation. However, KPYC12163 inhibits the fusion of MVBs with the plasma membrane preventing sEV release. This then results in the accumulation of MVBs, which stimulates the autolysosomal pathway to breakdown the excess MVBs in the cell.

sEV particles based on NTA (Figure S4). Indeed, the addition of GW4869, an sEV production inhibitor, significantly decreased the gLuc activity in the cell supernatant for both gLuc fusion proteins evaluated (Figure 1), substantiating the gLuc activity as an accurate reflection of the changes in sEV production. However, CD82-gLuc samples contained more soluble gLuc proteins than CD63-gLuc, as indicated by the significant reduction in gLuc activity upon ProK treatment (Figure 1). This would necessitate an additional step to remove the excess gLuc proteins for accurate quantification. Therefore, the gLuc fusion protein consisting of CD63, which is a common sEV marker, was selected as the fusion protein for subsequent screening. Nonetheless, sEVs are a heterogeneous group of vesicles that consist of distinct subpopulations depending on their size, cargo contents, and their producing cells, and a subpopulation of sEVs that lack CD63 has been reported previously (Yoshioka et al., 2013). Thus, it is important to recognise that regardless of which fusion protein is selected for sEV labelling, it could result in under- or over-estimation of the sEV amount, and multiple sEV markers should be evaluated for the most precise sEV quantification. Another limitation of this quantification method is that it relies on genetic modification to express the gLuc fusion proteins to label the sEVs for its quantification. Therefore, this method is only applicable to cell lines that can be genetically modified either by transient or stable transfection. This method would not be applicable to certain cells such as primary cells since neither options of genetic modification are feasible for these types of cells.

After two rounds of screening, two hit compounds, namely KPYC08425 and KPYC12163, that regulate sEV production were identified from our in-house chemical libraries. KPYC08425, which showed a significant increase in gLuc activity, is a hydroxyphenyl hydrazone, which is one of the commonly reported pan-assay interference compounds (PAINS). PAINS are chemical compounds that interact non-specifically with target proteins to produce false signals in numerous assays (Baell & Holloway, 2010; Baell & Nissink, 2018). However, evaluation of the effect of KPYC08425 on enzyme activity showed decreased gLuc activity upon addition of the compound (Figure 3), which suggests that the screening results may not be an artefact but an actual reflection of increased sEV production. Purification and quantification of sEVs from cells treated with KPYC08425 showed a 1.5-fold increase in sEV protein yield (Figure 4), validating KPYC08425 as a potential sEV production inducer. Nonetheless, its effect on sEV production is mild at best, and cytotoxicity becomes an issue at higher doses (data not shown). Hydroxyphenyl hydrazone derivatives have been reported to inhibit cell proliferation through iron sequestration in cancer cells (Li et al., 2017), which may be the cause of increased cellular toxicity. Therefore, further optimisation of the chemical compound is necessary to improve its efficacy.

KPYC12163, which showed a significant reduction in gLuc activity, is not a member of PAINS but still exhibited mild interference with the enzyme activity (Figure 3). However, considering the significant reduction in gLuc activity observed during the screening, it is likely that the compound indeed influenced sEV biogenesis/release. Subsequent dose-response assay showed not only a dose-dependent decrease in gLuc activity in the cell supernatant but also an increase in gLuc activity in the cell lysate (data not shown), suggesting that the compound interfered with sEV release. Purification of sEVs showed approximately 70% reduction in sEV protein yield for KPYC12163-treated cells compared to control (Figure 4), confirming its inhibitory effect on sEV production. All investigated cell lines, including cancerous and non-cancerous cell lines treated with KPYC12163, exhibited a tendency of decreased gLuc activity (Figure 5), suggesting that the compound likely inhibits a common sEV biogenesis pathway. Additionally, western blot analysis of the sEV markers showed a significant reduction in the band intensity for sEVs isolated from KPYC12163-treated cells (Figure 5), which implies a decrease in sEV protein yield per μg protein and, potentially, a qualitative change in the sEVs such as altered cargo contents.

Generally, sEVs are derived from the endosomal compartment known as MVBs; the membrane of MVB invaginates to form ILVs, which are secreted into the extracellular milieu upon MVB fusion with the plasma membrane. MVBs are mostly >250 nm in size and are enriched with various proteins such as class II MHC and tetraspanins (Altick et al., 2009; Piper & Katzmann, 2007). TEM observation of compound-treated cells showed increased accumulation of vacuoles that could be either cytoplasmic vacuolisation of the compounds or MVBs based on their size (Figure 5). Moreover, a slight increase in CD63-EGFP signals was observed in the compound-treated cells (Figure 5), which suggests the potential accumulation of MVBs, possibly caused by preventing the MVB-plasma membrane fusion pathway for sEV release. GW4869 has been reported to decrease the number of fusion events with the plasma membrane by Verweij et al. (2018), which would explain the increased vacuoles observed in the GW4869-treated cells. Considering that Lamp2c protein is also an sEV-tropic protein (Théry et al., 2018), it was assumed that like CD63-EGFP, mCherry-Lamp2c signals will also increase upon addition of the compound; surprisingly, mCherry-Lamp2c signals were decreased, and western blot analysis also confirmed the reduction of Lamp2c in KPYC12163-treated cell lysates.

In addition to its tropism in sEVs, Lamp proteins are also localised on the lysosomal membrane (Eskelinen, 2006). Lysosomes are one of the major players involved in macroautophagy (hereafter referred to as autophagy) that function to degrade cytosolic proteins and damaged organelles by fusion with autophagosomes (Feng et al., 2014). Since sEV biogenesis and autophagy are closely linked by the endo-lysosomal pathway to maintain cellular homeostasis (Xu et al., 2018), it could be reasoned that the accumulated MVBs (due to inhibited sEV release) induced the autophagy-lysosome pathway to clear the excess MVBs in the cell. Western blot analysis of LC3BII showed increased band intensity for KPYC12163-treated cells, suggesting the potential induction of the autolysosomal pathway. Other recently identified sEV inhibitors, such as sulfisoxazole, have also been reported to increase the degradation of MVBs through the autophagy-lysosome pathway (Im et al., 2019). Nonetheless, further investigation of the changes in the expression of sEV biogenesis/release pathway machineries upon treatment with KPYC12163 is necessary to determine the players involved in the inhibition of sEV release.

5 | CONCLUSION

By developing a highly sensitive luciferase-based sEV quantification assay using CD63-gLuc fusion protein, two novel sEV production modulators, KPYC08425 and KPYC12163, were identified. The developed assay can be easily adapted in various cell lines and requires minimal pretreatment (centrifugation $> 2000 \times g$ for 20 min), thus, can be utilised as a robust method for high throughput sEV quantification. Compounds identified from the screening showed notable impact on sEV protein yield, with KPYC08425 showing a mild increase and KPYC12163 showing a significant decrease in sEV production. These sEV production regulators can be a useful tool in a wide range of sEV-based research to understand its biological and pathological functions, as well as potentially, in sEV-based therapies.

AUTHOR CONTRIBUTIONS

Aki Yamamoto: Conceptualisation; Data curation; Formal analysis; Methodology; Writing – original draft; Writing – review & editing. Yuki Takahashi: Conceptualisation; Data curation; Formal analysis; Funding acquisition; Methodology; Supervision; Writing – original draft; Writing – review & editing. Shinsuke Inuki: Data curation; Formal analysis; Methodology; Resources; Writing – original draft; Writing – review & editing. Shumpei Nakagawa: Data curation; Methodology. Kodai Nakao: Data curation. Hiroaki Ohno: Supervision; Writing – original draft; Writing – review & editing. Masao Doi: Supervision; Writing – original draft; Writing – review & editing. Yoshinobu Takakura: Supervision; Writing – original draft; Writing – review & editing.

ACKNOWLEDGEMENTS

We thank Professor Shinya Oishi (Kyoto Pharmaceutical University) and Dr. Tsukasa Mizuhara (Kyoto University) for their assistance in the construction of the chemical library. This work was funded by JSPS KAKENHI (grant number 21K19908) from Japan Society for Promotion of Science.

CONFLICT OF INTEREST

The authors declare no conflict of interest.

ORCID

Aki Yamamoto https://orcid.org/0000-0003-2895-3922

REFERENCES

Altick, A. L., Baryshnikova, L. M., Vu, T. Q., & von Bartheld, C. S. (2009). Quantitative analysis of multivesicular bodies (MVBs) in the hypoglossal nerve: Evidence that neurotrophic factors do not use MVBs for retrograde axonal transport. *The Journal of Comparative Neurology*, *514*(6), 641–657. https://doi.org/10.1002/cne.22047

Baell, J. B., & Holloway, G. A. (2010). New substructure filters for removal of pan assay interference compounds (PAINS) from screening libraries and for their exclusion in bioassays. *Journal of Medicinal Chemistry*, *53*(7), 2719–2740. https://doi.org/10.1021/jm901137j

Baell, J. B., & Nissink, J. W. M. (2018). Seven year itch: Pan-assay interference compounds (PAINS) in 2017—Utility and limitations. *ACS Chemical Biology*, *13*(1), 36–44. https://doi.org/10.1021/acschembio.7b00903

Becker, A., Thakur, B. K., Weiss, J. M., Kim, H. S., Peinado, H., & Lyden, D. (2016). Extracellular vesicles in cancer: Cell-to-cell mediators of metastasis. *Cancer Cell*, *30*(6), 27066. https://doi.org/10.1016/j.ccell.2016.10.009

Catalano, M., & O'Driscoll, L. (2020). Inhibiting extracellular vesicles formation and release: A review of EV inhibitors. *Journal of Extracellular Vesicles*, *9*(1), 1703244. https://doi.org/10.1080/20013078.2019.1703244

Charoenviriyakul, C., Takahashi, Y., Morishita, M., Nishikawa, M., & Takakura, Y. (2018). Role of extracellular vesicle surface proteins in the pharmacokinetics of extracellular vesicles. *Molecular Pharmaceutics*, *15*(3), 1073–1080. https://doi.org/10.1021/acs.molpharmaceut.7b00950

Datta, A., Kim, H., McGee, L., Johnson, A. E., Talwar, S., Marugan, J., Southall, N., Hu, X., Lal, M., Mondal, D., Ferrer, M., & Abdel-Mageed, A. B. (2018). High-throughput screening identified selective inhibitors of exosome biogenesis and secretion: A drug repurposing strategy for advanced cancer. *Scientific Reports*, *8*(1), 8161. https://doi.org/10.1038/s41598-018-26411-7

el Andaloussi, S., Mäger, I., Breakefield, X. O., & Wood, M. J. A. (2013). Extracellular vesicles: Biology and emerging therapeutic opportunities. *Nature Reviews Drug Discovery*, *12*(5), 347–357. https://doi.org/10.1038/nrd3978

Emam, S. E., Ando, H., Abu Lila, A. S., Shimizu, T., Ukawa, M., Okuhira, K., Ishima, Y., Mahdy, M. A., Ghazy, F. S., & Ishida, T. (2018). A novel strategy to increase the yield of exosomes (extracellular vesicles) for an expansion of basic research. *Biological and Pharmaceutical Bulletin*, *41*(5), 733–742. https://doi.org/10.1248/bpb.b17-00919

Eskelinen, E.-L. (2006). Roles of LAMP-1 and LAMP-2 in lysosome biogenesis and autophagy. *Molecular Aspects of Medicine*, *27*(5–6), 495–502. https://doi.org/10.1016/j.mam.2006.08.005

Feng, Y., He, D., Yao, Z., & Klionsky, D. J. (2014). The machinery of macroautophagy. *Cell Research*, *24*(1), 24–41. https://doi.org/10.1038/cr.2013.168

García-Seisdedos, D., Babiy, B., Lerma, M., Casado, M. E., Martínez-Botas, J., Lasunción, M. A., Pastor, Ó., & Busto, R. (2020). Curcumin stimulates exosome/microvesicle release in an in vitro model of intracellular lipid accumulation by increasing ceramide synthesis. *Biochimica et Biophysica Acta (BBA) – Molecular and Cell Biology of Lipids*, *1865*(5), 158638. https://doi.org/10.1016/j.bbalip.2020.158638

Hikita, T., Miyata, M., Watanabe, R., & Oneyama, C. (2018). Sensitive and rapid quantification of exosomes by fusing luciferase to exosome marker proteins. *Scientific Reports*, *8*(1), 14035. https://doi.org/10.1038/s41598-018-32535-7

Im, E.-J., Lee, C.-H., Moon, P.-G., Rangaswamy, G. G., Lee, B., Lee, J. M., Lee, J.-C., Jee, J.-G., Bae, J.-S., Kwon, T.-K., Kang, K.-W., Jeong, M.-S., Lee, J.-E., Jung, H.-S., Ro, H.-J., Jun, S., Kang, W., Seo, S.-Y., Cho, Y.-E., … Baek, M.-C. (2019). Sulfisoxazole inhibits the secretion of small extracellular vesicles by targeting the endothelin receptor A. *Nature Communications*, *10*(1), 1387. https://doi.org/10.1038/s41467-019-09387-4

Khan, F. M., Saleh, E., Alawadhi, H., Harati, R., Zimmermann, W.-H., & El-Awady, R. (2018). Inhibition of exosome release by ketotifen enhances sensitivity of cancer cells to doxorubicin. *Cancer Biology & Therapy*, *19*(1), 25–33. https://doi.org/10.1080/15384047.2017.1394544

Kulshreshtha, A., Singh, S., Ahmad, M., Khanna, K., Ahmad, T., Agrawal, A., & Ghosh, B. (2019). Simvastatin mediates inhibition of exosome synthesis, localization and secretion via multicomponent interventions. *Scientific Reports*, *9*(1), 16373. https://doi.org/10.1038/s41598-019-52765-7

Lässer, C., Seyed Alikhani, V., Ekström, K., Eldh, M., Torregrosa Paredes, P., Bossios, A., Sjöstrand, M., Gabrielsson, S., Lötvall, J., & Valadi, H. (2011). Human saliva, plasma and breast milk exosomes contain RNA: Uptake by macrophages. *Journal of Translational Medicine*, *9*(1), 9. https://doi.org/10.1186/1479-5876-9-9

Li, F., Long, L., Xiao, J., Wang, C., Li, W., Li, S., Zhao, C., & Wang, L. (2017). A novel hydroxyphenyl hydrazone derivate YCL0426 inhibits cancer cell proliferation through sequestering iron. *Anti-Cancer Drugs*, *28*(10), 1131–1140. https://doi.org/10.1097/CAD.0000000000000557

Ludwig, N., Yerneni, S. S., Menshikova, E. v., Gillespie, D. G., Jackson, E. K., & Whiteside, T. L. (2020). Simultaneous inhibition of glycolysis and oxidative phosphorylation triggers a multi-fold increase in secretion of exosomes: Possible role of 2′,3′-CAMP. *Scientific Reports*, *10*(1), 6948. https://doi.org/10.1038/s41598-020-63658-5

Matsumoto, A., Takahashi, Y., Ogata, K., Kitamura, S., Nakagawa, N., Yamamoto, A., Ishihama, Y., & Takakura, Y. (2021). Phosphatidylserine-deficient small extracellular vesicle (SEV) is a major somatic cell-derived SEV subpopulation in blood. *Iscience*, *24*, 102839. https://doi.org/10.1016/j.isci.2021.102839

Piper, R. C., & Katzmann, D. J. (2007). Biogenesis and function of multivesicular bodies. *Annual Review of Cell and Developmental Biology*, *23*(1), 519–547. https://doi.org/10.1146/annurev.cellbio.23.090506.123319

Takahashi, Y., Nishikawa, M., Shinotsuka, H., Matsui, Y., Ohara, S., Imai, T., & Takakura, Y. (2013). Visualization and in vivo tracking of the exosomes of murine melanoma B16-BL6 cells in mice after intravenous injection. *Journal of Biotechnology*, *165*(2), 77–84. https://doi.org/10.1016/j.jbiotec.2013.03.013

Tang, J.-G., Wang, Y.-H., Wang, R.-R., Dong, Z.-J., Yang, L.-M., Zheng, Y.-T., & Liu, J.-K. (2008). Synthesis of analogues of flazin, in particular, flazinamide, as promising anti-HIV agents. *Chem Biodivers*, *5*(3), 447–460. https://doi.org/10.1002/cbdv.200890044

Théry, C., Witwer, K. W., Aikawa, E., Alcaraz, M. J., Anderson, J. D., Andriantsitohaina, R., Antoniou, A., Arab, T., Archer, F., Atkin-Smith, G. K., Ayre, D. C., Bach, J.-M., Bachurski, D., Baharvand, H., Balaj, L., Baldacchino, S., Bauer, N. N., Baxter, A. A., Bebawy, M., … Zuba-Surma, E. K. (2018). Minimal information for studies of extracellular vesicles 2018 (MISEV2018): A position statement of the international society for extracellular vesicles and update of the MISEV2014 guidelines. *Journal of Extracellular Vesicles*, *7*(1), 1535750. https://doi.org/10.1080/20013078.2018.1535750

Tkach, M., & Théry, C. (2016). Communication by extracellular vesicles: Where we are and where we need to go. *Cell*, *164*(6), 1226–1232. https://doi.org/10.1016/j.cell.2016.01.043

Trajkovic, K., Hsu, C., Chiantia, S., Rajendran, L., Wenzel, D., Wieland, F., Schwille, P., Brugger, B., & Simons, M. (2008). Ceramide triggers budding of exosome vesicles into multivesicular endosomes. *Science (1979)*, *319*(5867), 1244–1247. https://doi.org/10.1126/science.1153124

van Niel, G., D'Angelo, G., & Raposo, G. (2018). Shedding light on the cell biology of extracellular vesicles. *Nature Reviews Molecular Cell Biology*, *19*(4), 213–228. https://doi.org/10.1038/nrm.2017.125

Verweij, F. J., Bebelman, M. P., Jimenez, C. R., Garcia-Vallejo, J. J., Janssen, H., Neefjes, J., Knol, J. C., de Goeij-de Haas, R., Piersma, S. R., Baglio, S. R., Verhage, M., Middeldorp, J. M., Zomer, A., van Rheenen, J., Coppolino, M. G., Hurbain, I., Raposo, G., Smit, M. J., Toonen, R. F. G., … Pegtel, D. M. (2018). Quantifying exosome secretion from single cells reveals a modulatory role for GPCR signaling. *Journal of Cell Biology*, *217*(3), 1129–1142. https://doi.org/10.1083/jcb.201703206

Xu, J., Camfield, R., & Gorski, S. M. (2018). The interplay between exosomes and autophagy – Partners in crime. *Journal of Cell Science*, *131*(15), jcs215210. https://doi.org/10.1242/jcs.215210

Yáñez-Mó, M., Siljander, P. R.-M., Andreu, Z., Bedina Zavec, A., Borràs, F. E., Buzas, E. I., Buzas, K., Casal, E., Cappello, F., Carvalho, J., Colás, E., Cordeiro-da Silva, A., Fais, S., Falcon-Perez, J. M., Ghobrial, I. M., Giebel, B., Gimona, M., Graner, M., Gursel, I., … de Wever, O. (2015). Biological properties of extracellular vesicles and their physiological functions. *Journal of Extracellular Vesicles*, *4*(1), 27066. https://doi.org/10.3402/jev.v4.27066

Yoshioka, Y., Konishi, Y., Kosaka, N., Katsuda, T., Kato, T., & Ochiya, T. (2013). Comparative marker analysis of extracellular vesicles in different human cancer types. *Journal of Extracellular Vesicles*, *2*(1), 20424. https://doi.org/10.3402/jev.v2i0.20424

Zaborowski, M. P., Balaj, L., Breakefield, X. O., & Lai, C. P. (2015). Extracellular vesicles: Composition, biological relevance, and methods of study. *BioScience*, *65*(8), 783–797. https://doi.org/10.1093/biosci/biv084

Zhang, H., Lu, J., Liu, J., Zhang, G., & Lu, A. (2020). Advances in the discovery of exosome inhibitors in cancer. *Journal of Enzyme Inhibition and Medicinal Chemistr*, *35*(1), 1322–1330. https://doi.org/10.1080/14756366.2020.1754814

SUPPORTING INFORMATION

Additional supporting information can be found online in the Supporting Information section at the end of this article.

Molecular Oncology

FEBS PRESS
science publishing by scientists

Circulating exosomal *miR-363-5p* inhibits lymph node metastasis by downregulating *PDGFB* and serves as a potential noninvasive biomarker for breast cancer

Xin Wang[1], Tianyi Qian[1,2], Siqi Bao[3], Hengqiang Zhao[4,5], Hongyan Chen[6], Zeyu Xing[1], Yalun Li[7], Menglu Zhang[1], Xiangzhi Meng[1], Changchang Wang[1], Jie Wang[1], Hongxia Gao[1], Jiaqi Liu[1,5], Meng Zhou[3] and Xiang Wang[1]

1 Department of Breast Surgical Oncology, National Cancer Center/National Clinical Research Center for Cancer/Cancer Hospital, Chinese Academy of Medical Sciences and Peking Union Medical College, Beijing, China
2 Peking Union Medical College, Chinese Academy of Medical Sciences, Beijing, China
3 School of Biomedical Engineering, School of Ophthalmology & Optometry and Eye Hospital, Wenzhou Medical University, China
4 Department of Orthopedic Surgery, Peking Union Medical College Hospital, Peking Union Medical College and Chinese Academy of Medical Sciences, Beijing, China
5 Beijing Key Laboratory for Genetic Research of Skeletal Deformity, China
6 State Key Laboratory of Molecular Oncology, National Cancer Center/National Clinical Research Center for Cancer/Cancer Hospital, Chinese Academy of Medical Sciences and Peking Union Medical College, Beijing, China
7 Department of Breast Surgery, The Affiliated Yantai Yuhuangding Hospital of Qingdao University, China

Keywords
breast cancer; circulating exosome; lymph node metastasis; *miR-363-5p*; miRNA; PDGFB

Correspondence
J. Liu, Department of Breast Surgical Oncology, National Cancer Center/National Clinical Research Center for Cancer/Cancer Hospital, Chinese Academy of Medical Sciences and Peking Union Medical College, Beijing 100021, China
Tel: +086 158 102 633 54
E-mail: j.liu@cicams.ac.cn
M. Zhou, School of Biomedical Engineering, Wenzhou Medical University, Wenzhou 325027, China
Tel: +086 577 880 682 72
E-mail: zhoumeng@wmu.edu.cn
X. Wang, Department of Breast Surgical Oncology, National Cancer Center/National Clinical Research Center for Cancer/Cancer Hospital, Chinese Academy of Medical Sciences and Peking Union Medical College, Beijing 100021, China
Tel: +086 010 877 871 30
E-mail: xiangw@vip.sina.com

Sentinel lymph node (LN) biopsy is currently the standard procedure for clinical LN-negative breast cancer (BC) patients but it is prone to false-negative results and complications. Thus, an accurate noninvasive approach for LN staging is urgently needed in clinical practice. Here, circulating exosomal microRNA (miRNA) expression profiles in peripheral blood from BC patients and age-matched healthy women were obtained and analyzed. We identified an exosomal miRNA, *miR-363-5p*, that was significantly downregulated in exosomes from plasma of BC patients with LN metastasis which exhibited a consistent decreasing trend in tissue samples from multiple independent datasets. Plasma exosomal *miR-363-5p* achieved high diagnostic performance in distinguishing LN-positive patients from LN-negative patients. The high *miR-363-5p expression* level was significantly correlated with improved overall survival. Functional assays demonstrated that exosomal *miR-363-5p* modulates platelet-derived growth factor (PDGF) signaling activity by targeting PDGFB to inhibit cell proliferation and migration. Our study revealed, for the first time, plasma exosomal *miR-363-5p* plays a tumor suppressor role in BC and has the potential for noninvasive LN staging and prognosis prediction of BC.

Abbreviations
ALN, axillary lymph node; AUC, area under the curve; BC, breast cancer; cDNA, complementary DNA; CHCAMS, Chinese Academy of Medical Sciences; CI, confidence interval; DE, differentially expressed; DMEM, Dulbecco's modified Eagle's medium; ER, estrogen receptor; HR, hazard ratio; LN, lymph node; LNM, lymph node metastasis; mRNA, messenger RNA; miRNA, microRNA; NC, negative control; NTA, nanoparticle tracking analysis; PDGF, platelet-derived growth factor; rRNA, ribosomal RNA; ROC, receiver operating characteristic; SLNB, sentinel lymph node biopsy; TEM, transmission electron microscopy; TPM, total mapped reads.

Molecular Oncology **15** (2021) 2466–2479 © 2021 The Authors. Published by FEBS Press and John Wiley & Sons Ltd.

Xin Wang, Tianyi Qian and Siqi Bao
contributed equally to this study.

(Received 22 October 2020, revised 14 April
2021, accepted 28 May 2021, available
online 25 June 2021)

doi:10.1002/1878-0261.13029

---

1. Introduction

Breast cancer (BC) is the most common malignant tumor in females, with a global annual incidence of 266 120 (30%) and 40 920 (14%) deaths [1]. Axillary lymph node (ALN) metastasis is one of the most important independent risk factors of the prognosis of early BC [2]. Sentinel lymph node (LN) biopsy (SLNB) and ALN dissection are two major procedures for evaluation of ALN status and treatment of ALN metastasis. Currently, SLNB is recommended as the standard approach for ALN evaluation in clinically node-negative BC patients [3]. Although unnecessary axillary clearance procedures might be spared, sentinel LN could have a false-negative rate of 7.3%, which leads to patient under-treatment and causes an increased risk of recurrence [4,5]. Additionally, the presence of SLNB complications, especially lymphedema, is still inevitable. The incidence rate is 3.5% in BC patients who received SLNB alone without ALN dissection [6]. Thus, it is highly important to develop an accurate and non-invasive method to identify patients at low risk of ALN metastasis before surgery. Patients without ALN metastasis would benefit vastly if SLNB could be avoided safely using presurgery ALN status evaluation.

Exosomes are 30- to 100-nm microvesicles formed in multivesicular bodies and released into the extracellular environment by most cell types [7]. Abundant studies have shown that exosomes can serve as mediators of cell-to-cell communication by delivering cargo molecules, especially nucleic acids, that regulate the tumor microenvironment and promote cancer metastasis and progression [8–10]. Meanwhile, circulating exosomes of cancer patients were shown to have higher concentrations than in healthy individuals and are considered reliable markers in cancer diagnosis [11,12]. The circulating exosomes contain a large selection of messenger RNA (mRNA), microRNA (miRNA), long non-coding RNA, proteins and lipids [13–15]. The miRNA are small non-coding RNA that regulate the cellular process by suppressing target mRNA translation and are highly expressed in exosomes [16]. Recent studies have shown that exosomal miRNA exhibit essential biological effects on tumor metastasis [17,18]. In addition, there is growing evidence suggesting the potential role of exosomal miRNA in the early detection of cancer metastasis [13,19–21]. However, the relation between tumor-derived exosomal miRNA and the LN metastases in BC is still unclear. Biomarkers based on circulating exosomes for clinical applications are not well developed.

We conducted a prior study to investigate the potential use of circulating exosomal miRNA in the detection of LN metastasis (LNM). In this study, small RNA deep sequencing (RNA-seq) analysis was used, aiming to characterize the miRNA expression landscape in the circulating exosomes from BC patients. The candidate miRNA responsible for BC LNM were generated by comparing the miRNA expression difference between patients with or without LNM. Additionally, candidate miRNA were verified in multiple independent patient datasets. Furthermore, *in silico* and experimental studies were performed to identify potentially relevant target genes of the candidate miRNA in order to improve our understanding of mechanisms underlying the LNM in BC.

2. Materials and methods

2.1. Patient enrollment and sample preparation

All participants were enrolled through the Genetic Investigation of Inherited and Familial Tumor Syndrome study between January 2018 and June 2018 from the Cancer Hospital, Chinese Academy of Medical Sciences (CHCAMS). Patients were eligible for enrollment if they had an evident histologic diagnosis of BC and no distant metastasis. The positive estrogen receptor (ER) was defined as more than 1% of tumor cells staining positive for ER proteins. The HER2-

positive cells were defined as tumor cells that stain strongly (3+) for ERBB2 protein or in which the ERBB2 gene was amplified. Age-matched healthy women were recruited as a control group. Peripheral blood samples of 10 mL from these BC patients and 10 age-matched healthy women were collected at CHCAMS. Blood samples were collected in vacuum tubes with EDTA and centrifuged at 3000 ***g*** for 15 min at 4 °C. The collected supernatant (5 mL plasma) was preserved at −80 °C before use. This study was conducted in accordance with the Declaration of Helsinki. All participants signed a written informed consent. Ethics approval for the study was obtained from the Research Ethics Committee of CHCAMS. Two independent BC datasets with miRNA profiles and clinical data were from UCSC Xena Browser (TCGA, http://xena.ucsc.edu/public; n = 1044) [22] and Gene Expression Omnibus (GEO, accession number GSE38167, https://www.ncbi.nlm.nih.gov/geo/query/acc.cgi?acc=GSE38167; n = 31) [23].

2.2. Exosome isolation

The collected plasma was thawed at 37 °C and then centrifuged at 3000 ***g*** for 15 min to remove cell debris. Aspirated supernatant was diluted sevenfold with PBS and centrifuged at 13 000 ***g*** for 30 min [24]. Large particles were removed using 0.22-µm filters. The collected supernatant was then ultra-centrifuged at 100 000 ***g***, 4 °C for 2 h (CP100NX; Hitachi, Brea, CA, USA). The pellet containing exosomes was re-suspended in PBS and ultra-centrifuged again at 100 000 ***g*** 4 °C for 2 h. The isolated exosomes were re-suspended in 100 µL PBS after PBS washing for further analysis.

2.3. Exosome characterization

The nanoparticle tracking analysis (NTA), transmission electron microscopy (TEM) and western blot analysis using rabbit polyclonal antibody CD63, TSG101 and calnexin were conducted following the previously reported protocols [25].

2.4. Exosomal RNA isolation and RNA analyses

The RNA were extracted from plasma-isolated exosomes using the miRNeasy® Mini kit (Qiagen, cat. No. 217004, Shanghai, China). RNA yields, as well as DNA contamination, were monitored on a 1.50% agarose gel. The NanoDrop 2000 spectrophotometer (ThermoFisher Scientific, Wilmington, DE, USA) was used to assess RNA concentration and purity. The integrity and distribution of RNA were analyzed using the Agilent Bioanalyzer 2100 system with RNA Nano 6000 Assay Kit (Agilent Technologies, Palo Alto, CA, USA).

2.5. Library preparation and sequencing

A total amount of 5 ng RNA per sample was depleted of ribosomal RNA (rRNA) using the RiboZero magnetic kit (Epicentre, Madison, WI, USA). Sequencing libraries were then generated using the Ovation® RNA-Seq System (NuGEN, San Carlos, CA, USA). A total amount of 2.5 µg RNA per sample was used as input material for sample preparation of small RNA libraries. The libraries were generated using the NEB Next Multiplex Small RNA Library Prep Set for Illumina (NEB, Ipswich, MA, USA). The index codes were added to attribute sequences to each sample. Finally, the PCR products were purified using the Agencourt AMPure XP system (Beckman Coulter, Brea, CA, USA). The library quality was evaluated on an Agilent Bioanalyzer 2100 (Agilent Technologies) and quantitative PCR. The cluster of the index-coded samples was generated by the acBot Cluster Generation System using TruSeq PE Cluster Kitv3-cBot-HS (Illumina, San Diego, CA, USA). At last, the sequencing was performed on the Illumina HiSeq platform using the library preparations and paired-end reads were generated.

2.6. Quantitative differential expression analysis of miRNA

The sequence alignment was performed using the Bowtie tool [26] with several databases, including the Silva database (https://www.arb-silva.de/), the GtRNAdb database (http://gtrnadb.ucsc.edu/), the Rfam database (http://rfam.sanger.ac.uk/) and the Repbase database (http://www.girinst.org/) [27]. Subsequently, the rRNA, transfer RNA, small nuclear RNA, small nucleolar RNA, and other non-coding RNA were filtered. The miRNA, including known miRNA and novel miRNA, were detected using the remaining reads, in which the novel miRNA were predicted according to the miRbase database and Human Genome (GRCh38), respectively. Read counts of the miRNA were generated from the mapping results and have been standardized as the total mapped reads (TPM) per million. Circulating exosomal miRNA profiles of samples with two conditions were compared using the two-tailed Student's t-test, and each miRNA with a $\log_2|\text{fold change}| > 0.58$ and $P < 0.05$ was considered a differential expression. Hierarchical clustering was performed with R package 'pheatmap' using the ward.D2 method using R statistical software, version 3.5.1 (R Foundation for Statistical Computing, Vienna, Austria).

2.7. Cell culture and transfection

The MCF-7 cell line was cultured at 37 °C with 5% CO_2. Dulbecco's modified Eagle's medium (DMEM, SH30022.01; HyClone, South Logan, UT, USA) with 10% FBS (FND500, ExCell Bio., Shanghai, China) was applied as a culture medium. In addition, 100 units per milliliter penicillin and 100 $\mu g \cdot mL^{-1}$ streptomycin (SV30010, HyClone, Logan, UT, USA) were added to DMEM. Until the density reached approximately 50–70%, cells were transfected for 48 h with *miR-363-5p* mimic, mock negative control (NC), *miR-363-5p* inhibitor or inhibitor NC (Ribo, Guangzhou, China) using Lipofectamine 2000 (Invitrogen, Carlsbad, CA, USA).

2.8. RNA extraction and quantification

The miRNA was extracted from MCF-7 cells with the miRcute miRNA isolation kit (DP501, Tiangen, Beijing, China). Total RNA was extracted from transfected MCF-7 cells with the total RNA rapid extraction kit (220010, Feijie Biological, Shanghai, China). After quality control, the FastQuant RT kit (KR106, Tiangen, Beijing, China) was used to reverse transcribe the miRNA or RNA sample into complementary DNA (cDNA). qRT-PCR was performed in an ABI 7300 real-time PCR system (Applied Biosystems, Foster City, CA, USA). SuperReal PreMix Plus (SYBR Green) mixture (FP205; Tiangen) was applied for reactions. The relative amounts of *miR-363-5p* to control *U6* and platelet-derived growth factor *B* (*PDGFB*) to control GAPDH transcripts were analyzed by the $2^{-\Delta\Delta Ct}$ method. Primers applied were listed as follows: *miR-363-5p*: forward: 5′-CGGGTGGATCACGATG-3′; reverse: 5′-CAGTGCAGGGTCCGAGGTAT-3′; U6: forward: 5′-CTCGCTTCGGCAGCACA-3′; reverse: 5′-AACGCTTCACGAATTTGCGT-3′ [28].

2.9. Cell proliferation assay

The MCF-7 cells were planted in 96-well plates with a density of 5×10^3 cells per well. The proliferation of cells at 0, 24, 48 and 72 h after transfection was examined using the CCK-8 proliferation assay kit (MA2018-L, Meilunbio, Dalian, China). At every time phase, 10 µL of CCK-8 reagent was added to the medium. Absorbance at 450 nm was measured after 3 h of incubation using a microplate spectrometer reader (Molecular Devices, San Jose, CA, USA).

2.10. Transwell migration assay and colony formation assay

After transfection with *miR-363-5p* or NC for 48 h, MCF-7 cell was washed twice with FBS-free medium, and then re-suspended in FBS-free medium at a density of 1×10^5 $cells \cdot mL^{-1}$. Transwell chamber (pore size 8.0 µm, 3422; Corning Costar, Cambridge, MA, USA) pretreated with the FBS-free medium was placed in a 24-well plate. After removing the pretreatment medium, 600 µL 10% FBS-containing medium was added to the lower chamber and a 100-µL cell suspension to the upper chamber was added with. After incubating for 48 h, the chambers were fixed and stained with methanol and 0.2% crystal violet. After staining, cells on the chamber surface were removed carefully with water and cotton swabs. The number of perforated cells in the outer layer of the basement membrane of each chamber (migrating cells) was counted in five random high-power fields with a phase-contrast microscope (NIB-100F, Nanjing Jiangnan Novel Optics, Nanjing, China).

Cell proliferation capacity was evaluated with colony formation assay using the protocol previously described by Liu *et al.* [29]. After transfection with *miR-363-5p* or NC for 48 h, MCF-7 cells were seeded in 24-well microplates with approximately 2000 cells per well. After adherent growth of 48 h, the cells were stained with crystal violet solution after methanol fixation and counted using IMAGEJ software (NIH, Bethesda, MA, USA). Three parallel experiments were conducted. The results were normalized using the proliferation data to minimize confounding.

2.11. Statistical analysis

Analyses were performed with R Statistical Software (version 3.5.3). Pre-set $P < 0.05$ was defined as statistically significant. Quantitative data were measured as mean ± standard deviation. The comparison of mean values between the two groups was analyzed using Student's *t*-test and Mann–Whitney *U*-test. Pearson's test was used to evaluate the exosome-tissue miRNA correlation and miRNA-target mRNA correlation. Receiver operating characteristic (ROC) curve analysis was used to determine the diagnostic performance, and the area under the curve (AUC) was calculated with the R package 'ROCit' [30]. The Kaplan–Meier method and log-rank test were applied to compare survival differences and the hazard ratio (HR) and 95% confidence interval (CI) were calculated using the R package 'Survival'.

3. Results

3.1. Characterization of exosomes from the plasma of breast cancer patients

In this study, 10 BC (Luminal-like) patients and 10 age-matched healthy women were enrolled. Clinical information about the patients is listed in Table 1. Ten BC patients were further divided into two groups according to their LN status, namely, four patients with LNM and six patients without LNM. Blood samples were collected from both BC patients and healthy controls. The integrity of exosome preparation was confirmed with TEM followed by western blot. The exosomes isolated from the plasma exhibited the classic cup-shaped morphology under TEM (Fig. S1A). Exosome markers *TSG101* and *CD63* expression were detected from the exosome isolated from the plasma (Fig. S1B). The NTA indicated that the average size of the vesicles was 105.7 nm and the main peak of particle diameter was at 85.5 nm (Fig. S1C). The results mentioned above demonstrated that the extracellular vesicles isolated from plasma samples are purified exosomes.

3.2. RNA-seq identified dysregulated exo-miRNA in breast cancer patients

To identify exo-miRNA that play a pivotal role in inducing BC LNM, circulating exosomal miRNA was isolated and profiled using small RNA deep sequencing analysis. A total of 1631 miRNA were mapped in exosomes isolated from plasma samples. To minimize noise and improve accuracy, the miRNA with TPM values of less than five were removed, leaving 367 miRNA for further analysis. Through differential expression analysis, 43 significantly differentially expressed (DE) miRNA were identified in breast tumor exosomes and seven significantly DE miRNA in breast tumor exosomes with LN-positive status. Figure 1A shows a different expression pattern of the 43 DE miRNA between BC patients and healthy controls. Figure 1B shows a different expression pattern of the seven DE miRNA between BC patients with and without LNM.

3.3. Identification of circulating exosomal *miR-363-5p* as a potential biomarker of axillary lymph node metastasis and prognosis

Integrative profiles analysis indicated that the aberrant expression of exosomal *miR-363-5p* is significantly associated with both BC (P = 0.047, Mann–Whitney U-test) and ALN metastasis (P = 0.019, Mann–Whitney U-test; Fig. 2A,B). Exosomal *miR-363-5p* expression was significantly higher in BC patients compared with healthy controls and was significantly lower in LN-positive patients compared with LN-negative patients (Fig. 2B). Since the miRNA concentration in exosomes is distinctively related to its cellular abundance [31], we also hypothesized that reliable circulating markers should coordinate with their expression alterations in tumor tissues. To verify the reliability of *miR-363-5p*, the expression levels of *miR-363-5p* in tumor tissues with and without LN were compared in two external independent patient datasets. The exosomal *miR-363-5p* exhibited a consistent expression trend in tissue samples, as observed in plasma samples (Fig. 2C). As shown in Fig. 2C, the expression level of *miR-363-5p* is significantly lower in LN-positive patients than those without LN both in TCGA

Table 1. Clinical information of BC patients used in the exosomal cohort. All patients were pathologically diagnosed with ER^+HER2^- stage I–II IDC or DCIS, according to the BC biologic subtype and TNM anatomic stage classification from AJCC UICC (8th edition). AJCC, The American Joint Committee on Cancer; IDC, invasive ductal carcinoma; DCIS, ductal carcinoma *in situ*; M, metastasis; N, lymph node; T, tumor; UICC, Union for International Cancer Control.

Patient	Gender	Age at diagnosis	Histology	Subtype	T stage	N stage	M stage	Stage	LN
A07-05	F	63	IDC	ER^+HER2^-	1c	1a	0	IIA	1/22
A07-07	F	49	IDC	ER^+HER2^-	1b	2a	0	IIA	2/24
A07-08	F	53	IDC	ER^+HER2^-	1c	0(sn)	0	IA	0/6
A07-09	F	67	IDC	ER^+HER2^-	2	0(sn)	0	IIA	0/5
A07-10	F	38	IDC	ER^+HER2^-	2	0(sn)	0	IIA	0/5
A07-11	F	55	DCIS	ER^+HER2^-	is	0(sn)	0	0	0/4
A07-12	F	57	IDC	ER^+HER2^-	1b	1a	0	IIA	1/23
A07-14	F	59	IDC	ER^+HER2^-	1c	0(sn)	0	IA	0/5
A07-17	F	64	IDC	ER^+HER2^-	2	0(sn)	0	IIA	0/6
A07-18	F	44	IDC	ER^+HER2^-	1c	1a	0	IIA	1/24

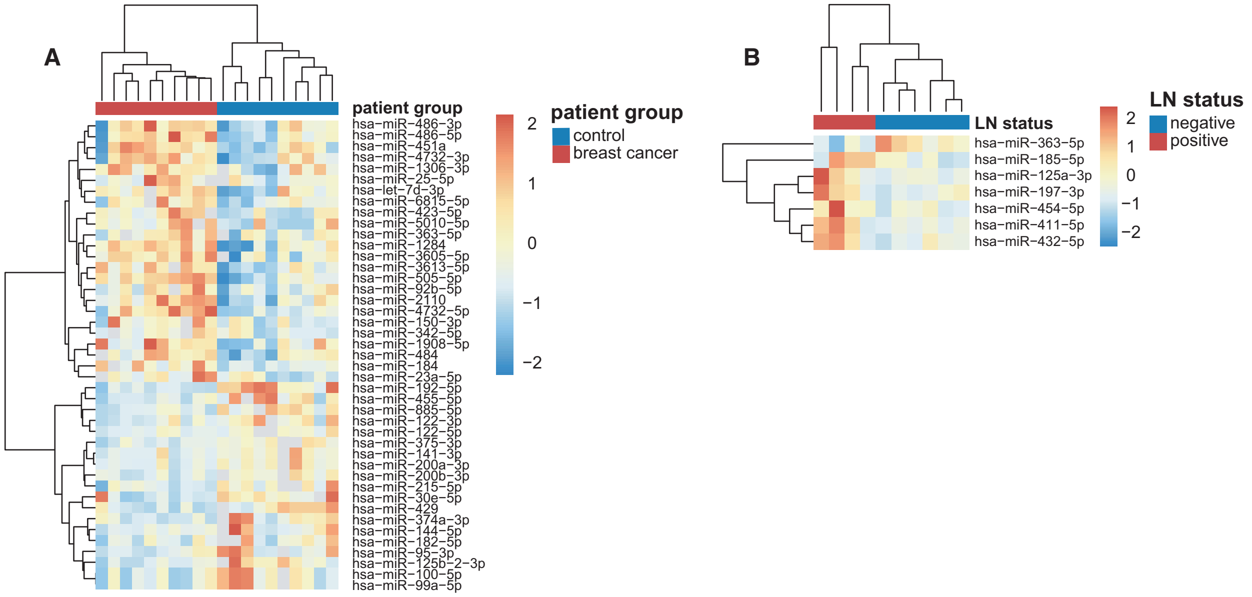

Fig. 1. Expression pattern of miRNA in plasma exosomes from BC patients. Heatmap depicting unsupervised hierarchical clustering based on the RNA sequencing expression values of DE plasma exosomal miRNA among BC patients and healthy individuals (A) and BC patients with positive LN and negative LN (B). DE miRNA were filtered by Student's *t*-test ($P < 0.05$) with fold change > 1.5 | < 0.67.

($P = 0.014$, Mann–Whitney *U*-test) and GSE38167 ($P = 0.013$, Mann–Whitney *U*-test) datasets. Further association analysis showed that a significant expression difference of miR-363 exists exclusively in ER^+ BC (Fig. S2), which is consistent with the subtype of in-house samples. We subsequently profiled the matched expression levels of the miRNA in tumor tissue of 10 BC patients using qRT-PCR. *MiR-363-5p* expression in LN-negative BC tissue samples was significantly higher compared with LN-positive patients ($P = 0.019$, Mann–Whitney *U*-test; Fig. 2D). In addition, our in-house data showed the exosomal concentrations of *miR-363-5p* correlated with its expression in tumor tissue (Pearson's $r = -0.679$ and $P = 0.0307$, Fig. 2E). Additionally, *miR-363-5p* expression in BC tissue was significantly higher than matched paratumor tissue (Fig. S3), which also consists with circulating exosomal expressions. These validation analyses indicated that *miR-363-5p* is a potential and stable noninvasive biomarker for further investigation.

3.4. Performance evaluation and validation of *miR-363-5p* in the in-house and multiple independent datasets

To evaluate retrospectively the predictive power of exosomal *miR-363-5p* to detect LNM, we performed ROC analysis and found that the *miR-363-5p* achieved high diagnostic performance with an AUC of 0.958 for the in-house dataset and 0.733 for the GSE38167 dataset, respectively (Fig. 3A,B). These results indicated that low *miR-363-5p* expression levels might serve as a potential biomarker for noninvasive LN staging of BC LNM. Furthermore, we assessed the association between *miR-363-5p* expression level and survival of BC patients and found that patients with low expression of *miR-363* had significantly worse overall survival (HR = 0.63, 95% CI 0.45–0.89; $P = 0.0075$, log-rank test; Fig. 3C). Moreover, in patients with negative LN upon the first diagnosis, low expression of *miR-363* in primary tumors correlated with a significantly worse outcome (HR = 0.23, 95% CI 0.09–0.60; $P = 0.00094$, log-rank test; Fig. 3D). Multivariate survival analysis using the proportional hazards model indicated that a high expression level of *miR-363* could serve as a protective prognostic marker of BC survival (HR = 0.58, $P = 0.043$, Fig. 3E).

3.5. *miR-363-5p* inhibits metastatic properties of breast cancer cell

The *miR-363-3p* and *miR-363-5p* (*miR-363**) are both mature forms of *miR-363*. Previous studies have focused on the biological function and pathophysiological significance of *miR-363-3p* but few have explored the role of *miR-363-5p*, possibly because of its relatively low abundance compared with *miR-363-3p*. To investigate the role of circulating exosomal *miR-363-5p*

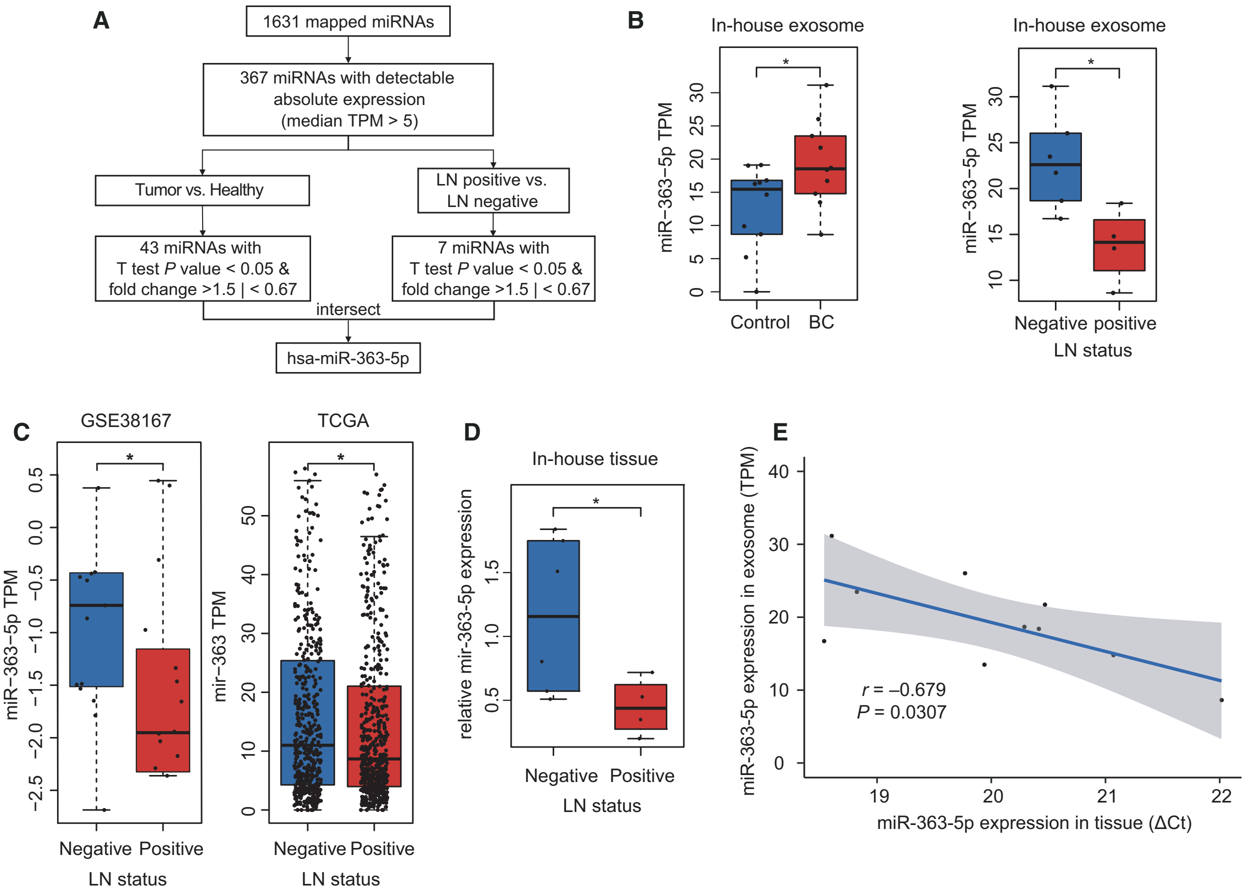

Fig. 2. The*miR-363-5p* is down-regulated in circulating exosome and tumor tissue of BC patients with positive LN. (A) Workflow of the filtration procedures used in identifying the potential markers. (B) Exosomal *miR-363-5p* expression pattern of in-house circulating exosome dataset, $*P < 0.05$ by unpaired Student's *t*-test. (C) The presence of LNM at diagnosis is associated with lower expression of *miR-363-5p* in BC tissues in public datasets. $*P < 0.05$ determined by the Mann–Whitney *U-test*. (D) In-house expression levels of *miR-363-5p* in BC tissues were determined using qRT-PCR, $*P < 0.05$ by unpaired Student's *t*-test. (E) The *miR-363-5p* in circulating exosome displayed consistent expression in matched tumor tissues. Pearson's correlation analysis was applied.

in BC progression, we hypothesized that *miR-363-5p* influences BC cell mobility. To keep the consistency of the sample subtype, we selected an ER-positive BC cell line MCF-7 and transfected BC cells with plasmids overexpressing *miR-363-5p* or NC. The results indicated that the overexpression of *miR-363-5p* significantly suppresses the migration (Fig. 4A,B), invasion (Fig. 4C–E), proliferation (Fig. 4F) and colony formation (Fig. 4G,H) of MCF-7 cells.

3.6. Exosomal *miR-363-5p* modulates platelet-derived growth factor signaling activity by targeting *PDGFB*

To identify reliable targets of *miR-363-5p*, we utilized both experimentally validated miRNA-target interaction databases and co-expression analysis (Fig. 5A). We analyzed miRNA and mRNA expression profiles of the TCGA BC dataset which yielded four mRNA

Fig. 3. Performance evaluation of *miR-363-5p* as a noninvasive predictor of LNM and prognosis. (A,B) The ROC curve of the *miR-363-5p* for BC LNM using in-house circulating exosomal miRNA data and public tissue expression data (GSE38167). (C,D) Kaplan–Meier survival analysis for all TCGA BC patients (C) and patients with negative LN upon first diagnosis (D). Statistical significance was determined by the log-rank test. (E) Multivariate proportional-hazards model showed survival impact of *miR-363-5p* along with clinical characteristics for TCGA BC patients. The result showed 95% CI of risk of mortality. $***P < 0.001$, $**P < 0.01$ and $*P < 0.05$ determined by Cox proportional hazards model.

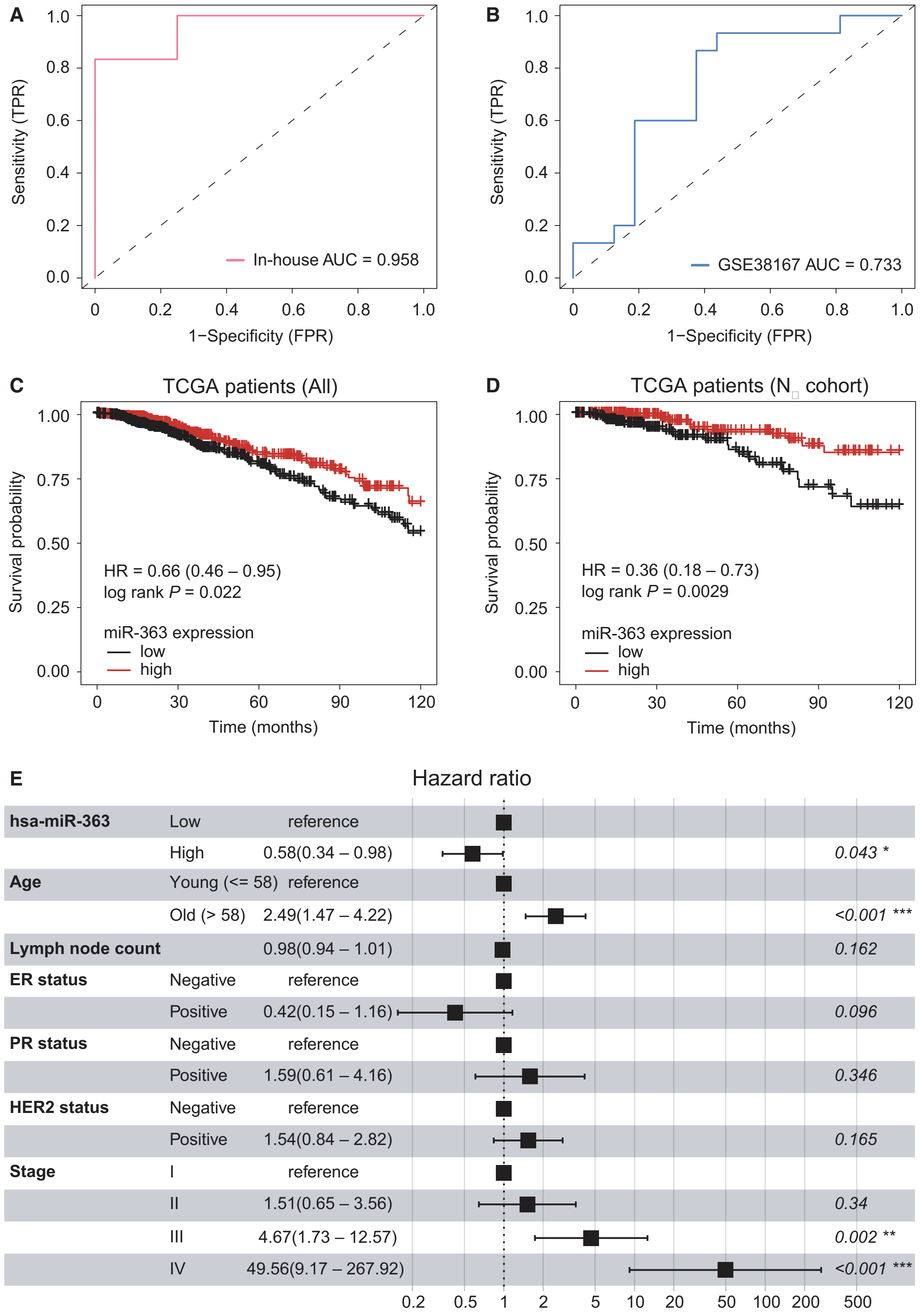
A
Sensitivity (TPR)
1−Specificity (FPR)
In-house AUC = 0.958
0 0.2 0.4 0.6 0.8 1.0
B
Sensitivity (TPR)
1−Specificity (FPR)
GSE38167 AUC = 0.733
C
TCGA patients (All)
Survival probability
Time (months)
1.00 0.75 0.50 0.25 0.00
0 30 60 90 120
HR = 0.66 (0.46 – 0.95)
log rank P = 0.022
miR-363 expression
low
high
D
TCGA patients (N cohort)
Survival probability
Time (months)
HR = 0.36 (0.18 – 0.73)
log rank P = 0.0029
miR-363 expression
low
high
E
Hazard ratio
hsa-miR-363 Low reference
High 0.58(0.34 – 0.98) 0.043 *
Age Young (<= 58) reference
Old (> 58) 2.49(1.47 – 4.22) <0.001 ***
Lymph node count 0.98(0.94 – 1.01) 0.162
ER status Negative reference
Positive 0.42(0.15 – 1.16) 0.096
PR status Negative reference
Positive 1.59(0.61 – 4.16) 0.346
HER2 status Negative reference
Positive 1.54(0.84 – 2.82) 0.165
Stage I reference
II 1.51(0.65 – 3.56) 0.34
III 4.67(1.73 – 12.57) 0.002 **
IV 49.56(9.17 – 267.92) <0.001 ***
0.2 0.5 1 2 5 10 20 50 100 200 500

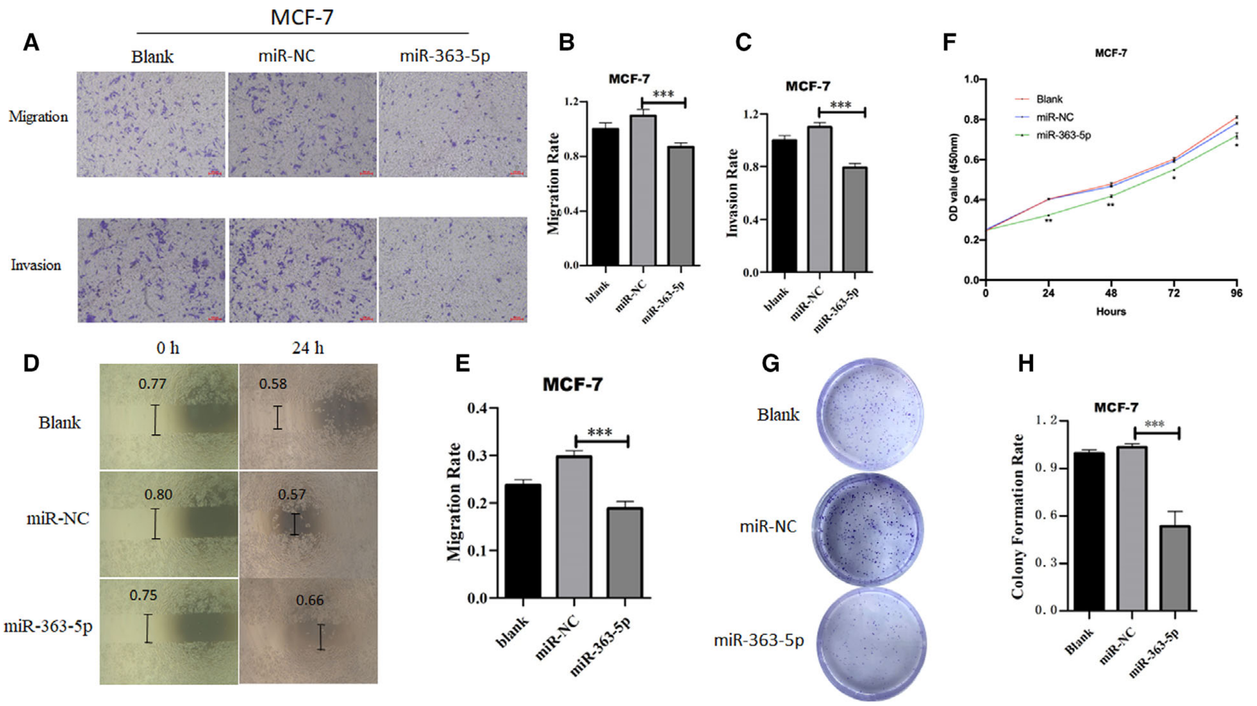

Fig. 4. The*miR-363-5p* inhibits metastatic properties of the BC cell. (A–C) Transwell migration assay and invasion assay of MCF-7 cells transfected with *miR-363-5p*-mimic or normal control (NC). Migrated cells were counted using ImageJ and representative images are shown. (D,E) Wound healing assay of MCF-7 transfected with *miR-363-5p*-mimic or NC. (F) Proliferation abilities of MCF-7 transfected with *miR-363-5p*-mimic or NC were detected via CCK-8 assay. (G,H) Colony formation assay of MCF-7 transfected with *miR-363-5p*-mimic or NC. Experiments were performed in triplicate and repeated three times with similar results. Scale bar: 20 μm. Results are shown as mean ± SE. ***$P < 0.001$, **$P < 0.01$ and *$P < 0.05$ determined by Student's *t*-test.

co-expressed with *miR-363-5p* based on the negative regulation of target gene expression and miRNA level. We also retrieved gene lists of experimentally established targets of *miR-363-5p* from two databases (mirTarbase and Tarbase). We merged the results from two databases, producing a list of 234 target genes. Among them, the *PDGFB* oncogene was the only one exhibiting a significant negative correlation (Pearson's $r = -0.208$, $P < 0.001$) with the *miR-363-5p* level in BC tissues from TCGA (Fig. 5B). The target location (Fig. 5C) was produced in the previous study and validated using PAR-CLIP [32]. These implied that the *PDGFB* oncogene might be a potential functional target of *miR-363-5p*. We, therefore, performed qRT-PCR for validation. Consistent with the bioinformatics analysis, qRT-PCR and western blot analysis also showed that the expression levels of *PDGFB* mRNA and protein were significantly downregulated by *miR-363-5p* overexpression, which is subsequently rescued by *miR-363-5p* knockdown as well (Fig. 5D,E). These findings indicated that *miR-363-5p* regulates *PDGFB* oncogene expression in BC. The *miR-363-5p* deficiency promoted metastasis via facilitating *PDGFB* expression, leading to the overactivity of PDGF signaling in cancer cells.

4. Discussion

Assessment of miRNA expression signatures in exosomes is a promising tool for cancer research and clinical diagnosis. In this study, we report the different miRNA signatures and identified several deregulated miRNA in BC patients with ALN metastasis compared with those without ALN metastasis. We identified that the level of exosomal *miR-363-5p* in ALN-positive BC patients was significantly lower than that in ALN-negative patients.

Evaluation of miRNA expression in tumor tissues is necessary, as the parallel down-regulation acts as the logical foundation of a tumor-derived diagnostic marker and is indispensable for mechanism interpretation. We investigated the *miR-363-5p* level in BC tissue of both in-house patients and external datasets. The results were consistent with that of plasma exosomes. Those patients who were diagnosed with LN-positive BC had a significantly lower level of *miR-363-5p*.

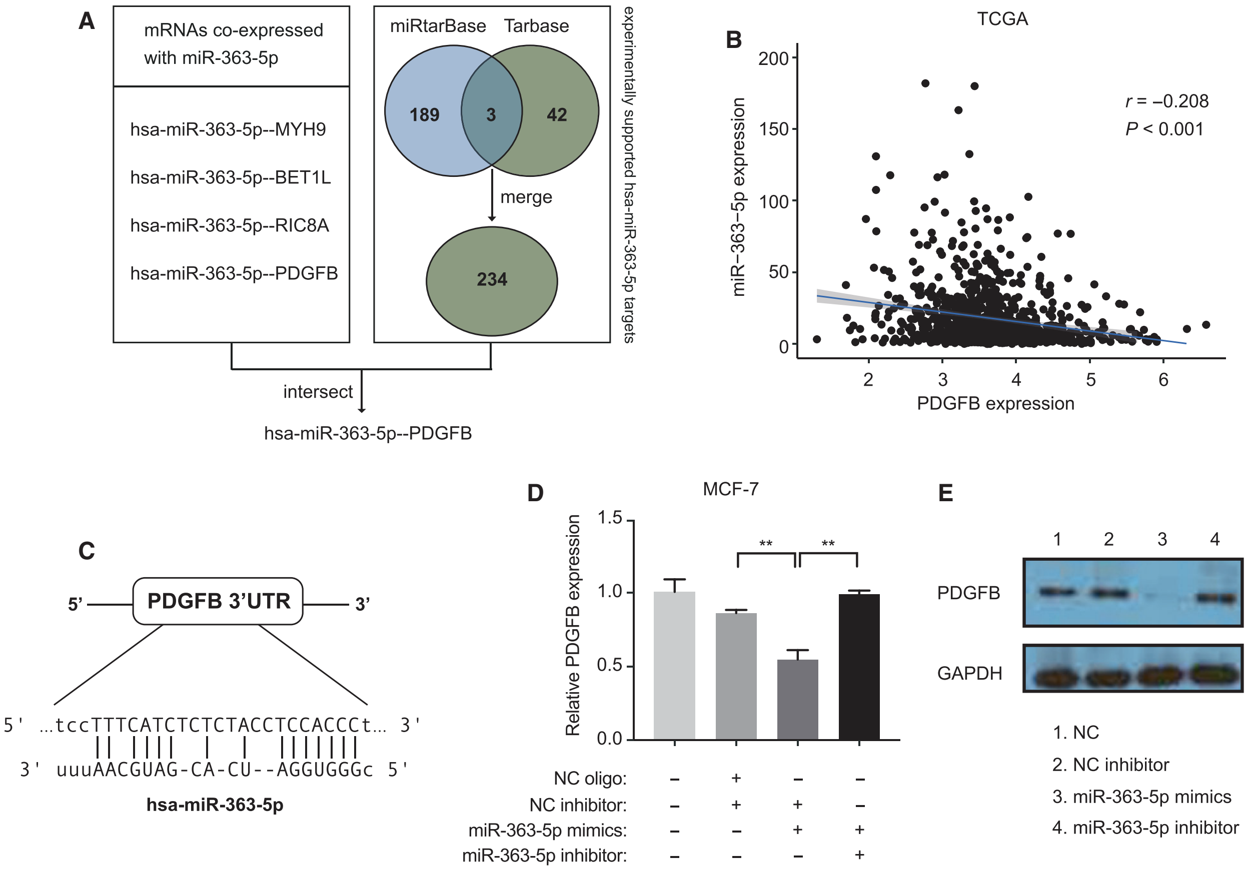

Fig. 5. The *miR-363-5p* suppresses *PDGFB* expression by binding to its 3′-UTR. (A) The strategy is applied in target identification. (B) A negative correlation between *miR-363-5p* expression and *PDGFB* mRNA levels in BC tissues was analyzed using Pearson's correlation analysis. (C) The *miR-363-5p* binding sequences in *PDGFB* 3′-UTR. (D) qRT-PCR. (E) Western blot assay of *PDGFB* expression level of MCF-7 transfected with *miR-363-5p*-mimic, *miR-363-5p*-inhibitor or normal control. Experiments were performed in triplicate and repeated three times with similar results. Results are shown as mean ± SE. ***P* < 0.01 determined by Student's *t*-test.

These results indicated that deregulated exosomal *miR-363-5p* level is associated with transcriptional changes in primary tumor tissue. These changes contribute substantially to LNM in BC.

We performed an *in silico* diagnostic test and verified that *miR-363-5p* alone has an AUC of 0.733–0.958 in predicting LNM in multiple independent datasets. Previous studies have shown that imaging approaches, namely, axillary ultrasound and MRI, perform similarly performance ALN staging; the AUC of MRI alone was 0.665 [33,34]. We consider that exosomal *miR-363-5p* can help elevate the accuracy of clinical prediction models if taken into consideration. Furthermore, survival analysis revealed that patients with lower *miR-363-5p* have a significantly worse prognosis, especially in node-negative patients at their initial diagnosis, suggesting that patient stratification using *miR-363-5p* can help distinguish individuals with a high risk of BC death. Node-negative patients with low *miR-363-5p* levels might consider adjuvant endocrine therapy.

In this study, we also investigated the functional significance of *miR-363-5p*. We found that restoration of *miR-363-5p* using mimics significantly inhibited BC cell migration, while it did not appear to affect proliferation. Studies have revealed that low *miR-363* expression is associated with carcinogenesis and metastasis [35,36]. Overexpression of *miR-106a-363* cluster (*miR20b*, *miR-363-3p* and *miR-363-5p*) exhibited an anti-proliferative effect on cancer cells [37]. This indicated that *miR-363-5p* would impact the migration ability instead of the proliferation. In combination with the data of this study, we hypothesized that miR-363 with its mature forms could cause opposite effects on cell proliferation and migration. The expression level of miR-363 may be upregulated during tumorigenesis, which is associated with increased proliferation in early cancer. Whereas miR-363 was downregulated during metastasis formation along with the phenotype switch from proliferation to migration, the anti-migration effect of *miR-363-5p* is likely transmitted by circulating exosomes secreted by the primary tumor. Our previous study constructed a prognosis model of node-negative patients, based mainly on receptor status and tumor size [38]. The miRNA signature can provide distinct tumor information on the tumor's cellular and molecular characteristics and would increase the accuracy of clinical prediction models. Our functional study supported *miR-363-5p* as a specific complementary predictor for LNM as well as patient prognosis.

It has been reported that *miR-363-5p* modulates endothelial cell-specific genes, including angiocrine factors [39], which is consistent with our results. We found that *miR-363-5p* regulates *PDGFB* by binding to its 3′-UTR, which inhibits the activation of PDGF/PDGFR-related pathways. It is reported that the metastatic potential of mammary epithelial cells depends on the PDGF-PDGFR loop [40]. PDGF autocrine activates *STAT1* and other pathways, contributing to the induction and maintenance of the EMT in BC. *PDGFB* and dimer protein PDGF-BB is an important lymphangiogenic factor and contributes to cancer lymphatic metastasis by stimulating MAP kinase activity [41,42]. *PDGFB* exhibited both proliferative and chemotactic effects on lymphatic endothelial cells and directly caused lymphatic metastasis in BC-bearing mice [43]. In summary, *miR-363-5p*/*PDGFB* might play a pivotal role in BC carcinogenesis and progression, especially related to LN staging. Furthermore, *miR-363-5p* might represent a relatively downstream element in a complicated regulation network; however, the different pathways involved in this process require further exploration.

Nevertheless, this study has several limitations. First, the present study only included ER^+ $HER2^-$ patients, and further verification is necessary for other molecular types. Secondly, the sample size of our discovery cohort is relatively small. However, the potential significance of the exosomal *miR-363-5p* in BC LNM has been shown.

5. Conclusion

In conclusion, our study identified exosome miRNA markers that help evaluate LN status in a noninvasive manner. Exosomal *miR-363-5p* showed good accuracy and was confirmed with a functional and molecular basis. These results indicate that exosomal *miR-363-5p* may be applicable in developing liquid biopsy strategies to diagnose LNM in BC effectively.

Ethics approval and consent to participate

All participants signed a written informed consent. Ethics approval for the study was obtained from the Research Ethics Committee of CHCAMS (reference number: NCC2017G-075).

Acknowledgements

We thank all the individuals, families, and physicians involved in the study for their participation. We thank the nurses from the Department of Breast Surgical Oncology of CHCAMS for assistance with patient enrollment. We thank Echo Biotech Co., Ltd, Beijing, P. R. China, for plasma exosome RNA-seq, helpful discussions and bioinformatics analysis. This research was funded in part by the National Natural Science Foundation of China (81802669 to JL), the CAMS Initiative Fund for Medical Sciences (2016-I2M-1-001 to Xiang Wang and 2017-I2M-3-004 to Xin Wang), and Zhejiang Provincial Natural Science Foundation of China (LY21C060004 to MZ).

Conflict of interest

The authors declare no conflict of interests.

Data accessibility

The datasets generated during the current study are not publicly available as the informed consent does not cover open data disclosure. Access to the data is available from the corresponding author on reasonable request according to approval from the ethical and data protection board.

Author contributions

Xin Wang established the study concept and coordinated laboratory assays. TQ, MZ and SB wrote the manuscript with support from Xin Wang, HC and JL. SB and HZ performed bioinformatics analysis. HC supervised laboratory assays. ZX, YL, XM, CW, JW and HG performed and supervised sample collection. JL coordinated the research. MZ and Xiang Wang contributed to the design and implementation of the research. All authors contributed to data interpretation, and read and approved the final manuscript.

References

1 Siegel RL, Miller KD & Jemal A (2018) Cancer statistics, 2018. *CA Cancer J Clin* **68**, 7–30.

2 Carter CL, Allen C & Henson DE (1989) Relation of tumor size, lymph node status, and survival in 24,740 breast cancer cases. *Cancer* **63**, 181–187.

3 Lyman GH, Somerfield MR, Bosserman LD, Perkins CL, Weaver DL & Giuliano AE (2017) Sentinel lymph node biopsy for patients with early-stage breast cancer: American Society of Clinical Oncology Clinical Practice Guideline Update. *J Clin Oncol* **35**, 561–564.

4 Kim T, Giuliano AE & Lyman GH (2006) Lymphatic mapping and sentinel lymph node biopsy in early-stage breast carcinoma: a metaanalysis. *Cancer* **106**, 4–16.

5 Pesek S, Ashikaga T, Krag LE & Krag D (2012) The false-negative rate of sentinel node biopsy in patients with breast cancer: a meta-analysis. *World J Surg* **36**, 2239–2251.

6 Langer I, Guller U, Berclaz G, Koechli OR, Schaer G, Fehr MK, Hess T, Oertli D, Bronz L, Schnarwyler B *et al.* (2007) Morbidity of sentinel lymph node biopsy (SLN) alone versus SLN and completion axillary lymph node dissection after breast cancer surgery: a prospective Swiss multicenter study on 659 patients. *Ann Surg* **245**, 452–461.

7 Théry C, Zitvogel L & Amigorena S (2002) Exosomes: composition, biogenesis and function. *Nat Rev Immunol* **2**, 569–579.

8 Luga V, Zhang L, Viloria-Petit AM, Ogunjimi AA, Inanlou MR, Chiu E, Buchanan M, Hosein AN, Basik M & Wrana JL (2012) Exosomes mediate stromal mobilization of autocrine Wnt-PCP signaling in breast cancer cell migration. *Cell* **151**, 1542–1556.

9 Mu W, Rana S & Zoller M (2013) Host matrix modulation by tumor exosomes promotes motility and invasiveness. *Neoplasia* **15**, 875–887.

10 Peinado H, Alečković M, Lavotshkin S, Matei I, Costa-Silva B, Moreno-Bueno G, Hergueta-Redondo M, Williams C, García-Santos G, Ghajar C *et al.* (2012) Melanoma exosomes educate bone marrow progenitor cells toward a pro-metastatic phenotype through MET. *Nat Med* **18**, 883–891.

11 Huang X, Yuan T, Liang M, Du M, Xia S, Dittmar R, Wang D, See W, Costello BA, Quevedo F *et al.* (2015) Exosomal miR-1290 and miR-375 as prognostic markers in castration-resistant prostate cancer. *Eur Urol* **67**, 33–41.

12 Melo SA, Luecke LB, Kahlert C, Fernandez AF, Gammon ST, Kaye J, LeBleu VS, Mittendorf EA, Weitz J, Rahbari N *et al.* (2015) Glypican-1 identifies cancer exosomes and detects early pancreatic cancer. *Nature* **523**, 177–182.

13 An T, Qin S, Xu Y, Tang Y, Huang Y, Situ B, Inal JM & Zheng L (2015) Exosomes serve as tumour markers for personalized diagnostics owing to their important role in cancer metastasis. *J Extracell Vesicles* **4**, 27522.

14 Sun J, Zhang Z, Bao S, Yan C, Hou P, Wu N, Su J, Xu L & Zhou M (2020) Identification of tumor immune infiltration-associated lncRNA for improving prognosis and immunotherapy response of patients with non-small cell lung cancer. *J Immunother Cancer* **8**, e000110.

15 Yan C, Zhang Z, Bao S, Hou P, Zhou M, Xu C & Sun J (2020) Computational methods and applications for identifying disease-associated lncRNA as potential biomarkers and therapeutic targets. *Mol Ther Nucleic Acids* **21**, 156–171.

16 Valadi H, Ekstrom K, Bossios A, Sjostrand M, Lee JJ & Lotvall JO (2007) Exosome-mediated transfer of mRNA and microRNA is a novel mechanism of genetic exchange between cells. *Nat Cell Biol* **9**, 654–659.

17 Epstein DM (2014) Special delivery: microRNA-200-containing extracellular vesicles provide metastatic message to distal tumor cells. *J Clin Investig* **124**, 5107–5108.

18 Zhuang G, Wu X, Jiang Z, Kasman I, Yao J, Guan Y, Oeh J, Modrusan Z, Bais C, Sampath D *et al.* (2012) Tumour-secreted miR-9 promotes endothelial cell migration and angiogenesis by activating the JAK-STAT pathway. *EMBO J* **31**, 3513–3523.

19 Bao S, Hu T, Liu J, Su J, Sun J, Ming Y, Li J, Wu N, Chen H & Zhou M (2021) Genomic instability-derived plasma extracellular vesicle-microRNA signature as a minimally invasive predictor of risk and unfavorable prognosis in breast cancer. *J Nanobiotechnol* **19**, 22.

20 Feng C, She J, Chen X, Zhang Q, Zhang X, Wang Y, Ye J, Shi J, Tao J, Feng M *et al.* (2019) Exosomal miR-196a-1 promotes gastric cancer cell invasion and metastasis by targeting SFRP1. *Nanomedicine* **14** , 2579–2593.

21 Zhang Z, Li X, Sun W, Yue S, Yang J, Li J, Ma B, Wang J, Yang X, Pu M *et al.* (2017) Loss of exosomal miR-320a from cancer-associated fibroblasts contributes to HCC proliferation and metastasis. *Cancer Lett* **397**, 33–42.

22 Goldman MJ, Craft B, Hastie M, Repecka K, McDade F, Kamath A, Banerjee A, Luo Y, Rogers D, Brooks AN *et al.* (2020) Visualizing and interpreting cancer genomics data via the Xena platform. *Nat Biotechnol* **38**, 675–678.

23 Avery-Kiejda KA, Braye SG, Mathe A, Forbes JF & Scott RJ (2014) Decreased expression of key tumour suppressor microRNA is associated with lymph node metastases in triple negative breast cancer. *BMC Cancer* **14**, 51.

24 Wang Q, Han CL, Wang KL, Sui YP, Li ZB, Chen N, Fan SY, Shimabukuro M, Wang F & Meng FG (2019) Integrated analysis of exosomal lncRNA and mRNA expression profiles reveals the involvement of lnc-

MKRN2-42:1 in the pathogenesis of Parkinson's disease. *CNS Neurosci Ther* **26**, 527–537.

25 Min L, Zhu S, Chen L, Liu X, Wei R, Zhao L, Yang Y, Zhang Z, Kong G, Li P *et al.* (2019) Evaluation of circulating small extracellular vesicles derived miRNA as biomarkers of early colon cancer: a comparison with plasma total miRNA. *J Extracell Vesicles* **8**, 1643670.

26 Langmead B, Trapnell C, Pop M & Salzberg SL (2009) Ultrafast and memory-efficient alignment of short DNA sequences to the human genome. *Genome Biol* **10**, R25.

27 Yang T, Ma H, Zhang J, Wu T, Song T, Tian J & Yao Y (2019) Systematic identification of long noncoding RNA expressed during light-induced anthocyanin accumulation in apple fruit. *Plant J* **100**, 572–590.

28 Ying J, Yu X, Ma C, Zhang Y & Dong J (2017) MicroRNA-363-3p is downregulated in hepatocellular carcinoma and inhibits tumorigenesis by directly targeting specificity protein 1. *Mol Med Rep* **16**, 1603–1611.

29 Liu C, Zhao Y, Wang J, Yang Y, Zhang Y, Qu X, Peng S, Yao Z, Zhao S, He B *et al.* (2020) FoxO3 reverses 5-fluorouracil resistance in human colorectal cancer cells by inhibiting the Nrf2/TR1 signaling pathway. *Cancer Lett* **470**, 29–42.

30 Khan MRAA (2019) ROCit: An R package for performance assessment of binary classifier with visualization. https://CRAN.R-project.org/package=ROCit

31 Koppers-Lalic D, Hackenberg M, Bijnsdorp IV, van Eijndhoven MAJ, Sadek P, Sie D, Zini N, Middeldorp JM, Ylstra B, de Menezes RX *et al.* (2014) Nontemplated nucleotide additions distinguish the small RNA composition in cells from exosomes. *Cell Rep* **8**, 1649–1658.

32 Hamilton MP, Rajapakshe KI, Bader DA, Cerne JZ, Smith EA, Coarfa C, Hartig SM & McGuire SE (2016) The landscape of microRNA targeting in prostate cancer defined by AGO-PAR-CLIP. *Neoplasia* **18**, 356–370.

33 Almerey T, Villacreses D, Li Z, Patel B, McDonough M, Gibson T, Maimone S, Gray R & McLaughlin SA (2019) Value of axillary ultrasound after negative axillary MRI for evaluating nodal status in high-risk breast cancer. *J Am Coll Surg* **228**, 792–797.

34 Liu Z, Feng B, Li C, Chen Y, Chen Q, Li X, Guan J, Chen X, Cui E, Li R *et al.* (2019) Preoperative prediction of lymphovascular invasion in invasive breast cancer with dynamic contrast-enhanced-MRI-based radiomics. *J Magn Reson Imaging* **50**, 847–857.

35 Nakano K, Miki Y, Hata S, Ebata A, Takagi K, McNamara KM, Sakurai M, Masuda M, Hirakawa H, Ishida T *et al.* (2013) Identification of androgen-responsive microRNA and androgen-related genes in breast cancer. *Anticancer Res* **33**, 4811–4819.

36 Sun Q, Zhang J, Cao W, Wang X, Xu Q, Yan M, Wu X & Chen W (2013) Dysregulated miR-363 affects head and neck cancer invasion and metastasis by targeting podoplanin. *Int J Biochem Cell Biol* **45**, 513–520.

37 Khuu C, Sehic A, Eide L & Osmundsen H (2016) Anti-proliferative properties of miR-20b and miR-363 from the miR-106a-363 cluster on human carcinoma cells. *Microrna* **5**, 19–35.

38 Klintman M, Nilsson F, Bendahl PO, Fernö M, Liljegren G, Emdin S & Malmström P (2013) A prospective, multicenter validation study of a prognostic index composed of S-phase fraction, progesterone receptor status, and tumour size predicts survival in node-negative breast cancer patients: NNBC, the node-negative breast cancer trial. *Ann Oncol* **24**, 2284–2291.

39 Costa A, Afonso J, Osório C, Gomes AL, Caiado F, Valente J, Aguiar SI, Pinto F, Ramirez M & Dias S (2013) miR-363-5p regulates endothelial cell properties and their communication with hematopoietic precursor cells. *J Hematol Oncol* **6**, 87.

40 Jechlinger M, Sommer A, Moriggl R, Seither P, Kraut N, Capodiecci P, Donovan M, Cordon-Cardo C, Beug H & Grunert S (2006) Autocrine PDGFR signaling promotes mammary cancer metastasis. *J Clin Invest* **116**, 1561–1570.

41 Cao R, Bjorndahl MA, Religa P, Clasper S, Garvin S, Galter D, Meister B, Ikomi F, Tritsaris K, Dissing S *et al.* (2004) PDGF-BB induces intratumoral lymphangiogenesis and promotes lymphatic metastasis. *Cancer Cell* **6**, 333–345.

42 Donnem T, Al-Saad S, Al-Shibli K, Busund LT & Bremnes RM (2010) Co-expression of PDGF-B and VEGFR-3 strongly correlates with lymph node metastasis and poor survival in non-small-cell lung cancer. *Ann Oncol* **21**, 223–231.

43 Schito L, Rey S, Tafani M, Zhang H, Wong CC, Russo A, Russo MA & Semenza GL (2012) Hypoxia-inducible factor 1-dependent expression of platelet-derived growth factor B promotes lymphatic metastasis of hypoxic breast cancer cells. *Proc Natl Acad Sci USA* **109**, E2707–E2716.

Supporting information

Additional supporting information may be found online in the Supporting Information section at the end of the article.

Fig. S1. Characterization of exosomes from the plasma of BC patients. (A) TEM displayed a cup-shaped exosome. Scale bar: 200 nm. (B) Exosome markers confirmed by western blot indicating the presence of

TSG101 and CD63 but the absence of calnexin. (C) NTA analysis revealed the main peak of 85.5 nm

Fig. S2. Association of *miR-363-5p* expression and LN status in different BC subtypes. The *miR-363-5p* expressions are significantly lower in nodal positive BC, exclusively in ER^+ BC samples.

Fig. S3. Tissue expression of *miR-363-5p* in in-house BC tissue and matched para-tumor tissue. The qPCR results indicated that expression levels of *miR-363-5p* in BC are significantly higher than in normal tissues. $^*P < 0.05$ determined by Student's *t*-test.

Received: 30 November 2022 | Revised: 21 February 2023 | Accepted: 10 March 2023

DOI: 10.1002/bit.28378

ARTICLE

BIOTECHNOLOGY and BIOENGINEERING WILEY

Enhanced bioprocess control to advance the manufacture of mesenchymal stromal cell-derived extracellular vesicles in stirred-tank bioreactors

Marta H. G. Costa[1,2] | **Margarida S. Costa**[1,2] | **Beatriz Painho**[1,2] | **Carolina D. Sousa**[2] | **Inês Carrondo**[2] | **Enrique Oltra**[3] | **Beatriz Pelacho**[3,4] | **Felipe Prosper**[3,4] | **Inês A. Isidro**[1,2] | **Paula Alves**[1,2] | **Margarida Serra**[1,2]

[1]Instituto de Tecnologia Química e Biológica António Xavier, Universidade Nova de Lisboa, Oeiras, Portugal

[2]iBET, Instituto de Biologia Experimental e Tecnológica, Oeiras, Portugal

[3]Department of Regenerative Medicine, Center for Applied Medical Research, University of Navarra, Pamplona, Spain

[4]Instituto de Investigación Sanitaria de Navarra (IdiSNA), Pamplona, Spain

Correspondence

Margarida Serra, iBET - Instituto de Biologia Experimental e Tecnológica, Apartado 12, Oeiras 2781-901, Portugal.
Email: mserra@ibet.pt

Funding information

Fundação para a Ciência e a Tecnologia; CardioPatch (SOE4/P1/E1063); iNOVA4Health, Grant/Award Numbers: UIDB/04462/2020, UIDP/04462/2020; LS4FUTURE (LA/P/0087/2020)

Abstract

Extracellular vesicles (EVs) derived from mesenchymal stromal cells (MSCs) act as signaling mediators of cellular responses. However, despite representing a promising alternative to cell-based therapies, clinical translation of EVs is currently limited by their lack of scalability and standardized bioprocessing. Herein, we integrated scalable downstream processing protocols with standardized expansion of large numbers of viable cells in stirred-tank bioreactors to improve EV production. Higher EV yields were linked to EV isolation by tangential flow filtration followed by size exclusion chromatography, rendering 5 times higher number of EVs comparatively to density gradient ultracentrifugation protocols. Additionally, when compared to static culture, EV manufacture in bioreactors resulted in 2.2 higher yields. Highlighting the role of operating under optimal cell culture conditions to maximize the number of EVs secreted per cell, MSCs cultured at lower glucose concentration favored EV secretion. While offline measurements of metabolites concentration can be performed, in this work, Raman spectroscopy was also applied to continuously track glucose levels in stirred-tank bioreactors, contributing to streamline the selection of optimal EV collection timepoints. Importantly, MSC-derived EVs retained their quality attributes and were able to stimulate angiogenesis in vitro, therefore highlighting their promising therapeutic potential.

KEYWORDS

bioprocess analytics, extracellular vesicles (EVs), mesenchymal stem/stromal cells (MSCs), metabolic preconditioning, Raman spectroscopy, stirred-tank bioreactors

---

Marta H. G. Costa and Margarida S. Costa contributed equally to this work.

1 | INTRODUCTION

The therapeutic potential of mesenchymal stromal cells (MSCs) in immunomodulation and tissue regeneration has been investigated in numerous clinical trials (reviewed in (Galderisi et al., 2022; Rodríguez-Fuentes et al., 2021)). In the past, MSC's therapeutic effects were mainly correlated with their ability to differentiate and, consequently, regenerate lost or damaged tissue by replacing injured cells. However, although it has been reported that transplanted MSCs migrate preferentially to the injured area, they show poor survival and low engraftment rates (Fu et al., 2017). These observations have drawn attention to the MSC secretome and its possible role in tissue repair and recovery from injury (Cases-Perera et al., 2022; Costa et al., 2017). Indeed, several studies have suggested that the beneficial effects observed after MSC transplantation in experimental models of tissue injury might be related to the paracrine activity of MSCs, as they secrete a large variety of soluble factors, such as growth factors (GFs), micro-RNAs (miRNAs) and extracellular vesicles (EVs), that may either activate target cells or stimulate neighboring cells to start repairing damaged tissue (Abels & Breakefield, 2016; Kumar et al., 2019; Yue et al., 2020).

Although initially perceived as cell waste vesicles, EVs have evolved as a relevant mechanism of intercellular communication being the first truly new biologic drug modality over the last three decades (reviewed by Finn & Konstantinov, 2020). EVs are delimited by a lipid bilayer membrane containing proteins, metabolites and nucleic acids and, given their small size (typically 50–1000 nm), EVs are the ideal candidate to cross the membrane of target cells (Herrmann et al., 2021; Théry et al., 2018).

EV-based therapies offer several advantages over cell transplantation regarding their low levels of immunogenicity, ability to cross the blood-brain barrier while recapitulating the parental cells' therapeutic effects and lower risk of tumorigenesis as they are not able to replicate (Banks et al., 2020; C. Y. Ng et al., 2022; Saleh et al., 2019). However, clinical translation of MSC-derived EVs is currently limited by their scalability and need to establish standard and reproducible manufacturing workflows (Paolini et al., 2022). Some studies have suggested that a clinical EV dose would require EV isolation from 500 million cells, a cell number estimated based on therapeutic dosages of transplanted MSCs (Adlerz et al., 2020; Phinney & Pittenger, 2017). While a clinical study has shown that $0.5–1.4 \times 10^{11}$ EVs might be required to treat patients with graft-versus-host disease (Kordelas et al., 2014), others have indicated that much higher EV numbers would be needed to reach effective therapeutic dosages ($>10^{14}$ particles per clinical dose) (K. S. Ng et al., 2019). To meet these large-scale manufacturing requirements, in this work, we propose to implement upstream strategies that could maximize EV yields, while integrating scalable downstream methodologies to isolate EVs. EVs can be isolated using a single or a combination of separation methods based on their size, charge, composition or density (Zhao et al., 2021). Although lacking scalability, basic research on EVs frequently explores ultracentrifugation to isolate EVs from conditioned medium (Phinney & Pittenger, 2017; Willis et al., 2017). Density gradient ultracentrifugation (DG-UC) has been linked to improved isolation with high purification efficiency in comparison to many commonly used techniques. However, it increases analytical time, complexity and associated costs, which hinders its applicability for large-scale therapeutic clinical settings (Lobb et al., 2015). In contrast with the conventional DG-UC protocol to isolate EVs, TFF-based method has been shown to be a more scalable alternative to isolate EVs in shorter periods of time (Kim et al., 2021). Additionally, SEC has been depicted as an efficient and reproducible approach for EV isolation, separating EVs from soluble proteins and other biomolecular contaminants, without altering their functional and morphological integrity (Gámez-Valero et al., 2016).

Additionally, although EV manufacturing is often performed in planar culture systems, microcarrier-based stirred cultures using spinner flasks (Haraszti et al., 2018), and vertical-wheel (de Almeida Fuzeta et al., 2020; Jalilian et al., 2022; Jeske et al., 2022), as well as hollow-fiber (Bellio et al., 2022; Gobin et al., 2021) bioreactors have supported MSC culture aiming at maximizing EV yields. Indeed, it has been reported that not only can bioreactors sustain higher cell densities (Cunha et al., 2015), therefore also increasing the number of secreted EVs per working volume of bioreactor, but also increase EV production per cell when MSCs are expanded in dynamic systems (de Almeida Fuzeta et al., 2020). However, hindering the development of current good manufacturing practices (cGMP)-compatible and standardized scalable strategies, most studies still lack the adoption of single-use (SU) bioreactors, implementation of adequate cell culture monitoring tools or rely on cell culture medium that is not chemically-defined, manufacturing considerations that our work proposes to address.

Preconditioning strategies, such as glucose (Garcia et al., 2015) or serum starvation (Gardiner et al., 2016), hypoxic cell culture (King et al., 2012; Zhu et al., 2018) or inducing physical (Patel et al., 2019) or chemical (Momen-Heravi et al., 2015; Patel et al., 2019; Saha et al., 2016; Wen et al., 2020) stresses, could boost EV yield. Since manipulation of cell culture conditions during EV manufacturing can influence the properties and function of EV-based products, identification of critical process parameters (CPP) that can impact the critical quality attributes (CQA) of EVs is essential to establish reproducible and clinical-ready EV-based products. The development of process analytical technology (PAT) tools to monitor in real-time key CPP can increase final product safety and quality (Gerzon et al., 2022). Therefore, their integration in EV manufacturing workflows to continuously measure cell culture parameters, such as metabolite concentration (Baradez et al., 2018), cell viability and growth (Baradez et al., 2018; Isidro et al., 2021), can contribute to ensure that optimal EV potency and quantity are reached. Particularly, online process monitoring using Raman spectroscopy has been implemented in the biopharmaceutical industry due to its suitability for integration in manufacturing steps (Buckley & Ryder, 2017).

In this work, we propose the use of a bioreactor-based platform to maximize the yields of the generated EVs while implementing scalable

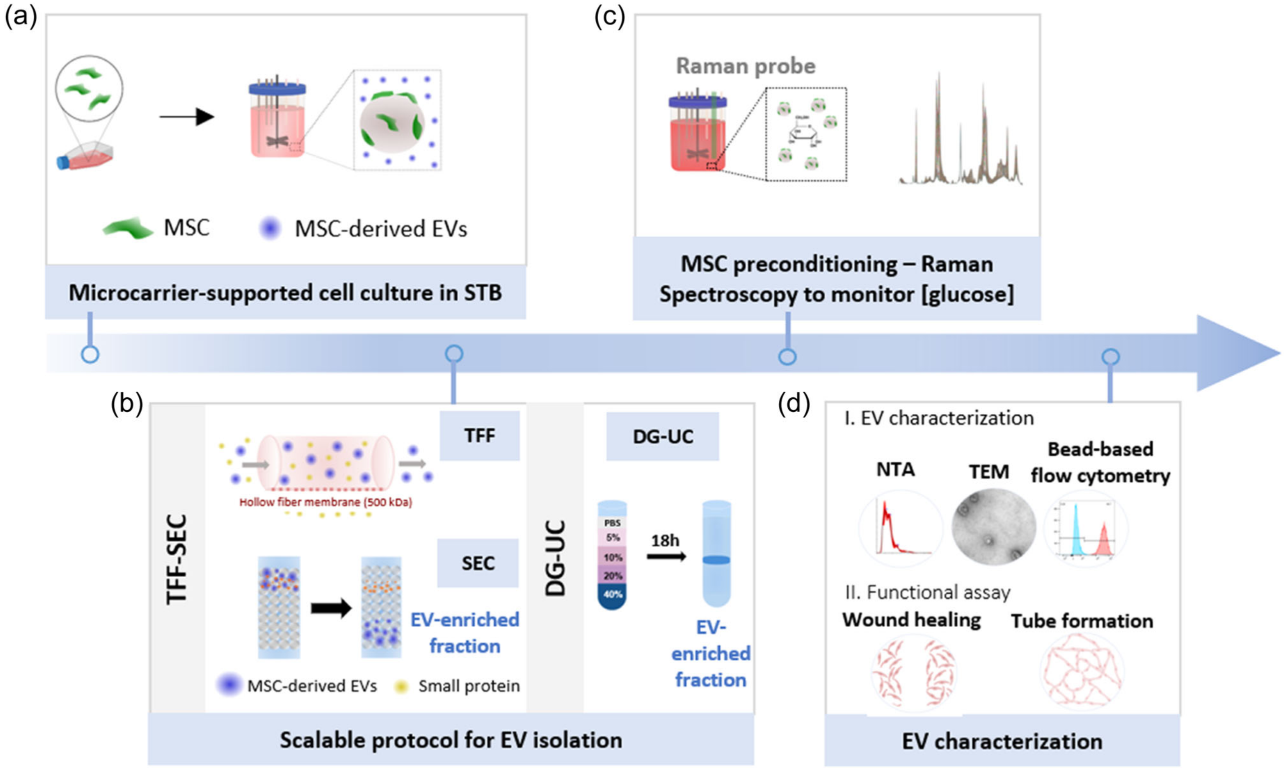

FIGURE 1 Schematic representation of the scalable manufacturing workflow implemented to maximize the yields of MSC-derived EVs. (a) MSC, isolated from AT, and cultured under static conditions were expanded in STB. Cell culture was performed in a chemically-defined medium, MesenCult™, and supported by xeno-free microcarriers, LC Synthemax™ II microcarriers. (b) Two distinct downstream processing strategies were evaluated regarding their ability to isolate EVs. EVs were concentrated and isolated from cell culture-conditioned medium relying on a size-based separation protocol (TFF-SEC) or on their density (DG-UC). (C) Metabolic preconditioning strategies, exploring higher and lower levels of glucose concentration in STB, were evaluated regarding their ability to improve EV yields. Raman spectroscopy in-line sensors were integrated during EV manufacture in STB to continuously monitor glucose levels. (D) Particle characterization was performed to ensure purity and characteristic attributes of the manufactured EVs were retained while functional assays (wound healing and tube formation assay) assessed the therapeutic potential of EVs secreted by MSC expanded in T-flasks or in STB. AT, adipose tissue; DG-UC, density gradient ultracentrifugation; EVs, extracellular vesicles; LC, low concentration; MSC, mesenchymal stromal cell; STB, stirred-tank bioreactors.

and standardized downstream processing strategies (Figure 1). Aiming to address the main challenges of EVs mass production for therapeutic purposes, we have explored the benefits of using chemically-defined cell culture medium and SU stirred-tank bioreactors towards the manufacture of safer and more reproducible EV batches. Additionally, by integrating scalable upstream and downstream cGMP-compatible processing technologies, and by highlighting the role of PAT tools, namely Raman Spectroscopy, to continuously monitor and, therefore, more tightly control CPP, such as metabolite concentration, our work will hopefully contribute towards the establishment of more standardized cell cultures and EV production.

2 | MATERIALS AND METHODS

2.1 | hAT-MSC culture in static culture systems

Human MSCs, isolated from adipose tissue (hAT-MSCs), of three distinct donors, kindly provided by Universidad de Navarra, were obtained after informed consent from discarded liposuction samples of healthy donors meeting all the serology and clinical history criteria to be an allogeneic donor (all from female donors, 20, 49, and 57 years old). hAT-MSCs were routinely propagated at a cell density of $1.8–2.0 \times 10^3$ cell/cm^2 in T225 flasks (ThermoFisher Scientific), pre-coated with Animal Component-Free Attachment Substrate (STEMCELL Technologies™) diluted at a ratio of 1 to 300 in Dulbecco's phosphate-buffered saline (DPBS, Gibco®, ThermoFisher Scientific) for 1 h at room temperature (RT). hAT-MSCs were cultured in Mesencult™ medium (STEMCELL Technologies™) supplemented with 1% (v/v) of GlutaMAX™ (Gibco®, ThermoFisher Scientific) and 0.2% (v/v) of MesenCult™-ACF Plus supplement (STEMCELL Technologies™) and kept at 37°C and 5% CO_2 in a humidified atmosphere. Complete medium exchange was performed every 3–4 days. Upon reaching 80%–90% confluency, hAT-MSCs were washed with DPBS and incubated with TrypLE™ Select (1x) (Gibco®, ThermoFisher Scientific) for 10 min at 37°C (5804 centrifuge, Eppendorf®). After detachment, cells were resuspended in MesenCult medium and centrifuged at 300 *g* for 10 min at 18–22°C. Total cell number and viability were estimated using the NucleoCounter® NC-202™ automated cell counter (ChemoMetec). hAT-MSCs (in passages P4 or P5) were either re-seeded in a T-flask (static control) kept at 3% O_2 by controlling the partial pressure of nitrogen (N_2) inside the incubator (Sanyo) or inoculated in stirred-tank bioreactors (STB), as described in the following section, with cells cultured under hypoxic conditions (3% O_2). Whenever required, cells were cryopreserved in a liquid/vapor-phase nitrogen container in a freezing solution (90% fetal bovine serum (FBS) and 10% dimethyl sulfoxide (DMSO), from Gibco®, ThermoFisher Scientific and WAK-Chemie Medical GmbH, respectively) at a cell concentration of 2–5 million cell/mL.

2.2 | hAT-MSC expansion in stirred-tank bioreactors

Adapted from a protocol previously developed by our group (Cunha et al., 2017), hAT-MSCs were cultured for 7 days in BioBLU 0.3c Single-Use Vessels (Eppendorf™), equipped with a pitched-blade 45° impeller, at 37°C with a surface aeration rate of 0.1 vvm, pH level controlled at 7.2 and dissolved oxygen (pO_2) of 3% O_2 (corresponding to 14.3% of air saturation). Low Concentration (LC) Synthemax® II Corning® microcarriers (Sigma-Aldrich) were used at a final concentration of 16 g/L. hAT-MSCs, previously expanded in T225 flasks, were inoculated at a cell density of 4×10^3 cell/cm^2 in a total volume of 100 mL of MesenCult. During the first 24 h, an intermittent agitation regime (agitation cycles of 1 min of agitation at 60 rpm and 59 min with agitation off) was performed, after which the bioreactors were continuously agitated between 60 and 70 rpm in a final working volume of 200 mL. On day 4, 50% (v/v) of culture medium was exchanged. In addition to this feeding strategy, daily glucose supplementation (Gibco®, ThermoFisher Scientific), starting on Day 2 of cell culture, along with a 50% culture medium exchange on Day 4, was evaluated so that glucose levels were retained close to the glucose concentration present in the fresh medium (5.5 mM). On Day 7, the culture medium was collected for EV isolation, and the cells were detached from the microcarriers surface using TrypLE™ Select (1X) at 37°C with the following cycles of agitation: 5 min at 135 rpm followed by a pulse of 5 s at 180 rpm, for a total incubation time of 15–20 min. After harvesting, the cell/microcarrier suspension was recovered from the bioreactor and filtrated through a cell strainer (sterile nylon mesh) with pore size of 70 µm (Falcon) into a 225 mL conical centrifuge tube (Falcon). The cell suspension was then centrifuged at 300 *g* for 10 min at RT. After cell concentration and viability analysis using the NucleoCounter® NC-202™ automated cell counter (ChemoMetec), cells were cryopreserved as mentioned before.

2.3 | Raman spectroscopy

Raman spectra were acquired using Kaiser Raman Rxn2 Analyzer (785 nm wavelength; Endress-Hauser) on a time interval of 1 h (laser power of 400 mW) where 75 scans were collected with an exposure time of 10 s per scan (Baradez et al., 2018). A stainless steel bIO™ probe Raman was autoclaved before being inserted in the BioBLU® vessel. Pretreatment of the Raman spectra was performed to remove outliers, after which data was smoothed using a Savitsky-Golay filter and a rubberband method was used for baseline correction. Spectroscopic data were modeled using Partial Least Squares (PLS) Regression. Raman peaks were correlated with offline measurements of glucose concentration.

2.4 | Isolation and concentration of EVs from conditioned medium

Two distinct methods were explored to isolate and concentrate EVs from conditioned medium (processed volume of 100 mL) collected 7 days following hAT-MSC expansion in either planar cultures or in STB: DG-UC or TFF-SEC.

In both methods, the conditioned medium was submitted to two low-speed centrifugation steps: 300 *g* for 10 min followed by 2000 *g* for 10 min (5804 centrifuge, Eppendorf®) (both at 4°C), to remove cell debris. To minimize the impact of storage conditions on EVs stability and, consequently, on their bioactivity, the supernatant was stored at 4°C for a maximum of 3 days until further EV concentration and isolation, after which EVs were stored at −80°C.

EVs, isolated from the conditioned medium following the DG-UC method, were processed as described by Louro et al. (2022). Briefly, the conditioned medium was ultracentrifuged in 30 mL polypropylene centrifuge tubes (Beckman Coulter®) for 2h45 at 4°C using an Ultracentrifuge Optima LE-80K C0L02K09 (SW28 rotor, Beckman Coulter®). The generated EV pellet was resuspended in 800 µL of DPBS for subsequent isolation using an iodixanol discontinuous density gradient as described by Van Deun et al. with minor modifications (Van Deun et al., 2014). The discontinuous bottom-up iodixanol density gradient was assembled by sequentially layering 4 mL each of 40, 20% and 10% (w/v) iodixanol solutions, followed by 3.5 mL of 5% iodixanol solutions, and 1 mL of DPBS from the bottom to the top of a 16.8 mL polypropylene centrifuge tube (Beckman Coulter®). The prepared gradient was centrifuged for 18 h at 4°C, at 25,000 rpm in the Ultracentrifuge Optima LE-80K C0L02K09 (SW28 rotor, Beckman Coulter®), using maximal acceleration and minimum brake. After centrifugation, 16 gradient fractions of 1 mL were collected from the center of the tube, from top to bottom, and fractions 1–4, 5–7, 8–9, 10–12, and 13–16 were pooled together. To concentrate EVs and remove the remaining iodixanol, an additional ultracentrifugation step of 2h45 at 4°C, at 25,000 rpm was performed.

To implement a more scalable method and purify EVs from large volumes of conditioned medium, the TFF-SEC method was applied. Before loading into a SEC column, following the centrifugation steps, the conditioned medium was concentrated into a volume of 2 mL using a MicroKros Hollow Fiber Filter Module with 500 kDa cut-off filters (Spectrum® MicroKros). Flow was supplied using either syringes or a peristaltic pump (SARTOFLOW® Slice 200) with a flow rate of 30 mL/min. In the final step, the conditioned medium was exchanged with DPBS to concentrate the conditioned medium back to 2 mL. Afterwards, EV isolation was performed by SEC using a qEV SEC column (Izon) with a 70 nm pore size to separate particles based on their size. The column was first primed with DPBS after which 0.5 mL of the TFF-concentrated solution was loaded into the column and eluted with DPBS. After sample addition, the first 3 mL collected were discarded. Immediately after, 20 fractions of 0.5 mL were collected. When required, pooled SEC fractions were concentrated using Amicon-2 10 kDa centrifugal filter units (Merck Milipore), through centrifugation at 4000 *g* for 20 min followed by a spin down for 2 min at 1000 *g* (both at 4°C). All samples were stored at −80°C until further analysis.

2.5 | Analytical methods for characterization of hAT-MSCs

2.5.1 | Cell concentration and viability

Cell concentration and viability were assessed using a NucleoCounter® NC-202™ automated cell counter (ChemoMetec) according to the manufacturer's instructions. Cell viability was qualitatively evaluated following incubation with fluorescein diacetate (FDA) and propidium iodide (PI), both from Sigma-Aldrich. Fluorescence images were acquired using a fluorescence microscope (DMI6000, Leica Microsystems GmbH) and analyzed with ImageJ open-source software.

2.5.2 | Analysis of extracellular metabolite concentration

Cell culture supernatant from both STB and static controls was centrifuged for 5 min at 500 *g* at RT to remove cell debris and stored at −20°C until further metabolite analysis. The Cedex Bio Analyzer (Roche) was used to quantify concentrations of glucose (Glc), lactate (Lac), ammonia (NH_3), and glutaMAX (L-alanine-L-glutamine).

2.5.3 | Flow cytometry of hAT-MSC surface markers

Immunophenotypic analysis of hAT-MSCs specific surface markers and hematopoietic contaminants was performed by flow cytometry before and after expansion in both planar systems and STB using the following antibodies: CD29-PE, CD73-PE, CD90-FITC, CD105-PE (Biolegend®), CD34-PE, CD45-PE (BD Biosciences®) and HLA-DR-PE (Biolegend®). Isotype controls were also prepared (PE and FITC mouse IgG1 and PE mouse IgG2 (Biolegend®)). Briefly, samples with a cell concentration of 1×10^6–3×10^6 cell/mL prepared in 100 µL of DPBS supplemented with 1% (v/v) FBS were incubated with the labeled antibodies at RT for 20–30 min in the dark. Following incubation and washing with DPBS supplemented with 1% (v/v) FBS, cells were resuspended in 300 µL of DPBS with 1% (v/v) FBS. Samples were acquired using the BD FACS Celesta (BD Biosciences) and a minimum of 10,000 events per sample were recorded. The analysis of the acquired data was performed using FlowJo™ software (Becton, Dickinson Company).

2.5.4 | Trilineage differentiation of hAT-MSCs

The ability of hAT-MSCs to differentiate into the adipogenic, osteogenic and chondrogenic lineages was evaluated. During osteogenic and adipogenic differentiation, hAT-MSCs were cultured in 24-well plates (Corning®), seeded at 1×10^4 cell/cm^2 per well in 1 mL of Mesencult medium. When cells reached approximately 90% of confluency, cell culture medium was exchanged to osteogenic or adipogenic differentiation medium (PromoCell) and incubated for 14 days at 37°C, according to manufacturer's instructions. The ability of hAT-MSCs to differentiate into the chondrogenic lineage was assessed in 3D cultures of cell aggregates kept in chondrogenic differentiation medium (PromoCell) for 21 days at 37°C. Complete medium exchange was performed in all conditions every 3–4 days. The trilineage differentiation ability of hAT-MSCs was qualitatively assessed upon staining with Alizarin Red S (osteocytes), Oil Red-O (adipocytes), and Alcian blue 8GX (chondrocytes). The staining images were captured in a computer-assisted light microscope (MC170 HD, Leica Microsystems GmbH).

2.6 | Characterization of MSC-derived EVs

2.6.1 | Nanoparticle tracking analysis (NTA)

EV size distribution profiles and concentration measurements were obtained by nanoparticle tracking analysis (NTA) using the NanoSight NS300 (Malvern Panalytical) equipped with a 405 nm laser and NTA software version 3.3. Samples of 1 mL were prepared by diluting the EV solution with DPBS to obtain a final concentration in the range of 10^6–10^9 particle/mL. For each sample, three videos of 30 s were recorded. The videos were obtained with identical software settings: camera level of 13–15, screen gain 1–2, and detection threshold 3–4.

2.6.2 | Protein quantification

Total protein content was quantified in EV samples using the ThermoFisher Scientific microBCA Protein Assay Kit. Both EV samples (diluted in DPBS to obtain a final concentration in the range of 0.5–20 µg/mL) and standard protein solutions were prepared and incubated with the microBCA Working Reagent for 2 h at 37°C. Afterwards, the absorbance was measured at 562 nm on a plate reader (Infinite M200 Pro, Tecan).

2.6.3 | Bead-based flow cytometry

The EV-specific surface markers CD81, CD63, and CD9 were assessed by bead-based flow cytometry. Briefly, the exosome-Human CD81 Flow

Detection Reagent (Invitrogen™, ThermoFisher Scientific) was used, comprising superparamagnetic beads coated with a primary monoclonal antibody specific for CD81, that were first washed with DPBS using a DynaMag™-2 Magnet (ThermoFisher Scientific). EV samples were incubated with 5×10^4 beads overnight at 4°C in 1.5 mL low protein binding collection tubes (ThermoFisher Scientific) on an oscillator mixer at a ratio of 3.0×10^4–3.3×10^4 particles per bead. After being centrifuged at 900 *g* for 1 min at RT, the beads were washed twice with DPBS (using a magnetic rack to retain the bead-bound EV samples), resuspended in DPBS and incubated with 5 μL (diluted in 100 μL of DPBS) of the panel of antibodies of interest—CD9-PE, CD63-PE or CD81-PE (Biolegend®)—for 30 min at 4°C protected from light. Samples were washed and resuspended in DPBS and, finally, analyzed in a flow cytometer (BD FACS Celesta (BD Biosciences)). Analysis of the data was done using FlowJo™ software.

2.6.4 | Transmission electron microscopy (TEM)

EV morphology was assessed by TEM. First, 100 mesh copper grids formvar/carbon were precoated and glow discharged. Samples were mixed (1:1) with formaldehyde 4% (w/v) in 0.1 M DPBS solution for 5 min and then incubated for another 5 min at RT to allow them to adhere to the grids. Grids were washed with 10 drops of dH_2O and stained with 1 drop of 2% (w/v) uranyl acetate for 5 min at RT protected from light. Imaging was done on a Tecnai G2 Spirit BioTWIN Transmission Electron Microscope (FEI Company™) operating at 120 kV and data collected with Olympus-SIS Veleta CCD Camera.

2.7 | Cell-based assays for analysis of EV uptake and bioactivity

HUVECs were purchased from Lonza and cultured in Endothelial Cell Growth Medium supplemented according to manufacturer's instructions (complete EGM™-2, Lonza®). Culture medium was exchanged every 3 days and cells were passaged upon reaching 80%–90% of confluency.

2.7.1 | EV uptake assay

EVs were labeled with PKH26 Red Fluorescent Cell Linker Mini Kit for General Cell Membrane Labeling (Sigma Aldrich). Briefly, EVs in 100 μL Diluent C suspension were labeled with 1.5 μL PKH26 and incubated for 3 min, after which a solution of 100 μL of 0.1% BSA was used to quench the dye. A mock dye treatment was prepared by mixing DPBS with Diluent C. To remove non-EV-associated dye aggregates, the EV and control samples were run through SEC column (qEV 70 nm pore size, Izon) as previously described. HUVECs were seeded in 24-well plates and, after 16 h, treated with PKH26-labeled EVs or with a PKH26 mock dye solution. After 3 h, cells were imaged using an inverted fluorescence microscope (DMI6000, Leica Microsystems GmbH). Additionally, HUVECs were stained with DAPI (ThermoFisher Scientific) and CD31 (anti-CD31 antibody diluted in 0.2% (v/v) FSG, 1:50; clone JCF0A, M0823, DAKO Omnis, Agilent Technologies; mouse IgG isotype control, 1:50, sc-3877, Santa Cruz Biotechnology).

2.7.2 | Tube formation assay

HUVECs, kept for 15-16 h in Endothelial Cell Growth Medium without any supplementation (basal EGM™-2), were seeded at 1.2×10^4 cell/well of a 96-well culture plate (Corning®) pre-coated with 50 μL of Matrigel® Growth Factor Reduced Basement Membrane Matrix (Corning®). HUVECs were treated with hAT-MSC-derived EVs at a ratio of 6×10^3 particle/cell prepared in basal EGM™-2, with basal EGM™-2 or complete EGM™-2 used as negative and positive controls, respectively. Cells were incubated in a humidified incubator (5% CO_2, 37°C) for 8 h. Images of the tube formation were obtained using the IncuCyte™ software instrument (Essen BioScience) and analyzed using the Angiogenesis Analyzer toolset of Fiji software (Carpentier et al., 2020; Schindelin et al., 2012).

2.7.3 | Wound healing assay

HUVECs were seeded (3×10^4 cell/well) in a 96-well ImageLock™ tissue culture plate (Essen BioScience) in complete EGM™-2 and kept at 37°C and 5% CO_2 in a humidified atmosphere. After reaching confluency, a complete medium exchange was performed to basal EGM™-2 supplemented with 0.1% FBS (v/v) and cells were incubated for 12 h. Afterwards, wounds were created using a 96-pin WoundMaker™. After washing with DPBS, 200 μL of EV samples were diluted in basal EGM™-2 supplemented with 0.1% FBS (v/v) at a particle/cell ratio of 6×10^3. Basal EGM™-2 supplemented with 0.1% (v/v) FBS was used as negative control, whereas complete EGM™-2 was used as a positive control. Images of the wounds were automatically obtained and registered every 4 h using the IncuCyte™ software instrument (Essen BioScience) for a total of 20 h. The images obtained were analyzed using the ImageJ Wound Healing Size Analyzer toolset to calculate the percentage of wound closure relative to the initial wound area according to the following equation:

$$\text{Wound Closure (\%)} = \frac{A_0 - A_t}{A_0} \times 100\%$$

where A_0 is the initial wound area and A_t is the wound area at *t* hours after the wound was created.

2.8 | Statistical analysis

Data are shown as mean ± standard deviation of at least three replicates (except for the functional assays where two biological replicates were used). Statistical significance was determined by one-way analysis of variance (ANOVA) with Tukey's multiple comparison test using the GraphPad Prism 7 software. $^{*}p < 0.05$, $^{**}p < 0.01$, $^{***}p < 0.001$, $^{****}p < 0.0001$ were considered significant.

3 | RESULTS AND DISCUSSION

To scale-up the production of EVs, we have integrated upstream and dowsntream processing strategies for EV manufacture using both scalable and cGMP-compatible technologies (Figure 1a,b). Additionally, since MSC respond to external stimuli, we highlighted the potential of PAT tools (i.e., Raman spectroscopy) to continuously monitor the cell culture microenvironment, namely the concentration of glucose throughout hAT-MSC culture in STB (Figure 1c), aiming at increasing EV yields while preserving their structure and bioactivity (Figure 1d).

3.1 | Towards process scalability—enhanced EV recovery using TFF-SEC versus DG-UC

Several distinct methodologies for isolation of EVs, relying on their density, size or surface markers (Reiner et al., 2017), have been employed and shown to impact the purity and omics profile of EV populations (Van Deun et al., 2014). Herein, aiming at implementing a scalable protocol for EV isolation and concentration from hAT-MSC conditioned medium, we explored a size-based separation method using TFF-SEC and evaluated its performance in comparison with the gold standard, although not scalable, protocol exploring DG-UC.

Standard particle characterization was performed for MSC-derived EV samples isolated by both methods (DG-UC and TFF-SEC). NTA was conducted across all five pooled fractions recovered after DG-UC (fractions 1–4, 5–7, 8–9, 10–12, and 13–16) and across all 20 fractions resultant from SEC to evaluate particle concentration and size distribution. Additionally, bead-based flow cytometry was performed to confirm the expression of the transmembrane protein CD81, an EV protein marker, in the fractions under evaluation.

Following isolation with DG-UC protocol, results show that fraction 8–9 presented the highest number of particles and high CD81 expression (87 ± 17%) (Figure 2a) while, upon EV isolation performed by TFF-SEC protocol, most particles were present in fractions 2–5, with these expressing high levels of CD81 (83 ± 12%) (Figure 2b). Both fraction 8–9, isolated by DG-UC, and the four enriched fractions (fractions 2–5), obtained following the TFF-SEC protocol, evidenced similar size distribution, ranging between 50 and 400 nm, but mostly enriched in smaller EVs (≤200 nm). While fraction 8–9 isolated by DG-UC presents a mean size of 165.5 ± 1.4 nm and a particle concentration peak occurring at 117.0 ± 8.3 nm (Figure 2c), TFF-SEC fractions present an overall mean size of 156.8 ± 3.7 nm and peak concentration occurring for the particle size of 114.6 ± 7.2 nm (Figure 2d). Of notice, for both EVs isolated following DG-UC and TFF-SEC protocols, the size of 61.4%–72.0% EVs ranged from 100 to 200 nm with 10.3%–14.2% and 15.7%–24.5% presenting a size below 100 nm and above 200 nm, respectively (Figure 2e). Although the presence of contaminants was not specifically addressed, to further evaluate the level of contaminating non-EV protein present in each TFF-SEC isolated fraction, we have quantified the total protein content by microBCA assay. Proteins were mostly eluted in later fractions, with very low levels present in fractions 2–5 (Figure 2f), indicating the suitability of the TFF-SEC protocol to limit the co-isolation of protein contaminants.

Isolation by TFF-SEC (from 100 mL of conditioned medium) yielded higher EV concentration in comparison to the DG-UC protocol, resulting in an overall fold increase of 5.2 ± 0.5 (Figure 2g). These results confirm that TFF- and SEC-based technology can be employed to efficiently isolate EVs (Watson et al., 2018). Additionally, and contrary to DG-UC protocol, which is time-consuming (taking approximately 23 h per isolation procedure), and operator dependent (Corso et al., 2017), SEC offers increased reproducibility and, if combined with TFF, can process large volumes of conditioned medium, in shorter periods of time (approximately 3 h). Therefore, given the scalability and higher EV recovery yields obtained when TFF-SEC is implemented in comparison with the DG-UC protocol, subsequent experiments performed to isolate and further characterize hAT-MSC-derived EVs were conducted with cell culture-conditioned medium processed by TFF-SEC.

3.2 | Raman spectroscopy in-line sensors can increase process control in stirred-tank bioreactors through continuously monitoring glucose concentration

To establish scalable manufacture of MSC-derived EVs, adding to downstream processing for EV isolation by TFF-SEC, we have implemented a baseline process using microcarrier technology combined with stirred-tank bioreactor, previously developed by our group (Cunha et al., 2017). Cell expansion in STB possesses several advantages over expansion in planar systems, such as easier scale up, enhanced process monitoring and control, flexible modes of operation, and lower cost for production (Bellani et al., 2020). Additionally, exposure of MSCs to biophysical or biochemical stimuli could contribute to optimize the number of EVs secreted per cell and tailor the manufactured EVs towards a desired function. Several studies have shown that hypoxia preconditioning can result in increased number of released EVs as well as impact EV's cargo composition, enhancing their proangiogenic and cardioprotective properties (Collino et al., 2019; Salomon et al., 2013; Xue et al., 2018; Zhu et al., 2018). Furthermore, Garcia et al. (2015) showed that glucose starvation in cardiomyocytes can also trigger EV secretion and promote EVs' proangiogenic effects while other studies have combined both EV manufacturing in a 3D scaffold-perfusion bioreactor and chemical preconditioning using ethanol to enhance the vascularization ability of endothelial cell-derived EVs (Patel et al., 2019).

Although strategies like ethanol preconditioning can augment the production of EVs, they are not suited to simultaneously formulate both cell and EVs as they could impact the viability of cell products. On the contrary, as proposed in this work, metabolic preconditioning, such as tailoring glucose concentration throughout culture time, coupled with cell culture at low oxygen levels (3% O_2), could

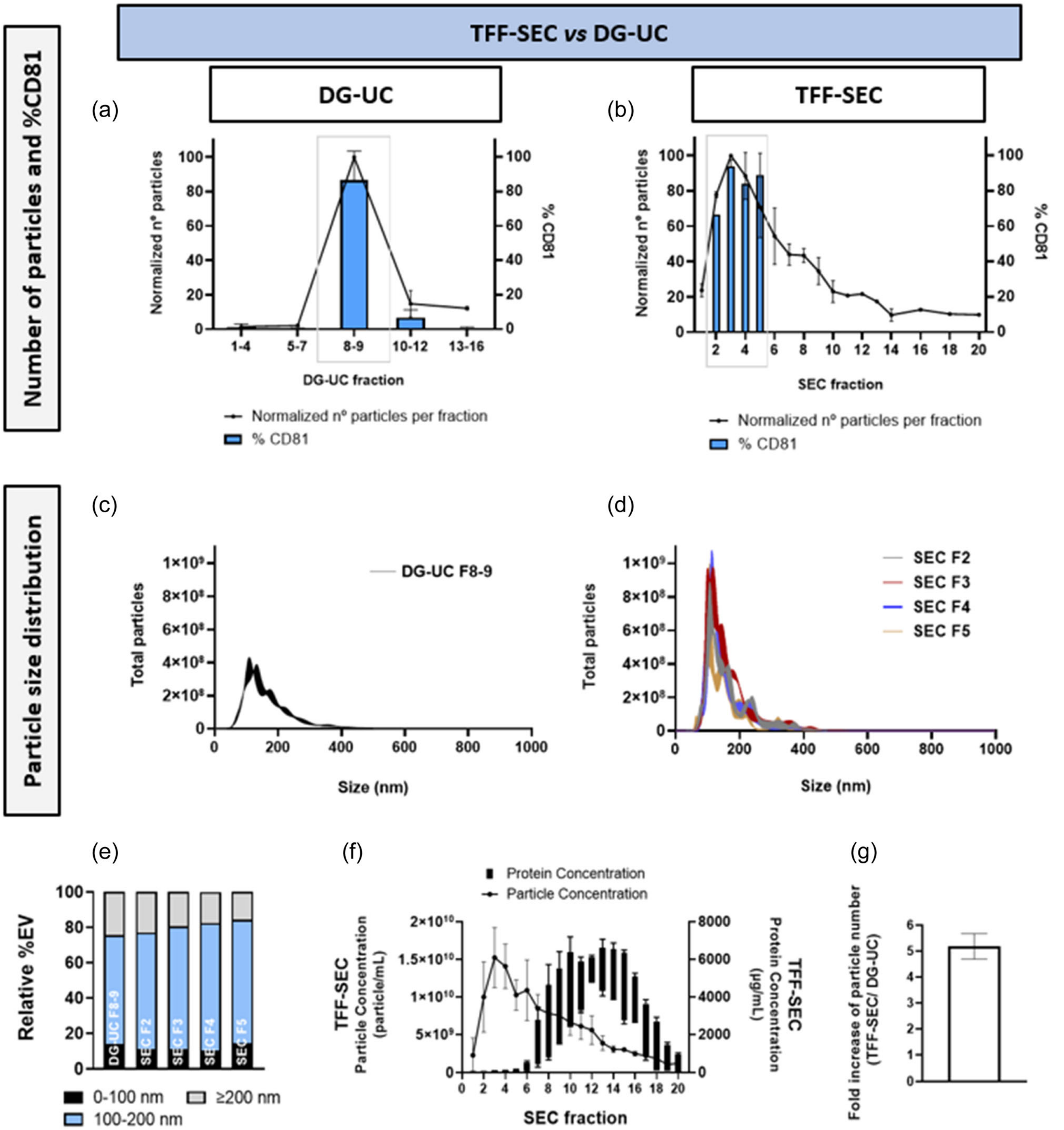

FIGURE 2 Characterization of EV samples isolated by either DG-UC or TFF-SEC. Profile of EV-enriched fractions assessed by NTA and bead-based flow cytometry following isolation by DG-UC (a) or by TFF-SEC (b). Particle number was normalized to fraction containing the highest concentration of particles (fraction 8–9 for DG-UC protocol and fraction 3 for TFF-SEC). EV size distribution, assessed by NTA, of EV-enriched fractions—fraction 8–9 isolated by DG-UC (c) and fractions 2–5 isolated by TFF-SEC (d)—is represented as mean ± SD (shadowed area). (e) Relative EV distribution ranged in three size classes (<100 nm, 100–200 nm and ≥200 nm). (f) Particle and protein concentration in fractions 1–20 following EV isolation by TFF-SEC. (g) Fold increase of EV yield, measured as total isolated particles per million viable cells, following isolation by TFF-SEC relatively to DG-UC. Data are represented as mean ± SD (*n* = 2). DG-UC, density gradient ultracentrifugation; EVs, extracellular vesicles; NTA, nanoparticle tracking analysis; TFF-SEC, tangential flow filtration-size-exclusion chromatography.

constitute a valuable strategy to increase EV production yields while not compromising cell growth.

To assess the impact of decreasing glucose concentration on the ability of hAT-MSCs to secrete EVs, two different feeding strategies were implemented during hAT-MSC culture in STB: (i) while, in the first condition, a 50% (v/v) medium exchange was performed on Day 4 of cell culture (STB), (ii) in the second cell culture strategy, in addition to the 50% (v/v) culture medium exchange on Day 4, glucose was daily supplemented, from Day 2 onward, to maintain concentration levels close to the glucose concentration present in the fresh cell culture medium (STB + glc) (Figure 3a,b). While similar glucose levels were observed in the STB + glc condition amongst different cell donors and bioreactor batches on the harvest day (4.04 ± 0.24 mM), the variability of glucose concentration observed in the non-glucose supplemented STB (0.85 ± 0.82 mM), ranging from 0.01 mM to 1.86 mM on the harvest day (Figure 3c), suggests that a tighter control over the fluctuation of metabolite levels could contribute towards the establishment of more reproducible EV manufacturing workflows. Having the ability to continuously monitor metabolite levels in real-time, such as glucose concentration, in-line Raman spectroscopy sensors could provide added benefits towards enhanced bioprocess control, potentially facilitating decision-making of the time of both cell and EV harvest. Contrary to cell culture in static systems where monitoring and controlling CPP could be challenging, cell culture in STB facilitates the adjustment of operational parameters to improve EV yields. To this purpose, we have applied Raman spectroscopy to continuously monitor glucose levels in STB. High level of agreement was observed between Raman acquired data and off-line glucose concentration measurements throughout culture ($R^2 = 0.923$) (Figure 3d). The ability of Raman spectroscopy to provide real-time measurements of nutrients consumption (i.e., glucose) could therefore constitute an attractive PAT tool to contribute to develop closed manufacturing processes of both cells and cell-derived EVs. Given the potential use of Raman spectroscopy to inform the timings of key process steps, including cell harvest and collection of conditioned medium for EV isolation, the impact of donor-dependent cellular responses or deviations in cell culture parameters during the manufacture of distinct EV batches could potentially be minimized.

Importantly, besides the role of PAT tools to contribute to standardize bioprocesses, the most commonly utilized medium for

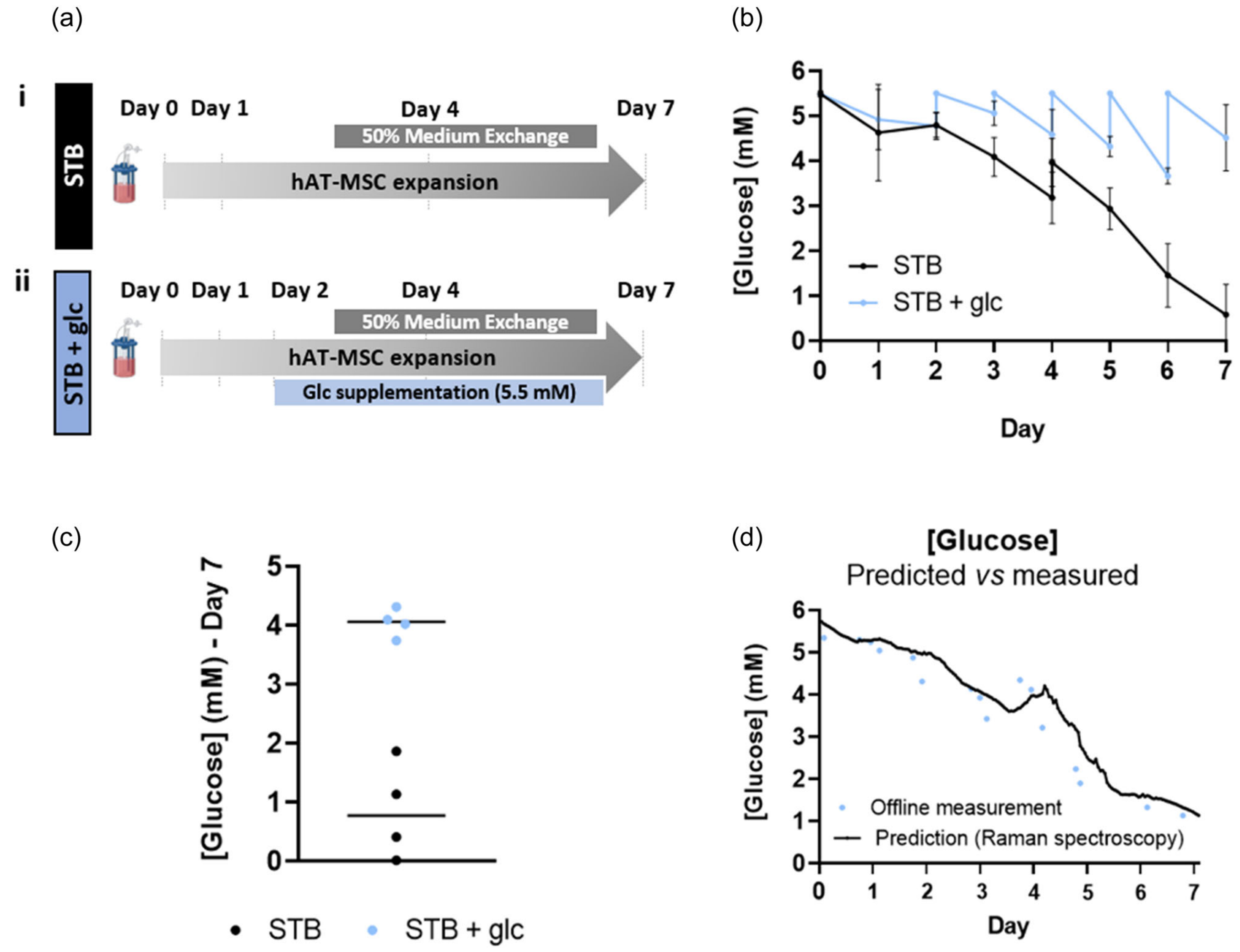

FIGURE 3 Tailoring glucose concentration during hAT-MSC culture in STB. (a) Schematic representation of the feeding strategies implemented during hAT-MSC culture in STB: (i) STB: 50% medium exchange on day 4 of culture; (ii) STB + glc: 50% medium exchange on Day 4 of culture and daily glucose supplementation from Day 2 onward. (b) Glucose concentration profile during MSC expansion in STB (*n* = 4). (c) Glucose concentration on the harvest day for both cell culture conditions evaluated in STB (STB and STB + glc). (d) Correlation between offline measurements of glucose concentration (circles) and chemometric model using PLS method following Raman spectroscopy analysis (*n* = 1). hAT-MSC, human MSCs, isolated from adipose tissue; MSC, mesenchymal stromal cell; STB, stirred-tank bioreactors.

MSC expansion still relies on using supplements such as FBS or human platelet lysate (hPL), which poses several disadvantages, including batch-to-batch variability and contamination concerns (de Almeida Fuzeta et al., 2020; Gottipamula et al., 2013). Furthermore, such supplements contain large amount of EVs that can be co-isolated with EVs secreted by cells, thus contaminating the end products (Adlerz et al., 2020). Therefore, to avoid lot-to-lot variations and produce more reproducible cell and EV populations, in this work, we used a chemically-defined and serum-free medium, Mesencult™. Contrary to most studies focused on EV manufacture where cell culture and EV isolation comprise two separate steps, frequently requiring that, during the EV isolation step, medium exchange from FBS- or hPL-supplemented media is performed to EV-depleted culture medium, our study proposes the use of a chemically-defined medium to simultaneously support the manufacture of both MSCs and MSC-derived EVs. Cells expanded in MesenCult™ medium reached a concentration of 1.2 ± 10^5 cell/mL following 7 days of culture (fold increase of 5.1 ± 0.2) and retained high viability throughout culture in STB (Figure 4a,b).

To ensure that the quality attributes of hAT-MSCs were maintained following expansion in STB and in static culture systems, both trilineage differentiation potential and cell immunophenotype were investigated before and after cell expansion (Figure 4c,d), in accordance with the criteria established by the International Society for Cell and Gene Therapy (Dominici et al., 2006). MSCs, expanded in either STB or static T-flasks, retained their trilineage differentiation ability, successfully differentiating into adipocytes, osteocytes and chondrocytes (Figure 4c). Additionally, 98% of the cell populations were positive for CD29, CD73, CD90, with over 85% MSCs being positive for CD105, whilst for CD34, CD45 and HLA-DR less than 2% of the cell populations were positive for these markers (Figure 4d).

3.3 | Enhancing EV manufacturing yields through scalable manufacture of MSC-derived EVs in stirred-tank bioreactors at low glucose concentration levels

The yields and bioactivity of EVs manufactured in STB was compared with EVs secreted by cells cultured in T-flasks. Although, for MSC-derived EV production, flask-based culture systems have often been used, several studies have associated bioreactor culture with higher EV yields (de Almeida Fuzeta et al., 2020; Haraszti et al., 2018). Total particle counts determined by NTA were used to compare EV production in individual runs (three distinct cell donors) when cells are exposed to different cell culture conditions, considering the total number of secreting cells (EVs/10^6 cell—Figure S1a) and total volume of conditioned medium (Figure S1b). Cells expanded in STB yielded the highest EV numbers ($6.58 \pm 1.97 \times 10^8$ particle/mL and $6.65 \pm 2.35 \times 10^9$ particle/10^6 cell) while lower EV yields were obtained following hAT-MSC culture under static condition ($3.25 \pm 1.34 \times 10^8$ particle/mL and $2.25 \pm 1.32 \times 10^9$ particle/10^6 cell) (Figure 5a,b). Statistically significant increase in EV production is observed following cell culture in STB, with an overall fold increase of 2.2 ± 0.9 relatively to EVs obtained in static systems. Despite low glucose concentration levels were reached on the harvest day in both static and dynamic systems (0.01 ± 0.00 mM and 0.85 ± 0.82 mM, respectively), significantly higher secretion of EVs was observed when MSC were expanded in STB. A recent study by Jeske et al. (Jeske et al., 2022) showed that shear stress associated with cell culture in vertical-wheel bioreactors not only promotes higher EV secretion from MSCs compared to flask-based culture systems, but also modulates their miRNA and protein cargo molecules, including upregulation of several miRNAs that have implications in angiogenesis and wound healing. Additionally, and although not addressed in this study, it is likely that differences in EV secretion levels following cell culture in STB or T-flasks could not solely be attributed to their culture in a dynamic versus static system. Factors such as the overall cell concentration reached in distinct cell culture platforms and the effect of a tighter control of dissolved oxygen or pH, for instance, reached in STB in comparison to static cultures might also play a role.

Besides the importance of selecting adequate cell culture systems to maximize EV yields, and supported by the observations performed by Garcia et al., suggesting the role of low glucose concentration levels on promoting enhanced EV secretion by cardiomyocytes (Garcia et al., 2015), we have investigated if hAT-MSC culture at distinct glucose concentrations could impact their ability to secrete EVs. Of notice, while $5.47 \pm 1.86 \times 10^8$ particle/mL and $4.98 \pm 2.2 \times 10^9$ particle/10^6 cell were obtained in the condition STB + glc, increased EV concentration ($6.58 \pm 1.97 \times 10^8$ particle/mL) and EVs secreted per cell ($6.65 \pm 2.35 \times 10^9$ particle/10^6 cell) was observed for the STB condition (Figure 5a,b), showing an overall increase associated with cell culture at lower glucose concentration. A fold change of 1.2 and 1.4 in EV concentration and secretion per cell, respectively, is observed when hAT-MSCs are cultured in STB without glucose supplementation relatively to STB daily supplemented with glucose. Interestingly, besides the study conducted by Garcia et al. reporting that glucose starvation in cardiomyocytes increased EV secretion (Garcia et al., 2015), simultaneous inhibition of glycolysis and oxidative phosphorylation has also been shown to stimulate secretion of EVs (Ludwig et al., 2020).

Since it is estimated that EV doses per patient would require from 10^{10} to 10^{14} particles, it is critical to maximize EV production in scalable platforms so that the clinical translation of EVs could be extended to a larger number of therapies. Herein, $1.32 \pm 0.39 \times 10^{11}$ EVs were isolated on Day 7 following cell inoculation in 0.2 L STB, suggesting that, depending on the clinical condition to be addressed, 0.1–150 L of conditioned medium would be required to reach clinically relevant EV doses. Nonetheless, it is likely that cell culture in STB, when coupled with bioprocess intensification strategies such as medium perfusion, for instance, could result in higher EV yields and, therefore, contribute to further decrease the batch sizes.

Overall, we have observed that, together with cell expansion in STB, cell culture at low glucose concentration levels can contribute to improve EV manufacturing yields and should therefore be considered when implementing EV production workflows aiming at generating large EV doses for clinical applications.

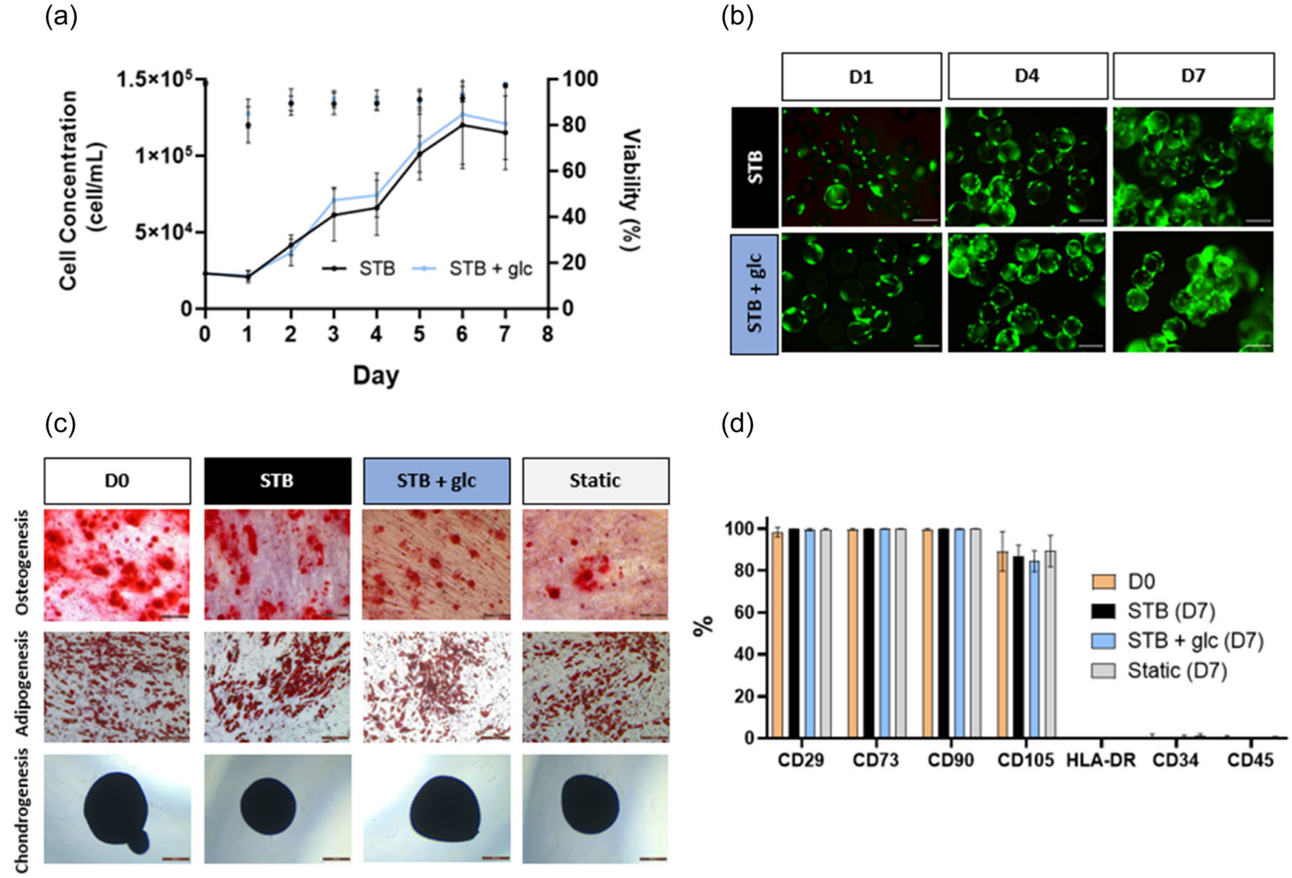

FIGURE 4 Expansion of hAT-MSC in STB. (a) Cell concentration profile throughout 7 days of hAT-MSC culture in stirred-tank bioreactors (both cell concentration and viability of STB and STB + glc conditions are represented). (b) Representative live/dead images of MSC cultured on LC Synthemax™ II microcarriers on Days 1, 4, and 7 following inoculation in STB. Viable cells are depicted in green (FDA stained) whereas dead cells are stained in red by PI. Scale bar = 200 µm. (c) Trilineage differentiation potential of hAT-MSC before and after expansion in STB or static cultures. Osteocytes are stained by Alizarin Red S (calcium deposits), adipocytes are detected by lipid droplet staining with Oil Red O and chondrocytes are detected by Alcian Blue staining of extracellular matrix proteins. Scale bar = 200 µm. (d) Expression of surface markers of hAT-MSC. Error bars represent the standard deviation of the average of 4 (growth curve) or 3 (flow cytometry) independent replicates. FDA, fluorescein diacetate; hAT-MSC, human MSCs, isolated from adipose tissue; MSC, mesenchymal stromal cell; PI, propidium iodide; STB, stirred-tank bioreactors.

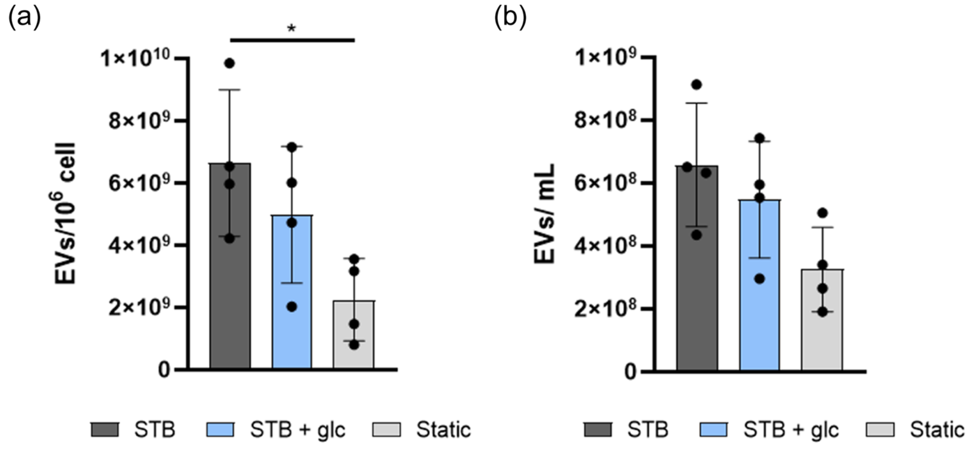

FIGURE 5 hAT-MSC culture in STB at low glucose concentration levels increases EV yields. (a) Average EVs/10^6 cell and (b) EVs/mL following MSC expansion in static and bioreactor culture systems and exposed to distinct concentrations of glucose. Data are represented as mean ± SD ($n = 4$). *$p < 0.05$ indicate significance by one-way ANOVA followed by Tukey's multiple comparison test. ANOVA, analysis of variance; EV, extracellular vesicle; hAT-MSC, human MSCs, isolated from adipose tissue; MSC, mesenchymal stromal cell; SD, standard deviation; STB, stirred-tank bioreactors.

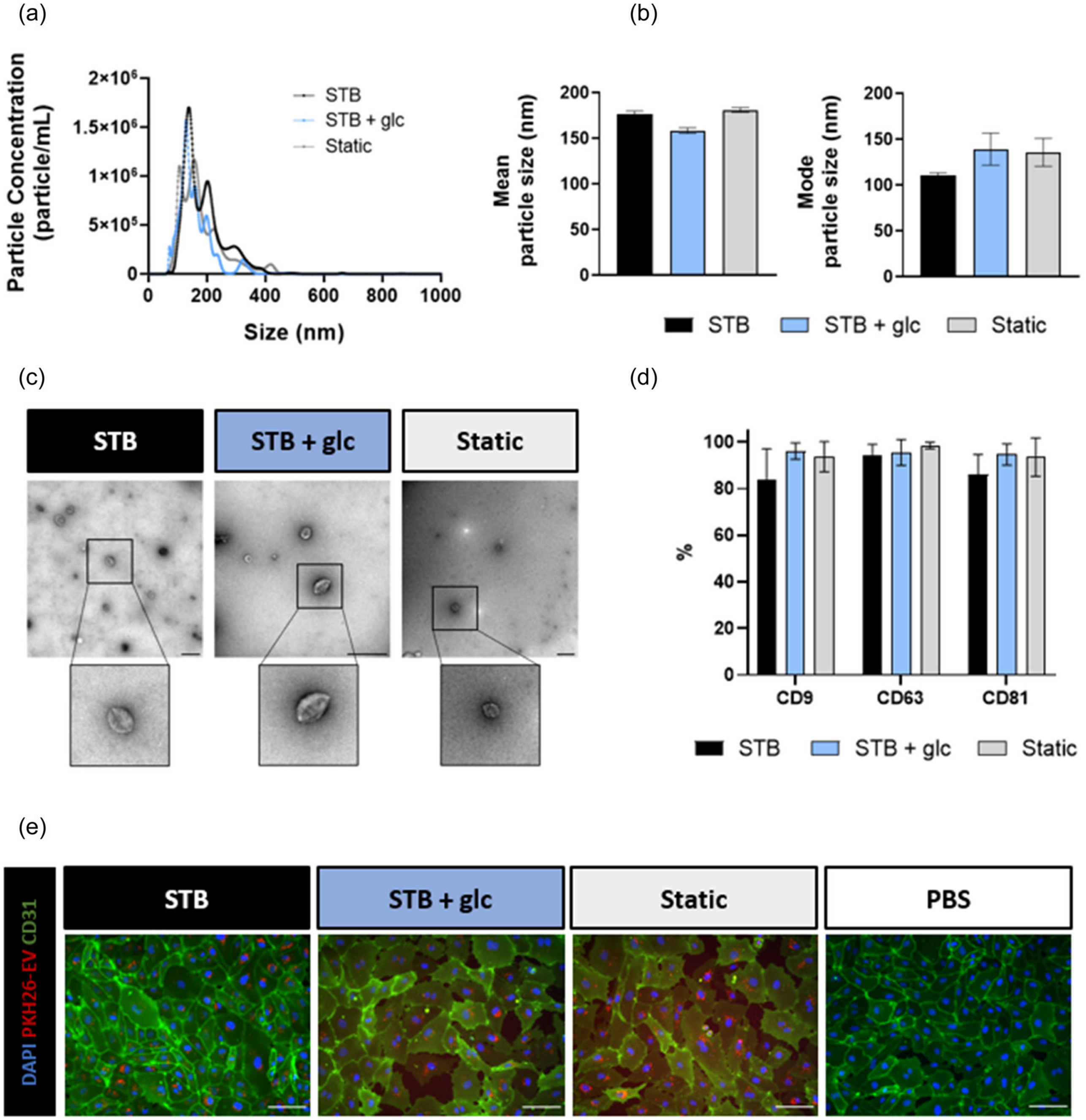

FIGURE 6 Characterization of MSC-derived EVs obtained after cell expansion in STB or in T-flasks and isolated by TFF-SEC. (a) Representative size distribution profiles of MSC-derived EVs analyzed by NTA. (b) Mean and mode particle size (nm) of EVs secreted by MSC following expansion in static or STB. (c) Representative negative staining TEM images of EVs. Scale bar = 500 nm. (d) Flow cytometry analysis of expression of EV characteristic markers CD9, CD63, and CD81. Data are represented as mean ± SD ($n = 3$). (e) Representative immunofluorescence images of PKH26-labeled EVs uptake by HUVECs. HUVECs, stained for the transmembrane protein CD31 (green), were incubated with PKH26-EVs (red-labeled) for 3 h. Cell nuclei were stained with DAPI (blue). Scale bar = 100 μm. DAPI, 4′,6-diamidino-2-phenylindole; EV, extracellular vesicle; HUVECs, human umbilical vein endothelial cells; MSC, mesenchymal stromal cell; NTA, nanoparticle tracking analysis; SD, standard deviation; STB, stirred-tank bioreactors; TEM, transmission electron microscopy; TFF-SEC, tangential flow filtration-size-exclusion chromatography.

3.4 | MSC-derived EVs manufactured in stirred-tank bioreactors retain their quality and reveal improved bioactivity

To meet clinical demands of larger EV doses, besides the selection of adequate upstream and downstream platforms, it is critical that the integration of PAT tools to decrease process variability is accompanied by the manufacture of EV products that are safe and potent. We have therefore characterized EVs regarding their size, identity and therapeutic potential. EVs isolated by TFF-SEC following MSC culture in static flasks or STB were quantified by NTA. Fractions 2–4 of SEC were pooled and concentrated using Amicon 10 kDa. The size of EVs ranged from 50 to

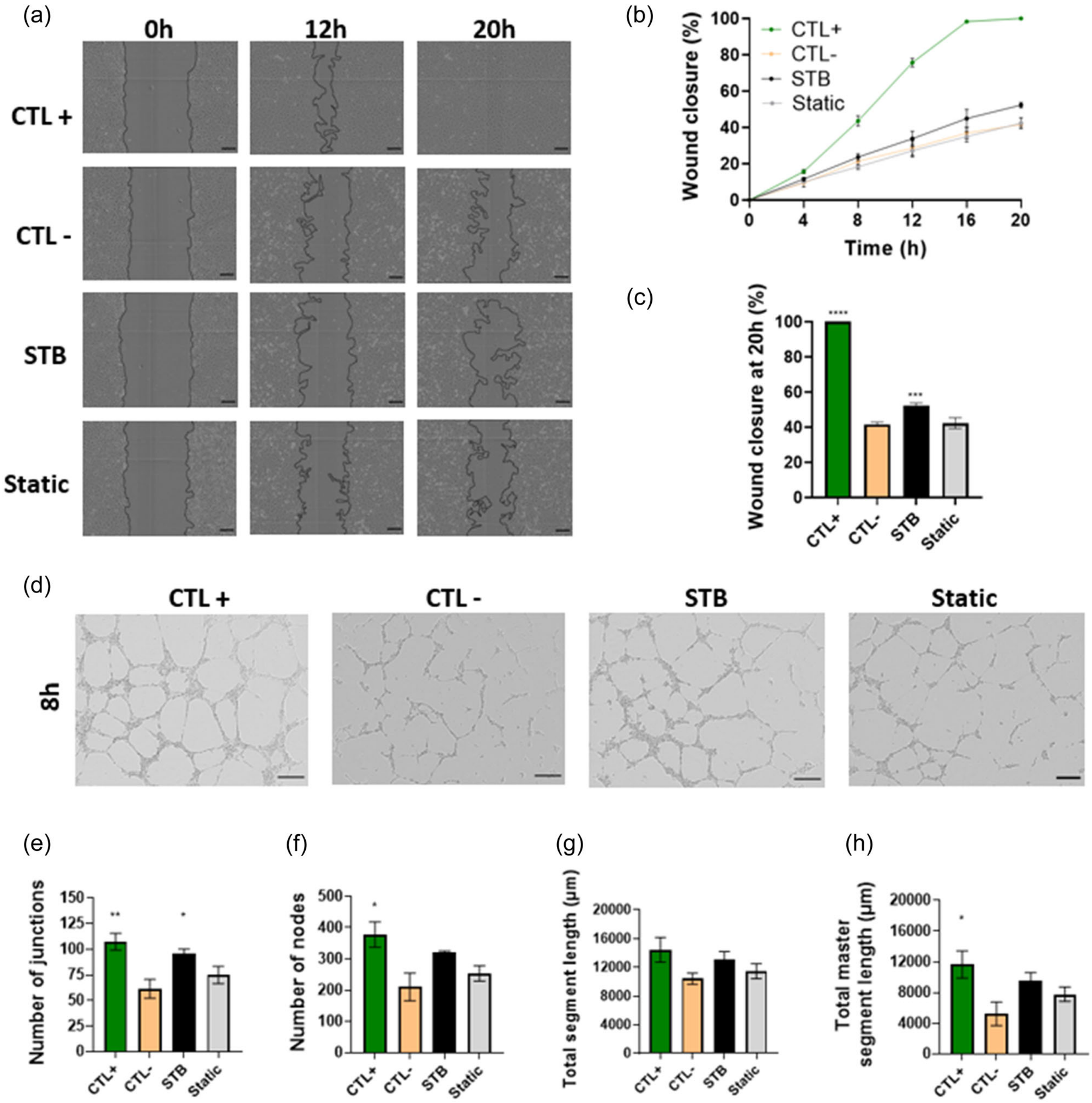

FIGURE 7 MSC-derived EVs promote angiogenesis and migration of HUVECs. (a) Representative images of wound healing assay at 0 h, 12 h, and 20 h postscratch to evaluate HUVEC migration in response to treatment with MSC-derived EVs. Scale bar = 200 µm. (b) Quantification of percentage of wound closure throughout time and (c) at 20 h post-scratch and EV treatment. Wound closure is quantified relatively to the wound area created after mechanical disruption of the HUVECs monolayer. (d) Representative images of tube formation assay following HUVEC incubation with MSC-derived EVs (secreted by cells cultured under static or dynamic conditions) and evaluated 8 h post HUVECs seeding. Scale bar = 200 µm. The ability of MSC-derived EVs (prepared at a concentration of 6000 EVs/HUVEC) to promote tube formation was quantitatively assessed by measuring the number of junctions (e), number of nodes (f), total segment length (g) or total master segment length (h). HUVEC culture in EGM-2 complete medium or basal medium were used as positive and negative controls, respectively. Data are represented as mean ± SD ($n = 2$). $*p < 0.05$, $**p < 0.01$, $***p < 0.001$, $****p < 0.0001$ indicate significance tested relatively to the negative control by one-way ANOVA followed by Tukey's multiple comparison test. EV, extracellular vesicle; HUVECs, human umbilical vein endothelial cells; MSC, mesenchymal stromal cell; SD, standard deviation; STB, stirred-tank bioreactors.

400 nm (Figure 6a), with mean and mode particle sizes ranging between 158–181 nm and 110–139 nm, respectively (Figure 6b).

Trasmitted electron microscopy (TEM) analysis showed that EVs retained their typical cup-shaped morphology (Figure 6c) and EV characteristic expression of the surface markers CD9, CD63 and CD81, assessed by bead-based flow cytometry, was observed for EVs generated following cell culture in both bioreactor and static systems (Figure 6d). Confirming the ability of endothelial cells (HUVECs) to uptake EVs, EVs were labeled with PKH26, a dye that is integrated in the lipidic membrane of EVs. Fluorescence images indicate that EVs from all groups were internalized by the recipient cells 3 h after their addition (Figure 6e).

To assess the proangiogenic and migration potential of HUVECs in response to EV signaling, wound healing (Figure 7a–c) and tube formation (Figure 7d–h) assays were performed. Interestingly, only EVs secreted by MSCs cultured in STB increased cell migration (Figure 7b,c), resulting in a wound closure, 20 h after EV treatment, of 52.3 ± 1.5% relatively to the lower level obtained following HUVECs incubation with EVs derived from MSC static culture (42.3 ± 3.1%), and similarly to the levels obtained in the negative control, basal medium with 0.1% (v/v) FBS (41.7 ± 1.1%). However, both EVs secreted by cells cultured in T-flasks or STB induced the formation of capillary-like structures in vitro. Despite EV treatment promoting an increase in the number of nodes and longer segments, statistical significance was only observed for EVs manufactured in STB regarding their ability to promote the formation of a more interconnected network of tubes, as evidenced by the higher number of junctions when compared to basal medium alone (Figure 7d–h).

Our results indicate that hAT-MSC-derived EVs produced in STB can promote an increase in both capillary-like tube formation and cell migration to a greater extent when compared to EVs derived from static culture conditions. Therefore, besides the higher EV yields when lower glucose concentration levels are reached in STB, these data suggests that, in agreement with previous studies (Jeske et al., 2022), EVs manufactured under stirred culture conditions have enhanced bioactivity in wound healing settings. Indeed, previous studies have reported that MSC-derived EV's angiogenic potential rely mainly on their capacity to release bioactive molecules, such as vascular endothelial growth factor (VEGF), platelet-derived growth factor (PDGF), and transforming growth factor-β (TGF-β), which have been shown to promote modulation of the angiogenic phenotype of endothelial cells (Maacha et al., 2020). Additionally, Garcia et. al. (Garcia et al., 2015) showed that cardiomyocytes, in the presence of low concentration of glucose, not only produced a higher amount of EVs but also showed that glucose starvation modulates EV cargo molecules. Of particular interest, these EVs overexpressed several miRNAs (miRNA-17, miRNA-19, miRNA-20, and miRNA-126) that stimulate phenotypical and functional changes in endothelial cells and, therefore, promote angiogenesis (Landskroner-Eiger et al., 2013). Subsequent experiments should focus on dissecting the transcriptome and proteome of EVs secreted by hAT-MSCs subjected to distinct stimuli (stirred vs. static cell culture, higher vs. lower glucose concentration microenvironment) to gain insight into the specific signals directed to cells that are responsible for the angiogenic potential of the manufactured EVs.

4 | CONCLUSIONS

The ability of EVs to efficiently deliver biologically active molecules to target recipient cells turns them into a drug delivery modality with huge therapeutic potential. However, progress in the EV field is limited by the scalability and GMP-compliance of the platforms that are currently used to manufacture EVs. Herein, we have shown that TFF-SEC protocol yielded 5 times higher number of EV comparatively to conditioned medium processed by DG-UC. Additionally, while higher EV yields were obtained when cell expansion is performed in STB in comparison to EVs secreted by cells cultured under static conditions (overall fold increase of 2.2 ± 0.9), the role of metabolic preconditioning to maximize EV yields was highlighted in a scalable bioprocess supported by cell expansion in stirred-tank bioreactors. Therefore, we propose the use of PAT tools, such as Raman Spectroscopy, to help designing reproducible bioprocesses where the time of collection of the condition medium, supported by continuously tracking metabolite levels in STB, is selected to maximize cell expansion and EV secretion yields.

ACKNOWLEDGMENTS

The authors acknowledge A.L. Sousa and E.M. Tranfield from the Electron Microscopy Facility at the IGC for the transmission electron microscopy work. Rafael Fernandes, from Endress-Hauser, is also acknowledged for his support during the Raman spectroscopy studies. This work was supported by EU Interreg Sudoe—funded project CardioPatch (SOE4/P1/E1063), iNOVA4Health—UIDB/04462/2020 and UIDP/04462/2020, a program financially supported by FCT/Ministério da Ciência, Tecnologia e Ensino Superior, through national funds. The Associate Laboratory LS4FUTURE (LA/P/0087/2020) is also acknowledged.

DATA AVAILABILITY STATEMENT

The data that support the findings of this study are available from the corresponding author upon reasonable request.

ORCID

Marta H. G. Costa https://orcid.org/0000-0003-3356-725X
Inês A. Isidro http://orcid.org/0000-0002-0237-5805

REFERENCES

Abels, E. R., & Breakefield, X. O. (2016). Introduction to extracellular vesicles: Biogenesis, RNA cargo selection, content, release, and uptake. *Cellular and Molecular Neurobiology*, *36*(3), 301–312. https://doi.org/10.1007/s10571-016-0366-z.Introduction

Adlerz, K., Patel, D., Rowley, J., Ng, K., & Ahsan, T. (2020). Strategies for scalable manufacturing and translation of MSC-derived extracellular vesicles. *Stem Cell Research*, *48*, 101978. https://doi.org/10.1016/j.scr.2020.101978

Banks, W. A., Sharma, P., Bullock, K. M., Hansen, K. M., Ludwig, N., & Whiteside, T. L. (2020). Transport of extracellular vesicles across the blood-brain barrier: Brain pharmacokinetics and effects of inflammation. *International Journal of Molecular Sciences*, *21*(12), 4407. https://doi.org/10.3390/ijms21124407

Baradez, M.-O., Biziato, D., Hassan, E., & Marshall, D. (2018). Application of Raman spectroscopy and univariate modelling as a process analytical technology for cell therapy bioprocessing. *Frontiers in Medicine*, *5*, 47. https://doi.org/10.3389/fmed.2018.00047

Bellani, C. F., Ajeian, J., Duffy, L., Miotto, M., Groenewegen, L., & Connon, C. J. (2020). Scale-up technologies for the manufacture of adherent cells. *Frontiers in Nutrition*, *4*(7), 575146. https://doi.org/10.3389/fnut.2020.575146

Bellio, M. A., Kanashiro-Takeuchi, R. M., Takeuchi, L., Kulandavelu, S., Lee, Y.-S., Balkan, W., Young, K. C., Hare, J. M., & Khan, A. (2022). Systemic delivery of large-scale manufactured Wharton's jelly mesenchymal stem cell-derived extracellular vesicles improves cardiac function after myocardial infarction. *The Journal of Cardiovascular Aging*, *2*, 9. https://doi.org/10.20517/jca.2021.21

Buckley, K., & Ryder, A. G. (2017). Applications of Raman spectroscopy in biopharmaceutical manufacturing: A short review. *Applied Spectroscopy*, *71*(6), 1085–1116. https://doi.org/10.1177/0003702817703270

Carpentier, G., Berndt, S., Ferratge, S., Rasband, W., Cuendet, M., Uzan, G., & Albanese, P. (2020). Angiogenesis analyzer for ImageJ—A comparative morphometric analysis of "endothelial tube formation assay" and "fibrin bead assay". *Scientific Reports*, *10*(1), 11568. https://doi.org/10.1038/s41598-020-67289-8

Cases-Perera, O., Blanco-Elices, C., Chato-Astrain, J., Miranda-Fernández, C., Campos, F., Crespo, P. V., Sánchez-Montesinos, I., Alaminos, M., Martín-Piedra, M. A., & Garzón, I. (2022). Development of secretome-based strategies to improve cell culture protocols in tissue engineering. *Scientific Reports*, *12*(1), 10003. https://doi.org/10.1038/s41598-022-14115-y

Collino, F., Lopes, J. A., Corrêa, S., Abdelhay, E., Takiya, C. M., Wendt, C. H. C., de Miranda, K. R., Vieyra, A., & Lindoso, R. S. (2019). Adipose-derived mesenchymal stromal cells under hypoxia: Changes in extracellular vesicles secretion and improvement of renal recovery after ischemic injury. *Cellular Physiology and Biochemistry*, *52*(6), 1463–1483. https://doi.org/10.33594/000000102

Corso, G., Mäger, I., Lee, Y., Görgens, A., Bultema, J., Giebel, B., Wood, M. J. A., Nordin, J. Z., & Andaloussi, S. E. (2017). Reproducible and scalable purification of extracellular vesicles using combined bind-elute and size exclusion chromatography. *Scientific Reports*, *7*(1), 11561. https://doi.org/10.1038/s41598-017-10646-x

Costa, M. H. G., McDevitt, T. C., Cabral, J. M. S., da Silva, C. L., & Ferreira, F. C. (2017). Tridimensional configurations of human mesenchymal stem/stromal cells to enhance cell paracrine potential towards wound healing processes. *Journal of Biotechnology*, *262*, 28–39. https://doi.org/10.1016/j.jbiotec.2017.09.020

Cunha, B., Aguiar, T., Carvalho, S. B., Silva, M. M., Gomes, R. A., Carrondo, M. J. T., Gomes-Alves, P., Peixoto, C., Serra, M., & Alves, P. M. (2017). Bioprocess integration for human mesenchymal stem cells: From up to downstream processing scale-up to cell proteome characterization. *Journal of Biotechnology*, *248*, 87–98. https://doi.org/10.1016/j.jbiotec.2017.01.014

Cunha, B., Aguiar, T., Silva, M. M., Silva, R. J. S., Sousa, M. F. Q., Pineda, E., Peixoto, C., Carrondo, M. J. T., Serra, M., & Alves, P. M. (2015). Exploring continuous and integrated strategies for the up- and downstream processing of human mesenchymal stem cells. *Journal of Biotechnology*, *213*, 97–108. https://doi.org/10.1016/j.jbiotec.2015.02.023

de Almeida Fuzeta, M., Bernardes, N., Oliveira, F. D., Costa, A. C., Fernandes-Platzgummer, A., Farinha, J. P., Rodrigues, C. A. V., Jung, S., Tseng, R. J., Milligan, W., Lee, B., Castanho, M. A. R. B., Gaspar, D., Cabral, J. M. S., & da Silva, C. L. (2020). Scalable production of human mesenchymal stromal cell-derived extracellular vesicles under serum-/xeno-free conditions in a microcarrier-based bioreactor culture system. *Frontiers in Cell and Developmental Biology*, *8*, 553444. https://doi.org/10.3389/fcell.2020.553444

Dominici, M., Le Blanc, K., Mueller, I., Slaper-Cortenbach, I., Marini, F. C., Krause, D. S., Deans, R. J., Keating, A., Prockop, D. J., & Horwitz, E. M. (2006). Minimal criteria for defining multipotent mesenchymal stromal cells. The International Society for Cellular Therapy position statement. *Cytotherapy*, *8*(4), 315–317. https://doi.org/10.1080/14653240600855905

Finn, J., & Konstantinov, K. (2020). Exosome-based therapeutics: Ready for prime time. *Cell and Gene Therapy Insights*, *6*(4), 597–605. https://doi.org/10.18609/cgti.2020.070

Fu, Y., Karbaat, L., Wu, L., Leijten, J., Both, S. K., & Karperien, M. (2017). Trophic effects of mesenchymal stem cells. *Tissue Engineering Part B: Reviews*, *23*(6), 515–528. https://doi.org/10.1089/ten.TEB.2016.0365

Galderisi, U., Peluso, G., & Di Bernardo, G. (2022). Clinical trials based on mesenchymal stromal cells are exponentially increasing: Where are we in recent years. *Stem Cell Reviews and Reports*, *18*(1), 23–36. https://doi.org/10.1007/s12015-021-10231-w

Gámez-Valero, A., Monguió-Tortajada, M., Carreras-Planella, L., Franquesa, M., Beyer, K., & Borràs, F. E. (2016). Size-exclusion chromatography-based isolation minimally alters extracellular vesicles' characteristics compared to precipitating agents. *Scientific Reports*, *6*(1), 33641. https://doi.org/10.1038/srep33641

Garcia, N. A., Ontoria-Oviedo, I., González-King, H., Diez-Juan, A., & Sepúlveda, P. (2015). Glucose starvation in cardiomyocytes enhances exosome secretion and promotes angiogenesis in endothelial cells. *PLoS One*, *10*(9), e0138849. https://doi.org/10.1371/journal.pone.0138849

Gardiner, C., Vizio, D. D., Sahoo, S., Théry, C., Witwer, K. W., Wauben, M., & Hill, A. F. (2016). Techniques used for the isolation and characterization of extracellular vesicles: Results of a worldwide survey. *Journal of Extracellular Vesicles*, *5*(1), 32945. https://doi.org/10.3402/jev.v5.32945

Gerzon, G., Sheng, Y., & Kirkitadze, M. (2022). Process analytical technologies – advances in bioprocess integration and future perspectives. *Journal of Pharmaceutical and Biomedical Analysis*, *207*, 114379. https://doi.org/10.1016/j.jpba.2021.114379

Gobin, J., Muradia, G., Mehic, J., Westwood, C., Couvrette, L., Stalker, A., Bigelow, S., Luebbert, C. C., Bissonnette, F. S., Johnston, M., Sauvé, S., Tam, R. Y., Wang, L., Rosu-Myles, M., & Lavoie, J. R. (2021). Hollow-fiber bioreactor production of extracellular vesicles from human bone marrow mesenchymal stromal cells yields nanovesicles that mirrors the immuno-modulatory antigenic signature of the producer cell. *Stem Cell Research & Therapy*, *12*(1), 127. https://doi.org/10.1186/s13287-021-02190-3

Gottipamula, S., Muttigi, M. S., Kolkundkar, U., & Seetharam, R. N. (2013). Serum-free media for the production of human mesenchymal stromal cells: A review. *Cell Proliferation*, *46*(6), 608–627. https://doi.org/10.1111/cpr.12063

Haraszti, R. A., Miller, R., Stoppato, M., Sere, Y. Y., Coles, A., Didiot, M.-C., Wollacott, R., Sapp, E., Dubuke, M. L., Li, X., Shaffer, S. A., DiFiglia, M., Wang, Y., Aronin, N., & Khvorova, A. (2018). Exosomes produced from 3D cultures of MSCs by tangential flow filtration show higher yield and improved activity. *Molecular Therapy*, *26*(12), 2838–2847. https://doi.org/10.1016/j.ymthe.2018.09.015

Herrmann, I. K., Wood, M. J. A., & Fuhrmann, G. (2021). Extracellular vesicles as a next-generation drug delivery platform. *Nature Nanotechnology*, *16*(7), 748–759. https://doi.org/10.1038/s41565-021-00931-2

Isidro, I. A., Vicente, P., Pais, D. A. M., Almeida, J. I., Domingues, M., Abecasis, B., Zapata-Linares, N., Rodriguez-Madoz, J. R., Prosper, F., Aspegren, A., Alves, P. M., & Serra, M. (2021). Online monitoring of hiPSC expansion and hepatic differentiation in 3D culture by dielectric spectroscopy. *Biotechnology and Bioengineering*, *118*(9), 3610–3617. https://doi.org/10.1002/bit.27751

Jalilian, E., Massoumi, H., Bigit, B., Amin, S., Katz, E. A., Guaiquil, V. H., Anwar, K. N., Hematti, P., Rosenblatt, M. I., & Djalilian, A. R. (2022). Bone marrow mesenchymal stromal cells in a 3D system produce higher concentration of extracellular vesicles (EVs) with increased complexity and enhanced neuronal growth properties. *Stem Cell Research & Therapy*, *13*(1), 425. https://doi.org/10.1186/s13287-022-03128-z

Jeske, R., Liu, C., Duke, L., Canonicco Castro, M. L., Muok, L., Arthur, P., Singh, M., Jung, S., Sun, L., & Li, Y. (2022). Upscaling human mesenchymal stromal cell production in a novel vertical-wheel bioreactor enhances extracellular vesicle secretion and cargo profile. *Bioactive Materials*, X22002997. https://doi.org/10.1016/j.bioactmat.2022.07.004

Kim, J. Y., Rhim, W.-K., Yoo, Y.-I., Kim, D.-S., Ko, K.-W., Heo, Y., Park, C. G., & Han, D. K. (2021). Defined MSC exosome with high yield and purity to improve regenerative activity. *Journal of Tissue Engineering*, *12*, 204173142110086. https://doi.org/10.1177/20417314211008626

King, H. W., Michael, M. Z., & Gleadle, J. M. (2012). Hypoxic enhancement of exosome release by breast cancer cells. *BMC Cancer*, *12*(1), 421. https://doi.org/10.1186/1471-2407-12-421

Kordelas, L., Rebmann, V., Ludwig, A.-K., Radtke, S., Ruesing, J., Doeppner, T. R., Epple, M., Horn, P. A., Beelen, D. W., & Giebel, B. (2014). MSC-derived exosomes: A novel tool to treat therapy-refractory graft-versus-host disease. *Leukemia*, *28*(4), 970–973. https://doi.org/10.1038/leu.2014.41

Kumar, L. P. K., Kandoi, S., Misra, R., S, V., K, R., & Verma, R. S. (2019). The mesenchymal stem cell secretome: A new paradigm towards cell-free therapeutic mode in regenerative medicine. *Cytokine & Growth Factor Reviews*, *46*, 1–9. https://doi.org/10.1016/j.cytogfr.2019.04.002

Landskroner-Eiger, S., Moneke, I., & Sessa, W. C. (2013). MiRNAs as modulators of angiogenesis. *Cold Spring Harbor Perspectives in Medicine*, *3*(2):a006643. https://doi.org/10.1101/cshperspect.a006643

Lobb, R. J., Becker, M., Wen Wen, S., Wong, C. S. F., Wiegmans, A. P., Leimgruber, A., & Möller, A. (2015). Optimized exosome isolation protocol for cell culture supernatant and human plasma. *Journal of Extracellular Vesicles*, *4*(1), 27031. https://doi.org/10.3402/jev.v4.27031

Louro, A. F., Paiva, M. A., Oliveira, M. R., Kasper, K. A., Alves, P. M., Gomes-Alves, P., & Serra, M. (2022). Bioactivity and miRNome profiling of native extracellular vesicles in human induced pluripotent stem cell-cardiomyocyte differentiation. *Advanced Science*, *9*(15), 2104296. https://doi.org/10.1002/advs.202104296

Ludwig, N., Yerneni, S. S., Menshikova, E. V., Gillespie, D. G., Jackson, E. K., & Whiteside, T. L. (2020). Simultaneous inhibition of glycolysis and oxidative phosphorylation triggers a multi-fold increase in secretion of exosomes: Possible role of 2′,3′-cAMP. *Scientific Reports*, *10*(1), 6948. https://doi.org/10.1038/s41598-020-63658-5

Maacha, S., Sidahmed, H., Jacob, S., Gentilcore, G., Calzone, R., Grivel, J.-C., & Cugno, C. (2020). Paracrine mechanisms of mesenchymal stromal cells in angiogenesis. *Stem Cells International*, *2020*, 1–12. https://doi.org/10.1155/2020/4356359

Momen-Heravi, F., Bala, S., Kodys, K., & Szabo, G. (2015). Exosomes derived from alcohol-treated hepatocytes horizontally transfer liver specific miRNA-122 and sensitize monocytes to LPS. *Scientific Reports*, *5*(1), 9991. https://doi.org/10.1038/srep09991

Ng, C. Y., Kee, L. T., Al-Masawa, M. E., Lee, Q. H., Subramaniam, T., Kok, D., Ng, M. H., & Law, J. X. (2022). Scalable production of extracellular vesicles and its therapeutic values: A review. *International Journal of Molecular Sciences*, *23*(14), 7986. https://doi.org/10.3390/ijms23147986

Ng, K. S., Smith, J. A., McAteer, M. P., Mead, B. E., Ware, J., Jackson, F. O., Carter, A., Ferreira, L., Bure, K., Rowley, J. A., Reeve, B., Brindley, D. A., & Karp, J. M. (2019). Bioprocess decision support tool for scalable manufacture of extracellular vesicles. *Biotechnology and Bioengineering*, *116*(2), 307–319. https://doi.org/10.1002/bit.26809

Paolini, L., Monguió-Tortajada, M., Costa, M., Antenucci, F., Barilani, M., Clos-Sansalvador, M., Andrade, A. C., Driedonks, T. A. P., Giancaterino, S., Kronstadt, S. M., Mizenko, R. R., Nawaz, M., Osteikoetxea, X., Pereira, C., Shrivastava, S., Boysen, A. T., van de Wakker, S. I., van Herwijnen, M. J. C., Wang, X., … Bergese, P. (2022). Large-scale production of extracellular vesicles: Report on the "massivEVs" ISEV workshop. *Journal of Extracellular Biology*, *1*, e63.

Patel, D. B., Luthers, C. R., Lerman, M. J., Fisher, J. P., & Jay, S. M. (2019). Enhanced extracellular vesicle production and ethanol-mediated vascularization bioactivity via a 3D-printed scaffold-perfusion bioreactor system. *Acta Biomaterialia*, *95*, 236–244. https://doi.org/10.1016/j.actbio.2018.11.024

Phinney, D. G., & Pittenger, M. F. (2017). Concise review: MSC-derived exosomes for cell-free therapy. *Stem Cells*, *35*(4), 851–858. https://doi.org/10.1002/stem.2575

Reiner, A. T., Witwer, K. W., van Balkom, B. W. M., de Beer, J., Brodie, C., Corteling, R. L., Gabrielsson, S., Gimona, M., Ibrahim, A. G., de Kleijn, D., Lai, C. P., Lötvall, J., del Portillo, H. A., Reischl, I. G., Riazifar, M., Salomon, C., Tahara, H., Toh, W. S., Wauben, M. H. M., … Lim, S. K. (2017). Concise review: Developing best-practice models for the therapeutic use of extracellular vesicles. *Stem Cells Translational Medicine*, *6*(8), 1730–1739. https://doi.org/10.1002/sctm.17-0055

Rodríguez-Fuentes, D. E., Fernández-Garza, L. E., Samia-Meza, J. A., Barrera-Barrera, S. A., Caplan, A. I., & Barrera-Saldaña, H. A. (2021). Mesenchymal stem cells current clinical applications: A systematic review. *Archives of Medical Research*, *52*(1), 93–101. https://doi.org/10.1016/j.arcmed.2020.08.006

Saha, B., Momen-Heravi, F., Kodys, K., & Szabo, G. (2016). MicroRNA cargo of extracellular vesicles from alcohol-exposed monocytes signals naive monocytes to differentiate into M2 macrophages. *Journal of Biological Chemistry*, *291*(1), 149–159. https://doi.org/10.1074/jbc.M115.694133

Saleh, A. F., Lázaro-Ibáñez, E., Forsgard, M. A.-M., Shatnyeva, O., Osteikoetxea, X., Karlsson, F., Heath, N., Ingelsten, M., Rose, J., Harris, J., Mairesse, M., Bates, S. M., Clausen, M., Etal, D., Leonard, E., Fellows, M. D., Dekker, N., & Edmunds, N. (2019). Extracellular vesicles induce minimal hepatotoxicity and immunogenicity, *Nanoscale* 11(14), 6990–7001. https://doi.org/10.1039/C8NR08720B

Salomon, C., Ryan, J., Sobrevia, L., Kobayashi, M., Ashman, K., Mitchell, M., & Rice, G. E. (2013). Exosomal signaling during hypoxia mediates microvascular endothelial cell migration and vasculogenesis. *PLoS One*, *8*(7), e68451. https://doi.org/10.1371/journal.pone.0068451

Schindelin, J., Arganda-Carreras, I., Frise, E., Kaynig, V., Longair, M., Pietzsch, T., Preibisch, S., Rueden, C., Saalfeld, S., Schmid, B., Tinevez, J.-Y., White, D. J., Hartenstein, V., Eliceiri, K., Tomancak, P., & Cardona, A. (2012). Fiji: An open-source platform for biological-image analysis. *Nature Methods*, *9*(7), 676–682. https://doi.org/10.1038/nmeth.2019

Théry, C., Witwer, K. W., Aikawa, E., Alcaraz, M. J., Anderson, J. D., Andriantsitohaina, R., Antoniou, A., Arab, T., Archer, F., Atkin-Smith, G. K., Ayre, D. C., Bach, J.-M., Bachurski, D., Baharvand, H., Balaj, L., Baldacchino, S., Bauer, N. N., Baxter, A. A., Bebawy, M., … Jovanovic-Talisman, T. (2018). Minimal information for studies of extracellular vesicles 2018 (MISEV2018): A position statement of the International Society for Extracellular Vesicles and update of the MISEV2014 guidelines. *Journal of Extracellular Vesicles*, *7*(1), 1535750. https://doi.org/10.1080/20013078.2018.1535750

Van Deun, J., Mestdagh, P., Sormunen, R., Cocquyt, V., Vermaelen, K., Vandesompele, J., Bracke, M., De Wever, O., & Hendrix, A. (2014). The impact of disparate isolation methods for extracellular vesicles on downstream RNA profiling. *Journal of Extracellular Vesicles*, *3*(1), 24858. https://doi.org/10.3402/jev.v3.24858

Watson, D. C., Yung, B. C., Bergamaschi, C., Chowdhury, B., Bear, J., Stellas, D., Morales-Kastresana, A., Jones, J. C., Felber, B. K., Chen, X., & Pavlakis, G. N. (2018). Scalable, cGMP-compatible purification of extracellular vesicles carrying bioactive human heterodimeric IL-15/lactadherin complexes. *Journal of Extracellular Vesicles*, *7*(1), 1442088. https://doi.org/10.1080/20013078.2018.1442088

Wen, Y., Chen, Y., Wang, G., Abhange, K., Xue, F., Quinn, Z., Mao, W., & Wan, Y. (2020). Factors influencing the measurement of the secretion rate of extracellular vesicles. *The Analyst*, *145*(17), 5870–5877. https://doi.org/10.1039/D0AN01199A

Willis, G. R., Kourembanas, S., & Mitsialis, S. A. (2017). Toward exosome-based therapeutics: Isolation, heterogeneity, and fit-for-purpose potency. *Frontiers in Cardiovascular Medicine*, *4*, 63. https://doi.org/10.3389/fcvm.2017.00063

Xue, C., Shen, Y., Li, X., Li, B., Zhao, S., Gu, J., Chen, Y., Ma, B., Wei, J., Han, Q., & Zhao, R. C. (2018). Exosomes derived from hypoxia-treated human adipose mesenchymal stem cells enhance angiogenesis through the PKA signaling pathway. *Stem Cells and Development*, *27*(7), 456–465. https://doi.org/10.1089/scd.2017.0296

Yue, B., Yang, H., Wang, J., Ru, W., Wu, J., Huang, Y., Lan, X., Lei, C., & Chen, H. (2020). Exosome biogenesis, secretion and function of exosomal miRNAs in skeletal muscle myogenesis. *Cell Proliferation*, *53*(7). https://doi.org/10.1111/cpr.12857

Zhao, Z., Wijerathne, H., Godwin, A. K., & Soper, S. A. (2021). Isolation and analysis methods of extracellular vesicles (EVs). *Extracellular Vesicles and Circulating Nucleic Acids*. https://doi.org/10.20517/evcna.2021.07

Zhu, J., Lu, K., Zhang, N., Zhao, Y., Ma, Q., Shen, J., Lin, Y., Xiang, P., Tang, Y., Hu, X., Chen, J., Zhu, W., Webster, K. A., Wang, J., & Yu, H. (2018). Myocardial reparative functions of exosomes from mesenchymal stem cells are enhanced by hypoxia treatment of the cells via transferring microRNA-210 in an nSMase2-dependent way. *Artificial Cells, Nanomedicine, and Biotechnology*, *46*(8), 1659–1670. https://doi.org/10.1080/21691401.2017.1388249.Myocardial

SUPPORTING INFORMATION

Additional supporting information can be found online in the Supporting Information section at the end of this article.

JIPB Journal of Integrative Plant Biology

New Technology
https://doi.org/10.1111/jipb.13181

Effective methods for isolation and purification of extracellular vesicles from plants

Yifan Huang[1,2], Shumei Wang[3], Qiang Cai[1,2]* and Hailing Jin[3]*

1. State Key Laboratory of Hybrid Rice, College of Life Science, Wuhan University, Wuhan 430072, China
2. Hubei Hongshan Laboratory, Wuhan 430072, China
3. Department of Microbiology and Plant Pathology and Center for Plant Cell Biology, Institute for Integrative Genome Biology, University of California, Riverside, CA 92507, USA

*Correspondences: Qiang Cai (qiang.cai@whu.edu.cn); Hailing Jin (hailingj@ucr.edu). Both Drs. Cai and Jin are responsible for the distribution of the materials associated with this article

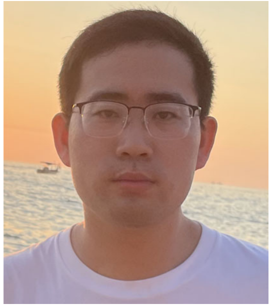
Yifan Huang


Hailing Jin

ABSTRACT

Plant extracellular vesicles (EVs) play critical roles in the cross-kingdom trafficking of molecules from hosts to interacting microbes, most notably in plant defense responses. However, the isolation of pure, intact EVs from plants remains challenging. A variety of methods have been utilized to isolate plant EVs from apoplastic washing fluid (AWF). Here, we compare published plant EV isolation methods, and provide our recommended method for the isolation and purification of plant EVs. This method includes a detailed protocol for clean AWF collection from *Arabidopsis thaliana* leaves, followed by EV isolation via differential centrifugation. To further separate and purify specific subclasses of EVs from heterogeneous vesicle populations, density gradient ultracentrifugation and immunoaffinity capture are then utilized. We found that immunoaffinity capture is the most precise method for specific EV subclass isolation when suitable specific EV biomarkers and their corresponding antibodies are available. Overall, this study provides a guide for the selection and optimization of EV isolation methods for desired downstream applications.

Keywords: cell-to-cell communication, extracellular vesicles, isolation methods, plants interacting with pathogens

Huang, Y., Wang, S., Cai, Q., and Jin, H. (2021). Effective methods for isolation and purification of extracellular vesicles from plants. J. Integr. Plant Biol. **63:** 2020–2030.

INTRODUCTION

Cell-to-cell communication between plants and pathogens requires the secretion and delivery of molecular signals into extracellular environments and their subsequent transport into interacting organisms. This process is critical for both plant defense and pathogen virulence (Kimura et al., 2001; Mahlapuu et al., 2016; Toruno et al., 2016). Recent studies have demonstrated that RNAs, including regulatory small RNAs (sRNAs), are able to move between pathogens and their hosts and regulate biological processes in recipient cells (Knip et al., 2014; Zhang et al., 2016b; Cai et al., 2018, 2019b; Huang et al., 2019). Previously, the mechanisms underlying sRNA movement through multiple barriers and into the opposing host or fungal cells were largely unknown. However, recent studies have shown that extracellular vesicles (EVs) can traffic sRNAs from plants to their pathogens (Cai et al., 2018). Plant EVs have also generated further interest because of their numerous functions in bioactive molecule exchange and cell-to-cell communication (Mathieu et al., 2019; Cai et al., 2021; Kameli et al., 2021).

EVs are small, lipid bilayer-enclosed vesicles containing various protein and RNA cargoes, and are released by cells of both eukaryotic and prokaryotic organisms into the extracellular space (Colombo et al., 2014; van Niel et al., 2018). EVs are a heterogeneous group of vesicles with different sizes and intracellular origins. For example, exosomes, microvesicles and apoptotic bodies each represent a major class of EVs, and originate from multivesicular bodies (MVBs), the plasma membrane, or apoptotic cells during apoptosis, respectively (Akers et al., 2013; Colombo et al., 2014; van Niel et al., 2018). In plants, EVs were initially observed in carrot cell cultures by transmission electron microscopy (TEM) in 1967 (Halperin and Jensen, 1967). Since then, plant EVs have been observed in plant–fungal interaction sites by TEM, such as in *Blumeria graminis f.* sp. *hordei* infected barley epidermal cells (An et al., 2006a, 2006b), *Botrytis cinerea*-infected *Arabidopsis* leaf cells (Cai et al., 2018), and *Rhizophagus irregularis* arbuscules in rice root (Roth et al., 2019). Transmission electron microscopy and confocal microscopy have both identified plant MVBs fused with the plasma membrane at fungal or oomycete invasion sites, suggesting that plant exosomes are released by MVB mediated secretion (An et al., 2006a, 2006b, 2007; Nielsen et al., 2012; Bozkurt et al., 2014; Cai et al., 2018).

It is worth noting that plant EVs are nanovesicles primarily from the apoplastic washing fluid (AWF). However, nanovesicles isolated from disrupted whole leaf tissue are not pure EVs, as they contain cytoplasmic intracellular membrane contaminants (Liu et al., 2020). Currently, plant EVs have been isolated from the AWF of several plant tissues, including *Arabidopsis* leaves (Rutte and Innes, 2017; Cai et al., 2018; He et al., 2021), sunflower seeds and seedlings (Regente et al., 2009, 2017), and *Nicotiana benthamiana* leaves (Movahed et al., 2019). In *Arabidopsis* leaves, to our knowledge, at least three known EV subtypes exist: Tetraspanin (TET) 8-positive EVs derived from MVBs, which can be considered plant exosomes (Cai et al., 2018, 2021), Penetration 1 (PEN1)-positive EVs (Rutte and Innes, 2017), and EVs produced by exocyst-positive organelle's (EXPO) fusion with the plasma membrane (Wang et al., 2010; Ding et al., 2014). Recent work has shown that endogenous sRNAs are secreted by plant EVs as a defense mechanism against fungal pathogens (Cai et al., 2018). Further efforts revealed that TET8-positive exosomes are the major class of plant EVs responsible for sRNA transport, along with several RNA binding proteins which contribute to sRNA selective loading and stabilization in EVs (He et al., 2021).

Numerous methods for the isolation of EVs in mammalian systems have been developed in the last decade. Of these methods, separation by differential centrifugation is considered the standard, specifically for the isolation of small EVs or exosomes (Thery et al., 2006; Mathivanan et al., 2012). This method has several substeps, including centrifugation at 300 × *g* to sediment cells, at 2,000 × *g* to remove dead cells and apoptotic bodies (large vesicles), at 10,000–15,000 × *g* to remove cell debris and microvesicles (medium vesicles), and a final centrifugation step at ≥100,000 × *g* (100,000–200,000 × *g*) to pellet small EVs, especially exosomes (Thery et al., 2006; Crescitelli et al., 2013; Konoshenko et al., 2018; Willms et al., 2018; Jeppesen et al., 2019). The EV pellet is then washed once to remove non-EV proteins by resuspension and the final centrifugation step is repeated (Thery et al., 2006; Konoshenko et al., 2018). Specific subtypes of EVs can be further purified from this pellet through high speed density gradient ultracentrifugation or bead-based immunoaffinity capture (Thery et al., 2006; Jeppesen et al., 2019).

While animal EVs have been well studied over the past decades, plant EVs remain poorly investigated. This is mainly due to the lack of accepted EV isolation protocols. Because plant EVs are present primarily in the apoplastic space, the most critical step of EV isolation is isolation of clean AWF, which is obtained by a simple, well-established infiltration-centrifugation method (Wang et al., 2005; Sanmartin et al., 2007; Hatsugai et al., 2009; O'Leary et al., 2014). Based on established animal EV purification protocols, plant EV separation involves differential centrifugation of AWF, with two consecutive steps of low speed centrifugation at 2,000 × *g* and 10,000 × *g*, to remove dead cells, cell debris, and large vesicles, followed by high speed centrifugation at 100,000 × *g* to pellet small EVs (Prado et al., 2014; Cai et al., 2018; Movahed et al., 2019; Liu et al., 2020; He et al., 2021). In some studies, a lower centrifugal force, 40,000 × *g*, was used to isolate EVs. For example, this speed was used to isolate EVs derived from sunflower seeds and seedlings (Regente et al., 2009, 2017). Furthermore, EVs pelleted at this speed in *Arabidopsis* contain PEN1-positive EVs (Rutte and Innes, 2017). Note that in distinct protocols for plant EV isolation, the differences lie not only in the speed of centrifugation for the final EV sedimentation, but also in AWF collection. Thus far, there is no standard protocol for plant EV isolation from AWF across different plant species. Therefore, in this study, we compared the results from different EV isolation methods and propose a standardized method for plant EV isolation and purification from *Arabidopsis*. We utilized high speed density gradient centrifugation to separate and purify EV subtypes based on their different densities. Furthermore, we also describe a recently developed immunoaffinity capture method, using bead-based antibodies that recognize the plant EV-enriched TET8 protein, allowing the precise capture of the specific TET8-positive EV subtype.

RESULTS

Isolation of plant EVs by differential centrifugation

Differential centrifugation is the most commonly used method for EV isolation from cell culture supernatants and biological fluids (Thery et al., 2006; Willms et al., 2018). The methods used to isolate plant EVs share similarities with those used to isolate mammalian EVs, with the additional first step of AWF collection (Figure 1). Based on the commonly used infiltration-centrifugation method for plant AWF collection, we developed a protocol for the extraction of AWF from *Arabidopsis* leaves with an optimized vacuum infiltration and centrifugation method (O'Leary et al., 2014; Cai et al., 2018; He et al., 2021). Initially, fully expanded rosette leaves were detached from plants at the base of the leaf using a razor blade to limit contamination by the vasculature stream, which contains mobile RNAs and ribonucleoprotein complexes (Zhang et al., 2009; Liu and Chen, 2018). Cytoplasmic contaminants from damaged cells were removed by washing the cut leaves in distilled water (Figure 1A). The detached leaves were gently infiltrated with the infiltration buffer by negative pressure within a needleless syringe, then the leaves were carefully arranged to have the cut side of the leaf bases toward the bottom of the tube to avoid cell damage during centrifugation (Figure 1A). Apoplastic washing fluid was then collected by centrifugation at 900 × *g* (Figure 1A). EVs were subsequently isolated from AWF by the following centrifugation steps (Figure 1B). (i) The AWF was centrifuged for 10 min at 4°C at 2,000 × *g* to remove large cell debris (Figure S1). (ii) The supernatants were filtered through a 0.45 μm filter to remove the largest vesicles. (iii) The supernatant was moved into new ultracentrifuge tubes, and large vesicles were removed with another centrifugation step at 10,000 × *g* for 30 min at 4°C (Figure S1). (iv) The plant EV fraction was then pelleted using high speed (100,000 × *g*) centrifugation for 1 h. (v) The pellet was washed to remove potential protein aggregates via a second round of ultracentrifugation at 100,000 × *g*. The EV pellet obtained through this step is called the P100 fraction (Figure S1). P100 fraction can be further used for the analysis of sRNA content in EVs. To confirm that sRNAs were located inside EVs, not out of EVs, the P100 fraction can be treated with nuclease or proteinase plus nuclease before RNA extraction (Figure 1C). If sRNAs were largely resistant to degradation by nuclease or proteinase plus nuclease treatment but became susceptible in the presence of Triton-X-100 (a detergent that can rupture EVs), these sRNAs can be determined as located inside EVs. For example, EV-enriched sRNAs, TAS1c-siR483, TAS2-siR453 and miRNA166 can be detected in nuclease-treated EVs or proteinase plus nuclease-treated EVs, indicating they located inside EVs (Cai et al., 2018) (Figure 1D).

Technical evaluation of AWF collection from *Arabidopsis* leaves

Extraction of AWF is a crucial step to obtain high quality plant EVs with few contaminants. In parallel with the detached leaves method described above (Figure 1A, Method 1), we performed a second method (Figure S2, Method 2) in order to compare the purity and quality of EVs obtained. In Method 2, the entire aerial part of plants was harvested by cutting the stem directly above the roots. Plant tissues were then vacuumed and centrifuged to collect the AWF (Figure S2)

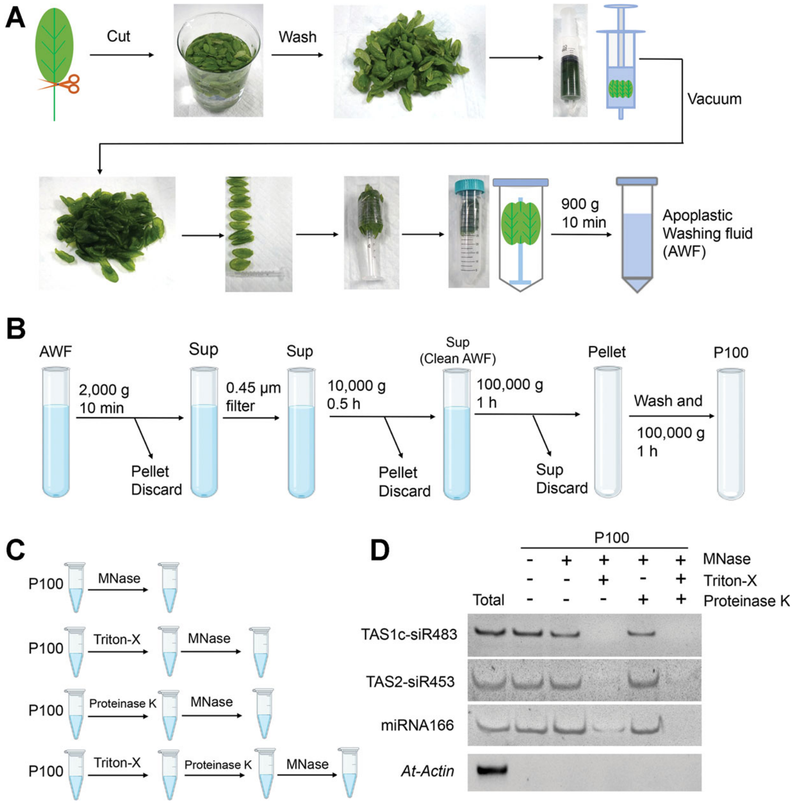

Figure 1. Schematic of the plant extracellular vesicle (EV) isolation and small RNA (sRNA) detection

(A) Images show the various steps in apoplastic washing fluid (AWF) isolation from *Arabidopsis* (detached leaves protocol, Method 1 in Figure 2). The distinct proximal (petiole) part of leaves was removed using scissors, and the distal (blade) zones of leaves were collected. The leaves were placed in a syringe and gently vacuumed with infiltration buffer. The syringe with taped leaves was placed into a 50 mL conical tube, and then centrifuged at 900 × *g* to collect the AWF. **(B)** Schematic of EVs isolated by differential centrifugation of AWF from *Arabidopsis*. The clean AWF was centrifuged at 100,000 × *g* to obtain the P100 EV fraction. Sup, supernatant. **(C)** Schematic of EVs treated with micrococcal nuclease (MNase) and proteinase K. **(D)** EV-enriched sRNAs (TAS1c-siR483, TAS2-siR453 and miRNA166) were detected in nuclease-treated EVs or proteinase plus nuclease-treated EVs. *Actin* gene was used as the control. The "total" lane indicates total RNAs from leaves.

(Rutte and Innes, 2017; Baldrich et al., 2019). Previously we showed that fungal infection increases EV secretion (Cai et al., 2018; He et al., 2021). Here, we used *B. cinerea*-infected *Arabidopsis* to increase the yield of isolated EVs in both methods. Ideally, AWF should be free of contamination from cell debris and cytoplasmic molecules, such as chlorophyll, the major pigment (green) in chloroplasts (O'Leary et al., 2014). However, AWF extracted by Method 2 was green in color indicating obvious contamination of cytoplasmic molecules, whereas AWF extracted by Method 1 was clear with no visible chlorophyll contamination (Figure 2A). Additionally, Western blot analysis demonstrated that both the AWF and P100 fraction obtained using Method 2 were enriched in Rubisco proteins as compared to the AWF and P100 fraction extracted by Method 1 (Figure 2B). To be more precise, we directly visualized the vesicles in the P100 fractions prepared from AWF extracted by Method 1 and Method 2 using TEM. The P100 fraction obtained via Method 2 contains large amounts of non-vesicle structures/materials, while very little non-vesicle material was observed in the P100 fraction obtained via Method 1 (Figure 2C). These results indicate that the detached leaves method (Method 1) is a superior choice for AWF collection to reduce contamination in EV preparations.

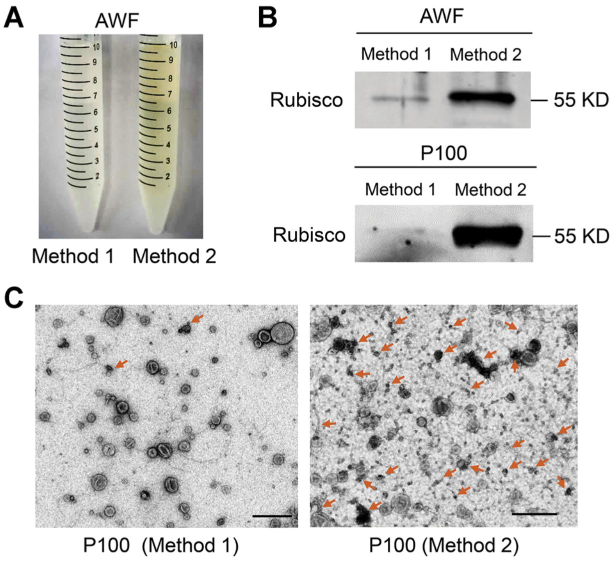

Figure 2. The detached leaves protocol (Method 1) for apoplastic washing fluid (AWF) isolation is better than the whole plant protocol (Method 2) in *Arabidopsis*

(A) Comparison of the color of AWF isolated by Method 1 and Method 2. The same amount of plants (50 plants) was used for both methods. **(B)** Detection of Rubisco protein in both AWF and their P100 extracellular vesicle (EV) fraction by Western blot using Rubisco antibody, protein size is indicated by KD. To perform the Western blot of AWF samples, equivalent amounts of AWF (10 µL) collected by both methods in **(A)** were used. To perform the Western blot of EV samples, all AWF collected in **(A)** was centrifuged at 100,000 × *g* to get P100 fractions. Both P100 pellets were resuspended in 100 µL infiltration buffer, and 10 µL of this suspension was used for the Western blot. **(C)** Representative transmission electron microscopy (TEM) images of P100 fraction isolated from AWF collected by Method 1 and Method 2. Non-vesicle structures marked by arrows. Scale bars, 500 nm.

Technical evaluation of final ultracentrifugation speed for plant EV isolation

In differential centrifugation steps, the final supernatant is ultracentrifuged to pellet the EVs. In animal systems, genuine exosomes (or small EVs in general) are usually sedimented at speeds of 100,000–200,000 × *g* (Thery et al., 2006; Kowal et al., 2016; Konoshenko et al., 2018; Jeppesen et al., 2019). For plant EV isolation, two final ultracentrifuge speeds, 100,000 × *g* (Prado et al., 2014, 2015; Cai et al., 2018; Movahed et al., 2019; Liu et al., 2020; He et al., 2021) and 40,000 × *g* (Regente et al., 2009; Rutte and Innes, 2017; Baldrich et al., 2019), have been used in different studies. Here, we compared the EV fractions, P100 and P40, obtained by a final ultracentrifugation step at 100,000 × *g*, or 40,000 × *g*, respectively (Figure 3A). The pellet obtained from further centrifugation of the supernatant of the P40 fraction at 100,000 × *g* was named the P100 minus P40 (P100-40) fraction (Figure 3A). Subsequently, the morphology of EVs were examined by TEM (Jung and Mun, 2018). Plant EVs in the P100 fraction showed similar morphology to animal EVs isolated by centrifugation at 100,000 × *g* (Figure 3B) (Thery et al., 2006; Jung and Mun, 2018), and were unlikely to be deformed or broken during 100,000 × *g* centrifugation (Figure 3B). In comparison to the P100 fraction, there were fewer EVs present in the P40 fraction, while a substantial amount of EVs were isolated after centrifugation of the supernatant of the P40 fraction at 100,000 × *g* (P100-40) (Figure 3B). Therefore, it is not appropriate to consider the supernatant of P40 a non-vesicle fraction (Baldrich et al., 2019). Corroborating this conclusion, isolation of EV fractions from transgenic plants co-expressing TET8-GFP (green fluorescent protein) and mCherry-PEN1 proteins contained a large amount of TET8-positive EVs in the P100-40 fraction (Figure 3C). In addition, TET8-positive EVs represent a majority of the EVs in both the P100-40 fraction (85%) and the P100 fraction (65%), while PEN1-positive EVs represent a majority of the EVs (72%) in the P40 fraction (Figure 4A). These results demonstrate that centrifugation at 100,000 × *g* collects much more EVs than centrifugation at 40,000 × *g* for plant EV isolation. Further, centrifugation at 40,000 × *g* results in a loss of large amounts of TET8-positive EVs, the exosomes.

We also analyzed plant EV size using TEM imaging. TEM micrographs of the P100 fraction showed that a majority of the vesicles (92%) had diameters ranging between 30 and 150 nm (Figure 4B). This result demonstrates that plant EVs in the P100 fraction are similar in size to an EV subtype termed exosomes (30–150 nm in diameter) (Colombo et al., 2014; Kowal et al., 2016; Mathieu et al., 2019). In the P40 fraction, 40% of the vesicles observed had diameters larger than 100 nm, while only 13% of the vesicles in the P100-40 fraction were in this size range (Figure 4B), suggesting that centrifugation at 40,000 × *g* pellets larger vesicles. In addition, the majority of vesicles (82%) observed in the P100-40 fraction had diameters ranging between 30 and 100 nm (Figure 4B). These results suggest that centrifugation at 100,000 × *g* isolates plant EVs, especially small EVs like

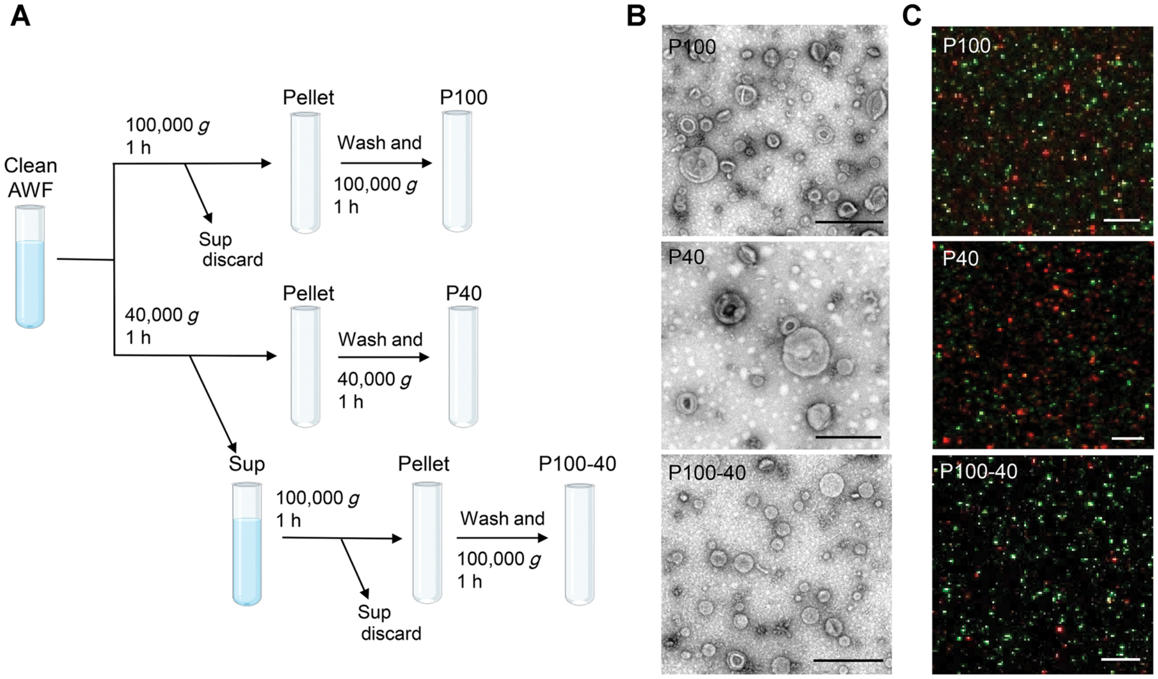

Figure 3. Centrifugation at 100,000 × *g* enriches plant extracellular vesicles (EVs) much more efficiently than at 40,000 × *g*

(A) Schematic of EV isolation by ultracentrifugation of apoplastic washing fluid (AWF) from *Arabidopsis*. EVs were isolated from clean AWF (isolated by Method 1) via ultracentrifugation at 40,000 × *g* (P40 fraction) and 100,000 × *g* (P100 fraction) for 1 h. For the P100-40 fraction, the supernatant (Sup) of the P40 fraction was centrifuged a second time at 100,000 × *g* for 1 h. **(B)** Representative transmission electron microscopy (TEM) images of P100 fraction, P40 fraction and P100-40 fraction isolated from *Botrytis cinerea*-infected wild-type *Arabidopsis*. Scale bars, 500 nm. **(C)** Confocal microscopy of EV fractions (P100, P40 and P100-40) isolated from *B. cinerea*-infected *TET8-GFP*(green)/*mCherry-PEN1* (Red) double-fluorescence transgenic plants. Scale bars, 5 μm.

exosomes, at a much greater efficiency than centrifugation at 40,000 × *g*.

Density gradient fractionation separates plant EVs

Although Method 1 provides reasonably pure plant EVs (Figure 2), some applications may require extra purification steps. The overlapping sedimentation of exosomes, microvesicles and other large vesicles produces a mixture of vesicles in the ultracentrifugation fraction (Konoshenko et al., 2018). Density gradient fractionation separation is a classical method used to separate vesicles according to their flotation speed and equilibrium density (Colombo et al., 2014; Kowal et al., 2016; Jeppesen et al., 2019). This strategy separates EVs using sucrose or iodixanol gradient centrifugation of EV pellets prepared by differential centrifugation. Previous work has utilized sucrose gradients on EVs isolated from P100 fractions (He et al., 2021) and iodixanol (OptiPrep) gradients on EVs isolated from P40 fractions (Rutte and Innes, 2017) to facilitate the separation of subtypes of EVs. Because centrifugation at 100,000 × *g* enriches plant EVs much more efficiently than 40,000 × *g*, we used an iodixanol density gradient to further separate EVs from the P100 fraction and estimate their density using top-loading methods (Figure 5A). Using the TET8 antibody and TEM imaging, we identified that most of the TET8-positive EVs accumulated in the third fraction (F3) at an average density of 1.08 g/mL of iodixanol (Figure 5B, C).

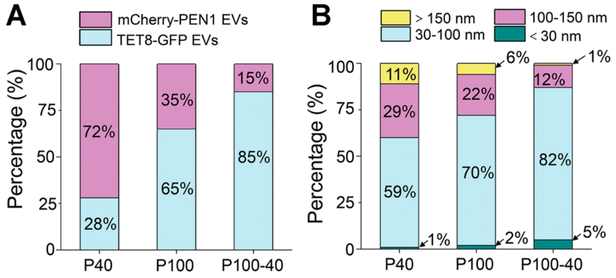

Figure 4. Quantification analysis of the distribution of extracellular vesicle (EV) subtypes and sizes in different centrifuge fractions

(A) Histograms for the distribution of Tetraspanin 8 green fluorescent protein (TET8-GFP) EVs and mCherry-PEN1 (Penetration 1) EVs isolated from *TET8-GFP/mCherry-PEN1* double-fluorescence transgenic plants in P40 (1937 vesicles analyzed), P100 (2114 vesicles analyzed) and P100-40 (1245 vesicles analyzed) fractions from confocal images. **(B)** Histograms for the size distribution of EVs in P40 (226 vesicles analyzed), P100 (222 vesicles analyzed) and P100-40 (232 vesicles analyzed) fractions from transmission electron microscopy (TEM) images.

This is similar to the density of exosomes in animal systems (1.08–1.12 g/mL) (Wubbolts et al., 2003; Iliev et al., 2018; Jeppesen et al., 2019). We further analyzed the size of vesicles in the F3 fraction. The majority of vesicles (83%) in the F3 fraction had diameters ranging between 30 and 100 nm, which is similar to EV sizes obtained in the P100-40 fraction (Figures 4B, 5C, D).

Immunoaffinity capture-based technique purifies specific classes of EVs

Immunoaffinity capture-based EV isolation is considered to be the most advanced method to purify specific classes of EVs (Thery et al., 2006; Kowal et al., 2016; Jeppesen et al., 2019; He et al., 2021). This technique relies on the use of an antibody to capture EVs with a specific protein marker on the surface of the EVs (Thery et al., 2006). Tetraspanins, such as CD81 or CD63, are ideal immuno-capture proteins since they are enriched on exosome membranes (Andreu and Yanez-Mo, 2014). He et al. developed an immunocapture purification method using beads coated with an antibody targeting the plant exosome marker TET8 (Figure 6A) (He et al., 2021). It is worth noting that antibody-recognized regions of the protein marker must be on the outer surface of the EVs. Thus, the antibody that specifically recognizes the large exposed extravesicular loop, EC2 domain of TET8, has been well designed to pull-down TET8-positive EVs from the P100 fraction (He et al., 2021). Using this method, TET8-positive EVs can be successfully purified from the P100 fraction (Figure 6B). Specificity of the immunoaffinity capture was examined using beads coated with an irrelevant antibody (immunoglobulin G) (Figure 6B). Thus, this approach can be easily used for isolating/purifying a specific subtype of EVs in plants. By using this method, EV-enriched sRNAs and RNA binding proteins, such as Argonaute 1 (AGO1), RNA helicase (RH) 11, RH37, annexin (ANN) 1 and ANN2 were clearly detected in the TET8-positive EVs (He et al., 2021). Thus, immunoaffinity isolation is the ideal method for the precise analysis of the cargo contents of specific EV subtypes.

DISCUSSION

In recent years, plant-derived EVs have garnered increased interest because of their essential role in cross-kingdom or cross-organism communication, and research in this field has exponentially increased (Cai et al., 2019a, 2021). Plant EVs have been isolated from the AWF of different plant tissues by differential centrifugation. So far, this method has been used for EVs isolated from *Arabidopsis* leaves (Rutte and Innes, 2017; Cai et al., 2018; He et al., 2021), sunflower imbibing seeds and seedlings (Regente et al., 2009, 2017), and *Nicotiana benthamiana* leaves (Movahed et al., 2019). Further, it has been reported that olive (*Olea europaea*) pollen grains released nanovesicles (28–60 nm in diameter) in media during pollen germination and pollen tube growth *in vitro* (Prado et al., 2014). These nanovesicles were isolated from the media by differential centrifugation (Prado et al., 2014). In addition to natural EVs, artificial plant-derived vesicles have been isolated from disrupted leaves or plant tissues via differential centrifugation (Zhang et al., 2016a; Kameli et al., 2021). Interestingly, these artificial vesicles have shown promising utility in drug delivery in human health and disease applications (Wang et al., 2013; Mu et al., 2014; Teng et al., 2018; Liu et al., 2020). Due to the existence of diverse EV separation methods developed in plants, in this study, we compared the quality of EVs isolated from two major published methods step-by-step and optimized a protocol for AWF collection and differential centrifugation with minimum contamination and high EV yield. Extra subsequent steps, such as immunoaffinity capture, were also introduced in detail to purify specific subclasses of EVs.

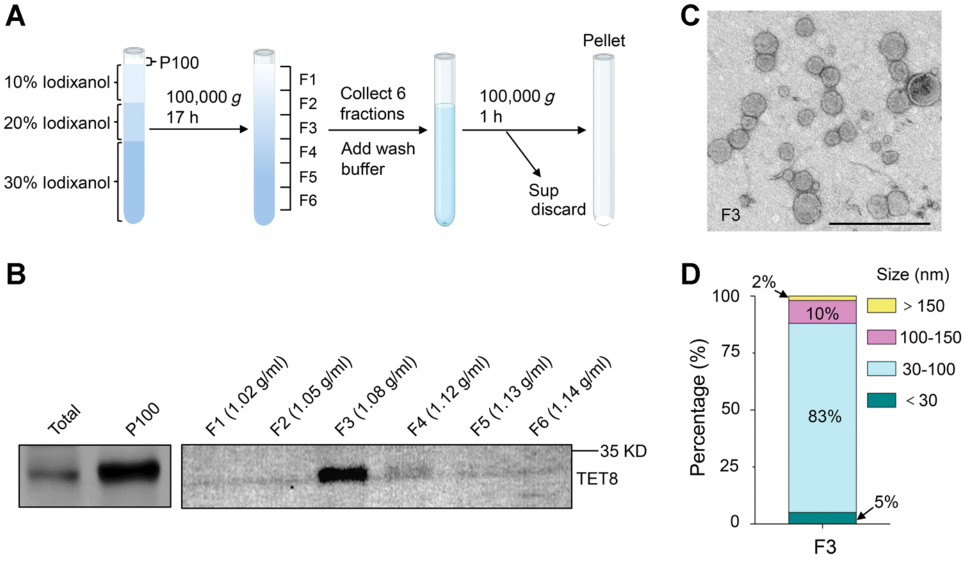

Figure 5. Characterization of P100 extracellular vesicles (EVs) using iodixanol gradients

(A) P100 fraction obtained after 100,000 × *g* centrifugation was allowed to float into an overlayed iodixanol gradient by top loading. Sup, supernatant. **(B)** Six fractions were collected and analyzed by Western blot, showing the Tetraspanin 8 (TET8)-positive EVs enriched in a single fraction (F3) with TET8 native antibody. **(C)** Representative transmission electron microscopy (TEM) images of F3 fraction in **(B)**. Scale bars, 500 nm. **(D)** Histogram for the size distribution of EVs in F3 fraction in **(C)** (284 vesicles analyzed).

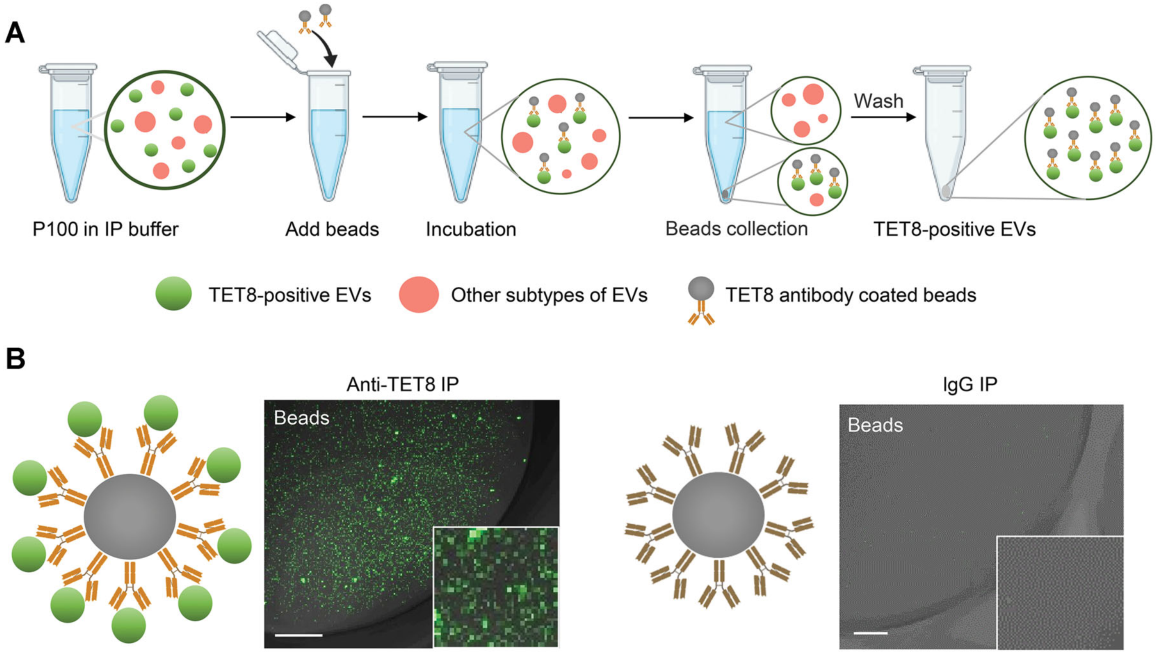

Figure 6. Immunoaffinity isolation is the most advanced method for the purification of specific subclasses of extracellular vesicles (EVs) in plants

(A) Schematic of P100 fraction subjected to immuno-isolation with beads coupled to antibodies against Tetraspanin 8 (TET8), or irrelevant rabbit immunoglobulin G as a negative control. **(B)** Confocal microscopy demonstrated that the TET8-positive EVs were pulled-down by TET8-specific antibody-linked beads. Scale bars, 10 μm.

In animal systems, EVs have been isolated from diverse bodily fluids, including blood, urine, saliva, breast milk, semen and cell culture media (Colombo et al., 2014). Unlike in animals, isolation of plant EVs first requires the collection of clean apoplastic fluids. Due to the fragility of plant leaves, collection of clean apoplastic fluids has been a challenge. Here, we found that using only the detached *Arabidopsis* rosette leaves with no petioles for AWF collection can minimize the contamination of cytosolic contents and vasculature fluid (Method 1 in Figure 2). Because phloem stream contains large amounts of mobile RNAs and ribonucleoprotein complexes (Zhang et al., 2009; Liu and Chen, 2018), this detached leaf protocol minimizes contamination by the vasculature fluids, making subsequent analyses on the RNA content in the apoplastic EVs more accurate. In contrast, the alternative AWF collection method which used the entire aerial part of a plant (Method 2 in Figure 2), can lead to cell breakage and contamination of intracellular contents and vasculature sap. Therefore, isolating AWF from detached leaves with no petioles is the preferable method for clean AWF collection before EV isolation.

Ultracentrifugation is the most commonly used technique for EV isolation from biofluids and cell culture supernatants. Similar to animal EV isolation, which overwhelmingly relies on a final ultracentrifugation step of 100,000 × *g*, plant EVs were also highly enriched in the fraction collected by ultracentrifugation at 100,000 × *g* from AWF (Cai et al., 2018; He et al., 2021). In this study, we have characterized and compared the quality of EVs isolated from both intermediate speed (40,000 × *g*) and high speed (100,000 × *g*) fractions. Consistent with our previous study (He et al., 2021), we found that a large amount of EVs, specifically TET8-positive EVs, remains in the P100-40 fraction. Thus, centrifugation at 100,000 × *g* has greater separation efficiency resulting in higher EV yield and small EVs, whereas centrifugation at 40,000 × *g* largely reduces the yield, and favors the collection of large EVs. Because PEN1-positive EVs represent a majority (72%) of EVs in the P40 fraction, centrifugation at 40,000 × *g* is suitable for the isolation of PEN1-associated EVs (Rutte and Innes, 2017; He et al., 2021). The majority of EVs (92%) recovered from P100 centrifugation and 94% of the EVs recovered from the supernatant of P40 fraction (P100-40) had sizes ranging between 30 nm and 150 nm in diameter (Figure 4), similar to the animal exosomes (Colombo et al., 2014; Kowal et al., 2016; Mathieu et al., 2019). It is worth noting that a small fraction of other large EV types, possibly microvesicles and other large vesicles, was also co-sedimented into the pellet by centrifugation at 100,000 × *g* (Figure 4B).

Utilizing density gradient centrifugation techniques post-ultracentrifugation allows for the isolation of EVs with higher purity than those isolated with ultracentrifugation alone, and can separate distinct EV subtypes based on their densities (Konoshenko et al., 2018; Jeppesen et al., 2019). Previously, we found that in P100 fractions floated in a sucrose density gradient, TET8-positive EVs and EV-associated sRNAs were enriched in the EV fractions at densities of 1.12–1.19 g/mL (He et al., 2021). In this study, P100 fractions were floated in an iodixanol density gradient, and TET8-positive vesicles were enriched in the gradient fraction of 1.08 g/mL, on average. The different densities of TET8-positive EVs in sucrose versus iodixanol could be a result of differences in the osmotic pressure of these two gradients. This result was similar to a previous study which also found that vesicles in P100 pellets derived from human dendritic cells exhibited slightly different densities in sucrose versus iodixanol gradients (Kowal et al., 2016). Note that PEN1-positive EVs collected at 40,000 × *g* were enriched in the iodixanol gradient fraction at densities ranging from 1.029 to 1.056 g/mL (Rutte and Innes, 2017), demonstrating that TET8-positive EVs and PEN1-positive EVs represent two distinct subpopulations of EVs with different densities. Further study is required to determine the density of other EV subtypes, such as Exo70E2-positive EVs, by its marker lines or the specific antibodies.

Density gradient centrifugation still has some disadvantages, as it is complex, laborious, and time-consuming (up to 2 d). Additionally, it is difficult to separate different subtypes of EVs with similar densities. Therefore, immunoaffinity isolation is the most precise method for the purification of a specific subtype of EVs (Thery et al., 2006; Kowal et al., 2016; Jeppesen et al., 2019; He et al., 2021). Co-isolation of non-vesicular contaminants from the cytoplasm and other unwanted vesicles can be prevented by the highly specific affinity interactions that occur between an antigen and an antibody. Ideal antigens are EV biomarkers which are highly concentrated on the EV membrane, for example, the major histocompatibility complex antigens and Tetraspanin proteins (Kowal et al., 2016; Jeppesen et al., 2019). In plants, we showed that TET8-positive EVs can be successfully isolated from P100 fractions by an antibody that specifically recognizes the EC2 domain of TET8. For future research, it would be ideal to purify other subclasses of plant EVs using the immunoaffinity isolation method. In summary, these findings should serve as a guide to choose and further optimize EV isolation methods in the plant field for their desired downstream applications.

MATERIALS AND METHODS

Plant materials

Arabidopsis thaliana ecotype Columbia-0 (*Col-0*) was used in this study. *Arabidopsis* marker lines *TET8*$_{pro}$*::TET8-GFP* and *TET8-GFP/mCherry-PEN*1 double-fluorescence lines (Cai et al., 2018; He et al., 2021), were used as previously described. *Arabidopsis* seeds were grown in soil side-by-side at 22°C for 4 weeks under short-day periods (12 h of light followed by 12 h of darkness).

Apoplastic washing fluid collection from *Arabidopsis* leaves

Apoplastic washing fluid collection from *Arabidopsis* leaves was modified from previous studies (O'Leary et al., 2014; Madsen et al., 2016). A typical experiment for EV isolation requires ~50 plants for each genotype/treatment. The distinct proximal (petiole) part of leaves was removed using scissors, and the distal (blade) zones of leaves were collected. After recording the biomass, leaves were washed three times with water. The leaves were carefully placed in a 200 mL syringe and gently vacuumed with an infiltration buffer (20 mmol/L L2-[*N*-morpholino]ethanesulfonic acid (MES) hydrate, 2 mmol/L $CaCl_2$, 0.1 mol/L NaCl, pH 6.0) for 20 s. Excess infiltration buffer on the leaf surface was removed by a clean paper towel and the leaves were then fixed onto a small plastic stick. The small plastic sticks with leaves were then placed into a 50 mL conical tube, keeping the apex of the leaf facing upward, and then centrifuged for 10 min at 4°C at 900 × *g* to collect the AWF.

Isolation of plant EVs by differential centrifugation

Plant EVs were isolated from *Arabidopsis* AWF. The AWF was centrifuged for 10 min at 4°C at 2,000 × *g* to remove large cell debris and then filtered through a 0.45 μm filter. Next, the supernatants were transferred into new ultracentrifuge tubes and centrifuged for 30 min at 4°C at 10,000 × *g*. After the pellet was discarded, the supernatants (the clean AWF) were centrifuged for 1 h at 4°C at 100,000 × *g* or 40,000 × *g* to obtain the P100 EV fraction or P40 EV fraction. To obtain the P100-P40 EV fraction, the supernatants of P40 were centrifuged again for 1 h at 4°C at 100,000 × *g*. All pellets were washed in 10 mL of infiltration buffer and finally re-centrifuged at the same speed before being resuspended in infiltration buffer for further study.

Micrococcal nuclease (MNase) and proteinase K treatment of plant EVs

To clarify sRNAs inside or outside EVs, P100 vesicles were treated with MNase and proteinase K. For MNase treatment, P100 vesicles was treated with 10 U of MNase (Thermo Fisher) for 15 min at 37°C with or without Triton-X-100. For proteinase K plus MNase treatment, P100 vesicles were treated with 20 μg/mL proteinase K (Invitrogen) for 1 h at 37°C with or without Triton-X-100. The proteinase activity was inhibited by adding 5 mmol/L phenylmethylsulfonyl fluoride for 10 min at room temperature. The sample was then treated with 10 U of MNase for 15 min at 37°C. For Triton-X-100 treatment, P100 vesicles were incubated with 1% (v/v) Triton-X-100 on ice for 30 min before proteinase and nuclease treatments. Immediately after proteinase and nuclease treatments, RNA was extracted for further detection of specific sRNAs. sRNA reverse transcription polymerase chain reaction was performed as previously described (Cai et al., 2018).

Iodixanol gradient separation of plant EVs

Discontinuous iodixanol gradients (OptiPrep, STEMCELL Technologies) were prepared as described previously with slight modifications (Kowal et al., 2016). Working solutions of 10% (v/v), 20% (v/v) and 30% (v/v) idoixanol were made by diluting an aqueous 60% OptiPrep stock solution in infiltration buffer (20 mmol/L MES hydrate, 2 mmol/L $CaCl_2$, 0.1 mol/L NaCl, pH 6.0). The gradient was formed by successively layering 4.8 mL of 30% solution, 2.1 mL of 20% solution, and 2 mL of 10% solution in a 13PA tube (himac) from bottom to top. About 0.4 mL of EVs resuspended in infiltration buffer were layered on top of the gradient. The tube was centrifuged for 100,000 × *g* for 17 h at 4°C (P40ST, CP80NX; himac). After stopping the centrifuge without breaks, 0.4 mL was removed from the top of the tube, and then six fractions of 1.4 mL each were collected from the top of the tube. These fractions were each diluted to 12 mL with infiltration buffer and centrifuged at 100,000 × *g* for 1 h at 4°C to obtain pellets from each fraction.

Transmission electron microscope analysis of plant EVs

Sample preparation of EVs for TEM analysis followed the protocol by Maroto et al. (2017). Ten microliters of EVs suspended in infiltration buffer were deposited onto 3.0 mm copper Formvar-carbon-coated electron microscopy grids (TED PELLA), and the sample was then wicked off using filter paper. The grids were negatively stained with 10 μL of 1% uranyl acetate and allowed to air dry before being imaged at 100 KV using a TEM (JEM-1400plus; JEOL). Extracellular vesicle size was assessed with Image J software.

Immunoaffinity capture of plant EVs

Immunoaffinity capture of plant EVs was performed as described previously (He et al., 2021). Briefly, antibodies for immunoaffinity capture, rabbit polyclonal anti-AtTET8 (Homemade) and normal rabbit immunoglobulin G (Thermo Fisher), were coated with protein A beads in immunoprecipitation (IP) buffer (20 mmol/L MES hydrate, 2 mmol/L $CaCl_2$, 0.1 mol/L NaCl, pH 7.5). Beads were then washed three times with IP buffer (containing 0.3% bovine serum albumin), and resuspended in the same buffer, to which P100 fraction was added, followed by overnight incubation at 4°C with rotation. Bead-bound EVs were collected and washed by IP buffer for further analysis.

Confocal microscopy analyses of plant EVs

For visualization of EV-associated GFP-fluorescence and mCherry-fluorescence, EV pellets or EV coated beads suspended in infiltration buffer were examined using a 40× water immersion or dip-in lens mounted on a confocal laser scanning microscope equipped with an argon/krypton laser (Leica TCS SP5).

ACKNOWLEDGEMENTS

We thank Rachael Hamby and Angela Chen for editing the paper. Work in the Q.C. Laboratory was supported by grants from the National Natural Science Foundation of China (32070288). Work in the H.J. laboratory was supported by grants from the National Institute of Health (R35 GM136379), the National Science Foundation (IOS2017314), the United States Department of Agriculture National Institute of Food and Agriculture (2021-67013-34258 and 2019-70016-29067), the Australian Research Council Industrial Transformation Research Hub (IH190100022), as well as the CIFAR Fungal Kingdom fellowship to H.J.

AUTHOR CONTRIBUTIONS

H.J. and Q.C. designed the experiments. Y.H. and S.W. performed the experiments. Y.H. and Q.C. analyzed the data. Q.C. and H.J. wrote the manuscript. All authors read and approved of its content.

Edited by: Liwen Jiang, Chinese University of Hong Kong, China

Received Aug. 14, 2021; **Accepted** Oct. 18, 2021; **Published** Oct. 20, 2021

REFERENCES

Akers, J.C., Gonda, D., Kim, R., Carter, B.S., and Chen, C.C. (2013). Biogenesis of extracellular vesicles (EV): Exosomes, microvesicles, retrovirus-like vesicles, and apoptotic bodies. J. Neurooncol. **113:** 1–11.

An, Q., Ehlers, K., Kogel, K.H., van Bel, A.J., and Huckelhoven, R. (2006a). Multivesicular compartments proliferate in susceptible and resistant MLA12-barley leaves in response to infection by the biotrophic powdery mildew fungus. New Phytol. **172:** 563–576.

An, Q., Huckelhoven, R., Kogel, K.H., and van Bel, A.J. (2006b). Multivesicular bodies participate in a cell wall-associated defence response in barley leaves attacked by the pathogenic powdery mildew fungus. Cell. Microbiol. **8:** 1009–1019.

An, Q., van Bel, A.J., and Huckelhoven, R. (2007). Do plant cells secrete exosomes derived from multivesicular bodies? Plant Signal. Behav. **2:** 4–7.

Andreu, Z., and Yanez-Mo, M. (2014). Tetraspanins in extracellular vesicle formation and function. Front. Immunol. **5:** 442.

Baldrich, P., Rutter, B.D., Zand, K.H., Podicheti, R., Meyers, B.C., and Innes, R.W. (2019). Plant extracellular vesicles contain diverse small RNA species and are enriched in 10 to 17 nucleotide "Tiny" RNAs. Plant Cell **31:** 315–324.

Bozkurt, T.O., Belhaj, K., Dagdas, Y.F., Chaparro-Garcia, A., Wu, C., Cano, L.M., and Kamoun, S. (2014). Rerouting of plant late endocytic trafficking toward a pathogen interface. Traffic **16:** 204–226.

Cai, Q., He, B., and Jin, H. (2019a). A safe ride in extracellular vesicles - Small RNA trafficking between plant hosts and pathogens. Curr. Opin. Plant Biol. **52:** 140–148.

Cai, Q., He, B., Wang, S., Fletcher, S., Niu, D., Mitter, N., Birch, P.R.J., and Jin, H. (2021). Message in a bubble: Shuttling small RNAs and proteins between cells and interacting organisms using extracellular vesicles. Annu. Rev. Plant Biol. **72:** 497–524.

Cai, Q., He, B., Weiberg, A., Buck, A.H., and Jin, H. (2019b). Small RNAs and extracellular vesicles: New mechanisms of cross-species communication and innovative tools for disease control. PLoS Pathog. **15:** e1008090.

Cai, Q., Qiao, L., Wang, M., He, B., Lin, F.M., Palmquist, J., Huang, S.D., and Jin, H. (2018). Plants send small RNAs in extracellular vesicles to fungal pathogen to silence virulence genes. Science **360:** 1126–1129.

Colombo, M., Raposo, G., and Thery, C. (2014). Biogenesis, secretion, and intercellular interactions of exosomes and other extracellular vesicles. Annu. Rev. Cell Dev. Biol. **30:** 255–289.

Crescitelli, R., Lasser, C., Szabo, T.G., Kittel, A., Eldh, M., Dianzani, I., Buzas, E.I., and Lotvall, J. (2013). Distinct RNA profiles in subpopulations of extracellular vesicles: Apoptotic bodies, microvesicles and exosomes. J. Extracell. Vesicles **2:** 20677.

Ding, Y., Wang, J., Lai, J.H.C., Chan, V.H.L., Wang, X., Cai, Y., Tan, X., Bao, Y., Xia, J., Robinson, D.G., and Jiang, L. (2014). Exo70E2 is essential for exocyst subunit recruitment and EXPO formation in both plants and animals. Mol. Biol. Cell **25:** 412–426.

Halperin, W., and Jensen, W.A. (1967). Ultrastructural changes during growth and embryogenesis in carrot cell cultures. J. Ultrastruct. Res. **18:** 428–443.

Hatsugai, N., Iwasaki, S., Tamura, K., Kondo, M., Fuji, K., Ogasawara, K., Nishimura, M., and Hara-Nishimura, I. (2009). A novel membrane fusion-mediated plant immunity against bacterial pathogens. Genes Dev. **23:** 2496–2506.

He, B., Cai, Q., Qiao, L., Huang, C.Y., Wang, S., Miao, W., Ha, T., Wang, Y., and Jin, H. (2021). RNA-binding proteins contribute to small RNA loading in plant extracellular vesicles. Nat. Plants **7:** 342–352.

Huang, C.Y., Wang, H., Hu, P., Hamby, R., and Jin, H. (2019). Small RNAs - Big players in plant-microbe interactions. Cell Host Microbe **26:** 173–182.

Iliev, D., Strandskog, G., Nepal, A., Aspar, A., Olsen, R., Jorgensen, J., Wolfson, D., Ahluwalia, B.S., Handzhiyski, J., and Mironova, R. (2018). Stimulation of exosome release by extracellular DNA is conserved across multiple cell types. FEBS J. **285:** 3114–3133.

Jeppesen, D.K., Fenix, A.M., Franklin, J.L., Higginbotham, J.N., Zhang, Q., Zimmerman, L.J., Liebler, D.C., Ping, J., Liu, Q., Evans, R., Fissell, W.H., Patton, J.G., Rome, L.H., Burnette, D.T., and Coffey, R.J. (2019). Reassessment of exosome composition. Cell **177:** 428–445, e418.

Jung, M.K., and Mun, J.Y. (2018). Sample preparation and imaging of exosomes by transmission electron microscopy. J. Vis. Exp. **131:** 56482.

Kameli, N., Dragojlovic-Kerkache, A., Savelkoul, P., and Stassen, F.R. (2021). Plant-derived extracellular vesicles: Current findings, challenges, and future applications. Membranes **11:** 411.

Kimura, M., Anzai, H., and Yamaguchi, I. (2001). Microbial toxins in plant-pathogen interactions: Biosynthesis, resistance mechanisms, and significance. J. Gen. Appl. Microbiol. **47:** 149–160.

Knip, M., Constantin, M.E., and Thordal-Christensen, H. (2014). Trans-kingdom cross-talk: Small RNAs on the move. PLoS Genet. **10:** e1004602.

Konoshenko, M.Y., Lekchnov, E.A., Vlassov, A.V., and Laktionov, P.P. (2018). Isolation of extracellular vesicles: General methodologies and latest trends. BioMed Res. Int. **2018:** 8545347.

Kowal, J., Arras, G., Colombo, M., Jouve, M., Morath, J.P., Primdal-Bengtson, B., Dingli, F., Loew, D., Tkach, M., and Thery, C. (2016). Proteomic comparison defines novel markers to characterize heterogeneous populations of extracellular vesicle subtypes. Proc. Natl. Acad. Sci. U.S.A. **113:** E968–977.

Liu, L., and Chen, X. (2018). Intercellular and systemic trafficking of RNAs in plants. Nat. Plants **4:** 869–878.

Liu, Y., Wu, S., Koo, Y., Yang, A., Dai, Y., Khant, H., Osman, S.R., Chowdhury, M., Wei, H., Li, Y., Court, K., Hwang, E., Wen, Y., Dasari, S.K., Nguyen, M., Tang, E.C., Chehab, E.W., de Val, N., Braam, J., and Sood, A.K. (2020). Characterization of and isolation methods for plant leaf nanovesicles and small extracellular vesicles. Nanomedicine **29:** 102271.

Madsen, S.R., Nour-Eldin, H.H., and Halkier, B.A. (2016). Collection of apoplastic fluids from *Arabidopsis* thaliana leaves. Methods Mol. Biol. **1405:** 35–42.

Mahlapuu, M., Hakansson, J., Ringstad, L., and Bjorn, C. (2016). Antimicrobial peptides: An emerging category of therapeutic agents. Front. Cell. Infect. Microbiol. **6:** 194.

Maroto, R., Zhao, Y., Jamaluddin, M., Popov, V.L., Wang, H., Kalubowilage, M., Zhang, Y., Luisi, J., Sun, H., Culbertson, C.T., Bossmann, S.H., Motamedi, M., and Brasier, A.R. (2017). Effects of storage temperature on airway exosome integrity for diagnostic and functional analyses. J. Extracell. Vesicles **6:** 1359478.

Mathieu, M., Martin-Jaular, L., Lavieu, G., and Thery, C. (2019). Specificities of secretion and uptake of exosomes and other extracellular vesicles for cell-to-cell communication. Nat. Cell Biol. **21:** 9–17.

Mathivanan, S., Fahner, C.J., Reid, G.E., and Simpson, R.J. (2012). ExoCarta 2012: Database of exosomal proteins, RNA and lipids. Nucleic Acids Res. **40:** D1241–D1244.

Movahed, N., Cabanillas, D.G., Wan, J., Vali, H., Laliberte, J.F., and Zheng, H. (2019). Turnip mosaic virus components are released into the extracellular space by vesicles in infected leaves. Plant Physiol. **180:** 1375–1388.

Mu, J., Zhuang, X., Wang, Q., Jiang, H., Deng, Z.B., Wang, B., Zhang, L., Kakar, S., Jun, Y., Miller, D., and Zhang, H.G. (2014). Interspecies communication between plant and mouse gut host cells through edible plant derived exosome-like nanoparticles. Mol. Nutr. Food Res. **58:** 1561–1573.

Nielsen, M.E., Feechan, A., Bohlenius, H., Ueda, T., and Thordal-Christensen, H. (2012). Arabidopsis ARF-GTP exchange factor, GNOM, mediates transport required for innate immunity and focal accumulation of syntaxin PEN1. Proc. Natl. Acad. Sci. U.S.A. **109:** 11443–11448.

O'Leary, B.M., Rico, A., McCraw, S., Fones, H.N., and Preston, G.M. (2014). The infiltration-centrifugation technique for extraction of apoplastic fluid from plant leaves using *Phaseolus vulgaris* as an example. J. Vis. Exp. **94:** 52113.

Prado, N., Alche, J.D., Casado-Vela, J., Mas, S., Villalba, M., Rodriguez, R., and Batanero, E. (2014). Nanovesicles are secreted during pollen germination and pollen tube growth: A possible role in fertilization. Mol. Plant **7:** 573–577.

Prado, N., De Linares, C., Sanz, M.L., Gamboa, P., Villalba, M., Rodriguez, R., and Batanero, E. (2015). Pollensomes as natural vehicles for pollen allergens. J. Immunol. **195:** 445–449.

Regente, M., Corti-Monzon, G., Maldonado, A.M., Pinedo, M., Jorrin, J., and de la Canal, L. (2009). Vesicular fractions of sunflower apoplastic fluids are associated with potential exosome marker proteins. FEBS Lett. **583:** 3363–3366.

Regente, M., Pinedo, M., San Clemente, H., Balliau, T., Jamet, E., and de la Canal, L. (2017). Plant extracellular vesicles are incorporated by a fungal pathogen and inhibit its growth. J. Exp. Bot. **68:** 5485–5495.

Roth, R., Hillmer, S., Funaya, C., Chiapello, M., Schumacher, K., Lo Presti, L., Kahmann, R., and Paszkowski, U. (2019). Arbuscular cell invasion coincides with extracellular vesicles and membrane tubules. Nat. Plants **5:** 204–211.

Rutte, B.D., and Innes, R.W. (2017). Extracellular vesicles isolated from the leaf apoplast carry stress-response proteins. Plant Physiol. **173:** 728–741.

Sanmartin, M., Ordonez, A., Sohn, E.J., Robert, S., Sanchez-Serrano, J.J., Surpin, M.A., Raikhel, N.V., and Rojo, E. (2007). Divergent functions of VTI12 and VTI11 in trafficking to storage and lytic vacuoles in *Arabidopsis*. Proc. Natl. Acad. Sci. U.S.A. **104:** 3645–3650.

Teng, Y., Ren, Y., Sayed, M., Hu, X., Lei, C., Kumar, A., Hutchins, E., Mu, J., Deng, Z., Luo, C., Sundaram, K., Sriwastva, M.K., Zhang, L., Hsieh, M., Reiman, R., Haribabu, B., Yan, J., Jala, V.R., Miller, D.M., Van Keuren-Jensen, K., Merchant, M.L., McClain, C.J., Park, J.W., Egilmez, N.K., and Zhang, H.G. (2018). Plant-derived exosomal micrornas shape the gut microbiota. Cell Host Microbe **24:** 637–652.

Thery, C., Amigorena, S., Raposo, G., and Clayton, A. (2006). Isolation and characterization of exosomes from cell culture supernatants and biological fluids. Curr. Protoc. Cell Biol. Chapter 3: Unit 3. 22.

Toruno, T.Y., Stergiopoulos, I., and Coaker, G. (2016). Plant-pathogen effectors: Cellular probes interfering with plant defenses in spatial and temporal manners. Annu. Rev. Phytopathol. **54:** 419–441.

van Niel, G., D'Angelo, G., and Raposo, G. (2018). Shedding light on the cell biology of extracellular vesicles. Nat. Rev. Mol. Cell Biol. **19:** 213–228.

Wang, D., Weaver, N.D., Kesarwani, M., and Dong, X. (2005). Induction of protein secretory pathway is required for systemic acquired resistance. Science **308:** 1036–1040.

Wang, J., Ding, Y., Wang, J., Hillmer, S., Miao, Y., Lo, S.W., Wang, X., Robinson, D.G., and Jiang, L. (2010). EXPO, an exocyst-positive organelle distinct from multivesicular endosomes and autophagosomes, mediates cytosol to cell wall exocytosis in *Arabidopsis* and tobacco cells. Plant Cell **22:** 4009–4030.

Wang, Q., Zhuang, X., Mu, J., Deng, Z.B., Jiang, H., Xiang, X., Wang, B., Yan, J., Miller, D., and Zhang, H.G. (2013). Delivery of therapeutic agents by nanoparticles made of grapefruit-derived lipids. Nat. Commun. **4:** 1867.

Willms, E., Cabanas, C., Mager, I., Wood, M.J.A., and Vader, P. (2018). Extracellular vesicle heterogeneity: Subpopulations, isolation techniques, and diverse functions in cancer progression. Front. Immunol. **9:** 738.

Wubbolts, R., Leckie, R.S., Veenhuizen, P.T., Schwarzmann, G., Mobius, W., Hoernschemeyer, J., Slot, J.W., Geuze, H.J., and Stoorvogel, W. (2003). Proteomic and biochemical analyses of human B cell-derived exosomes. Potential implications for their function and multivesicular body formation. J. Biol. Chem. **278:** 10963–10972.

Zhang, H.G., Cao, P., Teng, Y., Hu, X., Wang, Q., Yeri, A.S., Zhuang, X., Samykutty, A., Mu, J., Deng, Z.B., Zhang, L., Mobley, J.A., Yan, J., Van Keuren-Jensen, K., and Miller, D. (2016a). Isolation, identification, and characterization of novel nanovesicles. Oncotarget **7:** 41346–41362.

Zhang, S., Sun, L., and Kragler, F. (2009). The phloem-delivered RNA pool contains small noncoding RNAs and interferes with translation. Plant Physiol. **150:** 378–387.

Zhang, T., Zhao, Y.L., Zhao, J., Wang, S., Jin, Y., Chen, Z., Fang, Y., Hua, C., Ding, S., and Guo, H. (2016b). Cotton plants export microRNAs to inhibit virulence gene expression in a fungal pathogen. Nat. Plants **2:** 16153.

SUPPORTING INFORMATION

Additional Supporting Information may be found online in the supporting information tab for this article: http://onlinelibrary.wiley.com/doi/10.1111/jipb.13181/suppinfo

Figure S1. Representative transmission electron microscopy (TEM) images of fractions isolated by differential centrifugation of apoplastic washing fluid (AWF) from *Arabidopsis*

(A) Pellet of AWF centrifugation at 2,000 × *g*. Non-vesicle structures or cell debris marked by arrows. **(B)** Pellet of AWF centrifugation at 10,000 × *g*. (**C**) Pellet of AWF centrifugation at 100,000 × *g* (P100). Scale bars in **(A–C)**, 500 nm.

Figure S2. Work-flow of isolation of apoplastic washing fluid (AWF) from *Arabidopsis* (whole rosettes protocol, Method 2 in Figure 2)

Whole rosettes were harvested at the root by using scissors. The rosettes were placed in a syringe and gently vacuumed with infiltration buffer, and then placed root down into a 30 mL tube, which was then put into a 50 mL conical tube, and then centrifuged at 900 × *g* to collect the AWF.

Received: 24 February 2022 | Revised: 26 September 2022 | Accepted: 14 October 2022

DOI: 10.1002/jev2.12276

RESEARCH ARTICLE

Extracellular vesicles derived from the choroid plexus trigger the differentiation of neural stem cells

Zuzana Ditte[1,2] | **Ivan Silbern**[3,4] | **Peter Ditte**[1] | **Henning Urlaub**[3,4] | **Gregor Eichele**[1,2]

[1]Department of Genes and Behavior, Max Planck Institute for Multidisciplinary Sciences, Göttingen, Germany

[2]Biological Rhythms, Max Planck Institute for Dynamics and Self Organization, Göttingen, Germany

[3]The Bioanalytical Mass Spectrometry Group, Max Planck Institute for Multidisciplinary Sciences, Göttingen, Germany

[4]Institute for Clinical Chemistry, University Medical Center Göttingen, Göttingen, Germany

Correspondence
Zuzana Ditte, Department of Genes and Behavior, Max Planck Institute for Multidisciplinary Sciences, Göttingen, Germany.
Email: zuzana.ditte@mpinat.mpg.de

Abstract
The choroid plexus secrets cerebrospinal fluid (CSF) composed of electrolytes, cytokines, growth factors, metabolites and extracellular vesicles (EVs) that flow through the interconnected brain ventricles. On their course, CSF components can act as signals that affect, for example, neural stem cells (NSCs) residing in niches of the ventricular wall. We studied EV-born CSF signals in an in vitro culture system. We purified EVs from the secretome of a choroid plexus cell line (Z310 cells), and from primary choroid plexus cultures and co-cultured those EVs with NSCs isolated from the niche of the lateral and the third ventricle. EVs^{Z310} and EVs^{CHP} were purified by differential centrifugation. This yielded fractions of EVs of 50–150-nm diameter that induced a complex multicellular network formation and NSC differentiation. Both types of EV converted the round NSCs to cells that extended long processes that contacted nearby, alike-shaped cells. Mass spectrometry showed that the differentiation-inducing EV^{Z310} were enriched for membrane and membrane-associated proteins involved in cell differentiation, membrane trafficking, and membrane organization. We hypothesize that this type of EV $^{\text{Z310}}$ cargo causes changes of stem cell morphology that leads to multicellular networks in the niches. This cell-shape transition may represent an initial step in NSC differentiation.

KEYWORDS
brain ventricles, cerebrospinal fluid, choroid plexus derived vesicle, exosome assay, extracellular vesicles, mass spectrometry, neural stem cell differentiation

1 | INTRODUCTION

The mammalian ventricular system of the brain consists of two lateral ventricles, the third and the fourth ventricle (Figure 1). The ventricles are filled with cerebrospinal fluid (CSF) which is produced in and flows through the ventricles before being absorbed by arachnoid granulations and the lymphatic system (Hladky & Barrand, 2014). Ependymal cells form the ventricular walls and carry each a bundle of motile cilia that mediates directional CSF flow (Mirzadeh et al., 2010). This directional flow follows precise trajectories (Faubel et al., 2016) suggesting that in this way, CSF components are delivered to specific locations within the ventricular system (Eichele et al., 2020). Most of the CSF is generated and secreted by the choroid plexus (Damkier et al., 2010). CSF protects the brain from mechanical impacts and collects waste from the brain (Cserr, 1971). In addition, CSF contains signalling factors, ions, lipids and hormones required for proper brain development and function (Chau et al., 2015; Kaiser et al., 2019; Lehtinen et al., 2011; Lun et al., 2015; Silva-Vargas et al., 2016; Zappaterra & Lehtinen, 2012). CSF also contains extracellular vesicles (EVs) (Balusu et al., 2016; Fame & Lehtinen, 2020; Feliciano et al., 2014; Lun et al., 2015; Murillo et al., 2019; Street et al., 2012; Tietje et al., 2014; Vella et al., 2008; Yagi et al., 2017) that are bilayer membrane-enclosed vesicles, produced and secreted by

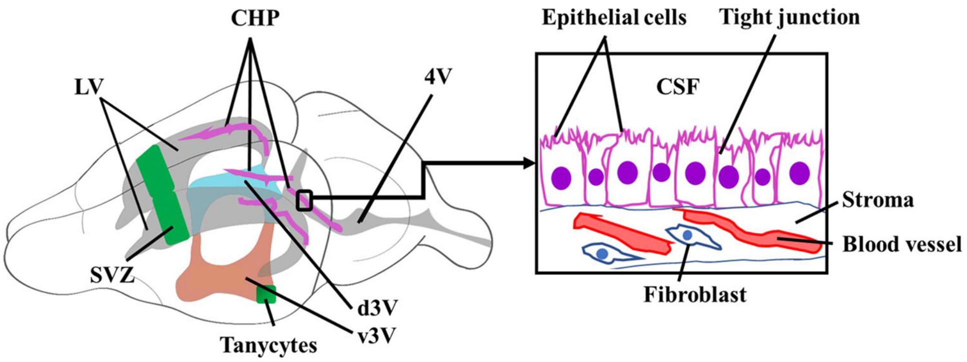

FIGURE 1 Architecture of the ventricles of the mouse brain. Lateral view of the adult mouse brain showing the ventricular system that consists of two lateral ventricles (LV, grey), the bipartite third ventricle (dorsal 3V, blue [d3V] and ventral 3V, orange [v3V]) and the fourth ventricle (4V, grey). Each ventricle has a choroid plexus (pink) that produces CSF. The choroid plexus (CHP, right box) consists of a secretory polarized epithelial cell layer and stroma composed of fibroblasts (Dorrier et al., 2022), immune cells and perivascular cells. The tight junctions between epithelial cells form the blood–CSF barrier (Ghersi-Egea et al., 2018). Neurogenic niches are the sub-ventricular zone (SVZ) and the tanycyte region (both green).

many cell types. EVs are loaded with proteins and nucleic acids (Johnstone et al., 1987; Kalra et al., 2012; Keerthikumar et al., 2016; Valadi et al., 2007; Van Niel et al., 2006). EVs termed microvesicles (size range of 100–1000 nm) form by outward budding of the plasma membrane. EVs termed exosomes (size 50–150 nm) form by an intracellular endocytic trafficking pathway involving multi-vesicular endosomes that release exosomes upon fusion with the plasma membrane (Van Niel et al., 2018; Mathieu et al., 2019). Because current purification procedures do not exclude the presence of microvesicles in exosome preparations and vice versa, one refers to these vesicles collectively as ‘EVs’.

EVs mediate communication in vitro and in vivo (Mathieu et al., 2019; Van Niel et al., 2018) between different cell types such as neurons and oligodendrocytes (Frühbeis et al., 2013), neurons and astroglia (Men et al., 2019; Morel et al., 2013) and neurons and Schwann cells (Lopez-Verrilli et al., 2013). EVs involved in intercellular communication do so in the pre-metastatic niche (Shurtleff et al., 2018), for instance by promoting breast cancer cells motility via Wnt-planar cell polarity signalling (Luga et al., 2012). EVs also play a role in the mesenchymal stem cell niche (Hayashi et al., 2017) and in the epithelial–mesenchymal niche (Nakano et al., 2017). Glioma-derived EVs drive the differentiation of embryonic neural stem cells (NSCs) to astrocytes (Sharma et al., 2020) and EVs are thought to regulate neurogenesis in the early postnatal mouse brain (Sharma et al., 2019). Recently, it was shown that Cyclin D1 contained in EVs produced by PC12 and N2A cell lines promote neural differentiation of embryonic stem cells (Song et al., 2021).

Injecting fluorescently labelled choroid plexus-derived EVs into the lateral ventricle showed that EVs could cross the ependymal cell layer and reach brain parenchyma (Balusu et al., 2016; Grapp et al., 2013). EVs have various effects on the nervous system. Balusu et al. (2016) showed that systemic inflammation of mice by intraperitoneal injection of lipopolysaccharide or tumour necrosis factor induced an increase in pro-inflammatory miRNAs in EVs produced by choroid plexus. These EVs also interacted with astrocytes and microglia to up-regulate inflammatory genes (Balusu et al., 2016). Lepko et al. (2019) found that miR-204 present in EVs that originate from the choroid plexus are taken up by NSCs of the sub-ventricular zone (SVZ) and maintain them in the quiescent state but primed for rapid neurogenesis (Lepko et al., 2019). Apparently, an EV-based long-distance signalling pathway regulates the number of quiescent NSCs in the SVZ.

In the adult mammalian brain, two NSC niches directly contact CSF and may thus have access to CSF-born EVs (Figure 1). By far the best-studied NSC niche is the SVZ that contains neural progenitors some of which (B1 cells) project a primary cilium into the lateral ventricle (Doetsch et al., 1999; Obernier & Alvarez-Buylla, 2019; Seri et al., 2004). A second niche lies in the posterior part of the ventral third ventricle (v3V, Figure 1), in a region populated by tanycytes. They project a primary cilium into v3V and have a single, long basal process that contacts distinct nuclei of the hypothalamus (Yoo & Blackshaw, 2018). A sub-set of tanycytes shows proliferation and neural differentiation in the postnatal rodent brain (Haan et al., 2013; Horiguchi et al., 2020; Pellegrino et al., 2018; Robins et al., 2013).

The CSF flow in the v3V (Faubel et al., 2016) could deliver EVs secreted by the choroid plexus to the stem cells (Faubel et al., 2016; Sawamoto et al., 2006). A direct link between CSF-born factors and NSC development and differentiation was seen in embryonic brain development (Chau et al., 2015; Feliciano et al., 2014; Lehtinen et al., 2011; Zappaterra & Lehtinen, 2012) and also in the adult brain (De Sonnaville et al., 2020; Kokovay et al., 2012; Lepko et al., 2019; Silva-Vargas et al., 2016). Several studies indicated a direct connection between EVs present in CSF and NSCs niches (Batiz et al., 2015; Feliciano et al., 2014; Lepko et al., 2019; Losurdo & Grilli, 2020; Lun et al., 2015; Willis et al., 2022; Zhang et al., 2017). Yet much needs to be learned about the chemical identity of EV-born neurogenic factors, how they are packaged into EVs, how they are delivered to and interact with the NSCs and which responses they evoke in their targets. We have developed an in vitro assay that can address some of these questions. We prepared EVs from the secretome of the rat Z310 choroid plexus cell line (EV^{Z310}), by a combination of differential centrifugation and flotation on an iodixanol density gradient (Crescitelli et al., 2020; Kowal et al., 2016). These EV^{Z310} were co-cultured with NSCs isolated either from the SVZ or from the tanycyte region. EVs were added to NSCs in medium or, alternatively, as dried-down deposits. In both cases, purified EVs^{Z310} induced the compact rounded NSCs to rapidly form intricate cellular networks in which multiple cells were contacting each other through long processes. EVs produced by choroid plexus primary culture evoked NSC differentiation in the similar manner. These dramatic morphological changes were accompanied by the induction of genes in the differentiating cells, genes that are characteristic of early neurons and astrocytes. Gene induction was dose-dependent and reached saturation at EV^{Z310} concentrations of 1.2–1.5 × 10^9 particles per millilitre. LC-MS/MS showed that the differentiation-inducing EV^{Z310} were enriched for membrane and membrane-associated proteins involved in cell differentiation, membrane trafficking and membrane organization. EVs purified from mouse embryonic fibroblasts (EV^{MEF}) had little effect on the NSCs and did not show an enrichment of membrane and membrane-associated proteins.

2 | MATERIALS AND METHODS

A list of the antibodies and primers, which were used, is provided in the Supplementary information.

2.1 | Cell culture

Immortalized Z310 rat choroidal epithelial cells were used as a choroid plexus substitute. Zhang et al. established the Z310 cell line in 2002 (Zheng & Zhao, 2002), starting with choroid plexus tissue collected from Sprague–Dawley rats (4–6 weeks old, both sexes). Such Z310 cells have been used in multiple studies, including those in which the choroid plexus primary culture and Z310 cells were compared side by side and were shown to be similar (Shi et al., 2008; Szmydynger-Chodobska et al., 2007). Based on this, various groups used Z310 cells as a choroid plexus primary culture substitute (Grapp et al., 2013; Hasselblatt et al., 2009; Kläs et al., 2010). MEFs, were isolated from 13.5-day-old C57BL/6N mouse embryos. The choroid plexus contains a small number of fibroblasts (in addition to immune cells and perivascular cells) (Dorrier et al., 2022) and thus using EVs from a cell type that also occurs in the choroid plexus, provides a control. After the removal of head, liver and heart, embryos were cut into small pieces which were digested with 0.05% trypsin-EDTA (Gibco) for 30 min at 37°C. The trypsin was inactivated by the addition of culture medium (see below), the cell suspension was pipetted repeatedly with a P1000 pipette and centrifuged for 5 min at 200 × *g*. Cell viability and count were determined by flow cytometry. Both Z310 and MEF cells were grown in DMEM supplemented with 10% FBS, 1x GlutaMAX and 50 units/Penicillin/Streptomycin (all Gibco) in a humidified incubator with 95% air, 5% CO_2 at 37°C. They were passaged twice a week and were regularly checked for Mycoplasma contamination.

2.2 | Purification of EVs by differential centrifugation

Cells with a confluency of 70%–80% were washed twice with PBS. To exclude carrying along EVs from serum, Z310 cells and MEFs were maintained for 2 days in serum-free conditioned medium. The medium was then aspirated without disturbing the cells and subjected to differential centrifugation, as described by Kowal et al. (2016) (Figure 2a). The percentage of live cells at the time of harvesting was determined by Trypan Blue (Sigma). The cell pellet was collected and resuspended in 0.4% (v/v) Trypan Blue. Dead and live cells were counted using a hemocytometer (Nexcelon, Bioscience). Greater than 90% of the cells were viable, for example, in the case of Z310 cells, viability was 92.5± 2.1%. Centrifugation steps (Figure 2a): 300 × *g* for 10 min to remove cells and cell debris, then at 2000 × *g* for 20 min (Eppendorf 5702R) and 10,000 × *g* for 40 min (Eppendorf 5417R) to remove larger vesicles. The 10K supernatant was concentrated at 0°C using Vivaspin (300000 MWCO, Sartorius, Göttingen, Germany). This concentrated supernatant was centrifuged at 100,000 × *g*, for 60 min (Sorvall WX-Ultra 80, Thermo Fisher Scientific, USA) in a TH-660 rotor (Thermo Fisher Scientific). The resulting pellet was re-suspended in ice-cold PBS and centrifugation was repeated under the same condition. The resulting pellet was re-suspended in PBS and stored at −80°C.

2.3 | Size distribution and particle concentration

EV size and concentration were determined using a nanoparticle tracking analyzer (Nanosight NS300, Malvern Panalytical, Kassel, Germany). Five 60s videos with more than 200 tracks were taken per sample and analysed using the Nanoparticle Analysis software. Results represent the mean of all five measurements per sample.

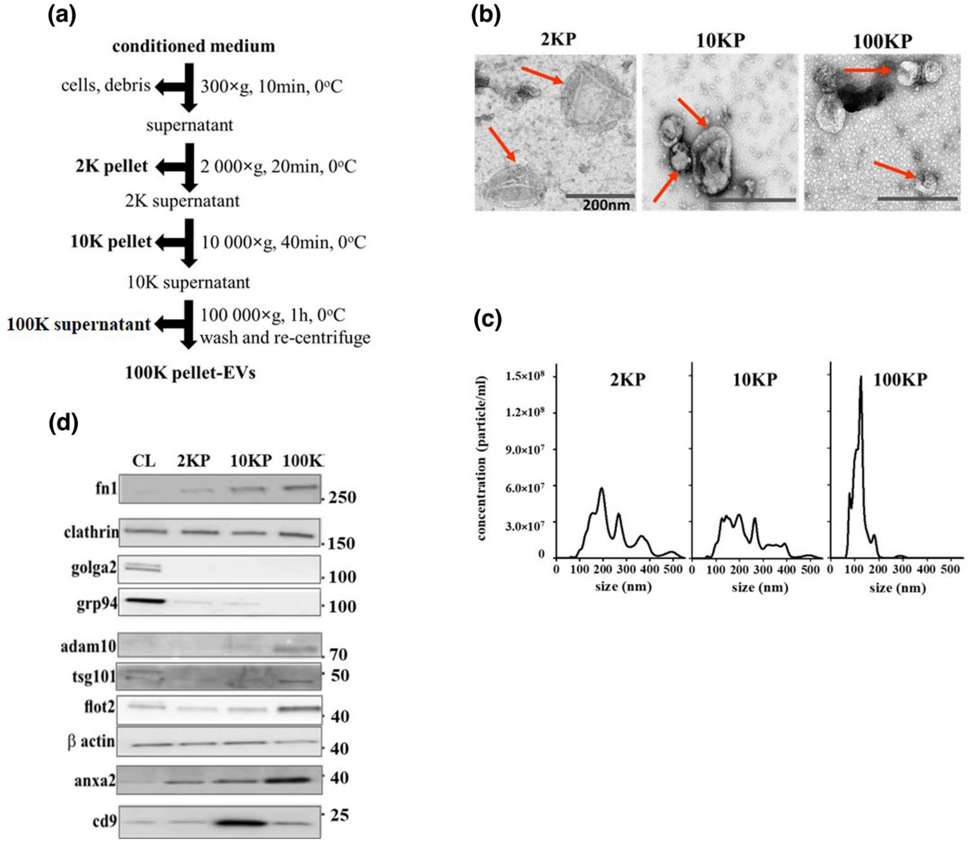

FIGURE 2 Purification and characterization of EVs from Z310 cell-conditioned medium. (a) Scheme of purification of EVs from Z310 or MEF-conditioned medium by differential centrifugation. (b) Representative electron micrographs of Z310-conditioned medium-derived vesicles (red arrows) present in the 2K, 10K and 100K Z310 pellets indicated in the scheme of Figure 2a. (c) Nanoparticle tracking analysis data showing the size distribution of the particles isolated from Z310-conditioned medium in the various pellets that are indicated in the purification scheme of Figure 2a. The 100K pellet contains EV^{Z310} in a size range of 50–150 nm. (d) Individual fractions obtained in different steps of purification of Z310 supernatant were analysed by Western blotting. Z310 cell lysate (CL) is the lane on the left.

2.4 | Transmission electron microscopy analysis

The 2KP, 10KP and 100KP pellets were visualized by negative staining. Samples were adsorbed on the surface of a carbon-coated copper grid and stained with 1% uranyl acetate. Grids were imaged by transmission electron microscopy, using a Talos L120C instrument (Thermo Fisher Scientific, Netherlands) equipped with a CMOS camera.

2.5 | Western blotting

Eighty percent confluent Z310 cells were washed twice with PBS and lysed in lysis buffer (25 mM Tris-HCl pH 7.4, 150 mM NaCl, 1 mM EDTA, 1% NP-40 und 5% glycerol) according to the manufacturer's protocol, supplemented with a protease inhibitor cocktail (Halt^{TM} Protease and Phosphatase inhibitor cocktail) (all Thermo Fisher Scientific). The protein concentration of each pellet and the cell lysate was determined using a BCA kit (Pierce^{TM}, Thermo Fisher Scientific). Equivalent quantities of proteins in pellets or in cell lysates were mixed with SDS loading buffer (1M Tris pH 6.8, 4% SDS, 20% glycerol, 10% mercaptoethanol, 0.2% bromophenol blue) heated at 95°C for 10 min and loaded on a 4%–20% polyacrylamide gradient gel (Bio-Rad Laboratories). Subsequently, samples were transferred to a PVDF membrane (Bio-Rad Laboratories). Membranes were blocked with 5% non-fat dry milk powder in TBST (0.1% Tween 20 in Tris-buffer saline) for 30 min, followed by overnight incubation with the appropriate primary antibody, at 4°C. After washing, membranes were incubated with the secondary antibody for 1 h at RT. All antibodies were diluted in blocking buffer according to the manufacturer's recommendations. After washing, membranes were developed using ECL Super signal West Femto (Thermo Fisher Scientific), and protein bands were visualized on an Image Quant LAS 4000 imager (GE Healthcare Bio-science AB, Sweden).

2.6 | Sample preparation for LC–MS/MS

Isolated EVs were lysed by adding an equal volume of lysis buffer (4% [wt/v] SDS 1 mM EDTA 100 mM Hepes, pH 8) supplemented with a protease inhibitor cocktail (cOmplete, Roche) and sonicated in a BioRuptor (Diagenode) with 30s on-and-off cycles for 5 min. Proteins were reduced, alkylated and purified as described (Hughes et al., 2014; Silbern et al., 2021). The digestion was accomplished overnight in 50 mM ammonium bicarbonate buffer using trypsin (Promega)-to-protein ratio (wt/wt) of 1:20. Vacuum-dried samples were re-dissolved in 2% (v/v) acetonitrile 0.1% (v/v) trifluoroacetic acid in water and subjected to LC–MS/MS analysis.

2.7 | LC–MS/MS acquisition

Samples were analysed using an Orbitrap Fusion Tribrid or a Q-Exactive HF-X (both Thermo Fisher Scientific) mass spectrometer interfaced via an LC set-up as described (Silbern et al., 2021). Peptides were separated using 118 min linear gradients ranging either (A) from 4% to 5.6%, 16%, 25.6%, 40%, 90% and back to 4% (v/v) acetonitrile over 3, 57, 30, 16, 6 and 6 min, respectively (Orbitrap Fusion) or (B) from 1.8% to 4%, 33.6%, 72% and back to 1.8% over 5, 101, 6, and 6 min (Orbitrap HF-X). The mass spectrometer was operated in a data-dependent acquisition mode. A survey scan was performed at 120,000 resolution and 50 ms maximum injection time (MaxIT). Thirty top-abundant peptide precursors (or keeping a constant duty cycle of 3 s) were selected for sequencing using a 1.6 *m/z* isolation window. Precursor ions were fragmented in an HCD cell and the normalized collision energy setting of 28% or 30%. MS/MS spectra were acquired in Orbitrap operated using 15,000 resolution and 54 ms MaxIT or 30,000 resolution and 120 ms MaxIT. Precursors were excluded from repeated sequencing for 30 s.

2.8 | LC–MS/MS data analysis

Raw MS data were processed by MaxQuant (version 1.6.2.10) (Cox et al., 2011) using default parameters. MS/MS spectra were searched against *Rattus norvegicus* and *Mus musculus* canonical protein sequences from Uniprot (Bateman, 2019) (December 2020, 29,940 and 17,051 sequences, respectively). Protein groups with at least two razor or unique peptides were considered as identified. IBAQ values (Schwanhäusser et al., 2011) attributed to the same gene name but several protein groups due to different origin (rat/mouse) were summed in order to achieve a single quantitative value per gene. In the following, only genes quantified in at least two $\mathrm{EV}^{\mathrm{Z310}}$ replicates were considered for further analysis: iBAQ values were log2-transformed, normalized by median-subtraction, and missing values were imputed by random sampling from a normal distribution centred at the 5%-intensity quantile and a standard deviation equal to a half of the standard deviation of each replicate's intensities. *Limma* R package (Smyth, 2005) was used to test for differential protein abundance in $\mathrm{EV}^{\mathrm{Z310}}$ and $\mathrm{EV}^{\mathrm{MEF}}$. Candidates satisfying the criteria of q-value < 0.01 (Storey, 2002) and an absolute $\log_2 \mathrm{FC} > 1$ were considered as differentially expressed.

2.9 | GO pathway enrichment analysis and protein–protein interaction network functional enrichment analysis

Proteins identified in EVs by MS were analysed by DAVID (Database for Annotation, Visualization and Integrated Discovery). Proteins identified in $\mathrm{EV}^{\mathrm{Z310}}$ belonging to the cellular component category 'vesicle' were used as input for STRING (protein–protein interaction networks functional enrichment analysis). To visualize functional interactions, MCL clustering was used. To contrast $\mathrm{EV}^{\mathrm{Z310}}$ and $\mathrm{EV}^{\mathrm{MEF}}$ proteomes, the GO category 'cellular component' was selected after functional annotation clustering. For each cellular component, the Benjamini-corrected p-value was displayed as bar graph, from the highest ranking to the lowest one. Analysis revealed main differences in sub-category 'membrane'. Proteins present in $\mathrm{EV}^{\mathrm{Z310}}$ but not in $\mathrm{EV}^{\mathrm{MEF}}$ were used as input for the subsequent STRING analysis.

2.10 | Iodixanol density gradient centrifugation

Flotation in an iodixanol gradient was performed as described in Crescitelli et al. (2020) with some modifications. The 100K pellet obtained after differential centrifugation was re-suspended in 1 mL of 40% iodixanol (v/v) (OptiPrep$^{\mathrm{TM}}$ Density Gradient Medium, Sigma) in PBS and bottom loaded. For the discontinuous iodixanol gradient equal volumes of solutions of 30%, 20% and 10% iodixanol were layered on the top of the sample (Figure 6a) and centrifuged in a 4-mL tube (Beckman Coulter, 328874) at 180,000 × g for 19h, at 0°C (Sorvall WX-Ultra 80, Thermo Fisher Scientific) in a TH-660 rotor (Thermo Fisher Scientific). Fractions of 500 μL from top to bottom were collected from the tube. An opaque band of EVs was recovered in fraction 6.

2.11 | NSC dissection and neurosphere expansion

Animal experiments were carried out in accordance with regulation of the Office of Consumer Protection and Food Safety of Lower Saxony and conformed to German Laws on Animal Welfare. To isolate NSCs from SVZ of the lateral ventricle and the tanycyte region of v3V, 6–8 weeks old male mice of the strain C57BL/6N were sacrificed. To isolated stem cells from the tanycyte area of the v3V, intact brain was placed in a brain matrix (Plano, GmbH) sub-merged in HBSS (Hank´s balanced solution with Ca and Mg, Gibco) supplemented with glucose (0.45%). Two razor blades were used to cut 3 mm thick coronal sections. Under the stereomicroscope, v3V was isolated and the tanycyte area was separated, using tungsten needles (for details see Faubel et al. (2016)). The NSCs from SVZ of the lateral ventricle were isolated according to Walker and Kempermann (Walker & Kempermann, 2014). SVZ and tanycyte tissues were minced with a scalpel blade, transferred to pre-warmed 0.05% Trypsin-EDTA and incubated for 10 min at 37°C with mixing every 3 min. Then the tissue was dissociated by gentle pipetting. The enzymatic reaction was stopped by mixing with pre-warmed trypsin inhibitor (0.125 mg/mL containing DNase I, 0.01 mg/mL), then spun down for 5 min at 300 × *g*. The pellet was re-suspended in medium and spun again. The final pellet was re-suspended in complete growth medium (Neurobasal Medium with supplement, see below) and passed through cell strainers (first 70 μm, then 40 μm) and placed into an ultra-low attachment surface 6-cm polystyrene dish (Corning, USA). After 7 days, neurospheres were visually inspected. The growth medium was changed every second day.

2.12 | Dissociation of neurospheres

The NSCs were grown in Neurobasal Medium supplement with 2% B27, 1% N2 supplement, 1x GlutaMAX, 50 units/mL Penicillin/Streptomycin (all Gibco), 20 ng/mL purified mouse receptor-grade epidermal growth factor (EGF), and 20 ng/mL recombinant bovine fibroblast growth factor (FGF-2) (both Peprotech). Neurospheres were passaged by centrifugation at 300 × *g* for 5 min. The pelleted spheres were re-suspended in prewarmed 0.05% Trypsin-EDTA and incubated at 37°C for 5 min, then an equal volume of trypsin inhibitor (0.125 mg/mL containing DNase I, 0.01 mg/mL) was added. The resulting individual cells were centrifuged for 5 min at 300 × *g*, and the cell pellet was resuspended in fresh medium. The cells were counted using a hemocytometer and seeded at a concentration 2×10^5 cells/mL for all experiments.

2.13 | Choroid plexus primary culture

To isolate choroid plexus from the lateral ventricle, 6–8 weeks old male mice (C57BL/6N) were sacrificed. Isolation and culture of primary mouse choroid plexus were performed essentially as previously described (Menheniott et al., 2010). Choroid plexus was removed from the lateral ventricle at ZT 5, and rinsed in HBSS supplemented with glucose. Thereafter, the HBSS was aspirated, pre-warmed Pronase (2 mg/mL) was added, followed by incubation at 37°C for 5 min. Growth medium was added to stop digestion, the cells were centrifuged for 5 min 300 × *g*, the supernatant was removed and the cell pellet was suspended in fresh medium. Another step of centrifugation followed (5 min 300 × *g*). The final pellet was suspended in complete DMEM growth medium (10% FBS, 50 units/mL Penicillin/Streptomycin, 10 ng/mL EGF) supplemented with 20 μM cytosine arabinose and plated on poly-D-lysine coated plates which were kept in a humidified incubator (95% air, 5% CO_2) at 37°C. The medium was changed every 48 h until cells became fully confluent.

2.14 | Differentiation assay with EVs in suspension

NSCs in neurobasal medium were seeded on an appropriate size petri dish (Thermo Fisher Scientific, Denmark, 153066) and EVs from the 100K pellets, re-suspended in PBS were added. Amounts of added EVs were normalized to their total protein concentration, as determined by a BCA assay. The NSCs were cultured in a CO_2 incubator for 24 h and bright field images of live cells were taken. After photography, the NSCs were processed for immunohistochemistry, qPCR or flow cytometry.

2.15 | Differentiation assay using EV dry drops

EVs were applied on the surface of the eight-chamber tissue culture slide (Corning, USA, 354108) as a 1-μL drop. The drop was dried (approximately 15 min) and then NSC (2×10^5 cells/mL) in culture medium were added and chambers were placed into a CO_2 incubator. Twenty-four later images of the chamber wells were taken. For the testing of stability of dried-down EVs, drops were applied to the wells of the eight-chamber slides which were then kept for 7 days at −20°C.

2.16 | Protease and nucleases protection assay

Proteinase K (Bioline) was added to a final concentration of 10 μg/mL to the EVs. Samples were incubated for 30 min on ice. Proteinase K was inactivated for 10 min by incubating with tetrapeptidyl chloromethyl ketone at a final concentration of 10 μg/mL (EMD Millipore) on ice. Then DNase (2U final concentration) was added and the sample was incubated at 37°C for 30 min. The reaction was stopped with DNase inhibitor (2U final concentration) (DNA free kit, DNase treatment and removal, Invitrogen, Thermo Fisher Scientific). Then RNase A (40U final concentration, 37°C, 30 min) (Qiagen) was added and inactivated by RNase inhibitor (40U/mL) (Invitrogen, Thermo Fisher Scientific). Samples were cleaned using an Amicon ultra centrifuge unit (Merck, Millipore) with PBS. The resulting EVs^{Z310} were then added to NSCs^{tz} or NSCs^{SVZ} for assessing their differentiation inducing capacity.

2.17 | Immunofluorescence

Cells on slides or in Petri dishes were fixed with 4% formaldehyde, washed with PBS (0.1% Triton) and blocked for 30 min (0.25% Triton and 0.25% BSA in PBS) at room temperature. Then cells were incubated overnight at 4°C with primary antibody. After the three washing steps with PBS (0.1% BSA, 0.1% Triton), incubation with secondary antibody for 1 h at room temperature followed. After five washes, coverslips were mounted with mounting medium with DAPI (Vectashield, Vectorlabs) and images were acquired using a Leica DMI 6000B fluorescence microscope, with LAS X software (Leica Microsystems, Germany).

2.18 | RNA preparation for qPCR analysis

Total RNA was extracted from cells using Trizol reagent (Ambion) or RNeasy kit (Qiagen) according to the manufacturer´s instructions. First genomic DNA was removed and then 1 μg RNA was reverse transcribed by iScript gDNA Clear cDNA synthesis Kit (Bio-Rad Laboratories) according to manufacturer's instructions. *Gapdh* was used for normalization. qPCR was performed with SsoAdvanced Universal SYBR Green Supermix (Bio-Rad Laboratories) on CFX96-Real-Time system (Bio-Rad Laboratories, Germany). For primers, see Supplementary information, Material.

2.19 | Flow cytometry

NSCs were analysed after 24 h of culturing in the presence of EVs. Single-cell suspensions were obtained after accutase-mediated (ESGRO Complete^{TM} Accutase, EMD Millipore) dissociation. Cells were then fixed with 4% formaldehyde for 15 min in the dark at room temperature. Washing and blocking steps were followed by overnight incubation with primary antibody at 4°C. After the washing steps, incubation with the appropriate fluorescent secondary antibody for 1 h at RT followed. The cells were analysed using a flow cytometer BD Accuri C6 (BD Bioscience, USA) and BD Accuri^{TM} C6 software.

2.20 | Proliferation assay

NSCs were seeded on 96-well flat-bottom tissue culture plates of good optical quality (Falcon) at a density of 2×10^5 cells per millilitre. Cells were cultured for 24 h in Neurobasal Medium (control) or in medium containing an increasing concentration of EV^{Z310} or EV^{MEF}. Thereafter, MTT solution was added and all subsequent steps were performed according to manufactures' instructions (Merck, Colorimetric (MTT) kit for cell survival and proliferation). Absorbance was measured with an ELISA plate reader (Infinite M2000 Pro Tecan) with a test and reference wavelength of 570 and 630 nm, respectively. For the Trypan Blue assay, NSCs were seeded on a 6-cm Petri dish at a density of 2×10^5 cells per millilitre and cultured in increasing concentration of EV^{Z310} or EV^{MEF} for 24 h. Trypan Blue staining was performed according to the manufacture's instruction (Sigma) and the number of cells was determined with a hemocytometer.

3 | RESULTS

3.1 | Characterization of EVs and their protein composition

We purified EVs secreted by rat Z310 choroid plexus cells (EV^{Z310}), by mouse choroid plexus primary culture (EV^{CHP}) and by mouse embryonic fibroblasts (EV^{MEF}). The Z310 cell line is a widely used surrogate for choroid plexus primary cells (for references for the Z310 cells usage see Materials and Methods). Conditioned media were collected and subjected to differential centrifugation (Figure 2a). Pellets obtained after each centrifugation step were analysed for particle size, particle concentration and the presence of EV protein markers (Thery et al., 2018) (Figures 2b–d and S1a–c). The 2K and 10K pellets had the highest total protein content and nanoparticle tracking analysis and electron microscopy revealed the presence of particles in the size range of 100–500 nm (Figure 2b,c). Centrifugation at 100,000 × g removed particles >200 nm and yielded predominantly particles of 100 nm, the size for exosomal EVs (Figures 2b,c and S1a,b). Choroid plexus primary culture cells expressed transthyretin (Figure S2a) and produced EVs in the size range of 30–120 nm (Figure S2b). Fibronectin 1 (Fn1), disintegrin and metalloproteinase domain-containing protein 10 (Adam10) and tumour susceptibility gene 101 (Tsg101) are typical for small EVs (Tkach et al., 2018) and they were noticeably enriched in the 100K pellet (Figure 2d). Annexin A2 (Anxa2) and flotillin2 (Flot2) were elevated in this fraction but were also present in the 2K and 10K pellets. By contrast, endoplasmin (Gpr94, Hsp90b1), a marker for large vesicles (Tkach et al., 2018), was present in the whole cell lysate (CL), barely detected in the 2K and 10K pellets, and absent in the 100K pellet. Golgi marker, golgin sub-family A member 2 (Golga2/Gm130) was found only in the cell lysate fraction (CL). β actin levels declined during purification, with a maximum in cell lysate and a minimum in the 100K pellet, for example, (Kowal et al., 2016) (Figure 2d). Figure S1c shows that in the 100K pellet containing EVs^{MEF}, EV markers (fn1, clathrin, alix, tstg101 and flot2) were present. By contrast, golga2 and grp94 were absent, as expected, in the EVs^{MEF} and found in MEF cell lysate.

The 100K Z310 pellet obtained after the ultracentrifugation was subjected to mass spectrometric analysis. One thousand and two hundred proteins were identified (Table S1) which is in the range as reported for EVs isolated from mouse CSF (Balusu et al., 2016). The MS data confirmed the presence of the typical EV markers. Examples are transmembrane or GPI-anchored tetraspanins (CD9, tetraspanin-8), integrins (integrins alfa, -beta), basement membrane-specific heparan sulphate proteoglycan core protein (Hspg2), basigin (Bsg), Adam10 and multidrug resistance-associated protein 1 (Abcc1). Cytosolic proteins were also recovered in EVs including Tsg101, programmed cell death 6-interacting protein (Pdcd6ip, Alix), vacuolar protein sorting-associated protein (Vps4a), arrestin domain-containing protein 1 (Arrdc1), Flot1/2, transforming protein RhoA (Rhoa), annexins (e.g., anxa1, -2, -5, -11), heat shock cognate 71kDa protein (Hspa8) and syntenin-1 (Sdcbp). MS analysis also identified secreted protein typically recovered with EVs (e.g., lactadherin-Mfge8). By contrast, neither cytokines (interleukins, interferons) nor growth factors were detected, with the exception of bone morphogenetic protein 1 (Bmp1). Bmp1, a metalloproteinase that was previously identified in the CSF and plays a role in the development of the CNS by stimulating progenitors in the SVZ (Lehtinen et al., 2011). Thus, Bmp1 could be one of the CSF-born neurogenic factors that are transported inside EVs. Proteins associated with other intracellular compartments such as the nucleus (histones) or mitochondria (Tomm20) but not with Golgi apparatus (Golga2) were also detected. The 100K pellet also contained ribosomal proteins and proteasomes, large protein complexes known to co-sediment with EVs (Konoshenko et al., 2018; Thery et al., 2018).

Gene ontology (GO) enrichment analysis of ‘cellular component’ categories showed that proteins identified in the 100K pellet were significantly enriched for ‘extracellular exosome’ ‘membrane’ and ‘vesicle’ sub-categories (Figure 3a). Other enriched sub-categories were ‘focal adhesion’, ‘adherent junction’, ‘extracellular matrix’, ‘neuron projection’, ‘neuronal cell body’, ‘dendrite’, ‘synapse’ and ‘axon’. Selected typical EV proteins retrieved from the sub-category ‘vesicle’ formed a STRING protein interaction network (Figure 3b). We picked this sub-category since it contained EV-typical markers discussed above. Our analysis revealed a functional association and a significant number of interactions (PPI enrichment p-value $< 1.e^{-16}$). MCL clustering (inflation parameter 1.9) revealed four major proteins clusters (Figure 3b). The biggest cluster (red) included proteins associated with ‘SNARE, vesicle fusion and transport’. Two additional clusters (yellow, green) represented proteins involved in endosomal sorting complex required for transport (ESCRT), cell adhesion, morphogenesis and cellular projections. Proteins involved in ER-Golgi transport formed the smallest cluster (blue). This result showed strong interactions of proteins relevant to EV biology.

Western blots were used to investigate whether proteins identified by mass spectrometry were present as full-length protein in EV^{Z310} lysates. We choose signal transducer and activator of transcription 3-stat3 (92 kDa), slit homolog 2 protein-slit2 (200 kDa) and transcription activator BRG1 also known as ATP-dependent chromatin remodeler-smarca4 (185kDa). Slit2 is a secreted extracellular matrix protein involved in axon guidance (Kaneko et al., 2018; Nguyen-Ba-Charvet & Chédotal, 2002; Sawamoto et al., 2006). Stat3 is a transcription factor and smarca4 is a transcriptional activator that both regulate GFAP expression (Brenner & Messing, 2021; Ito et al., 2018). Figure S1d demonstrates that these proteins are present in EV^{Z310} and electrophorese, according to the band size provided by the manufacturer.

EVs from MEFs (EV^{MEF}), were prepared and analysed as described for EV^{Z310} (Figures 2a and S1a–c) and underwent MS analysis. Five hundred and seventy proteins could be identified (Table S1), less than for EV^{Z310}. The likely cause for this difference is that Z310 cells but not MEFs are secretory cells. A Venn diagram (Figure 3c) reveals that ~40% of the EV^{MEF} proteins were also present in EV^{Z310}. Three hundred and twenty-nine proteins were exclusive for EV^{MEF} and 867 for EV^{Z310}. GO enrichment analysis for the category ‘cellular component’ showed in EV^{MEF} a significant enrichment of proteins in sub-categories ‘focal adhesion’, ‘extracellular matrix’ and ‘adherent junction’. This finding is consistent with a role of fibroblasts in the CNS including the choroid plexus to provide structural support by secretion of extracellular matrix proteins (Dorrier et al., 2021). The sub-category ‘membrane’ was much less enriched in EV^{MEF} than in EV^{Z310} and just a few EV^{MEF} components fell into the sub-categories related to neurons.

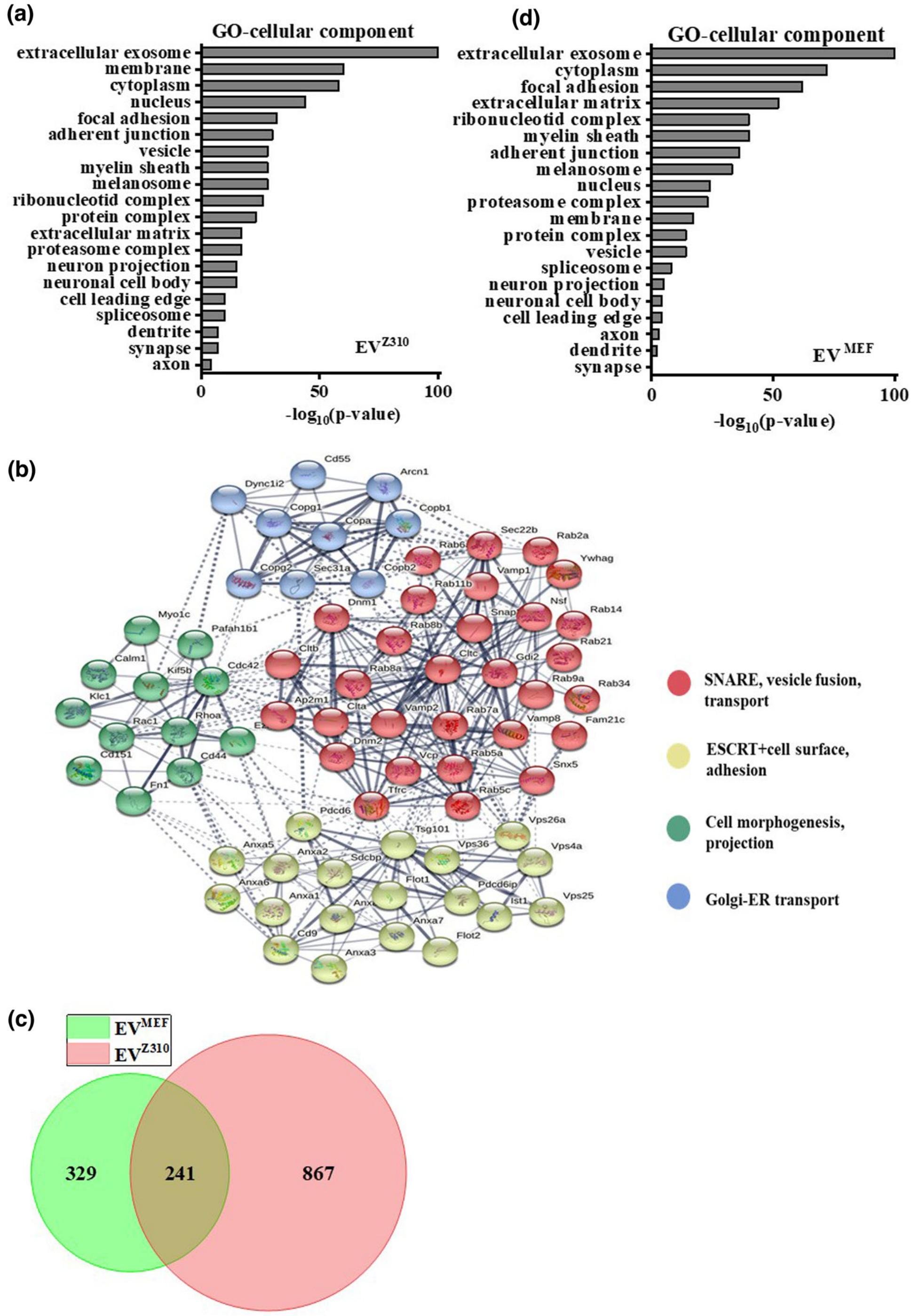

FIGURE 3 Analysis of EV^{Z310} and EV^{MEF} proteomes. (a) GO-cellular components of EVs^{Z310}. Note an enrichment in 'extracellular exosome', 'membrane', 'vesicles', 'neuronal projection', 'neuronal cell body', 'dendrite', 'synapse' and 'axon' sub-categories. (b) Protein–protein interactions in EVs^{Z310} proteome for the gene ontology sub-category 'vesicle', visualized by STRING. This indicates a functional interaction network. Solid lines inside clusters show direct physical protein interactions and dotted lines show functional interactions. (c) Venn diagram shows that EV^{Z310} and EV^{MEF} protein contents differ significantly. The diagram is based on combining three data sets (EV^{Z310}) and two data sets (EV^{MEF}) (see Supplementary Table 1). (d) GO-cellular components of EV^{MEF}. Comparison with EV^{Z310} shows differences in ranking of several categories such as 'membrane' that ranks high only in the EV^{Z310}. (e) Functional analysis of protein–protein interactions by STRING. Proteins identified exclusively in EV^{Z310} and falling into the gene ontology sub-category 'membrane' were included. Three main clusters of protein–protein interaction emerged.

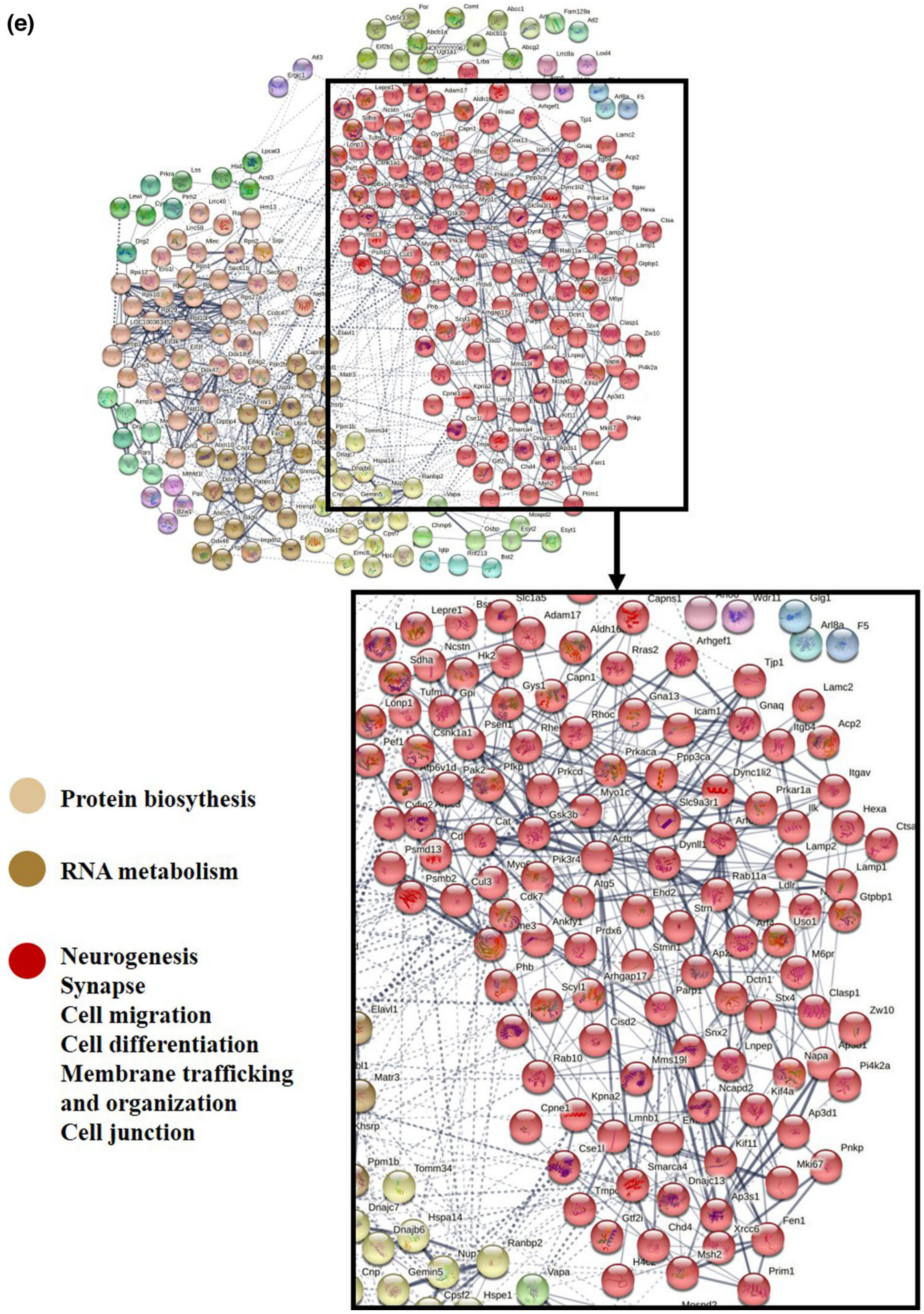

FIGURE 3 Continued

STRING functional analysis of the 248 EV^{Z310} proteins that were classified into the sub-category 'membrane' and not identified in EV^{MEF}, yielded three prominent clusters (Figure 3e). Two small clusters (brown) compiled proteins involved in 'RNA metabolism' and 'protein biosynthesis'. Examples are 60S ribosomal proteins L14 (Rpl14), Rpl27, Rpl36 and eukaryotic translation initiation factors (Eif4g2, Eif3k). Some of the ribosomal proteins that are present in 100K pellet co-purify with EVs (Kowal et al., 2016) may not be EV cargo (Thery et al., 2018). The red cluster comprised proteins associated with 'neurogenesis', 'cell differentiation', 'cell migration', 'membrane organization and trafficking'. Examples are Adam17 and a Rheb-Ras homolog enriched in brain where it plays a role in neural plasticity. Cdk5, which is also in the red cluster, is important for neural migration and CNS development and regulates cytoarchitecture, axon guidance and membrane transport (Dhavan & Tsai, 2001). Proteins involved in sub-category 'synapse' are sorting nexin-4 (Stx4) and N-ethylmaleimide-sensitive factor attachment protein alpha (Napa). Examples of the proteins found in sub-category 'cell migration' and 'membrane organization' are integrins, Itgb4 and integrin-linked protein kinase-Ilk, which are involved in cell adhesion, cell architecture and cell motility. Proteins of the 'membrane trafficking and organization' sub-categories are Ras-related protein Rab-10 (Rab10), EH domain-containing protein 2 (Ehd2), sodium-hydrogen antiporter 3 regulator (Slc9a3r1). We took the composition of the red cluster as an indicator that EV^{Z310} contains proteins that could control the NSC biology.

3.2 | EVs from the Z310 cell line induce NSC differentiation in a dose-dependent manner

As shown by MS analysis, EVs from the choroid plexus-derived Z310 cell line contain many proteins associated with membrane function and neuronal differentiation (Figure 3). It is possible that after their secretion by the choroid plexus into the CSF, some EVs are transported to the NSC niches (Figure 1) where they might affect NSC membrane and/or evoke the differentiation of the NSCs. To test this hypothesis, we prepared NSCs from the tanycyte region and the SVZ of mouse brain (Figure 1) and generated NSC aggregates (neurospheres) using standard methods (see Materials and Methods and Walker and Kempermann (2014)). In accordance with previous work (Haan et al., 2013; Robins et al., 2013; Walker & Kempermann, 2014), the NSCs from either region formed neurospheres (Figure S3a), that expressed typical NSC markers, such as *nestin*, *paired box protein 6 (Pax6), Gfap, Sox2* and *vimentin* (Figure S3b).

After the neurospheres were dissociated into single cells, EVs^{Z310} were added to them. We found that within 24 h, the NSCs from the tanycyte niche (NSC^{tz}) formed complex cellular networks in which individual cells cross-connected with each other through long processes (Figure 4a, first column, second row). NSCs from the SVZ niche (NSC^{SVZ}) yielded similar cellular networks (Figure 4a, second column, second row). In the case of EV^{Z310}-exposed $NSCs^{tz}$, 50 ± 2% of the attached cells were in contact with at least one neighbour and had ≥3 processes that were ≥ 20-μm long. In the case of $NSCs^{SVZ}$, this percentage was 50 ± 5%. Therefore, network-forming cells account for half of all attached cells. We rarely saw such processes in controls in which only culture medium was added to NSCs (Figure 4a, top row). Likewise, EV^{MEF} evoked clustering of just a few $NSCs^{tz}$ or $NSCs^{SVZ}$ and we did not observe a cell process-based network (Figure 4a, bottom row). The EV-free 100K supernatant from the differential centrifugation step (Figure 2a) added to $NSCs^{tz}$ or $NSCs^{SVZ}$ had no effect on these cells (Figure 4a, third row).

Immunostaining of fixed NSC^{tz} cultures with antibodies against intermediate filament proteins vimentin and nestin visualized the fine structure of the cellular processes and showed that processes originating from a particular cell can make multiple contacts with the neighbouring cells (Figure 4b, right column). Note, the glial fibrillary acidic protein (GFAP) expressing cell (Figure 4b, right column, third row), probably an astrocyte, contacts multiple times with the nestin-expressing cellular network. Network-forming cells account for half of all attached cells and the GFAP-positive cells belong chiefly to this group of attached, stellate cells. Single cells with a compact morphology (presumably residual NSCs) express GFAP at very low levels in the cytoplasm surrounding the nucleus (Figure 4b, first column, third row). The extracellular matrix protein fibronectin1 (fn1) co-localized with the tip of the processes (Figure 4b, right column, second row). Tuj1 (β3 tubulin) staining for early neurons revealed groups of interconnected cells (Figure 4b, right column, bottom row). Figure 4d shows staining for Stat3 protein in the nucleus of the GFAP-expressing astrocytes. Stat3 activates *Gfap* expression (Brenner & Messing, 2021; Ito et al., 2018). qPCR analyses showed that NSC morphological changes were accompanied by a significant transcriptional upregulation of the genes encoding for *fn1, stat3*, *vimentin, gfap* and also of the neuronal cadherin, *cadherin-2* (*Cdh2)* (Figure 4c).

EVs^{CHP} produced by choroid plexus primary cells had a similar effect on NSCs as EVs^{Z310}. Both induced cellular network formation and cell differentiation (Figure S2c,d). Our data suggest that EV^{Z310} can substitute for primary culture-derived EVs.

Since this study focusses primary on the early response of NSCs to EVs, the expression data we present cover, for the most part, the first 24 h after adding EV^{Z310}. As discussed below, during this period, the effect of the EVs on cell proliferation is very limited (Figure S4c–e). The percentage of cells expressing Tuj1 or GFAP is rather small by 24 h, but by 48 h, both proteins show a modest increase, at least, when a high dose of EVs^{Z310} was added. After 24 h, the fraction of Tuj1 or GFAP-expressing cells was 0.5% and 10%, respectively (304 μg/mL; Figure S4a,b). At 304 μg/mL, of EVs, and 48h of incubation, these percentages increased to 5% (Tuj1) and 12%–15% (GFAP), respectively. Previous work (Silva-Vargas et al., 2016) found that after 7 days of incubation with choroid plexus secretome, the corresponding percentages were 15% for neurons and 80% for astrocytes. Evidently, providing the entire choroid plexus secretome for a longer time leads to more pronounced differentiation of NSCs than seen with a short treatment with Z310-derived EV^{Z310}.

Flow cytometry was used to quantify the expression levels for GFAP and Stat3 proteins after coincubation of $NSCs^{tz}$ or $NSCs^{SVZ}$ with increasing doses of EVs (Figure 5a,b). The fraction of GFAP/stat3 $^{+}$ cells increased with increasing amounts of EVs^{Z310} (assessed by total protein content) added to the culture. When using EV^{MEF}, the fraction of GFAP/stat3 $^{+}$ cells remained at control levels (Figure 5a,b). The flow cytometry data are fully consistent with transcript quantification by qPCR. Levels of *gfap, fn1* and *stat3* expression showed a dose-dependent upregulation upon EV^{Z310}addition. Expression reached a saturation (Figure 5c) and the 50% effective dose (ED_{50}) was in the range of 50–70 μg/mL EV protein.

CSF from the cisterna magna, and the choroid plexus secretome induced the proliferation of NSCs (Silva-Vargas et al., 2016). This research as well as work by other authors (Lehtinen et al., 2011) focusses on NSC treatments with the inducing agent for 7 days, which is well beyond the time it takes to form cellular networks in our assay. Using an MTT or Trypan Blue proliferation

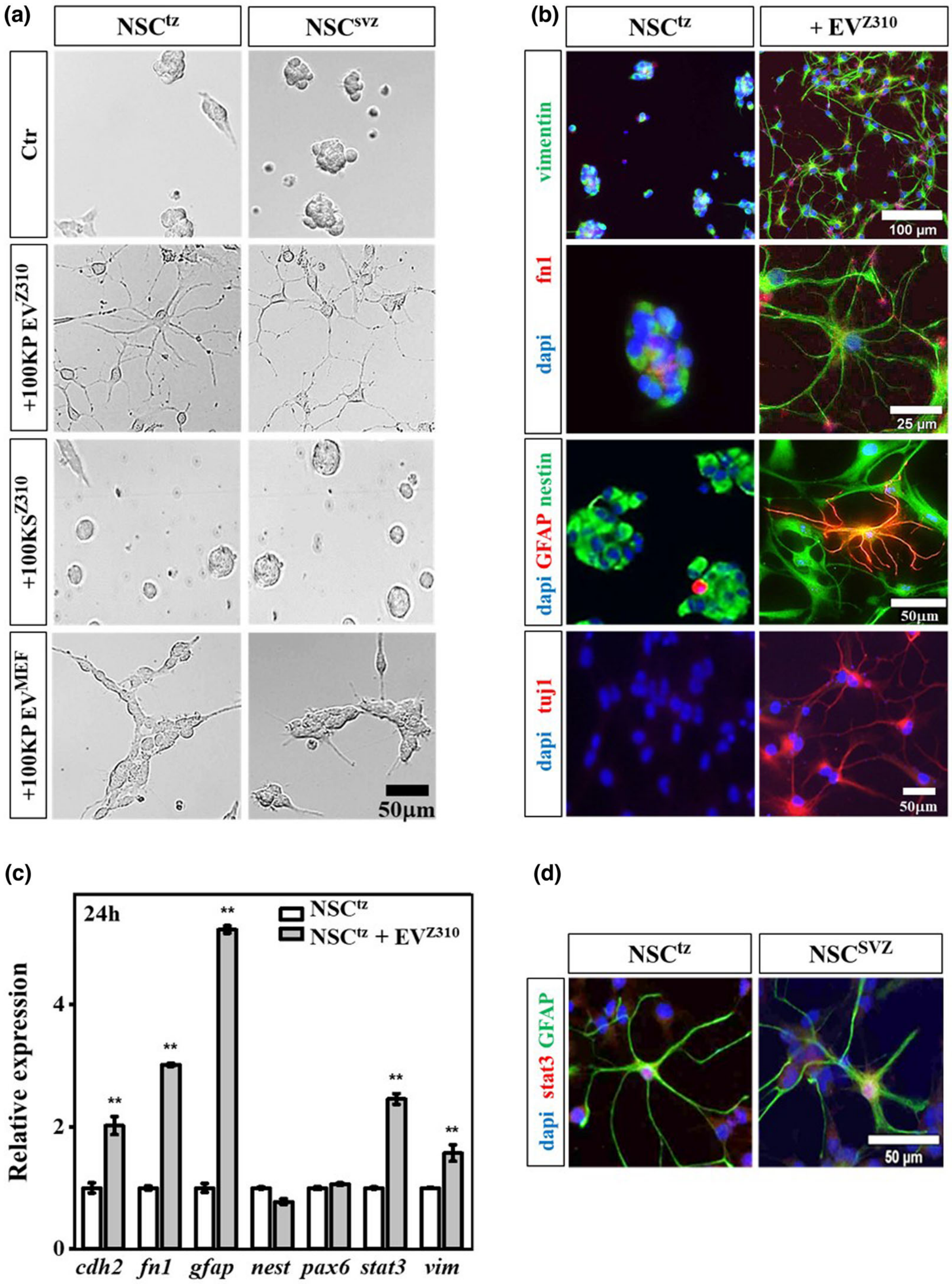

FIGURE 4 EV^{Z310} promote NSC differentiation into cellular networks. (a) Bright-field images of NSC^{tz} and NSC^{SVZ} co-cultured for 24 h with medium only (Ctr), with EV^{Z310}, with Z310 100K supernatant (100KS^{Z310}) or with EV^{MEF}. Total EV protein concentration was 76 μg/mL. (b) Immunostaining for various markers visualized cell structure and cell processes that formed in the presence of EVs^{Z310} (24 h). Astrocytes (GFAP) and early neurons (Tuj1, 48 h) were seen. NSCs cultured in medium without EVs^{Z310} did not form processes, but just spherical aggregates of an irregular shape. Note the punctate fn1 staining in the differentiating EV^{Z310}-treated NSC^{tz}. (c) qPCR showed upregulation of *cadh2, fn1, gfap, stat3* and *vimentin* expression 24 h after EV^{Z310}addition. Values are presented as means ± SD, three biological and three technical replicates were done ($^{**}p < 0.01$, Student's *t* test). (d) Immunofluorescence staining for astrocyte marker (GFAP) showed astrocytic cells with multiple processes and positive staining for nuclear Stat3 in NSC^{tz} and NSC^{SVZ} after a 24-h co-culture with EVs^{Z310}.

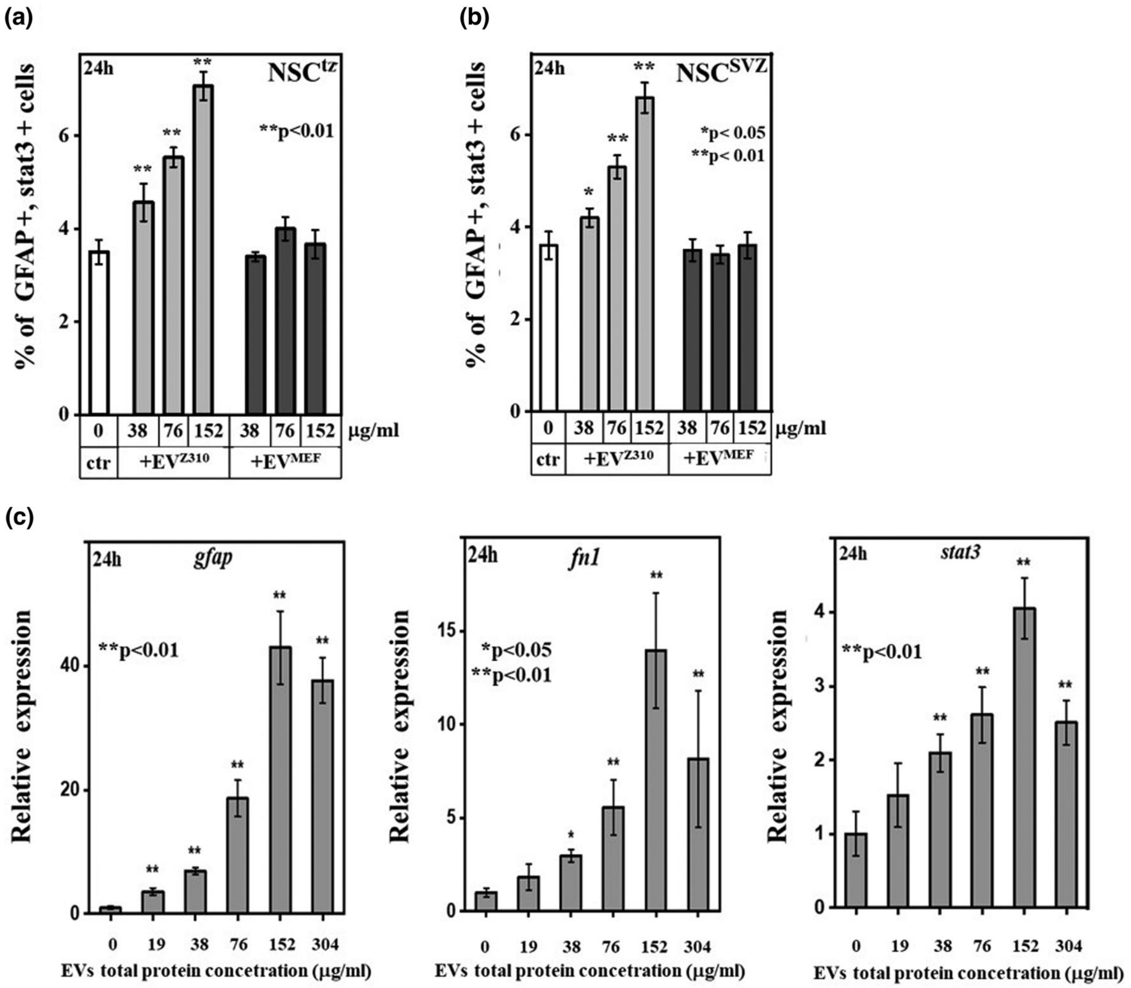

FIGURE 5 EV^{Z310} promote NSC differentiation in a dose-dependent manner. (a) Flow cytometry showed that after 24 h EV^{Z310} increased the number of GFAP- and Stat3 positive NSCs^{tz} in a dose-dependent manner (total protein concentration 38, 76, 152 μg/mL). In contrast, EV^{MEF} did not elevate the number of GFAP- and Stat3-positive cells above the control at all concentrations used. (b) Such a dose-dependent increase was also seen when NSCs^{SVZ} were co-cultured with EVs^{Z310}. (c) qPCR graphs demonstrated a dose-dependent increase of *gfap*, *fn1* and *stat3* mRNA 24 h after adding EVs^{Z310} to NSCs^{tz}. Values are means ± SD from three independent experiments ($*p < 0.05$, $**p < 0.01$, Student's *t* test).

assay, we found that the EVs^{Z310} have a small effect on NSC proliferation. Proliferation was increased by 10–15% within 24 h, depending on the source of the NSC and the concentration of EVs (Figure S4c,d). Adding EVs^{MEF} had no effect on NSC proliferation. Similar data were obtained with the Trypan Blue assay (Figure S4e). We conclude that the main effect of EVs is a cell shape change and cell network formation and, within the treatment time of <48 h, not a massive increase of cell proliferation.

3.3 | Efficient dry-drop assay to study the differentiation of NSCs

It is still considered challenging to purify EVs by centrifugation. A general recommendation is that EVs purified by differential centrifugation should be further purified on a density gradient, which separates vesicles according to their floatation speed and equilibrium density into vesicle sub-populations and also removes contaminants (Kowal et al., 2016; Tkach et al., 2018). Therefore, the 100K EV^{Z310} pellet (Figure 2a) was suspended in iodixanol and subjected to iodixanol density gradient centrifugation (Figure 6a). After the centrifugation, the gradient was partitioned into nine fractions. Fraction 6 was an opaque band that could easily be seen and hence be recovered as a single fraction. In this fraction, nanoparticle tracking analysis revealed a high concentration of particles (red lines in Figure 6b) in a size range of 100–150 nm with smaller peaks at 50 and 220 nm. Fractions 2 and 8 contained mostly particles >150 nm. Thus, this method provides an enrichment of particles in the 50–150-nm range. All nine fractions were analysed by Western blotting (Figure 6c). Clathrin was detected in fractions 4–9, flot2 in fractions 4–6 and both had maximum intensity in fraction 5. Fn1 and alix were detected only in fractions 4–6 and showed highest levels in fraction 6. Annexin2 was detected in fractions 3–7, and β actin in fractions 6 and 7. A comparison of the marker composition and particle

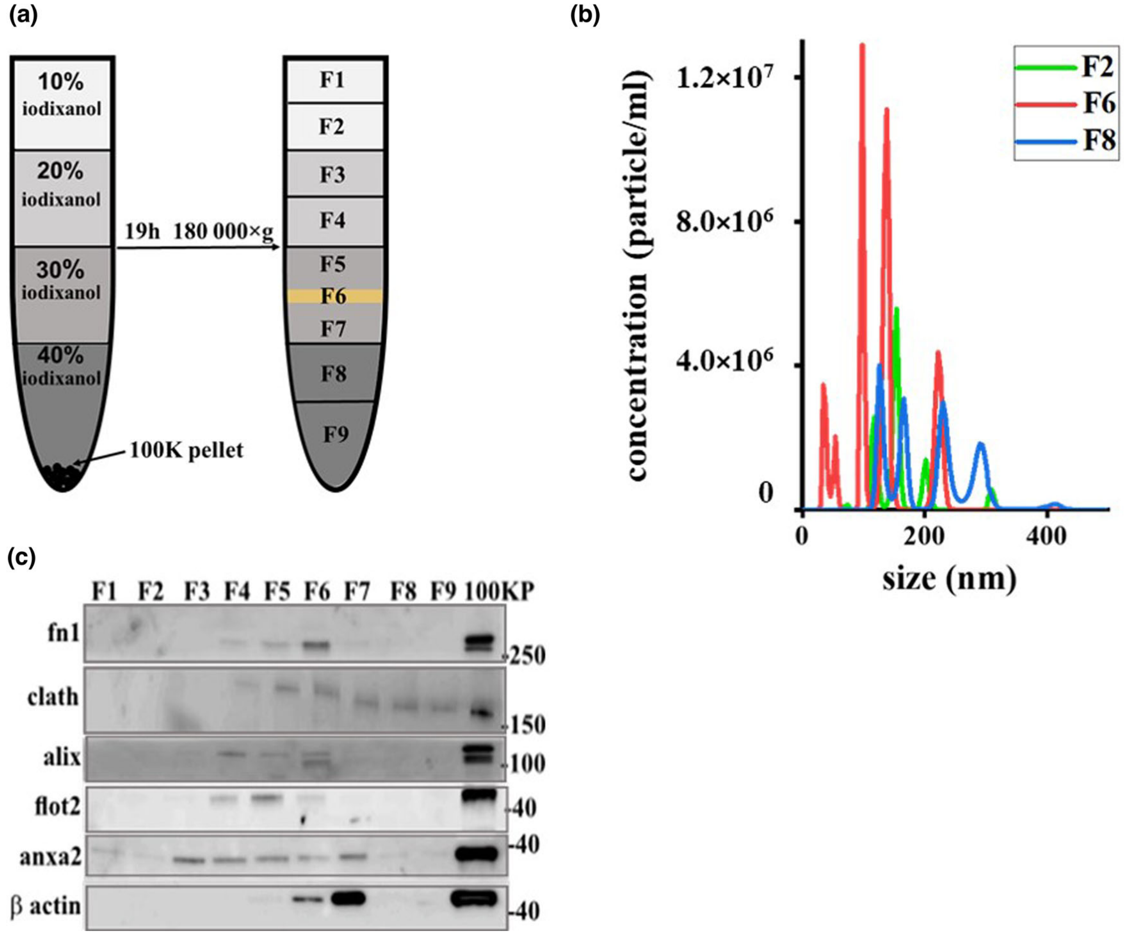

FIGURE 6 EV flotation on an iodixanol gradient produces sub-types of EVs. (a) Scheme of EV^{Z310} purification by density gradient separation. The 100K pellet obtained by differential centrifugation was re-suspended in 40% iodixanol and bottom loaded. After centrifugation, fraction 6 (yellow) was visible as an opaque band. (b) Particle size distribution in three fractions. Fraction 6 (red) showed the highest particle concentration and contained the majority of vesicles in the size range of 50–150 nm. Fractions 2 and 8 (green and blue) had a strong bias for larger vesicles (150–300 nm). (c) Western blot of the nine fractions and the starting material (100K pellet). Fraction 6 shows the highest level of fn1 and alix.

size of the various fractions with the composition of the starting material showed that the iodixanol gradient further separated the EVs of the 100K pellet into biochemically diverse sub-populations of EVs.

To efficiently examine multiple EV fractions for their ability to induce differentiation of NSC^{tz} and NSC^{SVZ} cultures, we developed a material saving 'dry-drop' activity assay. A 1-μL drop of each EV fraction (protein concentration 76 μg/mL) was applied to the bottom of each chamber of an eight-chamber tissue culture glass slide and left to dry for 15 min. Then, 200 μL of the NSC suspension (200,000 cells per millilitre) were added to the chambers and the slides were incubated for 24 h in a tissue culture incubator (Figure 7a). The organized network of attached NSCs^{tz} or NSCs^{SVZ} was readily visible and did not extend beyond the peripheral boundary of the dried drop (Figure 7b,d). The EVs from the 100K pellet and from fraction 6 provided excellent support for NSC attachment, network formation and robustly showed many attached cells that were GFAP-positive (top two rows in Figures 7d and 7e first and third bar). This agreement means that EVs from the 100K pellet obtained by differential centrifugation and those in fraction 6 of the density gradient have a very similar NSC differentiation capacity, but fraction 6 of the iodixanol gradient was biochemically purer than the initial 100K pellet (Figure 6c). This additional purification will help in the eventual purification of the active factors. Note that NSC attachment, network formation and development of the GFAP-positive astrocytes were less distinct for fractions 2 and 8 (Figure 7d, rows 3 and 4). The rest of the fractions were such that they lead to cell attachment only very sparsely and therefore only a few NSCs differentiated to astrocytes.

We also used the dry-drop assay to determine, whether the differentiation activity is merely co-purifying with EVs or is intrinsic to the vesicle. 100KP EVs were treated with proteinase and nucleases as previously described (Materials and Methods) (Shurtleff et al., 2017). A Western blot showed that Flot2 was proteinase K resistant, as expected, because this protein is contained in the interior of EVs (Figure 7c). Figures 7d (row 5) and 7e show that adding proteinase and nucleases to the EVs, had little effects on the percentage of the GFAP-positive cells developing within the drop. These results indicate that EVs themselves and not a spurious contamination in 100K pellet is causal for the effect of EVs on NSC network formation and differentiation. We also examined EVs^{MEF} in the dry-drop assay (Figure 7d, bottom row, and Figure 7e). Consistent with the results shown

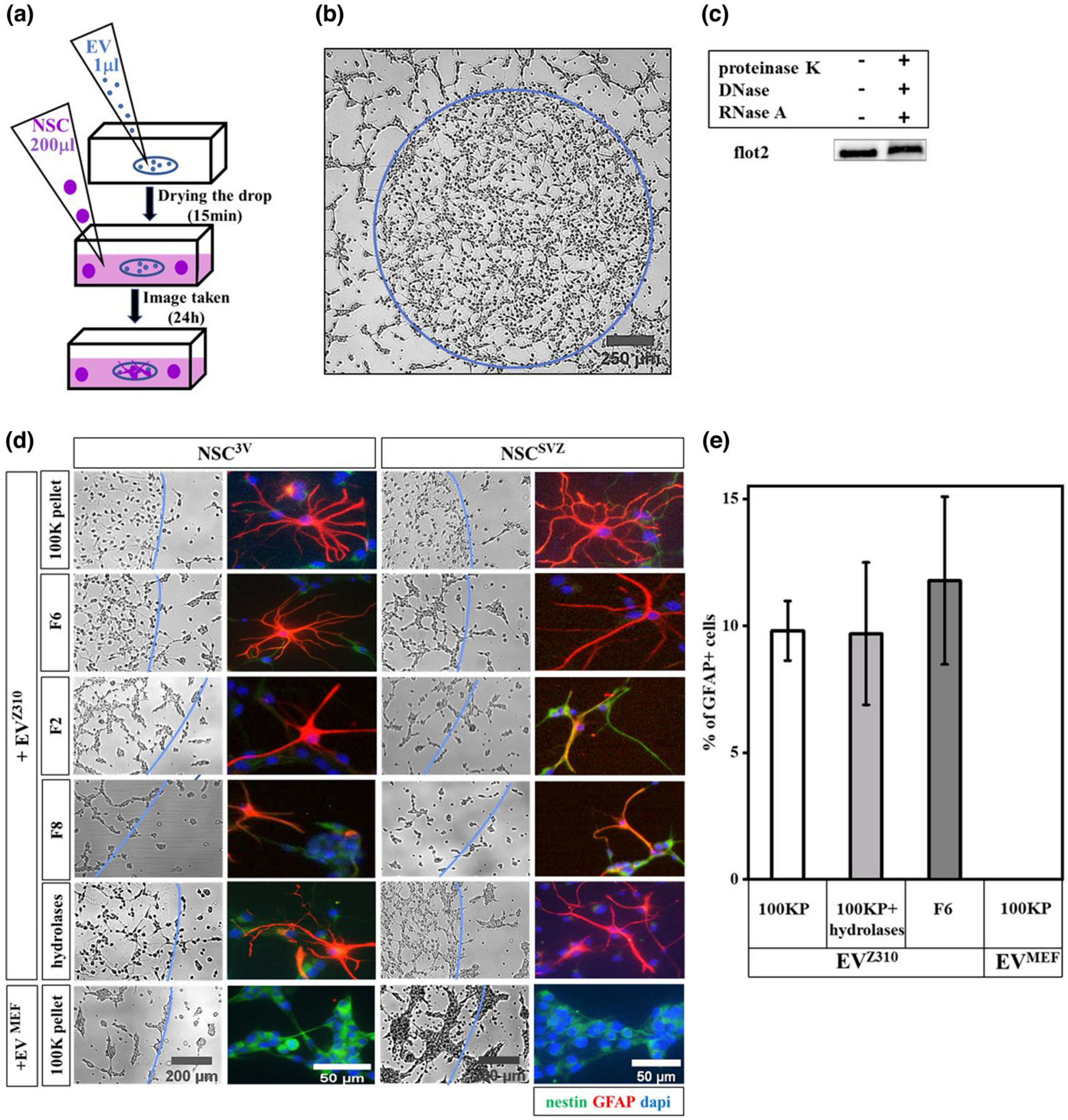

FIGURE 7 Dry-drop assay to assess EV biological activity. (a) Dry-drop assay: A 1 μL drop of EVs was deposited on the floor of an eight-chamber slide and let dry for 15 min. Thereafter (for up to a week later if slides are kept at −20°C), 200 μL of the NSC suspension were added to each chamber. The chambers were incubated for 24 h, at 37°C in a tissue culture incubator. (b) The NSC^{tz} attached and formed a cellular network only in the area of the EV drop (blue boundary). Cells outside the boundary were still floating or were at best weakly attached. (c) Level of Flot2 located inside EVs^{Z310} was not affected by sequential treatment with proteinase K, DNase and RNase. (d) Fraction number 6 obtained from the iodixanol gradient provided excellent support for NSC^{tz} and NSC^{SVZ} network formation. When EVs^{Z310} from fraction 6 were used, immunofluorescence revealed the presence of cells with astrocyte morphology that also expressed GFAP (row 2). Sequential treatment with hydrolases had no influence on the ability of EV^{Z310} to evoke differentiation (row 5). EVs^{MEF} did not provide proper support for network formation, regardless of the type of NSC used (bottom row). The blue line marks the periphery of the EV^{Z310} dried drop. (e) Percentage of GFAP-expressing cells in the area of the drop. Data were normalized to the cell number. Note the treatment with proteinase K and nucleases had no effect on the percentage of GFAP-expressing cells.

above (Figures 4a and 5a,b), EVs^{MEF} from the 100K pellet had no detectable activity in the dry-drop assay. When slide chambers containing EV^{Z310} drops were stored at −20°C for a week, there was no reduction in NSC attachment, network formation and differentiation to GFAP-positive astrocytes. Thus, the dry-drop assay provides a convenient method that allows an economic use of EV preparations.

4 | DISCUSSION

The interconnected, CSF-filled cavities of the ventricular system (Figure 1) with their motile cilia-powered transport machinery (Del Bigio, 2010) allow a targeted distribution of a variety of substances inside the brain. Many substances found in the CSF originate from the secretory epithelium of the choroid plexi that reach into the ventricular cavities. This secretome comprises metabolites, hormones, proteins, EVs, and so forth. Here we focus on two likely EV targets, the NSC niche of the SVZ (Doetsch et al., 1999; Obernier & Alvarez-Buylla, 2019) and the NSCs that reside in the tanycyte region (Haan et al., 2013; Robins et al., 2013). Both niches are in contact with CSF and hence in contact with EVs. We established an assay in which EVs^{Z310} secreted by the Z310-choroid plexus cell line were brought into contact with NSCs obtained from neurospheres that were generated either from the SVZ or the tanycyte region. Both, NSC^{SVZ} and NSC^{tz} formed, within 24 h, complex cellular networks that begun to express neuronal (Tuj1, *Cdh2*) and astrocytic markers (GFAP, *Gfap*). The differentiation-inducing activity resided in EV^{Z310} with a diameter of 50–150 nm that was purified by differential centrifugation and/or iodixanol density gradient centrifugation. The activity contained in EV^{Z310} was resistant to DNase, RNase and proteinase K treatment, suggesting that the inducing activity was an EV component protected by the EV bilayer membrane and was not a contaminant co-purifying with the EVs. It should be recalled that the NSC^{SVZ} used in our study are a mixture of quiescent, active NSCs and transit-amplifying cells that differ in both, expression levels of marker genes and the rate of proliferation (Silva-Vargas et al., 2016). In the case of NSC^{tz}, there is presently no evidence for the existence of such sub-types. Our neurospheres may not fully replicate a NSC niche because they are deprived of the influence of other niche cells (Langlet et al., 2013; Obernier & Alvarez-Buylla, 2019). Nevertheless, neurospheres have been effectively used in many studies investigating the process of NSC differentiation (Haan et al., 2013; Lepko et al., 2019; Robins et al., 2013; Silva-Vargas et al., 2016).

Our use of a choroid plexus cell line and of primary cultures has some limitations. Choroid plexus is the main producer of CSF but not the only one (Damkier et al., 2010). CSF-born EVs also originate, for example, from ependymal cells that form the walls of the ventricles. Such EVs are obviously missing in our preparation. Z310 cells are used as a surrogate for choroid plexus and they are derived from adult choroid plexus tissue (see references in Materials and Methods). In the adult animal, the composition of CSF, and by implication the cargo of CSF-born EVs will depend on physiological state of the organism (Cravatt et al., 1995; Myung et al., 2018; Tietje et al., 2014; Zhang et al., 2017). It is unlikely that the Z310-derived EVs reflect this complexity in full. Nevertheless, we were able to isolate a biological activity (EV^{Z310} and EV^{CHP}) that rapidly induces cell networks from two types of NSCs. EV^{CHP} was as effective in this process as EV^{Z310}, so the Z310 cells can be used as substitute source for choroid plexus-born EVs. This activity purifies over multiple centrifugation steps and yields a distinct EV fraction containing vesicles in 50–150-nm range. This simple purification scheme can readily be extended to a whole spectrum of other types of EVs isolated from different cells (astrocytes, ependymal cells) and from other brain tissues. Our high-throughput dry drop assay offers a test bed for cellular responses such as the formation of cellular processes or the expression of particular marker genes.

EVs^{MEF} secreted by MEFs had only a minor effect on NSCs. Cells formed small aggregates but never any of those cellular networks seen after treatment with EVs^{Z310} and EVs^{CHP}. In addition, none of the neural/glial differentiation markers was induced by EVs^{MEF}. EVs^{Z310} and EVs^{MEF} showed marked differences in their protein composition. This difference might shed light on the factors that evoke cell differentiation. The most significant difference was the presence of ∼250 ‘membrane’ proteins in the EV^{Z310}. String analysis of possible protein–protein interaction revealed interacting proteins involved in ‘neurogenesis’, ‘cell differentiation’, ’membrane trafficking and organization’.

Slit homolog 2 protein (Slit2), which is one of the proteins identified only in EV^{Z310} cargo by mass spectrometry and Western blotting, could contribute to the formation of cell processes that characterize the cell network. Slit proteins serve as repulsive axon guiding molecules via Slit-Robo signalling and it was suggested that choroid plexus is a source of Slit (Kaneko et al., 2018; Nguyen-Ba-Charvet & Chédotal, 2002; Sawamoto et al., 2006). Synaptogenesis is required for proper neuron function and we identified several synaptic proteins in EV^{Z310}, such as synaptotagmin1, and 2, and the synaptic vesicle membrane protein VAT-1. Synaptotagmins are calcium sensors participating in triggering neurotransmitter release at the synapse and also play a role in synaptic vesicle trafficking.VAT-1 is involved in synaptic vesicle transport.

EVs^{Z310} induced astrocytes that expressed a characteristic marker, GFAP. *Gfap* transcription is up-regulated by the transcription factor Stat3 and the transcriptional activator Brg1 (also known as Smarca4) (Brenner & Messing, 2021; Ito et al., 2018). Stat3 and Smarca4 were identified by MS in EV^{Z310} and confirmed by Western blotting. Stat3 also regulates *cdh2* expression via Jak/Stat pathway (Loh et al., 2019) and our qPCR data showed that *cdh2* expression was up-regulated upon EV^{Z310} addition. The EV^{Z310} also caries integrins and small GTPases, such as Ras Homolog Gene Family Member A (Rhoa) and RAC, which also regulate *cdh2* expression (Barcelona-Estaje et al., 2021). *Vimentin* is also induced by Stat3 signalling (Wu et al., 2004). While GFAP and Cdh2 were not identified in EV^{Z310}, these vesicles contain vimentin. There is also vimentin in NSCs prior to their exposure to EV^{Z310}. In this case, vimentin seen after EV-treatment could be a mixture of cellular and EV-derived vimentin. In our assays, we observed intense fn1 staining at or near the tip of the cellular processes. Such staining may arise from fibronectin1 contained in EV^{Z310} that locally aggregate. Note, however, that cells also express and secrete endogenous fn1 that could also be present at the tip, either inside or outside of the cell. Other adhesion proteins and scaffolding proteins (integrins, tetraspanins) are present in EVs^{Z310} and could act as guidance cues that control the outgrowth of the nascent NSC processes. Growing tips of axons can rapidly detect and react to the local guidance cues (Holt et al., 2019). Such guidance cues can also initiate local synthesis of different proteins in the distal part of axons (Cagnetta et al., 2018). In this case, EVs may not be taken up by the NSCs, but are acting as exogenous guidance posts. There are precedents for cellular responses to EVs that do not require EV internalization (Margolis

& Sadovsky, 2019; Mckelvey et al., 2015). EVs may collapse on the cell surface and release the protein cargo that subsequently interacts with cell surface receptors (Alabi & Tsien, 2013).

Since the purified EVs are heterogeneous, only a sub-set of the EV^{Z310}-specific proteins would be present in any given EV. EVs with a diameter of 150 nm have a volume that is nearly fifty times greater than that of a synaptic vesicle (40 nm) that contains about 160 protein molecules (Takamori et al., 2006; Taoufiq et al., 2020). Hence, a single EV could contain thousands of protein molecules. Assuming that the NSC targets incorporate multiple EVs, collectively such vesicles could confer entire signalling pathways to the target cells. In developmental biology, and the change in cell morphology is a developmental process, multiple signals converge on a single tissue. For example, the developing limb of vertebrates is controlled by a combination of growth- and transcription factors (Zuniga & Zeller, 2020). In this case, the signals are not packaged in EVs but are soluble local mediators. This is different for the NSC niches in the adult brain where signals must travel several millimetres even in mice and much farther in larger brains. A long-range transport of the multiple signals would benefit from an enclosure of signals in a carrier vesicle.

Induction of *gfap, stat3* and *fn1* expression was dependent on the amount of EVs added to the culture. Such dose dependence and the accompanying saturation suggest that EVs are involved in a receptor-mediated process. This could be an interaction with cell surface receptors or receptor-mediated EV uptake (Russell et al., 2019). Work by others shows that target cells internalize EVs in a time- and dosage-dependent manner (Bonsergent et al., 2021; Song et al., 2021). Bonsergent et al. suggested that EV uptake is a low-yield process, and only about 30% of internalized EVs were capable of delivering their contents. In their study, a dose response was observed but saturation could not be reached, even when a dose >100 μg/mL (doses refer to EV protein content) was used (Bonsergent et al., 2021). Song et al. observed that EV uptake by mouse embryonic stem cells was dose- and time-dependent over a 1-day period. EV internalization was detected at an EV level of 2×10^9 but increased significantly when the concentration was fivefold higher (Song et al., 2021). Sharma et al. showed that EV addition rescued the decrease of the total cell number and neurons in a loss-of-function neural model in dose-dependent manner (47.5–190 μg/mL) (Sharma et al., 2019). EV^{MEF} were inactive in our assay, even when a very high dose (608 μg/mL) was provided. The cause for this may be that the NSC target and fibroblast-derived EVs^{MEF} are not compatible. The combination of choroid plexus-derived EVs^{Z310} and NSCs, however, reproduces a naturally occurring situation. At a dose of 76 μg/mL protein (approximate the ED$_{50}$), a dry drop contains 1.6×10^6 EVs. A typical dry drop contains 2500 NSCs. Thus, there are ~800 EVs per cell. As pointed out above, EVs are heterogeneous and only a fraction may be acting in the network forming process. Thus, a rather small number of EVs may be sufficient to evoke cell differentiation.

Adding EVs^{Z310} suspended in buffer to the NSCs or, alternatively providing EVs as a dried-down drop-induced network formation. Even when the dry drops are kept at −20°C for a week, they were still very active. This indicates that the activity is stable in the EV for a significant length of time. Thus, our dry-drop assay allows testing of diverse EVs and multiple responsive cells in a short time and with minimal amounts of testing material. Moreover, this assay is high throughput. This allows a more efficient purification of EV proteins and other factors (e.g., miRNAs (Lepko et al., 2019; Yagi et al., 2017)) that mediate the effects that EVs exert on their target cells.

AUTHOR CONTRIBUTIONS

Zuzana Ditte and Gregor Eichele designed the study. Zuzana Ditte performed most of the experiment. Ivan Silbern performed mass spectrometric analysis. Zuzana Ditte and Peter Ditte performed qPCR. Peter Ditte isolated MEF. Zuzana Ditte, Ivan Silbern, Peter Ditte, Henning Urlaub and Gregor Eichele analysed and interpreted data, and revised the content critically. Zuzana Ditte and Gregor Eichele wrote the manuscript with inputs from other authors. All authors read and approved the final version of the manuscript.

ACKNOWLEDGEMENTS

We thank A. Stoykova, A.K Güntner and T. Rabe for helpful discussions. We thank D. Riedel from the Electron Microscopy facility (Department of Structural Dynamics, MPI-NAT), for the electron microscopy analyses. We thank M. Osborne for discussion and comments on the manuscript. The choroid plexus cell line Z310 was kindly provided by R. Steinfield from University Medical Center Göttingen, Germany. We further thank M. Raabe, A. Reinelt and T. Dehne for their assistance in the sample preparation for the MS analysis. This work was supported by the Max Plank Society. H.U. is funded by the Deutsche Forschungsgemeinschaft through collaborative research center SFB1286.

Open access funding enabled and organized by Projekt DEAL.

CONFLICT OF INTEREST

The authors declare that there is no conflict of interest.

DATA AVAILABILITY STATEMENT

The mass spectrometry data have been deposited on the ProteomeXchange Consortium via the PRIDE (Perez-Riverol et al., 2019) partner repository with the dataset identifier PXD031862.

REFERENCES

Alabi, A. A., & Tsien, R. W. (2013). Perspectives on kiss-and-run: Role in exocytosis, endocytosis, and neurotransmission. *Annual Review of Physiology*, *75*, 393–422.

Balusu, S., Van Wonterghem, E., De Rycke, R., Raemdonck, K., Stremersch, S., Gevaert, K., Brkic, M., Demeestere, D., Vanhooren, V., Hendrix, A., Libert, C., & Vandenbroucke, R. E. (2016). Identification of a novel mechanism of blood-brain communication during peripheral inflammation via choroid plexus-derived extracellular vesicles. *EMBO Molecular Medicine*, *8*(10), 1162–1183.

Barcelona-Estaje, E., Dalby, M. J., Cantini, M., & Salmeron-Sanchez, M. (2021). You talking to me? Cadherin and integrin crosstalk in biomaterial design. *Advanced Healthcare Materials*, *10*(6), e2002048.

Bateman, A. (2019). UniProt Consortium. UniProt: A worldwide hub of protein knowledge. *Nucleic Acids Research*, *47*(D1), D506–D515.

Batiz, L. F., Castro, M. A., Burgos, P. V., Velásquez, Z. D., Muñoz, R. I., Lafourcade, C. A., Troncoso-Escudero, P., & Wyneken, U. (2015). Exosomes as novel regulators of adult neurogenic niches. *Frontiers in Cellular Neuroscience*, *9*, 501.

Bonsergent, E., Grisard, E., Buchrieser, J., Schwartz, O., Théry, C., & Lavieu, G. (2021). Quantitative characterization of extracellular vesicle uptake and content delivery within mammalian cells. *Nature Communication*, *12*(1), 1864.

Brenner, M., & Messing, A. (2021). Regulation of GFAP expression. *ASN Neuro*, *13*, 175909142098120.

Cagnetta, R., Frese, C. K., Shigeoka, T., Krijgsveld, J., & Holt, C. E. (2018). Rapid cue-specific remodeling of the nascent axonal proteome. *Neuron*, *99*(1), 29–46.e4.

Chau, K. F., Springel, M. W., Broadbelt, K. G., Park, H.-Y., Topal, S., Lun, M. P., Mullan, H., Maynard, T., Steen, H., Lamantia, A. S., & Lehtinen, M. K. (2015). Progressive differentiation and instructive capacities of amniotic fluid and cerebrospinal fluid proteomes following neural tube closure. *Developmental Cell*, *35*(6), 789–802.

Cox, J. R., Neuhauser, N., Michalski, A., Scheltema, R. A., Olsen, J. V., & Mann, M. (2011). Andromeda: A peptide search engine integrated into the MaxQuant environment. *Journal of Proteome Research*, *10*(4), 1794–1805.

Cravatt, B. F., Prospero-Garcia, O., Siuzdak, G., Gilula, N. B., Henriksen, S. J., Boger, D. L., & Lerner, R. A. (1995). Chemical characterization of a family of brain lipids that induce sleep. *Science*, *268*(5216), 1506–1509.

Crescitelli, R., Lässer, C., Jang, S. C., Cvjetkovic, A., Malmhäll, C., Karimi, N., Höög, J. L., Johansson, I., Fuchs, J., Thorsell, A., Gho, Y. S., Olofsson Bagge, R., & Lötvall, J. (2020). Subpopulations of extracellular vesicles from human metastatic melanoma tissue identified by quantitative proteomics after optimized isolation. *Journal of Extracellular Vesicles*, *9*(1), 1722433.

Cserr, H. F. (1971). Physiology of the choroid plexus. *Physiological Reviews*, *51*(2), 273–311.

Damkier, H. H., Brown, P. D., & Praetorius, J. (2010). Epithelial pathways in choroid plexus electrolyte transport. *Physiology (Bethesda, Md.)*, *25*(4), 239–249.

Del Bigio, M. R. (2010). Ependymal cells: Biology and pathology. *Acta Neuropathologica*, *119*(1), 55–73.

De Sonnaville, S., Van Strien, M. E., Middeldorp, J., Sluijs, J. A., Van Den Berge, S. A., Moeton, M., Donega, V., Van Berkel, A., Deering, T., De Filippis, L., Vescovi, A. L., Aronica, E., Glass, R., Van De Berg, W. D. J., Swaab, D. F., Robe, P. A., & Hol, E. M. (2020). The adult human subventricular zone: Partial ependymal coverage and proliferative capacity of cerebrospinal fluid. *Brain Communications*, *2*(2), fcaa150.

Dhavan, R., & Tsai, L.-H. (2001). A decade of CDK5. *Nature Reviews Molecular Cell Biology*, *2*(10), 749–759.

Doetsch, F., Caillé, I., Lim, D. A., Garcã-A-Verdugo, J. M., & Alvarez-Buylla, A. (1999). Subventricular zone astrocytes are neural stem cells in the adult mammalian brain. *Cell*, *97*(6), 703–716.

Dorrier, C. E., Aran, D., Haenelt, E. A., Sheehy, R. N., Hoi, K. K., Pintarić, L., Chen, Y., Lizama, C. O., Cautivo, K. M., Weiner, G. A., Popko, B., Fancy, S. P. J., Arnold, T. D., & Daneman, R. (2021). CNS fibroblasts form a fibrotic scar in response to immune cell infiltration. *Nature Neuroscience*, *24*(2), 234–244.

Dorrier, C. E., Jones, H. E., Pintarić, L., Siegenthaler, J. A., & Daneman, R. (2022). Emerging roles for CNS fibroblasts in health, injury and disease. *Nature Reviews Neuroscience*, *23*(1), 23–34.

Eichele, G., Bodenschatz, E., Ditte, Z., Günther, A.-K., Kapoor, S., Wang, Y., & Westendorf, C. (2020). Cilia-driven flows in the brain third ventricle. *Philosophical Transactions of the Royal Society of London. Series B: Biological Sciences*, *375*, 20190154.

Fame, R. M., & Lehtinen, M. K. (2020). Emergence and developmental roles of the cerebrospinal fluid system. *Developmental Cell*, *52*(3), 261–275.

Faubel, R., Westendorf, C., Bodenschatz, E., & Eichele, G. (2016). Cilia-based flow network in the brain ventricles. *Science*, *353*(6295), 176–178.

Feliciano, D. M., Zhang, S., Nasrallah, C. M., Lisgo, S. N., & Bordey, A. (2014). Embryonic cerebrospinal fluid nanovesicles carry evolutionarily conserved molecules and promote neural stem cell amplification. *Plos One*, *9*(2), e88810.

Frühbeis, C., Fröhlich, D., Kuo, W. P., Amphornrat, J., Thilemann, S., Saab, A. S., Kirchhoff, F., Möbius, W., Goebbels, S., Nave, K.-A., Schneider, A., Simons, M., Klugmann, M., Trotter, J., & Krämer-Albers, E.-M. (2013). Neurotransmitter-triggered transfer of exosomes mediates oligodendrocyte-neuron communication. *Plos Biology*, *11*(7), e1001604.

Ghersi-Egea, J.-F., Strazielle, N., Catala, M., Silva-Vargas, V., Doetsch, F., & Engelhardt, B. (2018). Molecular anatomy and functions of the choroidal blood-cerebrospinal fluid barrier in health and disease. *Acta Neuropathologica*, *135*(3), 337–361.

Grapp, M., Wrede, A., Schweizer, M., Hüwel, S., Galla, H.-J., Snaidero, N., Simons, M., Bückers, J., Low, P. S., Urlaub, H., Gärtner, J., & Steinfeld, R. (2013). Choroid plexus transcytosis and exosome shuttling deliver folate into brain parenchyma. *Nature Communication*, *4*, 2123.

Haan, N., Goodman, T., Najdi-Samiei, A., Stratford, C. M., Rice, R., El Agha, E., Bellusci, S., & Hajihosseini, M. K. (2013). Fgf10-expressing tanycytes add new neurons to the appetite/energy-balance regulating centers of the postnatal and adult hypothalamus. *Journal of Neuroscience*, *33*(14), 6170–6180.

Hasselblatt, M., Mertsch, S., Koos, B., Riesmeier, B., Stegemann, H., Jeibmann, A., Tomm, M., Schmitz, N., Wrede, B., Wolff, J. E., Zheng, W., & Paulus, W. (2009). TWIST-1 is overexpressed in neoplastic choroid plexus epithelial cells and promotes proliferation and invasion. *Cancer Research*, *69*(6), 2219–2223.

Hayashi, T., Lombaert, I. M. A., Hauser, B. R., Patel, V. N., & Hoffman, M. P. (2017). Exosomal MicroRNA transport from salivary mesenchyme regulates epithelial progenitor expansion during organogenesis. *Developmental Cell*, *40*(1), 95–103.

Hladky, S. B., & Barrand, M. A. (2014). Mechanisms of fluid movement into, through and out of the brain: Evaluation of the evidence. *Fluids Barriers CNS*, *11*(1), 26.

Holt, C. E., Martin, K. C., & Schuman, E. M. (2019). Local translation in neurons: Visualization and function. *Nature Structural & Molecular Biology*, *26*(7), 557–566.

Horiguchi, K., Yoshida, S., Hasegawa, R., Takigami, S., Ohsako, S., Kato, T., & Kato, Y. (2020). Isolation and characterization of cluster of differentiation 9-positive ependymal cells as potential adult neural stem/progenitor cells in the third ventricle of adult rats. *Cell and Tissue Research*, *379*(3), 497–509.

Hughes, C. S., Foehr, S., Garfield, D. A., Furlong, E. E., Steinmetz, L. M., & Krijgsveld, J. (2014). Ultrasensitive proteome analysis using paramagnetic bead technology. *Molecular Systems Biology*, *10*(10), 757.

Ito, K., Noguchi, A., Uosaki, Y., Taga, T., Arakawa, H., & Takizawa, T. (2018). Gfap and Osmr regulation by BRG1 and STAT3 via interchromosomal gene clustering in astrocytes. *Molecular Biology of the Cell*, *29*(2), 209–219.

Johnstone, R. M., Adam, M., Hammond, J. R., Orr, L., & Turbide, C. (1987). Vesicle formation during reticulocyte maturation. Association of plasma membrane activities with released vesicles (exosomes). *Journal of Biological Chemistry*, *262*(19), 9412–9420.

Kaiser, K., Gyllborg, D., Procházka, J., Salašová, A., Kompaníková, P., & Bryja, V. (2019). WNT5A is transported via lipoprotein particles in the cerebrospinal fluid to regulate hindbrain morphogenesis. *Nature Communications*, *10*, 1498.

Kalra, H., Simpson, R. J., Ji, H., Aikawa, E., Altevogt, P., Askenase, P., Bond, V. C., Borràs, F. E., Breakefield, X., Budnik, V., Buzas, E., Camussi, G., Clayton, A., Cocucci, E., Falcon-Perez, J. M., Gabrielsson, S., Gho, Y. S., Gupta, D., Harsha, H. C., & Mathivanan, S. (2012). Vesiclepedia: A compendium for extracellular vesicles with continuous community annotation. *PLoS Biology*, *10*(12), e1001450. https://www.microvesicles.org

Kaneko, N., Herranz-Perez, V., Otsuka, T., Sano, H., Ohno, N., Omata, T., Nguyen, H. B., Thai, T. Q., Nambu, A., Kawaguchi, Y., Garcã-A-Verdugo, J. M., & Sawamoto, K. (2018). New neurons use Slit-Robo signaling to migrate through the glial meshwork and approach a lesion for functional regeneration. *Science Advances*, *4*(12), eaav0618.

Keerthikumar, S., Chisanga, D., Ariyaratne, D., Al Saffar, H., Anand, S., Zhao, K., Samuel, M., Pathan, M., Jois, M., Chilamkurti, N., Gangoda, L., & Mathivanan, S. (2016). ExoCarta: A web-based compendium of exosomal cargo. *Journal of Molecular Biology*, *428*(4), 688–692. https://www.exocarta.org

Kläs, J., Wolburg, H., Terasaki, T., Fricker, G., & Reichel, V. (2010). Characterization of immortalized choroid plexus epithelial cell lines for studies of transport processes across the blood-cerebrospinal fluid barrier. *Cerebrospinal Fluid Research*, *7*, 11.

Kokovay, E., Wang, Y., Kusek, G., Wurster, R., Lederman, P., Lowry, N., Shen, Q., & Temple, S. (2012). VCAM1 is essential to maintain the structure of the SVZ niche and acts as an environmental sensor to regulate SVZ lineage progression. *Cell Stem Cell*, *11*(2), 220–230.

Konoshenko, M. Y., Lekchnov, E. A., Vlassov, A. V., & Laktionov, P. P. (2018). Isolation of extracellular vesicles: General methodologies and latest trends. *Biomed Research International*, *2018*, 8545347.

Kowal, J., Arras, G., Colombo, M., Jouve, M., Morath, J. P., Primdal-Bengtson, B., Dingli, F., Loew, D., Tkach, M., & Thery, C. (2016). Proteomic comparison defines novel markers to characterize heterogeneous populations of extracellular vesicle subtypes. *Proceedings National Academy of Science United States of America*, *113*(8), E968–E977.

Langlet, F., Mullier, A., Bouret, S. G., Prevot, V., & Dehouck, B. (2013). Tanycyte-like cells form a blood-cerebrospinal fluid barrier in the circumventricular organs of the mouse brain. *Journal of Comparative Neurology*, *521*(15), 3389–3405.

Lehtinen, M. K., Zappaterra, M. W., Chen, X., Yang, Y. J., Hill, A. D., Lun, M., Maynard, T., Gonzalez, D., Kim, S., Ye, P., D'ercole, A., Wong, E. T., Lamantia, A. S., & Walsh, C. A. (2011). The cerebrospinal fluid provides a proliferative niche for neural progenitor cells. *Neuron*, *69*(5), 893–905.

Lepko, T., Pusch, M., Müller, T., Schulte, D., Ehses, J., Kiebler, M., Hasler, J., Huttner, H. B., Vandenbroucke, R. E., Vandendriessche, C., Modic, M., Martin-Villalba, A., Zhao, S., Llorens-Bobadilla, E., Schneider, A., Fischer, A., Breunig, C. T., Stricker, S. H., Götz, M., & Ninkovic, J. (2019). Choroid plexus-derived miR-204 regulates the number of quiescent neural stem cells in the adult brain. *EMBO Journal*, *38*(17), e100481.

Loh, C. Y., Chai, J. Y., Tang, T. F., Wong, W. F., Sethi, G., Shanmugam, M. K., Chong, P. P., & Looi, C. Y. (2019). The E-cadherin and N-cadherin switch in epithelial-to-mesenchymal transition: Signaling, therapeutic implications, and challenges. *Cells*, *8*(10), 1118.

Lopez-Verrilli, M.-A. A., Picou, F., & Court, F. A. (2013). Schwann cell-derived exosomes enhance axonal regeneration in the peripheral nervous system. *Glia*, *61*(11), 1795–1806.

Losurdo, M., & Grilli, M. (2020). Influential players of intercellular communication within adult neurogenic niches. *International Journal of Molecular Sciences*, *21*(22), 8819.

Luga, V., Zhang, L., Viloria-Petit, A. M., Ogunjimi, A. A., Inanlou, M. R., Chiu, E., Buchanan, M., Hosein, A. N., Basik, M., & Wrana, J. L. (2012). Exosomes mediate stromal mobilization of autocrine Wnt-PCP signaling in breast cancer cell migration. *Cell*, *151*(7), 1542–1556.

Lun, M. P., Monuki, E. S., & Lehtinen, M. K. (2015). Development and functions of the choroid plexus-cerebrospinal fluid system. *Nature Reviews Neuroscience*, *16*(8), 445–457.

Margolis, L., & Sadovsky, Y. (2019). The biology of extracellular vesicles: The known unknowns. *Plos Biology*, *17*(7), e3000363.

Mathieu, M., Martin-Jaular, L., Lavieu, G., & Thery, C. (2019). Specificities of secretion and uptake of exosomes and other extracellular vesicles for cell-to-cell communication. *Nature Cell Biology*, *21*(1), 9–17.

Mckelvey, K. J., Powell, K. L., Ashton, A. W., Morris, J. M., & Mccracken, S. A. (2015). Exosomes: Mechanisms of uptake. *Journal of Circulating Biomarkers*, *4*, 7.

Men, Y., Yelick, J., Jin, S., Tian, Y., Chiang, M. S. R., Higashimori, H., Brown, E., Jarvis, R., & Yang, Y. (2019). Exosome reporter mice reveal the involvement of exosomes in mediating neuron to astroglia communication in the CNS. *Nature Communication*, *10*(1), 4136.

Menheniott, T. R., Charalambous, M., & Ward, A. (2010). Derivation of primary choroid plexus epithelial cells from the mouse. *Methods in Molecular Biology*, *633*, 207–220.

Mirzadeh, Z., Han, Y.-G., Soriano-Navarro, M., Garcia-Verdugo, J. M., & Alvarez-Buylla, A. (2010). Cilia organize ependymal planar polarity. *Journal of Neuroscience*, *30*(7), 2600–2610.

Morel, L., Regan, M., Higashimori, H., Ng, S. K., Esau, C., Vidensky, S., Rothstein, J., & Yang, Y. (2013). Neuronal exosomal miRNA-dependent translational regulation of astroglial glutamate transporter GLT1. *Journal of Biological Chemistry*, *288*(10), 7105–7116.

Murillo, O. D., Thistlethwaite, W., Rozowsky, J., Subramanian, S. L., Lucero, R., Shah, N., Jackson, A. R., Srinivasan, S., Chung, A., Laurent, C. D., Kitchen, R. R., Galeev, T., Warrell, J., Diao, J. A., Welsh, J. A., Hanspers, K., Riutta, A., Burgstaller-Muehlbacher, S., Shah, R. V., & Milosavljevic, A. (2019). exRNA atlas analysis reveals distinct extracellular RNA cargo types and their carriers present across human biofluids. *Cell*, *177*(2), 463–477.

Myung, J., Schmal, C., Hong, S., Tsukizawa, Y., Rose, P., Zhang, Y., Holtzman, M. J., De Schutter, E., Herzel, H., Bordyugov, G., & Takumi, T. (2018). The choroid plexus is an important circadian clock component. *Nature Communication*, *9*(1), 1062.

Nakano, S., Yamamoto, S., Okada, A., Nakajima, T., Sato, M., Takagi, T., & Tomooka, Y. (2017). Role of extracellular vesicles in the interaction between epithelial and mesenchymal cells during oviductal ciliogenesis. *Biochemical and Biophysical Research Communications*, *483*(1), 245–251.

Nguyen-Ba-Charvet, K. T., & Chédotal, A. (2002). Role of Slit proteins in the vertebrate brain. *Journal of Physiology, Paris*, *96*(1-2), 91–98.

Obernier, K., & Alvarez-Buylla, A. (2019). Neural stem cells: Origin, heterogeneity and regulation in the adult mammalian brain. *Development (Cambridge, England)*, *146*(4), dev156059.

Pellegrino, G., Trubert, C., Terrien, J., Pifferi, F., Leroy, D., Loyens, A., Migaud, M., Baroncini, M., Maurage, C.-A., Fontaine, C., Prévot, V., & Sharif, A. (2018). A comparative study of the neural stem cell niche in the adult hypothalamus of human, mouse, rat and gray mouse lemur (Microcebus murinus). *Journal of Comparative Neurology*, *526*(9), 1419–1443.

Perez-Riverol, Y., Csordas, A., Bai, J., Bernal-Llinares, M., Hewapathirana, S., Kundu, D. J., Inuganti, A., Griss, J., Mayer, G., Eisenacher, M., Pérez, E., Uszkoreit, J., Pfeuffer, J., Sachsenberg, T., Yılmaz, Ş., Tiwary, S., Cox, J., Audain, E., Walzer, M., & Vizcaíno, J. A. (2019). The PRIDE database and related tools and resources in 2019: Improving support for quantification data. *Nucleic Acids Research*, *47*(D1), D442–D450.

Robins, S. C., Stewart, I., Mcnay, D. E., Taylor, V., Giachino, C., Götz, M., Ninkovic, J., Briancon, N., Maratos-Flier, E., Flier, J. S., Kokoeva, M. V., & Placzek, M. (2013). alpha-Tanycytes of the adult hypothalamic third ventricle include distinct populations of FGF-responsive neural progenitors. *Nature Communication*, *4*, 2049.

Russell, A. E., Sneider, A., Witwer, K. W., Bergese, P., Bhattacharyya, S. N., Cocks, A., Cocucci, E., Erdbrügger, U., Falcon-Perez, J. M., Freeman, D. W., Gallagher, T. M., Hu, S., Huang, Y., Jay, S. M., Kano, S. I., Lavieu, G., Leszczynska, A., Llorente, A. M., Lu, Q., & Vader, P. (2019). Biological membranes in EV biogenesis, stability, uptake, and cargo transfer: An ISEV position paper arising from the ISEV membranes and EVs workshop. *Journal of Extracellular Vesicles*, *8*(1), 1684862.

Sawamoto, K., Wichterle, H., Gonzalez-Perez, O., Cholfin, J. A., Yamada, M., Spassky, N., Murcia, N. S., Garcia-Verdugo, J. M., Marin, O., Rubenstein, J. L. R., Tessier-Lavigne, M., Okano, H., & Alvarez-Buylla, A. (2006). New neurons follow the flow of cerebrospinal fluid in the adult brain. *Science*, *311*(5761), 629–632.

Schwanhäusser, B., Busse, D., Li, N., Dittmar, G., Schuchhardt, J., Wolf, J., Chen, W., & Selbach, M. (2011). Global quantification of mammalian gene expression control. *Nature*, *473*(7347), 337–342.

Seri, B., Garcã-A-Verdugo, J., Collado-Morente, L., Mcewen, B. S., & Alvarez-Buylla, A. (2004). Cell types, lineage, and architecture of the germinal zone in the adult dentate gyrus. *Journal of Comparative Neurology*, *478*(4), 359–378.

Sharma, K. D., Schaal, D., Kore, R. A., Hamzah, R. N., Pandanaboina, S. C., Hayar, A., Griffin, R. J., Srivatsan, M., Reyna, N. S., & Xie, J. Y. (2020). Glioma-derived exosomes drive the differentiation of neural stem cells to astrocytes. *Plos One*, *15*(7), e0234614.

Sharma, P., Mesci, P., Carromeu, C., Mcclatchy, D. R., Schiapparelli, L., Yates, J. R., Muotri, A. R., & Cline, H. T. (2019). Exosomes regulate neurogenesis and circuit assembly. *Proceedings National Academy of Science United States of America*, *116*(32), 16086–16094.

Shi, L. Z., Li, G. J., Wang, S., & Zheng, W. (2008). Use of Z310 cells as an in vitro blood-cerebrospinal fluid barrier model: Tight junction proteins and transport properties. *Toxicology in Vitro*, *22*(1), 190–199.

Shurtleff, M. J., Temoche-Diaz, M. M., & Schekman, R. (2018). Extracellular vesicles and cancer: Caveat lector. *Annual Review of Cancer Biology*, *2*, 395–411.

Shurtleff, M. J., Yao, J., Qin, Y., Nottingham, R. M., Temoche-Diaz, M. M., Schekman, R., & Lambowitz, A. M. (2017). Broad role for YBX1 in defining the small noncoding RNA composition of exosomes. *Proceedings National Academy of Science United States of America*, *114*(43), E8987–E8995.

Silbern, I., Fang, P., Ji, Y., Christof, L., Urlaub, H., & Pan, K.-T. (2021). Relative quantification of phosphorylated and glycosylated peptides from the same sample using isobaric chemical labelling with a two-step enrichment strategy. *Quantitative Methods in Proteomics*, *2228*, 185–203. 2 Edition.

Silva-Vargas, V., Maldonado-Soto, A. R., Mizrak, D., Codega, P., & Doetsch, F. (2016). Age-dependent niche signals from the choroid plexus regulate adult neural stem cells. *Cell Stem Cell*, *19*(5), 643–652.

Smyth, G. K. (2005). limma: Linear models for microarray data. *Bioinformatics and Computational Biology Solution Using R and Bioconductor*, *2005*, 397–420.

Song, L., Tian, X., & Schekman, R. (2021). Extracellular vesicles from neurons promote neural induction of stem cells through cyclin D1. *Journal of Cell Biology*, *220*(9), e202101075.

Storey, J. D. (2002). A direct approach to false discovery rates. *Journal of the Royal Statistical Society Series B-Statistical Methodology*, *64*, 479–498.

Street, J. M., Barran, P. E., Mackay, C. L., Weidt, S., Balmforth, C., Walsh, T. S., Chalmers, R. T., Webb, D. J., & Dear, J. W. (2012). Identification and proteomic profiling of exosomes in human cerebrospinal fluid. *Journal of Translational Medicine*, *10*, 5.

Szmydynger-Chodobska, J., Pascale, C. L., Pfeffer, A. N., Coulter, C., & Chodobski, A. (2007). Expression of junctional proteins in choroid plexus epithelial cell lines: A comparative study. *Cerebrospinal Fluid Research*, *4*, 11.

Takamori, S., Holt, M., Stenius, K., Lemke, E. A., Grønborg, M., Riedel, D., Urlaub, H., Schenck, S., Brügger, B., Ringler, P., Müller, S. A., Rammner, B., Gräter, F., Hub, J. S., De Groot, B. L., Mieskes, G., Moriyama, Y., Klingauf, J., Grubmüller, H., & Jahn, R. (2006). Molecular anatomy of a trafficking organelle. *Cell*, *127*(4), 831–846.

Taoufiq, Z., Ninov, M., Villar-Briones, A., Wang, H.-Y., Sasaki, T., Roy, M. C., Beauchain, F., Mori, Y., Yoshida, T., Takamori, S., Jahn, R., & Takahashi, T. (2020). Hidden proteome of synaptic vesicles in the mammalian brain. *Proceedings National Academy of Science United States of America*, *117*(52), 33586–33596.

Thery, C., Witwer, K. W., Aikawa, E., Alcaraz, M. J., Anderson, J. D., Andriantsitohaina, R., Antoniou, A., Arab, T., Archer, F., Atkin-Smith, G. K., Ayre, D. C., Bach, J.-M., Bachurski, D., Baharvand, H., Balaj, L., Baldacchino, S., Bauer, N. N., Baxter, A. A., Bebawy, M., & Zuba-Surma, E. K. (2018). Minimal information for studies of extracellular vesicles 2018 (MISEV2018): A position statement of the International Society for Extracellular Vesicles and update of the MISEV2014 guidelines. *Journal of Extracellular Vesicles*, *7*(1), 1535750.

Tietje, A., Maron, K. N., Wei, Y., & Feliciano, D. M. (2014). Cerebrospinal fluid extracellular vesicles undergo age dependent declines and contain known and novel non-coding RNAs. *Plos One*, *9*(11), e113116.

Tkach, M., Kowal, J., & Thery, C. (2018). Why the need and how to approach the functional diversity of extracellular vesicles. *Philosophical Transactions of the Royal Society of London. Series B: Biological Sciences*, *373*(1737), 20160479.

Valadi, H., Ekström, K., Bossios, A., Sjöstrand, M., Lee, J. J., & Lötvall, J. O. (2007). Exosome-mediated transfer of mRNAs and microRNAs is a novel mechanism of genetic exchange between cells. *Nature Cell Biology*, *9*(6), 654–659.

Van Niel, G., D'angelo, G., & Raposo, G. (2018). Shedding light on the cell biology of extracellular vesicles. *Nature Reviews Molecular Cell Biology*, *19*(4), 213–228.

Van Niel, G., Porto-Carreiro, I., Simoes, S., & Raposo, G. (2006). Exosomes: A common pathway for a specialized function. *Journal of Biochemistry*, *140*(1), 13–21.

Vella, L. J., Greenwood, D. L. V., Cappai, R., Scheerlinck, J.-P., & Hill, A. F. (2008). Enrichment of prion protein in exosomes derived from ovine cerebral spinal fluid. *Veterinary Immunology and Immunopathology*, *124*(3-4), 385–393.

Walker, T. L., & Kempermann, G. (2014). One mouse, two cultures: Isolation and culture of adult neural stem cells from the two neurogenic zones of individual mice. *Journal of Visualized Experiments: JoVE*, *2014*(84), e51225.

Willis, C. M., Nicaise, A. M., Krzak, G., Ionescu, R.-B., Pappa, V., D'angelo, A., Agarwal, R., Repollés-de-Dalmau, M., Peruzzotti-Jametti, L., & Pluchino, S. (2022). Soluble factors influencing the neural stem cell niche in brain physiology, inflammation, and aging. *Experimental Neurology*, *355*, 114124.

Wu, Y., Diab, I., Zhang, X., Izmailova, E. S., & Zehner, Z. E. (2004). Stat3 enhances vimentin gene expression by binding to the antisilencer element and interacting with the repressor protein, ZBP-89. *Oncogene*, *23*(1), 168–178.

Yagi, Y., Ohkubo, T., Kawaji, H., Machida, A., Miyata, H., Goda, S., Roy, S., Hayashizaki, Y., Suzuki, H., & Yokota, T. (2017). Next-generation sequencing-based small RNA profiling of cerebrospinal fluid exosomes. *Neuroscience Letters*, *636*, 48–57.

Yoo, S., & Blackshaw, S. (2018). Regulation and function of neurogenesis in the adult mammalian hypothalamus. *Progress in Neurobiology*, *170*, 53–66.

Zappaterra, M. W., & Lehtinen, M. K. (2012). The cerebrospinal fluid: Regulator of neurogenesis, behavior, and beyond. *Cellular and Molecular Life Sciences*, *69*(17), 2863–2878.

Zhang, Y., Kim, M. S., Jia, B., Yan, J., Zuniga-Hertz, J. P., Han, C., & Cai, D. (2017). Hypothalamic stem cells control ageing speed partly through exosomal miRNAs. *Nature*, *548*(7665), 52–57.

Zheng, W., & Zhao, Q. (2002). Establishment and characterization of an immortalized Z310 choroidal epithelial cell line from murine choroid plexus. *Brain Research*, *958*(2), 371–380.

Zuniga, A., & Zeller, R. (2020). Dynamic and self-regulatory interactions among gene regulatory networks control vertebrate limb bud morphogenesis. *Current Topics in Developmental Biology*, *139*, 61–88.

SUPPORTING INFORMATION

Additional supporting information can be found online in the Supporting Information section at the end of this article.